

UNCLASSIFIED

AD NUMBER

AD349772

CLASSIFICATION CHANGES

TO: unclassified

FROM: confidential

LIMITATION CHANGES

TO:

Approved for public release, distribution
unlimited

FROM:

Notice: All release of this document is
controlled. All certified requesters shall
obtain release approval from Naval
Research Lab., Attn: Code 1221.1.
Washington, DC 20375.

AUTHORITY

NRL ltr, 20 Dec 2002; NRL ltr, 20 Dec 2002

THIS PAGE IS UNCLASSIFIED

UNCLASSIFIED

AD NUMBER
AD349772
CLASSIFICATION CHANGES
TO confidential
FROM secret
AUTHORITY
1976 per Group-3 document markings

THIS PAGE IS UNCLASSIFIED

~~SECRET~~

AD 349772

DEFENSE DOCUMENTATION CENTER

FOR

SCIENTIFIC AND TECHNICAL INFORMATION

CAMERON STATION, ALEXANDRIA, VIRGINIA



~~SECRET~~

NOTICE: When government or other drawings, specifications or other data are used for any purpose other than in connection with a definitely related government procurement operation, the U. S. Government thereby incurs no responsibility, nor any obligation whatsoever; and the fact that the Government may have formulated, furnished, or in any way supplied the said drawings, specifications, or other data is not to be regarded by implication or otherwise as in any manner licensing the holder or any other person or corporation, or conveying any rights or permission to manufacture, use or sell any patented invention that may in any way be related thereto.

NOTICE:

THIS DOCUMENT CONTAINS INFORMATION
AFFECTING THE NATIONAL DEFENSE OF
THE UNITED STATES WITHIN THE MEAN-
ING OF THE ESPIONAGE LAWS, TITLE 18,
U.S.C., SECTIONS 793 and 794. THE
TRANSMISSION OR THE REVELATION OF
ITS CONTENTS IN ANY MANNER TO AN
UNAUTHORIZED PERSON IS PROHIBITED
BY LAW.

SECRET

NRL Report 6077
Copy No. of 150 Copies

PROGRESS REPORT NO. 13

HYPERVELOCITY KILL MECHANISMS PROGRAM

[UNCLASSIFIED TITLE]

Sponsored by

Advanced Research Projects Agency
Ballistic Missile Defense Systems Branch
ARPA Order No. 149

Semiannual Technical Progress Report
for period ending 30 September 1963

SPECIAL HANDLING REQUIRED
NOT RELEASABLE TO FOREIGN NATIONALS

February 1964



U. S. NAVAL RESEARCH LABORATORY
Washington, D.C.

SECRET

Downgraded at 12 year intervals;
Not automatically declassified.

CATALOGED BY 60093 4-9-64
AS AD NO.

349772

CONTRIBUTORS

Aeronautical Research Associates of Princeton
AVCO Manufacturing Company - RAD Division
Ballistic Research Laboratories
General Electric Company - MSD
U.S. Naval Research Laboratory
Picatinny Arsenal

All distribution of this report is controlled. Qualified DDC users shall request through Director, U.S. Naval Research Laboratory, Washington D.C. - 20390.

This document contains information affecting the national defense of the United States within the meaning of the Espionage Laws, Title 18, U.S.C., Sections 793 and 794. The transmission or the revelation of its contents in any manner to an unauthorized person is prohibited.

SECRET

CONTENTS

	<u>Page Designation</u>
Problem Status	ii
Authorization	ii
PROGRAM SUMMARY	
INTRODUCTION	1
PROGRESS	1
REFERENCES	12
APPENDIX I - Review of Foaming Materials	1-1
HKM PROGRESS REPORTS	
I. IMPACT DAMAGE PHASE	
Ballistic Research Laboratories	A
U.S. Naval Research Laboratory	B
AVCO Mfg. Co. - RAD Division	C
II. AEROTHERMAL PHASE	
General Electric Co. - MSD	H
Aeronautical Research Associates of Princeton	L
III. VULNERABILITY	Q
IV. DISTRIBUTION LIST	Z

SECRET

Problem Status

This is the thirteenth progress report covering the work of the participants in the Hypervelocity Kill Mechanisms Program. Work on this problem is continuing.

Authorization

NRL Problem No. F04-11
ARPA Order No. 149-60
Amendments 1 through 7

SECRET

SUMMARY

W.W. Atkins - M.A. Parsechino
U.S. Naval Research Laboratory

INTRODUCTION

Progress Report No. 13 is a semiannual technical progress report covering the work of the participants in the Hypervelocity Kill Mechanisms Program for the period beginning 20 March 1963 through 30 September 1963. Reports covering the work completed during and prior to this reporting period are listed on the inside back cover of this report.

The work of this program has involved comprehensive studies designed to evaluate the feasibility of defeating the mission of an intercontinental ballistic missile by fragment impact and/or by subsequent re-entry heating effects. These effects include: direct kill by impact, extent of aggravation or increase in damage caused by aerothermal effects on an R/V during re-entry, aerodynamic instability of nose cones caused by damage to the heat shield and structure, impact and thermal damage to internal components and warheads, and perturbations on the performance of ICBM booster vehicles. The HKM Program is divided into the following four phases of work:

1. Impact Damage. - Initially BRL, NRL, AVCO and the Canadian Armament Research and Development Establishment were selected to study the effects of hypervelocity impacts on re-entry body materials and structures. Aerojet-General was selected to study the impact effects on propulsion systems. The work of Aerojet has been completed and the final report has been submitted to ASD for publication. The impact work performed by AVCO has also been completed and a final report is

SECRET

included in the body of this report (see Section C). The work completed by CARDE was reported in Progress Report No. 11. Only NRL and BRL are presently engaged in impact work for the HiKM Program.

2. Aerothermal. - In the early stages of the program, AVCO performed a multitude of experiments on cratered heat shield materials utilizing rocket exhaust and plasma jet facilities in order to determine the thermodynamic effects on a damaged vehicle during re-entry. In the later stages of the program, punctured vehicles (vented and unvented) were analyzed. GE and AVCO performed analytical and experimental studies on coupled and uncoupled flows, jet impingement, jet diffusion, and the determination of orifice coefficients for perforated re-entry vehicles. GE conducted an analytical study for determining the aerodynamic effects on a damaged vehicle during re-entry (the aeroballistic ranges and the wind tunnels of NOL and AEDC were utilized to provide experimental data). An effective kill mechanism did not evolve from these studies. During the latter part of the second year's effort ARAP was added to the participants in the aerothermal work and, at this time, a strong fundamental research effort was established to determine a rationale for coupled and uncoupled flows, impinging jets and wall jets. A flight test program utilizing a NASA propulsion and recovery system has been completed and the details of this program are described in Section H. These tests provided both external and internal heating data under actual environmental conditions.

3. Vehicle Vulnerability. - The vulnerability work initially conducted for determining the vulnerability of re-entry body, warhead, and associated arming and fuzing components by BRL and Picatinny Arsenal have been terminated. A final report on the vulnerability of nuclear warheads to aerothermal effects has been

SECRET

prepared by Picatinny Arsenal (see Section Q).

Aerojet-General, under the technical management of the Weapons Laboratories, Detachment 4, ASD, Eglin AFB has completed the investigations for determining the vulnerability to fragment impact of both liquid and solid rocket propulsion systems. An analysis of the vulnerability of both the United States and other vehicles is included in the Aerojet final report in publication by Det. 4, ASD.

4. Intelligence. - The intelligence phase of the work was designed to provide information and guide lines for the work performed in the other phases of the HKM Program. A report entitled "Soviet ICBM Re-entry Body Study" has been prepared by Raytheon. This report provides a description of the Soviet ICBM based on early Soviet missile tests in the Pacific.

PROGRESS

The work described below is a summary of the technical progress in each phase of the HKM Program for the period ending 30 September 1963.

1. Impact Damage Phase

The work covering the results of hypervelocity impacts into Astrolite, oblique tape wound refrasil (OTWR) and RAD 60 HD is discussed in considerable detail in the final report prepared by the AVCO Corporation (See Section C). This study was to determine the minimum impact conditions required to perforate a composite target consisting of an ablative material bonded to a metallic back-up structure. The thickness of the ablative materials used in these experiments was varied between one-half and one and one-half inches. The back-up structures were quarter-inch and three-eighth-inch aluminum and steel plates (flat and curved).

SECRET

Impact damage results are correlated in terms of the projectile energy, target thickness, and an effective target strength times a density weighted for thickness. Minimum perforation energies were determined to within 20 percent, and the distribution of fragments coming off the backface of a target after perforation has been analyzed.

Examination of the heat shield damage results shows that the hole size in a fixed thickness ablative increases with increasing projectile energy and is independent of the back-up thickness (or whether or not the back-up is perforated) and projectile size; however, this study does show some hole size dependence on the properties of the back-up material (see page C27). All impacts were made normal to the target surface with steel projectiles varying in mass between one-fourth and five-grams and launched up to 5.5 km/sec in velocity.

Failure of the back-up structure has been described in considerable detail. The results indicate that the mechanism of perforation shows some dependence on the projectile diameter to heat shield thickness ratio, as well as the heat shield to back-up structure thickness ratio.

The overall conclusion concerning perforation, as defined by the projectile parameters used in this study, is that perforation is caused by a complex combination of shock effects and the secondary impact of the broken projectile material on the back-up structure.

The correlation which best fits the AVCO data for determination of hole size diameter (D_A) in the ablative is

$$D_A = K_1 \frac{E^{2/3}}{t^n} \quad (1)$$

where K_1 and n are constants dependent on heat shield and

SECRET

back-up material properties, and t is the thickness of the ablative and bond. The data used to obtain this correlation includes that from non-perforation, minimum perforation and limited and complete perforation damage modes. Minimum perforation is defined as the damage mode where the ablative is completely perforated but the back-up structure is only bulged (fracturing, cracking, or petaling of the back-up material just begins at this point in the complete perforation process). Complete perforation is defined as the damage mode where the hole diameter in the back-up is equal to or greater than the hole diameter in the ablative.

When only complete perforation data from NRL, AVCO and CARDE using steel projectiles are analyzed, the expression for hole diameter in the ablative becomes

$$D_A = K_2 \left(\frac{E}{t} \right)^y, \quad (2)$$

where $K_2 = 2$ and $y = 0.36$, (ref. 1). Most of the targets utilized an aluminum back-up structure; however, a few targets used a steel substructure. These data also strongly indicated that hole diameter in the ablative is independent of back-up material and thickness.

Although the determination of hole size in only the ablative material of a composite structure appears to be independent of back-up material and thickness, the energy E required for complete perforation of the structure is dependent on both of these parameters. The empirically determined expression for minimum perforation energy (see ref. 1 and Section C) is

$$T \simeq K (E \sin^2 \theta)^{1/3}, \quad (3)$$

where T = total thickness of the ablative, bond and metallic

SECRET

back-up of the composite structure,

K = empirically determined constant dependent on the
back-up material,

E = projectile energy, and

θ = angle between trajectory and target surface.

The ablative materials used in the studies at NRL during this period included laminated and chopped phenolic nylon and reffrasil and the GE Series 124A. The thicknesses varied from one-half inch to two-inches. Back-up materials were steel, aluminum, and magnesium varying in thickness from one-eighth to one-fourth inch. One-inch-thick aluminum honeycomb was used for back-up material for the GE Series 124A ablative. The projectile velocities ranged from three to seven km/sec and angles of obliquity from 90° (normal impact) to 15° . Comparisons are made for impacts into actual re-entry vehicles and the flat plate composites used for simulation. Impact damage resulting from firings into these two types of targets was in very good agreement at the energy levels studied.

Experiments with large mass (high energy) impacts have shown that considerable structural damage was sustained by the target, i.e., severe cracking, debonding and delamination of ablative, as well as rupture of the metal back-up and rib structure. Recent experiments indicate that total structural damage can only be simulated by firings into actual vehicle segments. These results will be described in the next progress report by the NRL group.

Investigations by the BRL of impact damage to composite targets utilizing an inhibited jet charge (aluminum projectile, aspect ratio 3.5 to one) are continuing. The work consists of the evaluation of various non-metallic materials such as commercial grade polyethylene, phenolic glass-fabric laminate,

SECRET

phenolic nylon-fabric laminate and glass backed by steel, aluminum, or magnesium plates. All targets were impacted with aluminum inhibited jet projectiles having a mass of 3.2-grams and velocity of 9.2 km/sec (Scale I charge). The tests were conducted at both 30 and 90 degree angles of obliquity. The target-hole dimensions are used as a basis for evaluating the effects of angle of obliquity and thicknesses of various combinations of non-metallic and metallic plates. Damage behind the targets is shown on aluminum witness plates (Photographs in Section A). The results of the 30-degree angle firings indicate that the hole dimensions in the primary materials (non-metallic) are similar to those obtained from primary targets of equal thickness impacted at 90 degrees. These results are consistent with previously reported data of impacts into ablative targets (Reference 1).

The results from impacts at 90 degrees indicate that for the polyethylene, fiberglass and nylon, the hole sizes increased with decreased non-metallic target thickness for a given back-up thickness. For the same non-metallic thickness, the hole sizes did not vary appreciably with different back-up thicknesses for materials. These findings are consistent with other data from impacts into ablative materials for the complete perforation regime. However, it is suggested by AVCO, for the non-perforation and minimum perforation regions that the physical properties of the back-up metals do have some influence on the hole diameters in the non-metallic materials. This material-property effect is not apparent in the complete perforation cases probably because the impact energy is well above the required minimum perforation energy.

Figure 1 is a plot showing hole size in the primary material vs energy per unit thickness for the three non-metallic primary materials with steel back-ups (data points include incomplete

SECRET

perforations and firings at 30 degrees). These data are compared with equation (2), and the results show that 75% of the data points agree to within 25% of the values predicted by equation (2).

A comparison of equation (2) with data for the three primary materials with magnesium and aluminum back-ups is shown in Figure 2. It should be noted that in both figures nearly all of the data points fall below the curve, and equation (2) represents very close to an upper limit on hole sizes for the inhibited jet data. Considerable improvement in the accuracy of prediction can be achieved by determining a new K_2 constant for only the inhibited jet data. This new value of K_2 is approximately 1.5. This lower value of K_2 for these studies is primarily a result of the following differences:

- a. Properties of the non-metallic materials. The materials used in the inhibited jet experiments are significantly different from those used in the ablative experiments, and
- b. Material and shape of the projectile. Steel projectiles with a length to diameter ratio of approximately one were used to develop equation (2). Density and shape of the inhibited jet projectiles are significantly different.

Experiments are presently being conducted at NRL to determine the effect of projectile material on hole size as well as to damage effects behind the target. Extreme differences in the shape of the projectile may also require a change in the exponent of equation (2).

2. Aerothermal Phase

Under this phase ARAP, AVCO and GE have continued internal heating and structural studies needed to develop the technology required to assess the potential of thermal kill during the re-entry of an R/V, which has been damaged by hypervelocity impact prior to or during re-entry. Significant progress

SECRET

has been made in both flight and ground tests of vented models containing relatively small perforations. The two-flight program, conducted with the cooperation of the NASA Langley Research Center, resulted in the successful telemetry of data and the recovery of experimental payloads for both flights. Identical models to the flight models were tested in the GE Malta Rocket Exhaust Facility. Analysis of the results obtained indicate general agreement of internal heating patterns from flight and ground tests. However, several anomalies were disclosed:

a. The internal pressure in the first configuration (inlet at the stagnation point) was much higher than expected. For later portions of the flight, the values were greater than the computed external stagnation pressure.

b. The maximum internal heat flux for the above configuration fell far below theoretical predictions for most of the heating period of the flight, after agreeing well with theory at the time of peak heating rate.

c. In configuration two (inlet 60 degrees from the stagnation point) severe external heat shield ablation occurred immediately downstream from the inlet orifice. Only slight indications of such aggravated heating were present in the Malta rocket exhaust test of the same configuration.

d. Inlet orifice coefficients required for mass and energy conservation were on the order of 25 to 50 percent of the value derived from the Malta test for configuration two. Differences in external approach flow viscous effects appear to be a possible cause of this result.

The results of the flight test work have provided general confirmation of the conceptual models and theoretical analysis previously derived to predict internal pressure and heat flux of perforated re-entry vehicle compartments. It is expected that as additional experimental data become available in the

SECRET

basic problem areas of orifice flow characteristics, jet diffusion, and jet impingement heat transfer the anomalies discussed will yield to rational explanations. Complete details of the two-flight program are contained in Reference 2.

An internal heat transfer model for test work in the "coupled flow" regime (large holes in unvented vehicles) was designed, built, and tested in the Cornell Aeronautical Laboratory's Wave Superheater Hypersonic Tunnel. Relatively low internal fluxes were measured for all orifices tested over a range of $A/V^{2/3}$ from .01 to .20. Further testing of the model will be done at higher pressures at AEDC. Additional orifice flow experiments are under way at AEDC to determine flow characteristics of orifices having supersonic tangential approach flow. Flow rate, jet velocity profiles, and jet direction are being determined over a Mach number range from 1.5 to 5.0, for various orifice diameters, wall thicknesses, and orifice pressure ratios. Two tests will include flows through holes produced by hypervelocity impact into an actual ablative structure. Experiments for providing a comparison of the effects of drilled vs actual impact perforations in an ablative and metal back-up structure are scheduled for the GE Malta Rocket Exhaust Facility. The primary objective of this program is to determine the effect of relatively large perforations on the thermostructural behavior of unvented re-entry vehicle models. Also presented in Section H are the results from a thermal kill study on the C-1 Advanced Target Model, basic analytical developments in the thermal studies, and estimates of structure temperature rise due to coupled flow heating for determining the failure altitudes for the C-1 target and for the Mark 3.

A review of the work performed by ARAP is presented in Section L. These efforts include: a study of vented uncoupled

SECRET

flow produced by a hole at the stagnation point plus one or more holes on the aft portion of a vehicle; theoretical and experimental work on coupled flow phenomena; tests for determining effects of localized heating of composite materials; application of foam materials for protecting re-entry vehicle interiors from aerothermal effects; and theoretical and experimental studies of impinging and wall jets.

3. Vulnerability

Although all vulnerability work has been terminated, a final report on the vulnerability of nuclear warheads to aerothermal effects has been submitted and will be briefly summarized in this section. Distribution of this report has been made by Picatinny Arsenal to the various organizations on the HKM distribution list.

This report (listed on the inside back cover) presents the results of a study at PA on the feasibility of aerothermal kill of an incoming nuclear warhead.

Based on estimates previously reported in the aerothermal phase of the HKM Program, a solution has been presented for the response of a nuclear warhead to intense pulses of thermal energy. The thermal stresses and the forces developed on the most vulnerable segments of a nuclear warhead have been calculated and the magnitude of the lethal energy input for a number of structures has been established. The vulnerability estimates refer to typical U.S. weapons, and the flight histories in the study are typical of advanced ICBM's.

SECRET

REFERENCES

1. Persechino, M.A. "Hypervelocity Impacts Into Ablative Materials" Sixth Symposium, Hypervelocity Impact, Vol. IV, Page 235, May 1963 (S).
2. Nestler, D.E. "Results of Wallops Island HKM Internal Heating Flight Tests," GE Document No. 63SD885 of 4 November 1963 (S).

SECRET

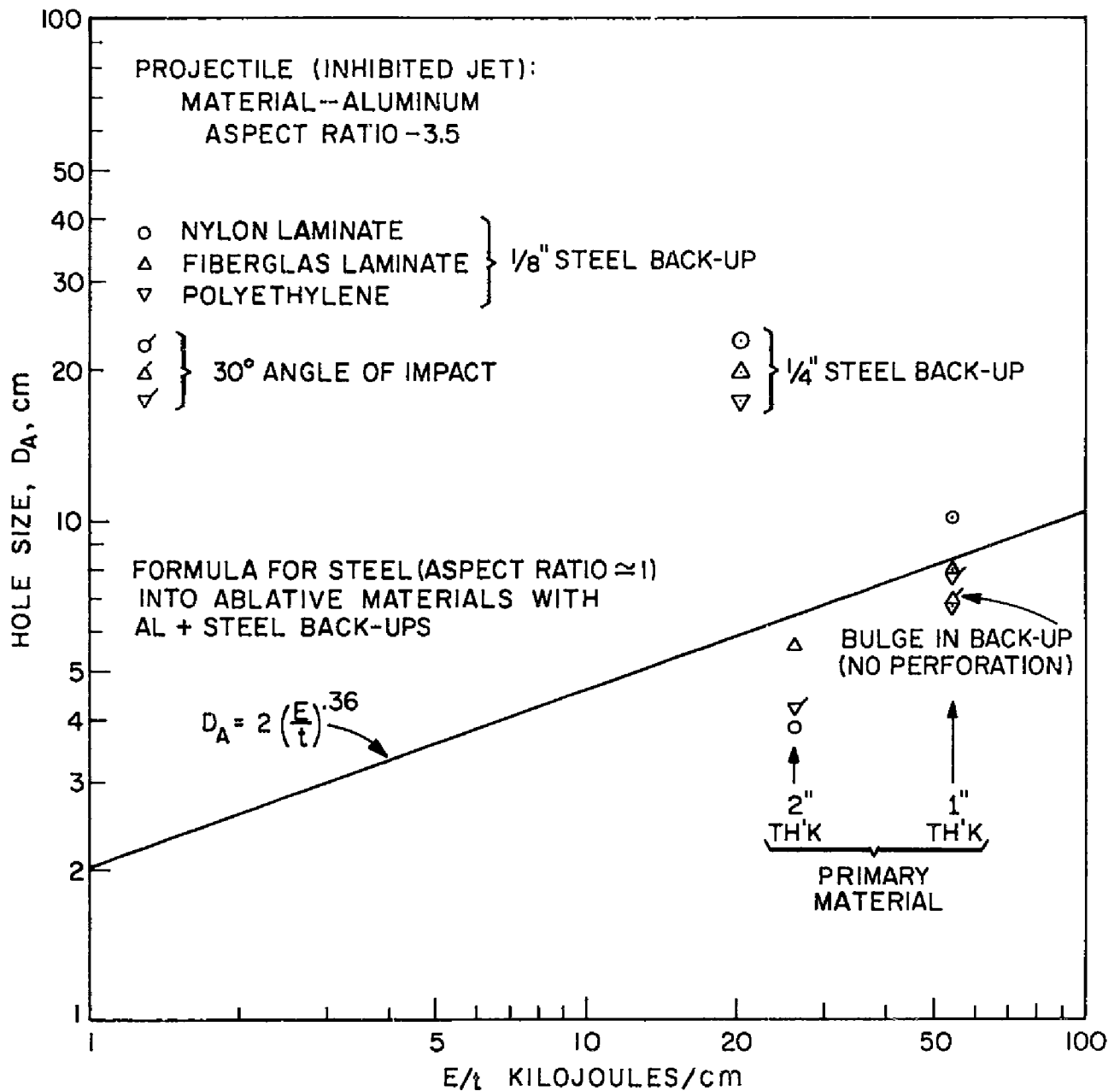


Fig.1 - Comparison of hole sizes produced by inhibited jets (aluminum) and steel projectiles fired into Fibreglas and plastic targets

SECRET

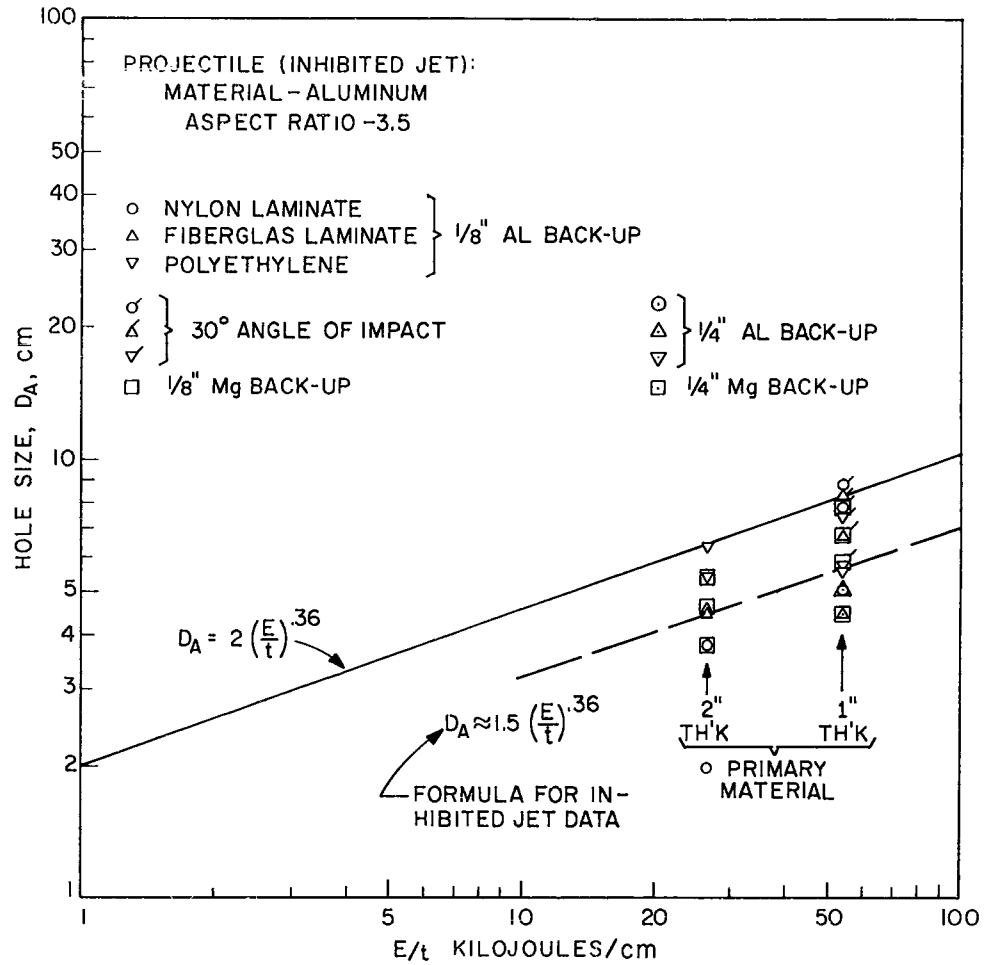


Fig.2 - Comparison of hole sizes produced by inhibited jets (aluminum) and steel projectiles fired into Fibreglas and plastic composite targets with Al and Mg back-ups

SECRET

APPENDIX

Brief Review of Information on Foam Materials

By

R.S. Snedeker

This paper is a brief review of information on existing foam materials. The use of such materials has been proposed as a possible means for preventing or inhibiting internal damage to re-entry vehicles by aerothermal effects.

June 1963

Aeronautical Research Associates of Princeton, Inc.
50 Washington Road, Princeton, New Jersey

1. Introduction.

This brief review has been prepared for the purpose of providing very general descriptive and technical information on foam materials. The use of such materials has been proposed as a possible means of preventing or inhibiting internal damage of certain reentry vehicles due to aerothermal effects which may occur after the skin of such a vehicle has been punctured in flight. For this application, a light weight foam material of high thermal stability could be used to fill all open interior cavities. Assuming that only slight mechanical damage to the foam occurs at impact, it is suggested that critical interior structures may be protected from the direct effects of the subsequent large reentry heat fluxes for a sufficiently long period to negate a possible kill due to such heating. It is assumed, of course, that the physical conditions prevailing would be such that an aerothermal kill would occur were it not for the presence of the foam, that is, no other effective hardening method has been used and the vulnerable regions of the interior structure are, indeed, exposed to possibly lethal heating. The information contained herein is indicative of at least some of the materials which might be used in this way. Its primary purpose is to provide background knowledge for the ultimate determination of the desirability of further, more detailed studies of the behavior of foams under severe mechanical and thermal loads. It is not intended that this information should represent any specific recommendation of a particular material for this purpose.

2. General description of foam materials.

Many new foam materials have been developed in the past decade. While the emphasis seems to have been in the area of synthetic organic materials (plastics), some newer foams and foam-like substances can now be made from ceramics (fused quartz) as well as graphite and some metals.

The principal organic foams which may have some value in the present application are the urethanes, epoxies, silicones, and phenolics. All of these materials can be fabricated in combination with various additives, or fillers, to enhance specific properties of importance. For example, the dielectric constant of a given foam may be adjusted by incorporating suitable amounts of metal powder. When the basic foam is combined with any variety of such fillers, the possible range of available foams is enormous. Indeed, within limits set only by the basis material, the properties of foams can be tailored both chemically and through varied production techniques to satisfy innumerable requirements.

Some of the foam properties and physical qualities which are of importance to this review are discussed below. Numerical data on some specific foams are presented in Section 4.

Physical Structure. Foam structure is usually described in terms of cells and cell walls or membranes. These cells, which are essentially bubbles in the basis material, may be entirely enclosed and isolated from adjacent cells (closed cell foam), or they may be entirely open and interconnected (open cell foam). For some foams, at least, it is possible to regulate the percentage content of open cells, so that any desired degree of porosity may be obtained.

While they are not true foams, there are two other material structures which should be mentioned in this context. They are the syntactic foams and the spun filament type materials. Syntactic foams are formed by packing

together small hollow spheres or other shapes and bonding them with a suitable adhesive. Although the hollow spheres themselves constitute a closed cell system, the spaces between them may be filled to an undetermined degree with the bonding substance so that the over-all effect may not be entirely that of a closed cell foam. The spun filament material is most familiar as the glass wool used for many insulation applications. Obviously, this material may be classed as "open cell."

Foaming methods. True foams may be produced in several ways depending on the materials involved. A gas from an outside source may be passed through the liquid ingredients to form the foam which is then cured either chemically or thermally so as to maintain its structure. The foaming process is sometimes enhanced by means of mechanical agitation or whipping of the mixture. On the other hand, certain ingredients, either liquid or powder, may be added to the basic constituents which then react chemically to form a gas which in turn creates the foam. Reactions of such foaming or blowing agents may be controlled chemically so as to generate a wide variety of cell structures and material densities. The degree of temperature dependence of these reactions may be varied so that the foam will not form until a certain activation temperature is reached. This technique has been applied, for instance, to the case of foams formed from a mixture of powdered ingredients designed to be activated by solar radiant heating. Regardless of the foaming method, much of the gas initially trapped in closed cells eventually diffuses out through the cell walls unless the foam's outer surfaces are sealed to prevent this. Therefore, the gaseous content of many foams is eventually just air under ambient conditions. Some foams designed for low thermal conductivity can maintain a substantial amount of their low conductivity gas only if

they are enclosed in an airtight space.

Most foams are formed simultaneously with the reaction that creates the basis material itself. For example, a resin and a curing agent when combined will produce a solid material if no blowing agent is used. Some of the properties of foams which depend only on this basis material, are, therefore, identical for foamed and solid forms.

Because of the variety of foaming techniques used for different materials, some foams may be made to foam in place while others must be made under more carefully controlled conditions and later cut to the desired shape. Ambient pressure conditions during foaming will, of course, have an effect on the structure of the resulting foam as will the build up of internal pressure due to physical confinement of the expanding material.

Density. A wide range of foam density is possible. Some foams can be made with densities of less than 2 lb/ft^3 , whereas heavier foams can approach the density of the solid material. Foams of the same density can be made to contain many small cells or only a few large cells in a given volume. In general, however, the smaller the cells, the greater the mechanical strength for a given density.

Rigidity. Foam rigidity is usually dependent upon the flexibility of the basis material. Ceramics or resins which are normally hard or brittle yield rigid foams, whereas the elastomeric substances and some of the other resins can be made very flexible. For a given material, the rigidity will depend on cell size and structure (percentage of closed cells) and foam density.

Elasticity. A foam's elasticity or ability to return to its original size and shape when a deforming load is removed,

need not depend on the elastic quality of the basis material alone. Some light weight foams with a high percentage of closed cells in which the cell walls are thin and highly flexible will regain their original shape as long as the cell walls are not stressed beyond their elastic limit. In this sense, of course, most materials have some elasticity. Foams made from the various rubbery materials will have elasticity which, again, depends on cell size and structure and density.

Mechanical strength. Foam strength is usually defined in terms of the compressive and flexural moduli because these quantities are most useful in analyzing foam behavior for most typical foam applications. Since foams have found their widest use as insulators against thermal loads or mechanical shock, where they are applied either as fillers, liners, or cores of composite structures, their tensile and shearing strengths have not been investigated very thoroughly. For some foams, strength properties may depend on the direction of the applied load since some foaming techniques produce a highly anisotropic material. As mentioned above, the compressive and flexural strength of foams is usually greater if the cells are small.

Thermal conductivity. Heat is conducted in foam not only directly through the solid cell wall and connecting material, but also across the cells through the gas they contain. Recently it has been possible to develop low thermal conductivity gases which when used in closed cell foams yield foam thermal conductivities as low as $.1 \text{ Btu/hr} - \text{ft}^2 - ^\circ\text{F/in.}$ For comparison, the conductivity of spun glass fiber material is $.26 \text{ Btu/hr} - \text{ft}^2 - ^\circ\text{F/in.}$ Much work has been done with foams to achieve low conductivities because of their wide use as insulators. A great deal of data are therefore available.

Specific heat. Because the mass of trapped gas in any foam is small compared to the mass of basis material, the specific heats of the foam and the basis material should be almost identical. The behavior of various foams when subjected to heating can be quite complex including a combination of several forms of breakdown depending on the chemical composition and the heat applied. Because of this, the ability of a foam to withstand high temperatures is generally stated in terms of a decomposition energy rather than a heat capacity or specific heat. Obviously, the concept of a latent heat of fusion or vaporization is also inappropriate for many such materials.

Types of failure. Aside from certain tests designed to determine compressive and flexural strength, pertinent information on mechanical failure of foams is rather meager. Recent work in the field of foam filled composite structures designed to prevent puncture by hypervelocity bodies has cast some light on the behavior of foams when subjected to penetration by small particles, but any detailed analysis of failure processes under these conditions seems to be lacking. It seems safe to conclude, however, that a foam subjected to a localized compressive load due either to structural impact or gas flows of high dynamic pressure, will fail when the local compressive strength of the cells is exceeded. If the material is fairly brittle, the cells will collapse and the resulting small particles will either lodge in the undamaged structure or be blown away. If the material is elastic, the compression will continue until a tearing action results in the surface layers of highly compressed cells. It appears that consideration of tensile strength may be important in the analysis of this type of failure. Obviously, some combination of these two mechanisms should result for foams of intermediate elasticity.

Thermal failure depends to a large degree on the chemical composition of the material used. Organic foams exhibit a variety of breakdown symptoms as the temperature is raised. These include discoloration, softening, deforming, and the like. At still higher temperatures, the degradation process can include the initial stages of chemical decomposition and even combustion, although it is possible to introduce materials which cause self extinguishment in such cases. In many organic foams, the carbon remaining after total chemical decomposition maintains a layer of foamlike structure equivalent to the char layer formed by solid ablatives under similar conditions. It appears that such a foam char layer could extend the foam's usefulness as an absorber of jet kinetic and thermal energy under HKM conditions.

It is likely that ceramic and metal foams will soften and melt at high temperatures and then fail mechanically, although no specific information on this type of failure mechanism has come to light at present. Information on the thermal degradation of refractory materials such as pyrolytic graphite foam is also lacking.

3. Use of foam packing as protection against aerothermal effects.

It will be instructive to review briefly the manner in which a foam packing may behave when subjected to potential aerothermal kill conditions. It is first assumed that the vehicle's skin is punctured by the hypervelocity impact of a pellet. Initial damage due to the impact itself is of some importance, since the cavity created in the packing may have a bearing on initial aerothermal conditions. The only studies that have come to light with some relevance to this problem are concerned with the hypervelocity impact resistance of composite materials, some of which contain foam cores sandwiched between metal outer and inner skins. One such study was conducted by the Goodyear Corp. using both rigid and flexible urethane foams with densities ranging from about 1 to 6 lb/ft³. Another study of similar structures by the General Electric Co. considered elastomeric foams (silicones). In this latter study, however, all observed impacts resulted in denting of the inner wall so conclusions about effects on the foam core alone must be confined to the region just inside the outer skin.

Considering the urethane results,* it appears that spall particles from the outer wall as well as fragments of the pellet create cavities in the foam which may be either ellipsoidal or cylindrical depending on the degree of pellet fragmentation occurring on impact. While the size of such cavities is a function of a number of material variables and impact conditions, it does appear that the principal cavity producing mechanism is the vaporization of the foam due to the heat generated on impact. In addition to this

*While the ensuing discussion is based on experience with urethane foams, it is likely that similar conclusions will apply for any pure organic foam, i.e. not including effects of fillers, since all organics tend to decompose at fairly low temperatures (anywhere between 400 and 900°F).

primary cavity damage, some degree of irregular localized mechanical penetration damage due to small particles seems to occur depending again on the materials being used. In some cases, there is also evidence of failure of the foam-to-skin bond around the impact hole. Measurements made under a variety of conditions seem to indicate a nearly linear relationship between the penetrated foam weight (cavity) and the foam density for a given type of foam (urethane). The flexibility or rigidity of the foam does not appear to be a factor in this relationship. Another mechanism which has been suggested as a possible contributing factor in foam failure is the sudden local build-up of pressure due to the products of vaporization during charring of the foam. Although no specific investigation of this problem has been uncovered, it is the opinion of some technologists that there is little likelihood of an appreciable effect of this kind. Of course under conditions which include high heating rates as well as impact, no such opinion seems possible since this also appears to be an unexplored problem.

If it is assumed that a cavity is created in the filler in the manner just discussed, it is apparent that an initial flow condition in the form of a jet through the hole may be established on reentry. On the other hand, if there were no cavity, but just a small opening in the skin with the foam surface nearly flush with it, it is conceivable that there would be more difficulty in establishing such a jet. Since this case represents a very large $A/V^{2/3}$, progressive formation of a cavity might take place due to some coupled flow effect, thus tending to steadily decrease $A/V^{2/3}$ (V here being the volume of the cavity in the foam). This process might continue and gradually become governed more by impingement effects than by coupling. The rate at which these processes occurred compared to rate of reentry heating build-up would, of course, ultimately determine the value of foam

as a hardener. Cavity enlargement under coupled flow conditions would probably be almost entirely due to thermal destruction of the foam, whereas under impingement conditions the mechanical effects of jet dynamic pressure would have to be considered. A simple test of a urethane foam under high enthalpy conditions was conducted by AVCO. In this test a rocket exhaust was passed parallel to the exposed surfaces of two foam samples held in containers set into the test section wall. With a stagnation enthalpy of 5200 Btu/lb and a running time of about 3 seconds, the two samples failed in the following manner: one sample had burned out of its container almost entirely, while the other had a spherical concave depression burned in the exposed surface. The first result was apparently inconclusive due to a suspected container leak, but the second seems to be indicative of the gradual cavity formation mentioned earlier.

Returning to the seemingly more realistic situation in which a cavity is created on impact, the key factor may be the initial value of $A/V^{2/3}$ so created. If the cavity is large, then the initial aerothermal condition would be impingement. If the cavity is small, a coupling effect would be in force at first. It is somewhat paradoxical that a foam that is damaged less on impact gives rise to the higher internal heating rates associated with coupled flows. Of course, it is quite possible that after a very short time the effects of two quite different initial conditions would be equalized due to the phenomenon just described. No reliable numerical evaluation of this situation appears to be possible on the basis of test data available at present.

Thermal and mechanical failure mechanisms of various types of foam have already been discussed briefly. It would seem that any valid analysis of these processes as applied to the geometry and environmental conditions being considered is impossible on the basis of available data. It does seem

SECRET

11

possible, however, to delineate with some justification certain basic characteristics for a foam which might be of some value as an anti-aerothermal hardening material. These characteristics and some of the candidate materials which have come to light are discussed in the next section.

4. Possible candidate materials for foam filling.

The most desirable qualities for a foam to have for the application in question are low density, high mechanical strength, and resistance to short term periods of high heat flux. Other considerations might include ease of fabrication or installation, noninflammability, bondability, isotropicity, etc. Obviously, some compromise must be made among the principal qualities listed. The secondary items appear to have some degree of latitude in their selection for many types of foam. For the purposes of introducing specific data on certain foams, the discussion will be limited to foams with densities below 15 lb/ft³.

Organic foams.

Since all organic foams (urethanes, epoxies, silicones, phenolics, etc.) decompose when heated to temperatures that are low compared to expected reentry temperatures, the prime consideration for the present application must be the time dependence of the degradation process. No specific information of this kind is known to us at present. However, some general idea of relative decomposition energies for various materials can be supplied. For organic foams, decomposition energies fall in the range of 500 to 800 Btu/lb. Presumably this range can be adjusted and perhaps even extended for a particular foam by using filler materials with higher specific heats than the foam. This technique, of course, introduces a weight penalty since the usual filler materials would undoubtedly weigh more than the foam they displaced. A more promising possibility - from the standpoint of successful hardening by this method - is the case of organic foams which leave a structurally sound char layer on the exposed surface after the organic substances have been completely destroyed. As in the case of solid plastic ablative materials, this char layer acts to protect the unaffected material below from both

SECRET

dynamic pressure and heating loads. Again no specific data have been found for foams, but it has been suggested that an upward extension of the decomposition energy to perhaps 4000 Btu/lb would be realistic. Although this figure is based on foams weighing more than 20 lb/ft³, it should not be substantially different for lighter materials. Specific heats for organic foams are in the range between .3 and .4 Btu/lb-°F.

Some information on specific organic foams which may be useful in this application with densities below 15 lb/ft³ follows:

Urethane. A self-extinguishing urethane foam manufactured by the Hooker Chemical Company, Durez Division, Tonawanda, New York is available. This foam can have densities as low as 3 lb/ft³ and can be foamed in place. A char structure of the type already mentioned remains after total destruction of the material by heating. A hetrofoam polyol, which provides the self-extinguishing property, and polyphenolisocyanate (PAPI) are the principal chemical constituents. Fillers can be used, and the foam will cure at room temperature. Heat conductivities as low as .1 Btu/hr-ft²-°F/in have been achieved for urethane foams, but the exact value for the above foam is not known at present. Urethanes are available in rigid or flexible forms with a wide range of percentage of open cell structures. Their degree of structural anisotropy varies with the foaming method. There are numerous manufacturers of urethane foams of specialized and nonspecialized types.

Epoxy. A principal developer and manufacturer of epoxy foams is the DeBell and Richardson Company, Hazardville, Connecticut. Epoxy foams have been made by this firm which have densities down to 2 lb/ft³. These foams are rigid and contain about 90 per cent closed cells. They cannot be foamed in place, but the carefully controlled manufacturing process results in a highly isotropic structure. (A foam-in-place epoxy powder is manufactured, however, by the Emerson and Cuming Corporation,

SECRET

Canton, Massachusetts. This company also manufactures hollow epoxy spheres which could be used as a syntactic. These spheres can have a bulk density as low as 7.5 lb/ft^3 and are stable at temperatures up to 350°F . Their compressive strength is 500 psi.) No cohesive char remains after complete vaporization, which can occur at about 500°F . It appears that epoxy foams are of particular value where structural strength is a factor. Typical mechanical properties for a 5 lb/ft^3 epoxy foam are 2700 psi for the flexure modulus and 2100 psi for the compressive modulus, both at room temperature. Under a compressive load of 90 psi, the cells of this foam will collapse. A shearing strength of about 300 psi has been measured for a sample of foam with a density of 13 lb/ft^3 . Thermal conductivity values are .26 and .29 $\text{Btu/ft}^2\text{-hr-}^\circ\text{F/in}$ for 5 and 13 lb/ft^3 foams, respectively.

Silicone. These foams are of the elastomeric type, and therefore cannot be made rigid. Principal developers and manufacturers of commercially available silicone foams are the Dow Corning Corporation, Midland, Michigan, the General Electric Company, Waterford, New York, and the Emerson and Cuming Corporation. Silicone foams can be made with very low densities, but a structurally useful foam must weigh at least 10 lb/ft^3 . Foaming in place is readily achieved using a mixture of either powdered or liquid ingredients, and the resulting cell structure is predominantly open (about 90%). These foams are noninflammable and will maintain their structural integrity under prolonged exposure to temperatures as high as 650°F . Compressive strength is in the 200 to 300 psi range at room temperature, with a marked drop-off with increasing temperature. A thermal conductivity of $.3 \text{ Btu/ft}^2\text{-hr-}^\circ\text{F/in}$ is typical. Silicone foam has found some application in combination with honeycomb and other similar supporting structures as a heat shield and impact resistant material, but data on char formation and ablative characteristics for unsupported foam have not come to light.

Phenolic. Phenolic foam is manufactured by the Union Carbide Plastics Company, New York, New York. This material is formed from a liquid resin by a process that results in a somewhat anisotropic product. It is a rigid, open cell, thermoset type plastic which will retain its dimensional stability after prolonged periods at temperatures up to 400°F and which can be foamed in place. Density can be as low as .33 lb/ft³. Average structural properties for a 2 lb/ft³ phenolic foam include compressive and flexural strengths of 25 psi, tensile strength of 20 psi, and a shearing modulus of 400 psi. A 4 lb/ft³ foam exhibits approximately double these values. The principal application of this material has been as an insulating core in a sandwich structure. Thermal conductivity is a function of density and mean temperature, but usually falls between .2 and .3 Btu/ft² - hr - °F/in. Although no quantitative information is available on char properties, it does appear that a cohesive char does remain after the organic material has been destroyed. The foam itself is self-extinguishing.

Inorganic foams.

Two inorganic true foams and one syntactic are available at densities below 15 lb/ft³. A fused quartz material has been developed as well as a syntactic consisting of silica spheres. Decomposition energies for these ceramics are in the neighborhood of 4000 Btu/lb, although it seems possible that values as high as 7000 Btu/lb may be achieved with further development. A foam of pyrolytic graphite is also available which can be expected to have a decomposition energy of about 25,000 Btu/lb. None of these materials can be foamed in place.

Fused quartz. This foam material is a product of Emerson and Cuming. It is a closed cell foam with a density of

12 lb/ft³. Short term exposure to temperatures as high as 3000°F is possible without melting. Thermal conductivity is approximately .3 Btu/ft² - hr - °F/in. On further local heating beyond the melting point, this foam will vaporize, but no over-all fracture will occur (presumably because of its low thermal expansion coefficient).

Silica spheres (syntactic). Another development of Emerson and Cuming, these micron-sized spheres have a bulk density of about 11 lb/ft³ and remain stable at temperatures as high as 2500°F. The density of a composite material consisting of these spheres plus a bonding agent will, of course, depend on the density of the latter. Compressive strength of the spheres alone is about 1000 psi under hydrostatic load conditions, and the thermal conductivity is about .4 Btu/ft²-hr-°F/in at room temperature.

Pyrolitic graphite. This material has been developed recently by the General Electric Company. The foam has a density of from 1 to 2 lb/ft³. No mechanical strength or thermodynamic data are available except that it maintains structural integrity at 2500°F and that it sublimates at 5500°F. Energy absorption of 25,000 Btu/lb is sufficient to cause oxidation.

5. Sources of information on foams.

In the course of the investigation of foam materials just described, use has been made of a number of information sources. The following listing of these sources is not intended to represent a complete list of foam manufacturers, developers, or literature sources; it is merely a review of the sources upon which the present memorandum is based.

Published articles and technical papers.

1. Technical Data on Plastics, February 1957.

Table of foam properties.

2. Subject Index, Bibliography, and Code Description of Technical Conference Papers on Plastics, 15 February 1961 - 23 February 1962, Plastics Technical Evaluation Center, Picatinny Arsenal, Dover, New Jersey. Plastic Report No. 11, June 1962.

Bibliography on foam papers.

3. Self-Erecting Flexible Foam Structures for Space Antennas. V. L. Vaughan, Jr., and E. L. Hoffman. NASA TN D-1610, 1963.

4. Modern Plastics Encyclopedia, 1962.

Table of foam thermal conductivities.

5. Plastics in Orbit. Modern Plastics, February 1962.

Article on applications of plastics including foams.
Some data and references.

6. Environmental Factors in Thermal Conductivity of Plastic Foams. G. A. Patten and R. E. Skochdopole. Modern Plastics, July 1962.

Article covering technical factors affecting foam production. Some data on properties. References.

7. Thermal Conductivity and Structure in Rigid Urethane Foams. R. H. Harding and B. F. James. Modern Plastics,

March 1962.

Article on thermal conductivity of foams. Experimental data and analysis. References.

8. Urethane Foams for Aerospace Application. H. R. Moore. Modern Plastics, June 1962.

Article on specialized applications of urethane foams. Environmental factors discussed. References.

9. Making Mines Safer. Modern Plastics, August 1962.

Article on unique application of self-extinguishing foam including data on air permeability.

There are numerous other technical papers covering chemical formulations and production techniques, but which have little direct bearing on the present problem.

Company technical memoranda.

1. High temperature composite structure. Seventh quarterly progress report. Martin Company Engineering Report No. 12317, April 1962.

Report on development of heat shield material composed of resin-impregnated ceramic foams.

2. Improved hypervelocity impact-resistant structures. R. R. Wallace and E. P. Bruce. General Electric Company, Missiles Systems Department, Philadelphia, Pennsylvania. Study of hypervelocity impact on built-up structural materials for reentry vehicles. Discussion of impact effects plus photographs.

3. A new system of protection from hypervelocity particles. B. W. Reynolds and R. H. Emmons. Goodyear Aircraft Corporation, Akron, Ohio. (Presented at Sixth Hypervelocity Impact Symposium, Cleveland, 1963.)

Extensive study of hypervelocity impact effects on

built-up wall materials for space vehicles. Experimental results and photographs. References.

Company commercial literature.

1. Emerson and Cuming, Incorporated, Canton, Massachusetts. Technical Bulletins on various foam products. Includes density, strength, and thermal specifications for urethane, epoxy, silicone, and ceramic foams of their manufacture.
2. Dow Corning Corporation, Midland, Michigan. Technical Bulletins on silicone foams; both liquid and powder forms. Data on density, strength, and thermal properties.
3. General Electric Company, Silicone Products Department, Waterford, New York. Technical data sheets on silicone rubbers. Mechanical and thermal data for solid material; no specific information on foamed forms.
4. Union Carbide Plastics Company, New York, New York. Technical bulletin on properties and uses of phenolic foams. Mechanical and thermal data and discussion of fabricating methods.
5. Hooker Chemical Company, Durez Division, Tonawanda, New York. Technical bulletin on self-extinguishing urethane foams. Mechanical, chemical, and thermal data.

There are several other companies known either to manufacture foams or to be engaged in the development of uses that may have some bearing in the present case. Among those which have not been contacted directly to date in this regard are:

Minnesota Mining and Manufacturing Company
Radioplane Division, Northrop Corporation
Narmco Materials Division, Telecomputing Corporation
Hughes Aircraft Company

Companies which have been contacted or visited are listed in the next subsection.

Company visits.

Discussions of the applicability of foams as aerothermal protective materials were held with personnel from several companies engaged in research on these materials. Much of the information presented in the foregoing review is based on these discussions. Companies visited and some of their areas of specialization are listed as follows:

1. Goodyear Aircraft Corporation (visited by Mr. Gray of ARAP). Discussions with Messrs. Reynolds, Baldwin, Stimler, Pake, Welling, and Romick. Use of foams in inflatable structures. Built-up materials for impact protection.
2. AVCO (visited by Mr. Gray of ARAP; meeting held at NRL). Discussions with Messrs. Lurie and Timmins. Experimental and developmental work on special applications of urethanes, epoxies, and silicones including study of high temperature capabilities.
3. General Electric Company, Silicone Products Department (visited by Mr. Snedeker of ARAP). Discussions with Messrs. Pfeifer, Lampe, and Preston. Research, development, and production of silicone rubber materials including foam.
4. General Electric Company, Missiles Systems Department (visited by Mr. Snedeker of ARAP). Discussions with Messrs. Stewart, Shaw, and Shenker. Research and development of specialized foam materials for reentry vehicle applications including silicones, ceramics, and pyrolytic graphite.
5. DeBell and Richardson Company (visited by Mr. Snedeker of ARAP). Discussions with Messrs. Mead and Schnitzer.

SECRET

21

Research, development, and production of plastics including epoxy foams for special applications.

6. Conclusions.

The principal intents of the present review have been to provide general background information on foams and to investigate the current research and development status of applications having some bearing on the use of foam as an interior protective packing material. As a result of the information gathered to date, it appears that little if any research is now under way with this specific application in mind. No data on combined thermal and dynamic pressure loading of such materials has been uncovered, although the Martin work on heat shields represents a similar loading condition with a different geometry. Data on mechanical properties of foams under varying pressure environments as well as air flow data are also lacking except for rather sketchy information on certain commercial and industrial applications (air filter elements, etc.). It is evident, therefore, that any further study of the possible value of foams for the application being considered will require more detailed experimental investigations under conditions more closely approximating those of an aerothermal kill.

CONFIDENTIAL

31

BALLISTIC RESEARCH LABORATORIES

HYPERVELOCITY KILL MECHANISMS PROGRAM (U)

ARPA Order 149-60

IMPACT DAMAGE PHASE (U)

Semi-Annual Progress Report
For Period Ending
20 September 1963

C. M. Glass
G. Kronman

ABERDEEN PROVING GROUND, MARYLAND

GROUP-3
DOWNGRADED AT 12 YEAR INTERVALS
NOT AUTOMATICALLY DECLASSIFIED

A

CONFIDENTIAL

CONFIDENTIAL

SUMMARY (U)

(C) Investigations of damage to composite targets resulting from hypervelocity impact is continuing at the Firestone Tire and Rubber Co. Three additional phases of the study have been completed with one observation per condition. All targets were impacted with the same aluminum projectile used in Phases I and II (3.2 grams at a velocity of 9.2 km/sec). The tests were conducted at both 30 degree and 90 degree angles of attack. The target hole dimensions are used as a basis for evaluating the effects of attack angle and thickness combinations of face-plates and back-up plates.

(C) Initial design work on the scale 2 inhibited-jet charge has been completed. This design will provide damage data for impacts of a 25 gram aluminum pellet with a velocity of 9.2 km/sec (1×10^6 joules). The pellet aspect ratio of 3.5 to 1 is the same as that obtained with the Scale I design.

(U) Thin metallic plate perforation studies are continuing at the Bureau of Mines. The data for impacts in the 2.0 to 5.0 km/sec velocity range were summarized in a previous report. Certain concepts, based upon these experiments, were established and the applicability of these concepts to higher impact velocities are being determined. The results of preliminary experiments with the 3.2 gram aluminum pellet at a velocity of 9.2 km/sec are compared with the earlier results obtained with projectiles in the lower velocity range.

COMPOSITE TARGETS (U)

(C) In Phase III of the composite target program, the four one-inch primary targets, glass, fiberglass, phenolic nylon, and polyethylene, - each with three different 1/8 inch back-up-2024T-3 aluminum, AZ 31BH-24 magnesium, and 4130 steel were impacted by the 3.2 gram aluminum pellet with a velocity of 9.2 km/sec (135×10^3 joules). The firings were conducted at a 30 degree impact angle (60 degree obliquity) to provide a direct comparison with the results of the 90° angle of attack firings in Phases I and II.

(C) For Phase IV of the test series, the composite targets consisted of two inches of the primary material backed by 1/8 inch of the secondary target. In Phase V, one-inch primary targets were backed with 1/4 inch secondary targets, with the glass target omitted. All targets were impacted at normal incidence with the 3.2 gram aluminum pellet at a velocity of 9.2 km/sec.

(C) The results of Phases III, IV and V tests are given in Table I which lists the "throat" or minimum hole diameter in primary target and the dimensions of the hole produced in the back-up material. Photographs depicting the degree of damage to both the primary and back-up targets are shown in Figures 1 through 28. Included in the photographs are the two 1/4 inch aluminum witness targets that were in close contact with each other and positioned 12 inches from the rear surface of the main target.

CONFIDENTIAL

CONFIDENTIAL

Individual shots can be identified by the serial numbers shown in the photographs.

(C) Since the present results are limited to a single observation for each condition, only a preliminary analysis of target damage can be accomplished at this time. A more detailed analysis will be made when additional impact data is obtained and when correlation of the damage with shock attenuation and pulse shape measurements are completed. These measurements are presently being made at the Bureau of Mines.

PRIMARY TARGET DAMAGE (U)

(C) The results of the 30 degree angle of attack firings indicated that the "throat" hole dimensions produced in the fiberglass and nylon-laminate materials are similar to results obtained from targets of equal thickness attacked at 90 degrees (Phase II tests). The hole sizes produced in the polyethylene targets appear to be independent of either the thickness of primary or secondary targets and angle of attack.

(C) The 90° attack angle results indicate that for the fiberglass and nylon targets the size of the holes produced increased with decreased target thickness for same back-up thickness. For the same primary target thickness the hole sizes did not vary appreciably with varying back-up thickness or material. The behavior of the polyethylene targets again was the same as described for the obliquity tests. The reaction of polyethylene, particularly at high stress levels, will vary quite drastically with temperature.

BACK-UP TARGET DAMAGE (U)

(C) The size of holes produced in the back-up materials for the various target combinations show the following features that are worthy of consideration; (a) for the 30 degree attack firings, the hole dimensions again are similar to results obtained from back-up plates in combinations of equal thickness; (b) the effect of rolling direction on the non-circular shaped holes appears to be more pronounced in some instances at the 30 degree angle of attack; (c) the size of the holes produced in the three back-up materials for the normal incidence firings is seen to increase with decreased plate thickness. This condition is more evident for primary target thicknesses of one inch.

(C) The largest holes were produced in the 1/8 inch aluminum back-ups and the smallest in the 1/4 inch steel back-ups. The hole sizes, produced in the 1/8 inch steel, however, were larger than those produced in the same thickness of magnesium. The composite target studies will continue with firings against a specific target arrangement at a 10 degree attack angle. Also, the targets used in phases II, IV and V will be impacted with a 25 gram aluminum pellet (aspect ratio of 3.5 to 1) at a velocity of 9.2 km/sec.

(U) Final design work on the scale 2 projector have been completed.

A-12

CONFIDENTIAL

THIN PLATE STUDIES (U)

(U) Research on impact damage to three different thickness of the same back-up materials used in the composite target studies was continued using the scale I inhibited-jet projector (3.2 gram aluminum pellet at 9.2 km/sec). The target thicknesses were 1/8 inch, 1/2 inch, and 2 inches. Firings were conducted to determine the spatial distributions of spall numbers and masses as well as the relationship between various parameters and spall particle size. The target perforation diameters and exit spall diameters for the three target thicknesses are plotted in Figure 29. The results are qualitatively similar to those obtained from the 5.0 km/sec projectile. For both projectile velocities, the spall diameters become increasingly more distinct from the perforation diameters as target thickness increases. Also for a given target thickness, the same correlation exists between the diameter of either the perforation or the spall and some strength characteristics of the target material. Magnesium targets produced the largest diameters and steel targets the smallest diameter.

(U) The radial distribution of spall particles for the 2-inch thick magnesium and aluminum targets are shown in Figures 30 and 31. The normalized distribution of spall numbers and a similar distribution for mass numbers are shown. The 2-inch steel target was not perforated. Although a spall was produced, the particles were too large and too few in number to be analyzed for radial distribution. The distributions are compared with data obtained with 3.2 and 4.0 km/sec projectile impacts into aluminum targets. The present data appear to be distributed in a manner similar to that previously observed.

(U) The distribution of spall numbers and spall masses obtained using depth of penetration measurements into fiberboard witness material for the three aluminum targets are shown in Figures 32 and 33. Data for magnesium targets are plotted in Figure 34 and 35.

(U) Several features that apply to both the aluminum and magnesium data are worthy of consideration; (a) the curves are maximum at the one-half inch penetration level and decrease monotonically with increasing penetration depth into the fiberboard witness target; (b) the distribution of numbers and masses of spall particles is found to be a function of target thickness. The percentage of the total spall numbers or mass captured by the first one-half inch thick sheet of fiberboard witness material is maximum for impacts into the thinnest metal targets; the percentage decreases with increasing target thickness; (c) the spall particle size is seen to increase with depth of penetration. This is evident when one compares a particular number distribution curve with its corresponding mass distribution curve. For impacts into 1/8-in. aluminum targets, 95% of the total number of particles are represented by only 72% of the total mass at the first penetration level, 4% of the total number contain 21% of the total mass at the second penetration level, and 1% of the total number contain 6% of the total mass at the third penetration level. Similar comparisons are noted for the other impacts.

(U)CLASS) TABLE I (U)
30° Angle of Attack

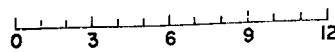
Serial Number	Prim. Target	Thick in.	Damage - Approx. Dimensions of Hole Throat	Back-Up		Damage-Approx. Dimensions of Area	See Fig. No.
				Target & Thick (in.)			
600-50	Polyethylene	1	2 x 1-1/2	Mg. 1/3		4 x 6-1/2	1
600-45	Polyethylene	1	3 x 4-1/2	Al 1/3		10 x 17	2
600-42	Polyethylene	1	2-1/2 x 3-1/2	Fe 1/3		6-1/2 x 10-1/2	3
600-39	Nylon-Laminate	1	3 x 3-3/8	Mg 1/3		7-1/2 x 12-1/2	4
600-47	Nylon-Laminate	1	3-1/2	Al 1/3		12 x 17	5
600-49	Nylon-Laminate	1			Poor Impact Conditions		
600-51	Fiberglass Laminate	1	2-1/2 x 3-1/2	Mg 1/3		6 x 9	6
600-46	Fiberglass Laminate	1	3 x 3-1/2	Al 1/3		12 x 15	7
600-41	Fiberglass Laminate	1	2-1/2 x 3	Fe 1/3		Dent	8
600-52	Glass	1	-	Mg 1/3		3 x 6	9
600-40	Glass	1	-	Al 1/3		3-1/2 x 6	10
600-48	Glass	1	-	Fe 1/3		Dent	11
600-68	Polyethylene	2	2-1/4	Mg 1/3		6-1/2	12
600-81	Polyethylene	2	2-1/2	Al 1/3		9 x 11-3/4	13
600-80	Polyethylene	2	1-5/8	Fe 1/3		10 x 10-1/2	14
600-78	Nylon-Laminate	2	1-1/2	Mg 1/3		6-5/8 x 9	15
600-79	Nylon-Laminate	2	3/4	Al 1/3		9-1/4 x 12	16
600-84	Nylon-Laminate	2	1-1/2	Fe 1/3		11	17
600-82	Fiberglass Laminate	2	1-3/4	Mg 1/3		5 x 6-1/2	18
600-83	Fiberglass Laminate	2	1-3/4	Al 1/3		9-1/2 x 13	19
600-75	Fiberglass Laminate	2	2	Fe 1/3		Dent	20
600-73	Polyethylene	2	2-1/4	Mg 1/4		5-1/4 x 3-3/4	21
600-69	Polyethylene	2	2	Al 1/4		3 x 2-5/8	22
600-66	Polyethylene	2	2-5/8	Fe 1/4		1-1/4	23
600-76	Nylon-Laminate	2	2	Al 1/4		6 x 7	24
600-71	Nylon-Laminate	2	4	Fe 1/4		2-1/4 x 1-7/8	25
600-74	Fiberglass Laminate	2	1-3/4	Mg 1/4		3	26
600-77	Fiberglass Laminate	2	2	Al 1/4		3 x 4-1/8	27
600-72	Fiberglass Laminate	1	3-1/4 x 3	Fe 1/4		1-1/4 x 1-1/2	28

90° Angle of Attack

1" POLYETHYLENE



1/8" MAGNESIUM
BACK-UP



1/4" ALUMINUM
WITNESS PLATE

(U) FIGURE 1 (U)

1/8" ALUMINUM
BACK-UP



0 3 6 9 12



1" POLYETHYLENE

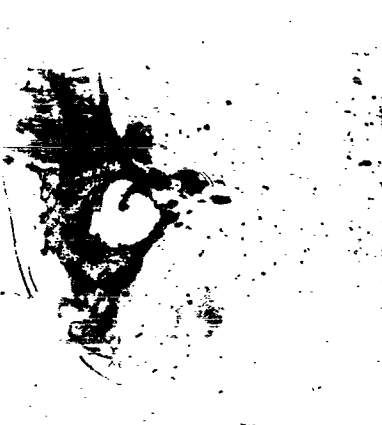


1/4" ALUMINUM

WITNESS PLATE

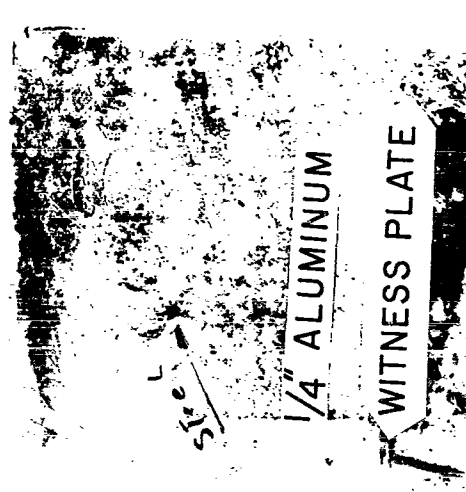
(U) FIGURE 2 (U)

1" POLYETHYLENE



1/4" ALUMINUM

WITNESS PLATE

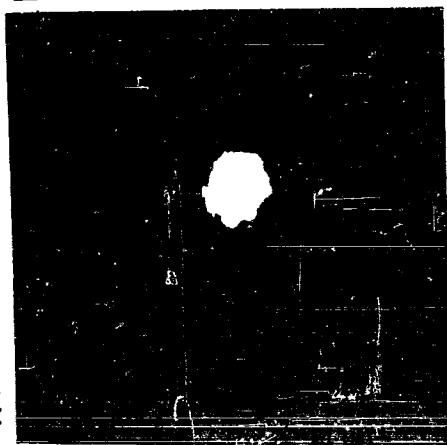


1/8" STEEL
BACK-UP



(U) FIGURE 3 (U)

1" NYLON FABRIC-PHENOLIC



1/8" MAGNESIUM
BACK-UP

0 3 6 9 12



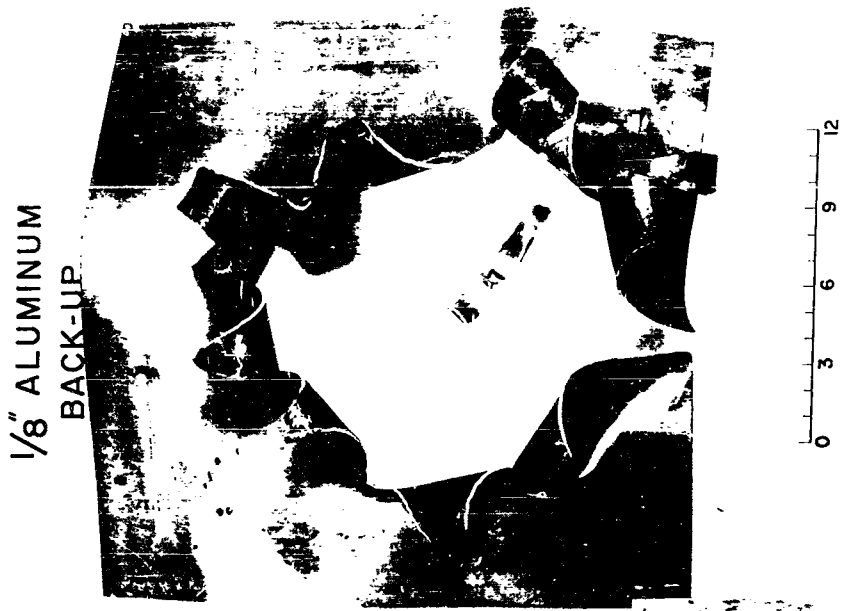
1/4" ALUMINUM



WITNESS PLATE

3

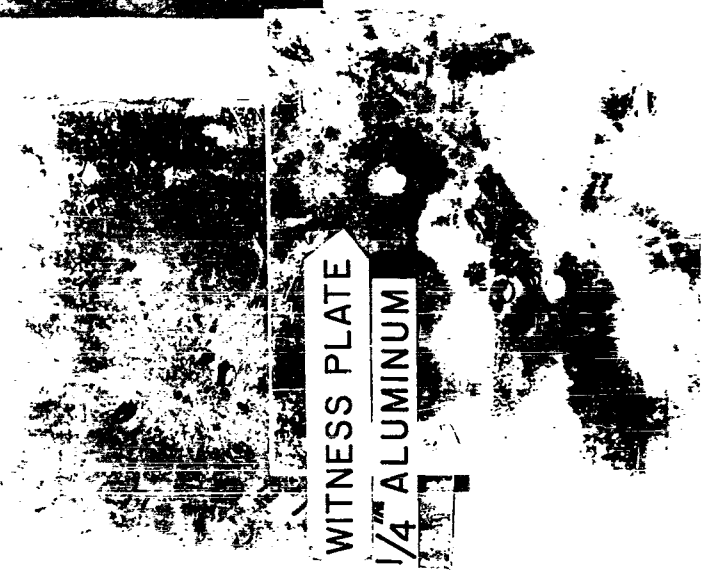
(U) FIGURE 4 (U)



1/8" ALUMINUM
BACK-UP



1" NYLON FABRIC-PHENOLIC



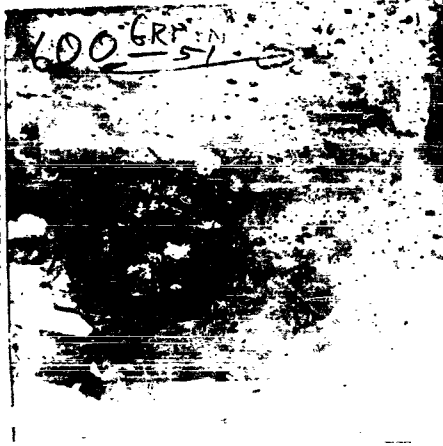
WITNESS PLATE
1/4" ALUMINUM

(U) FIGURE 5 (U)

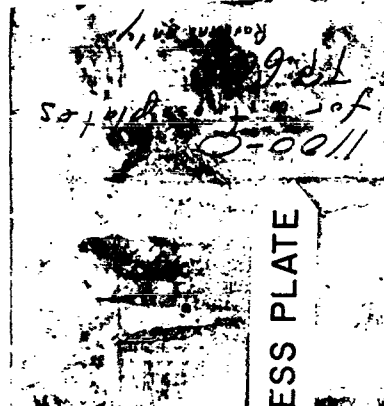
1/8" MAGNESIUM
BACK-UP



1" GLASS FABRIC-PHENOLIC

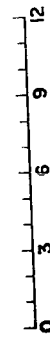


1/4" ALUMINUM WITNESS PLATE

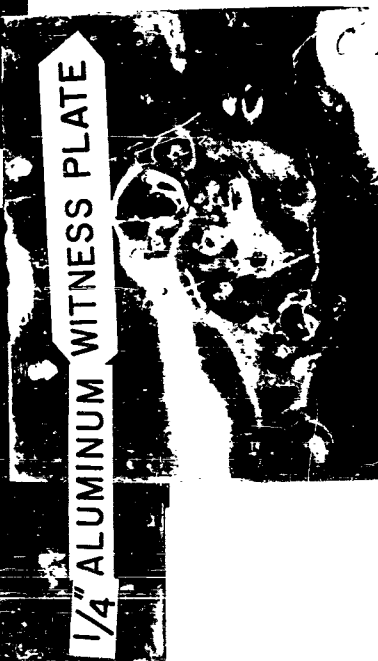
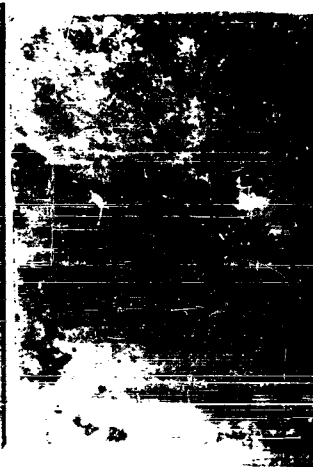


(U) FIGURE 6 (U)

1/8" ALUMINUM
BACK-UP

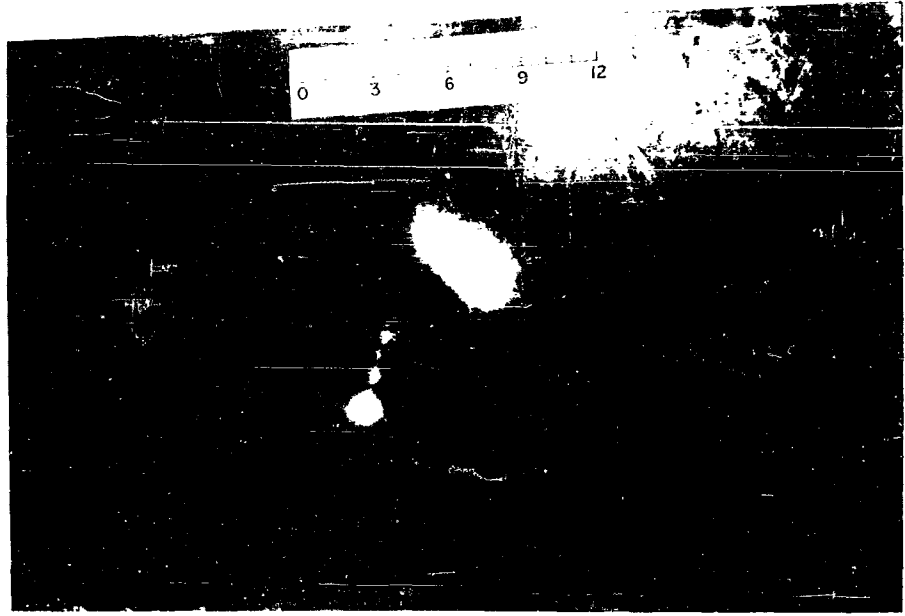


1" GLASS FABRIC-PHENOLIC



(U) FIGURE 7 (U)

1/8" STEEL
BACK-UP



1" GLASS FABRIC-PHENOLIC



(U) FIGURE 8 (U).

1/8" MAGNESIUM
BACK-UP

1" GLASS

0 3 6 9 12



1/4" ALUMINUM
WITNESS PLATE

(U) FIGURE 9 (U)

1/8" ALUMINUM
BACK-UP



1" GLASS

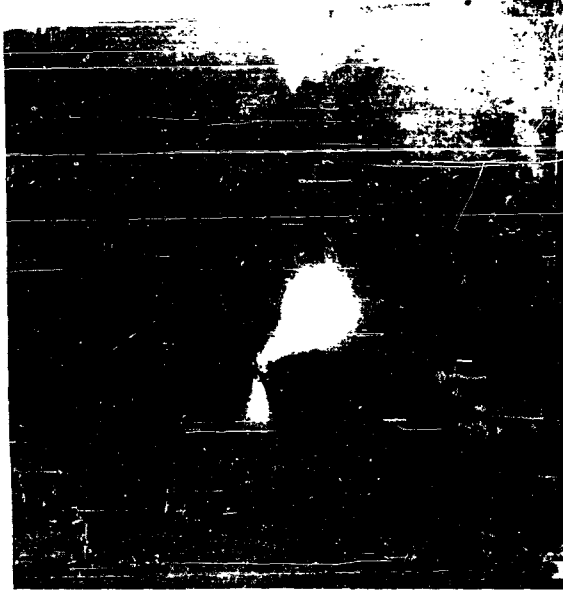


1/4" ALUMINUM
WITNESS PLATE

0 3 6 9 12

(U) FIGURE 10 (U)

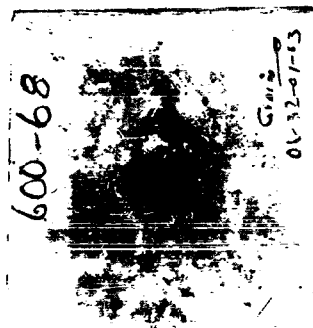
1/8" STEEL
BACK-UP



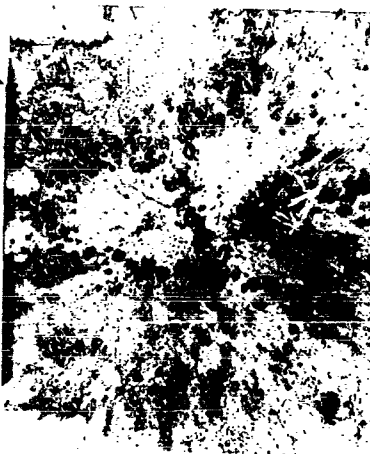
1" GLASS

(U) FIGURE 11 (U)

PRIMARY TARGET
2' POLYETHYLENE



1/8"
MAGNESIUM
BACK-UP



1/4" ALUMINUM
WITNESS PLATE

0 3 6 9 12

(U) FIGURE 12 (U)

PRIMARY TARGET
2" POLYETHYLENE



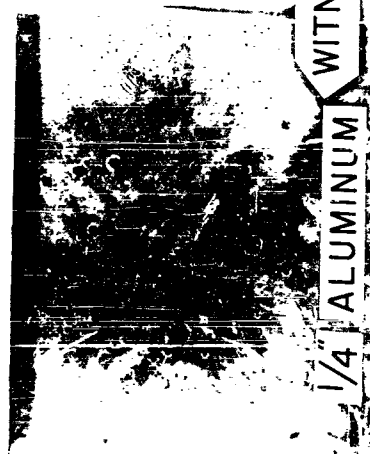
(U) FIGURE 13 (U)

PRIMARY TARGET
2" POLYETHYLENE



$\frac{1}{8}$ "
STEEL
BACK-UP

0 3 6 9 12

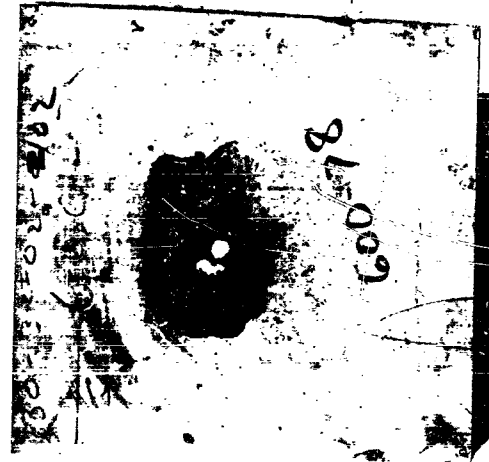


WITNESS PLATE

$\frac{1}{4}$ " ALUMINUM

(U) FIGURE 14 (U)

PRIMARY TARGET
2" NYLON FABRIC-PHENOLIC



1/8"
MAGNESIUM
BACK-UP

0 3 6 9 12

1/4" ALUMINUM WITNESS PLATE

(U) FIGURE 15 (U)

PRIMARY TARGET
2" NYLON FABRIC-PHENOLIC

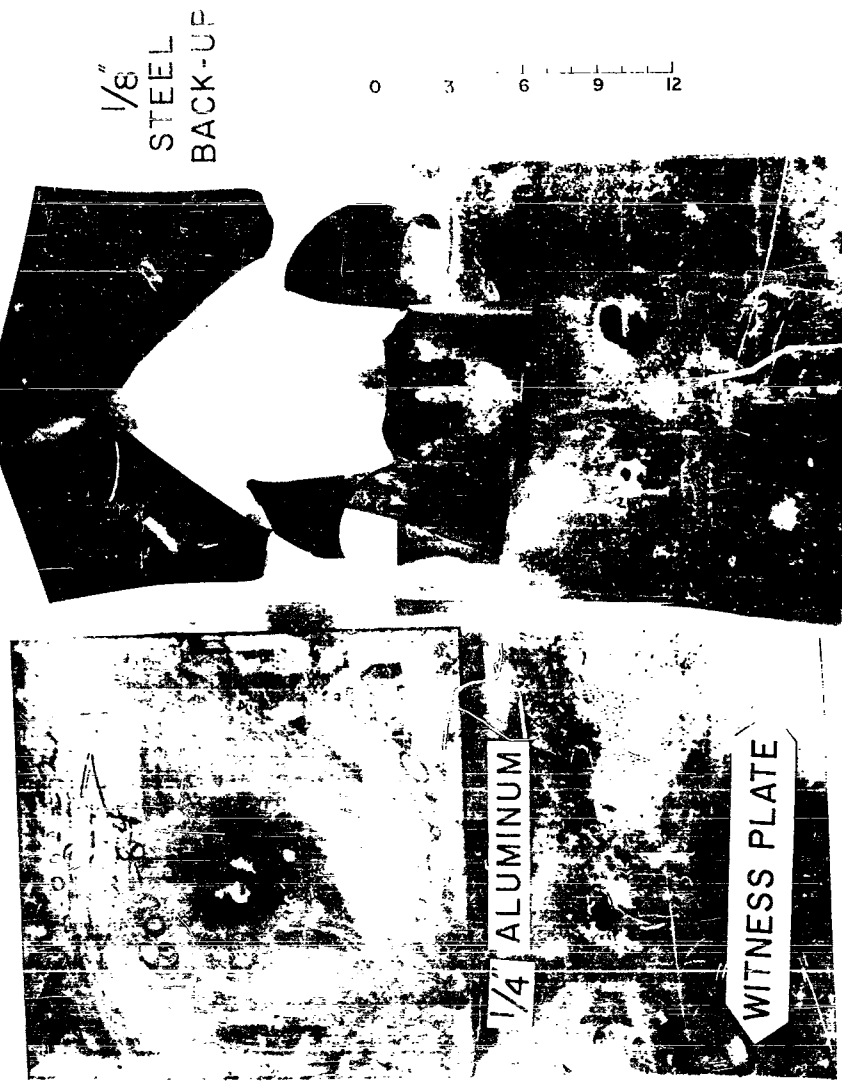


1/8"
BACK-UP
ALUMINUM

0 3 6 9 12

(U) FIGURE 16 (U)

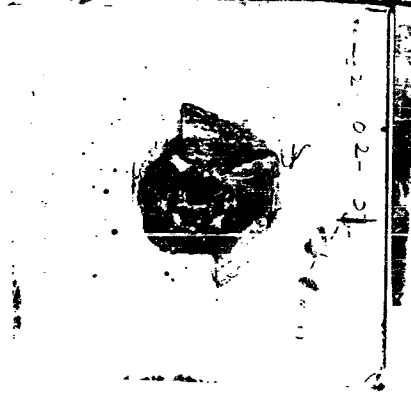
PRIMARY TARGET
2' NYLON FABRIC-PHENOLIC



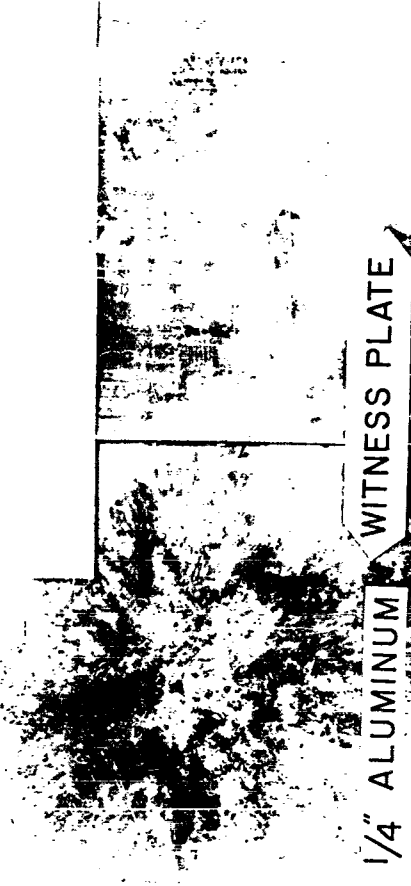
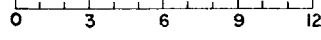
(U) FIGURE 17 (U)

PRIMARY TARGET

2" GLASS FABRIC-PHENOLIC



1/8"
MAGNESIUM
BACK-UP



1/4" ALUMINUM WITNESS PLATE

(U) FIGURE 18 (U)

PRIMARY TARGET

2" GLASS FABRIC-PHENOLIC

1/8"
ALUMINUM
BACK-UP

0 3 6 9 12

WITNESS PLATE

1/4" ALUMINUM

(U) FIGURE 19 (U)

PRIMARY TARGET
2" GLASS FABRIC-PHENOLIC

0 3 6 9 12



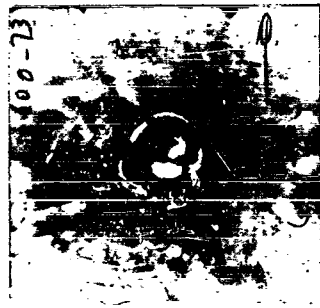
1/8"
STEEL
BACK-UP



(U) FIGURE 20 (U)

PRIMARY TARGET

1" POLYETHYLENE



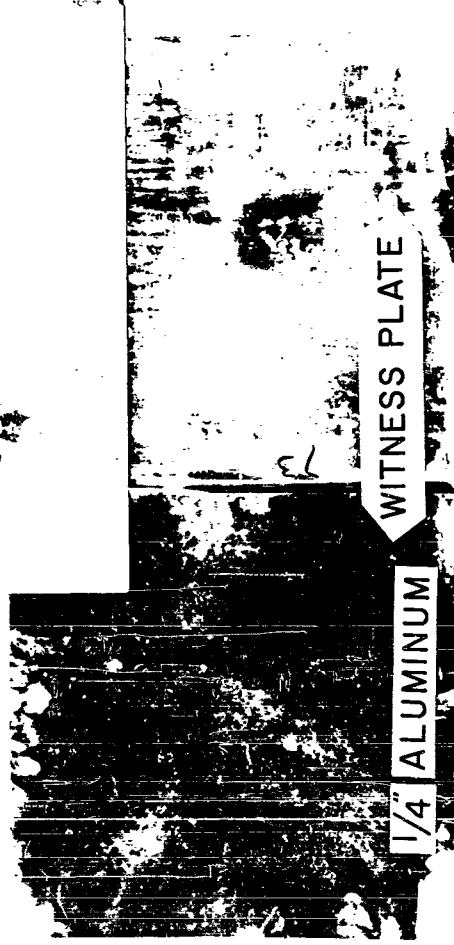
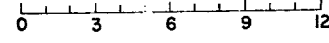
600-73



1/4"

~~ALUMINUM~~

BACK-UP



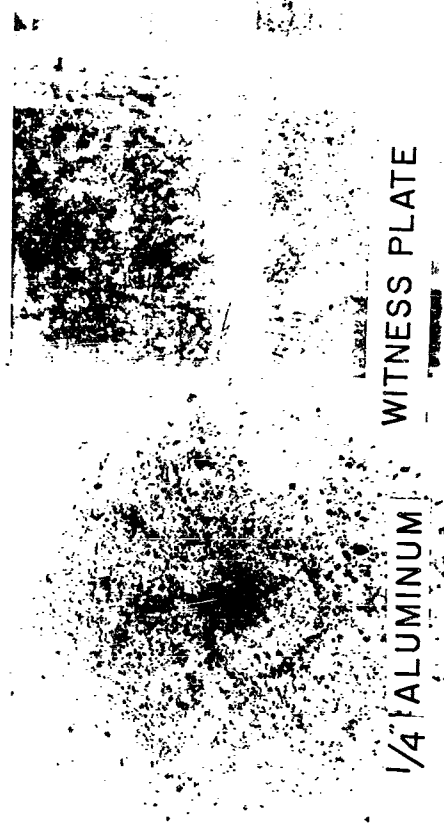
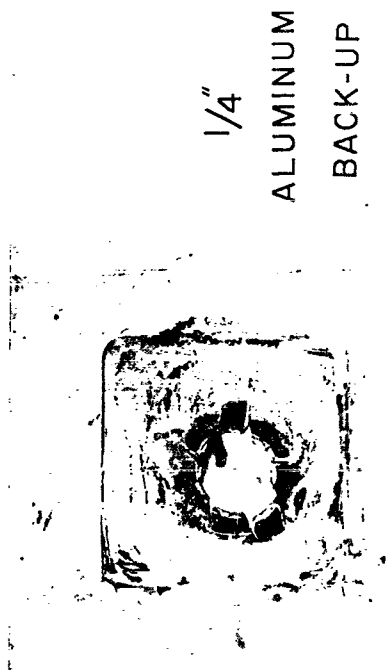
WITNESS PLATE

1/4" ALUMINUM

(U) FIGURE 21 (U)

PRIMARY TARGET

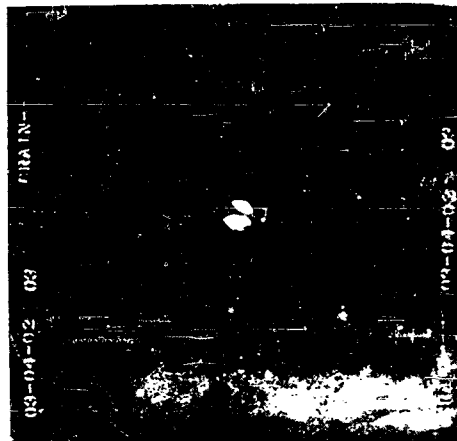
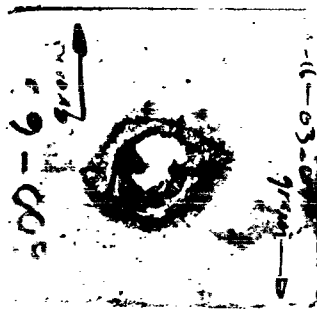
1" POLYETHYLENE



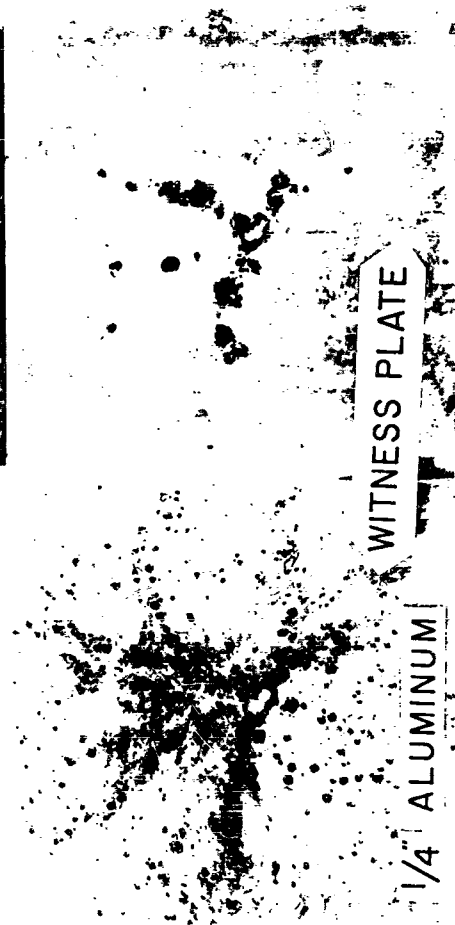
(U) FIGURE 22 (U)

PRIMARY TARGET

1" POLYETHYLENE



1/4"
STEEL
BACK-UP



0 3 6 9 12

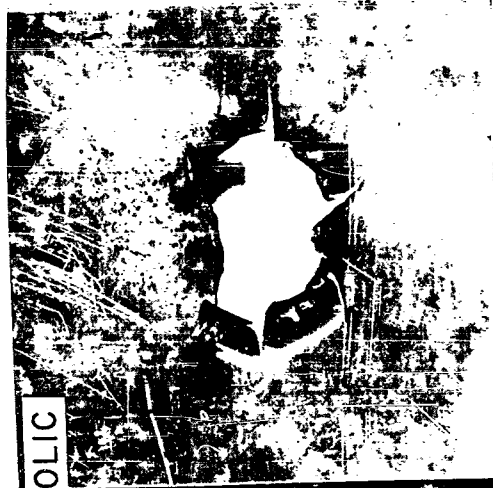
(U) FIGURE 23 (U)

PRIMARY TARGET

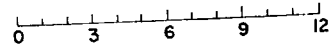
1" NYLON FABRIC-PHENOLIC



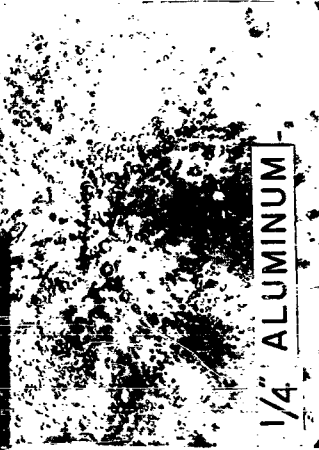
600-76



1/4"
ALUMINUM
BACK-UP



1/4" ALUMINUM

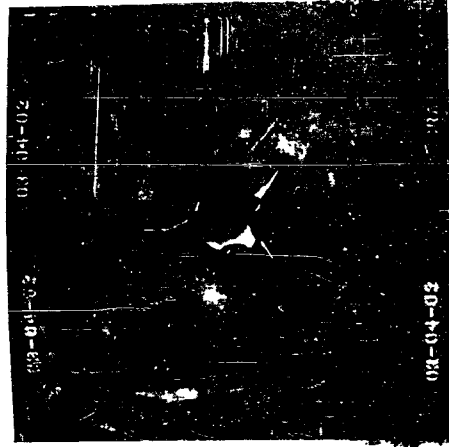


WITNESS PLATE

(U) FIGURE 24 (U)

PRIMARY TARGET

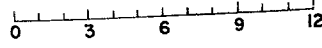
1" NYLON FABRIC-PHENOLIC



1/4"

STEEL

BACK-UP



WITNESS PLATE

(U) FIGURE 25 (U)

PRIMARY TARGET

1" GLASS FABRIC-PHENOLIC

600-74



600-74



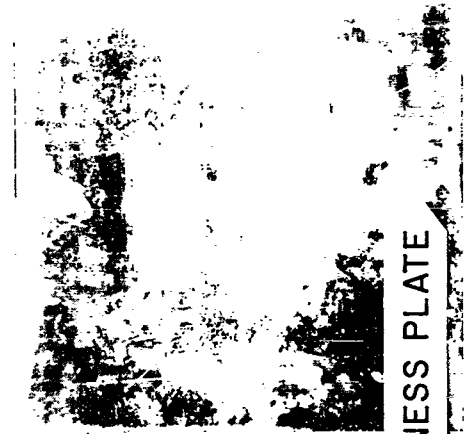
1/4"

MAGNESIUM

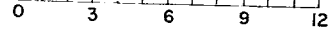
BACK-UP



1/4" ALUMINUM



WITNESS PLATE



(U) FIGURE 26 (U)

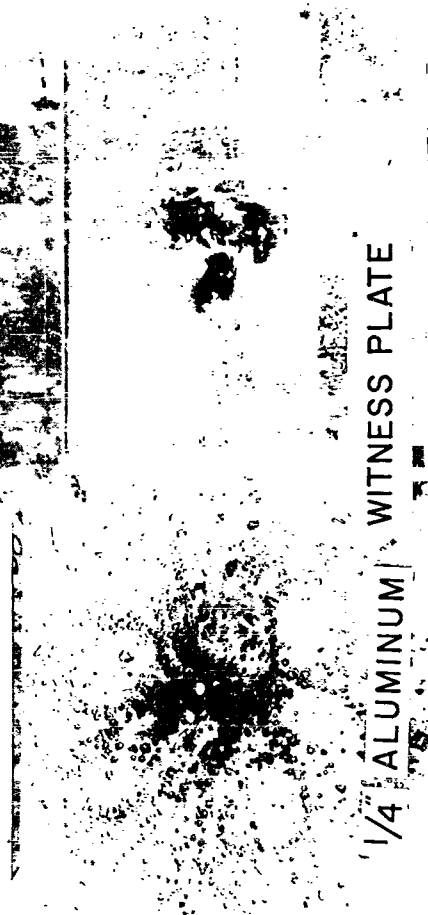
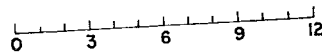
PRIMARY TARGET

1" GLASS FABRIC-PHENOLIC

20-76-02-03

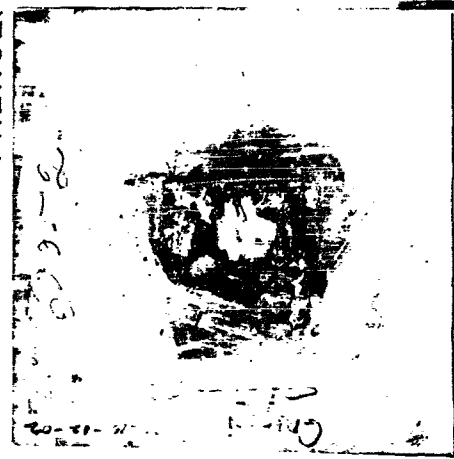


1/4"
ALUMINUM
BACK-UP



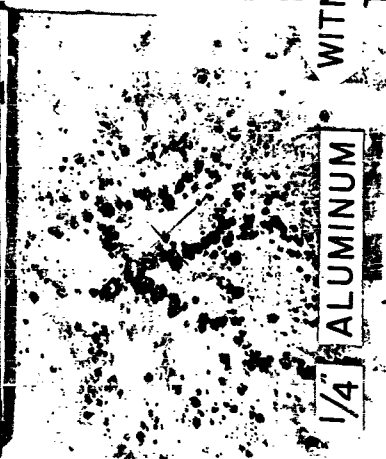
(U) FIGURE 27 (U)

PRIMARY TARGET
1" GLASS FABRIC-PHENOLIC



1/4"
STEEL
BACK-UP

0 3 6 9 12



1/4" ALUMINUM

WITNESS PLATE

(U) FIGURE 28 (U)

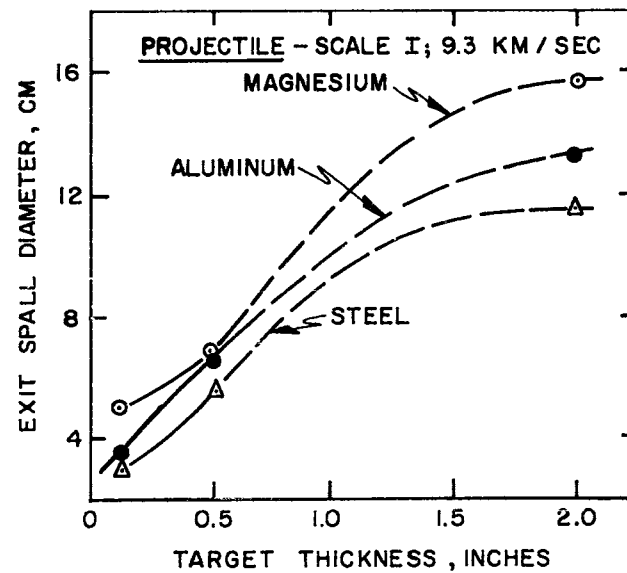
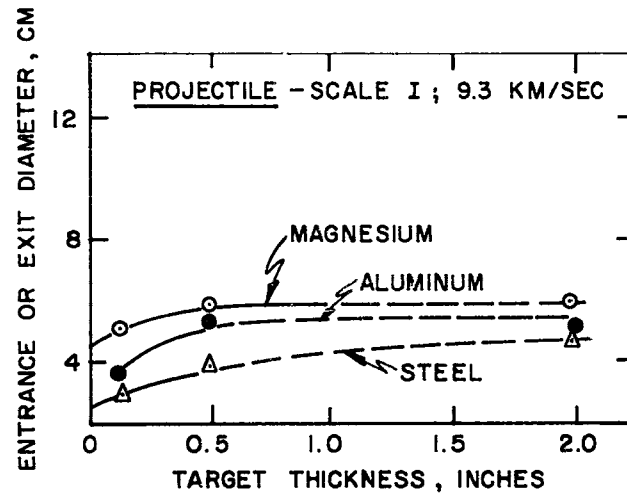


FIGURE 29 - PERFORATION AND SPALL DIAMETERS vs. TARGET THICKNESS FOR SEVERAL TARGET MATERIALS IMPACTED BY 9.3 KM/SEC, INHIBITED JET PROJECTILES.

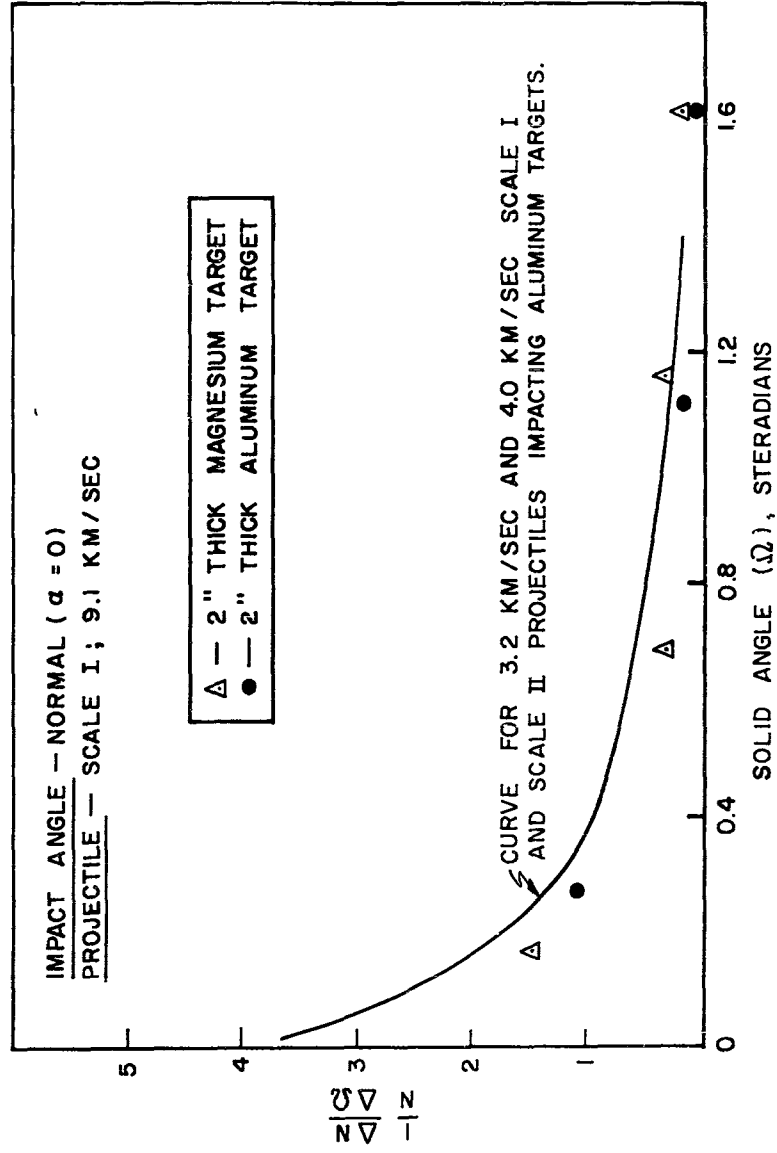


FIGURE 30—NORMALIZED DISTRIBUTION FOR TARGET SPALL NUMBERS

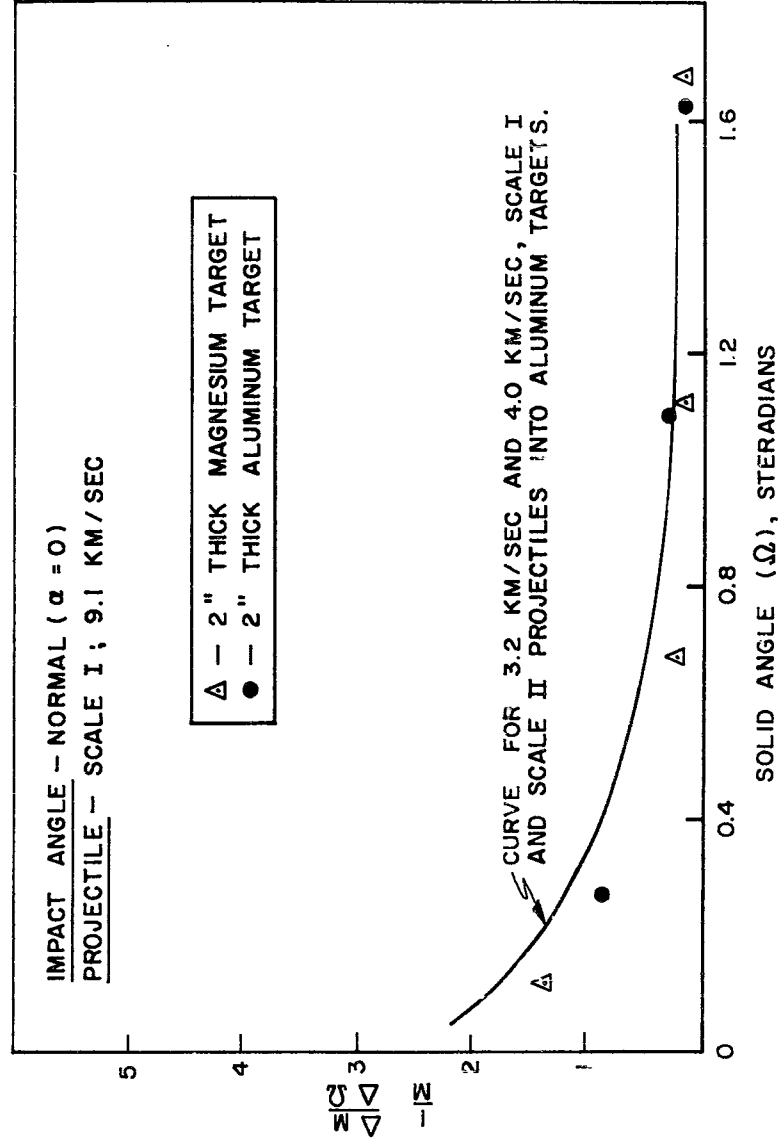


FIGURE 31 - NORMALIZED DISTRIBUTION FOR TARGET SPALL MASS

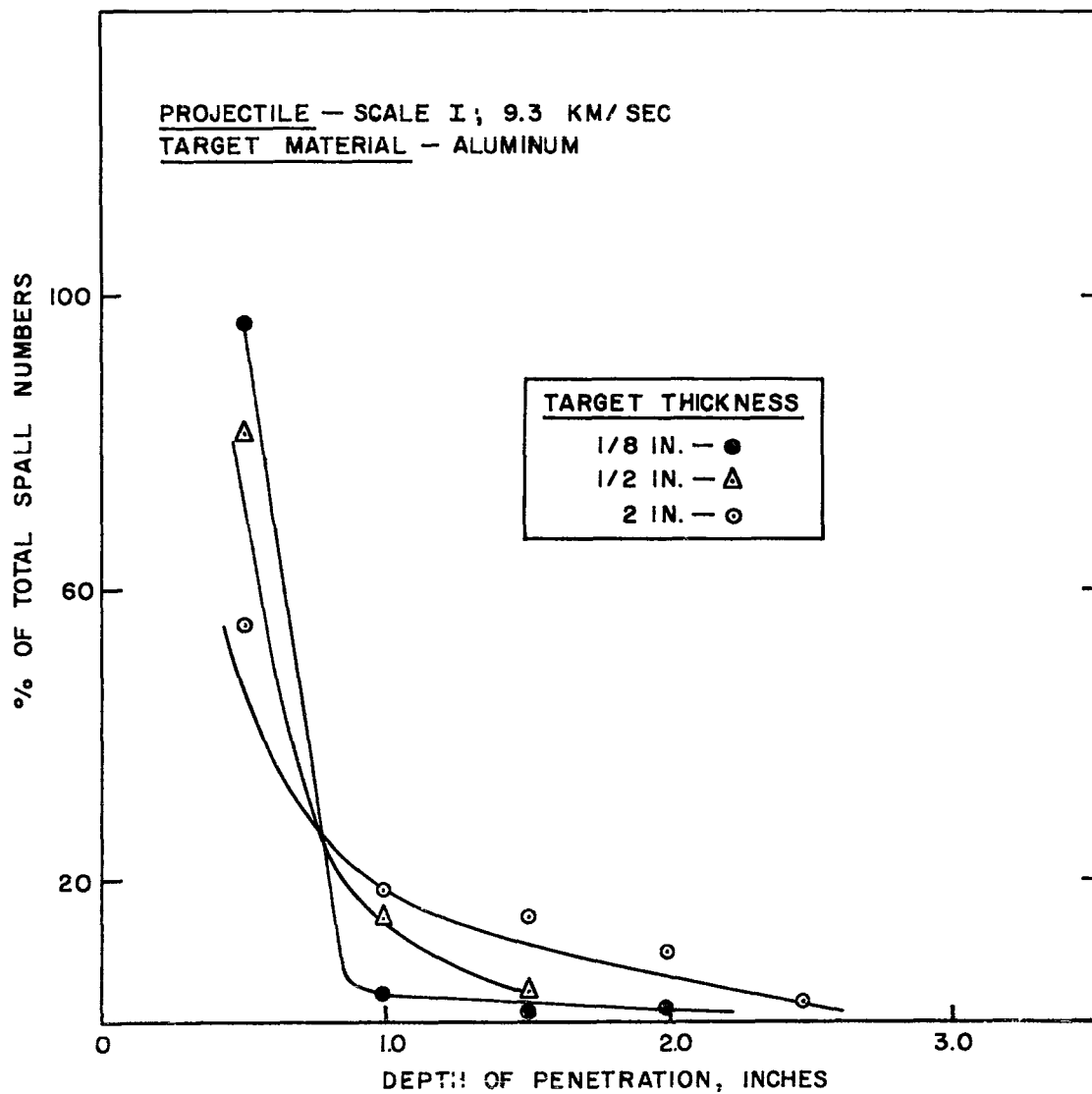


FIGURE 32 — NUMBERS OF ALUMINUM SPALL PARTICLES DISTRIBUTED
ACCORDING TO DEPTH OF PENETRATION INTO FIBERBOARD

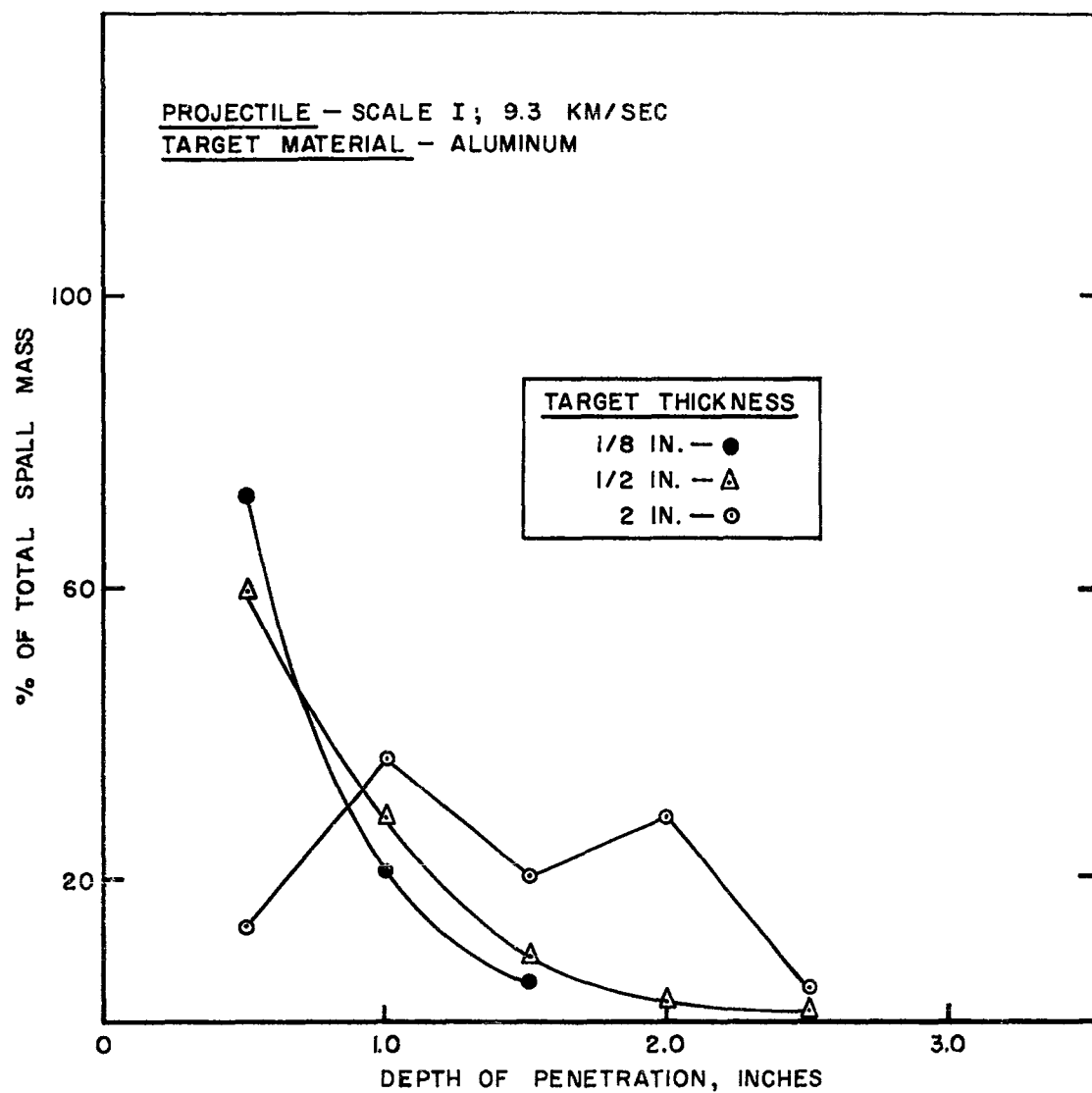


FIGURE 33 - MASSES OF ALUMINUM SPALL PARTICLES DISTRIBUTED
ACCORDING TO DEPTH OF PENETRATION INTO FIBERBOARD

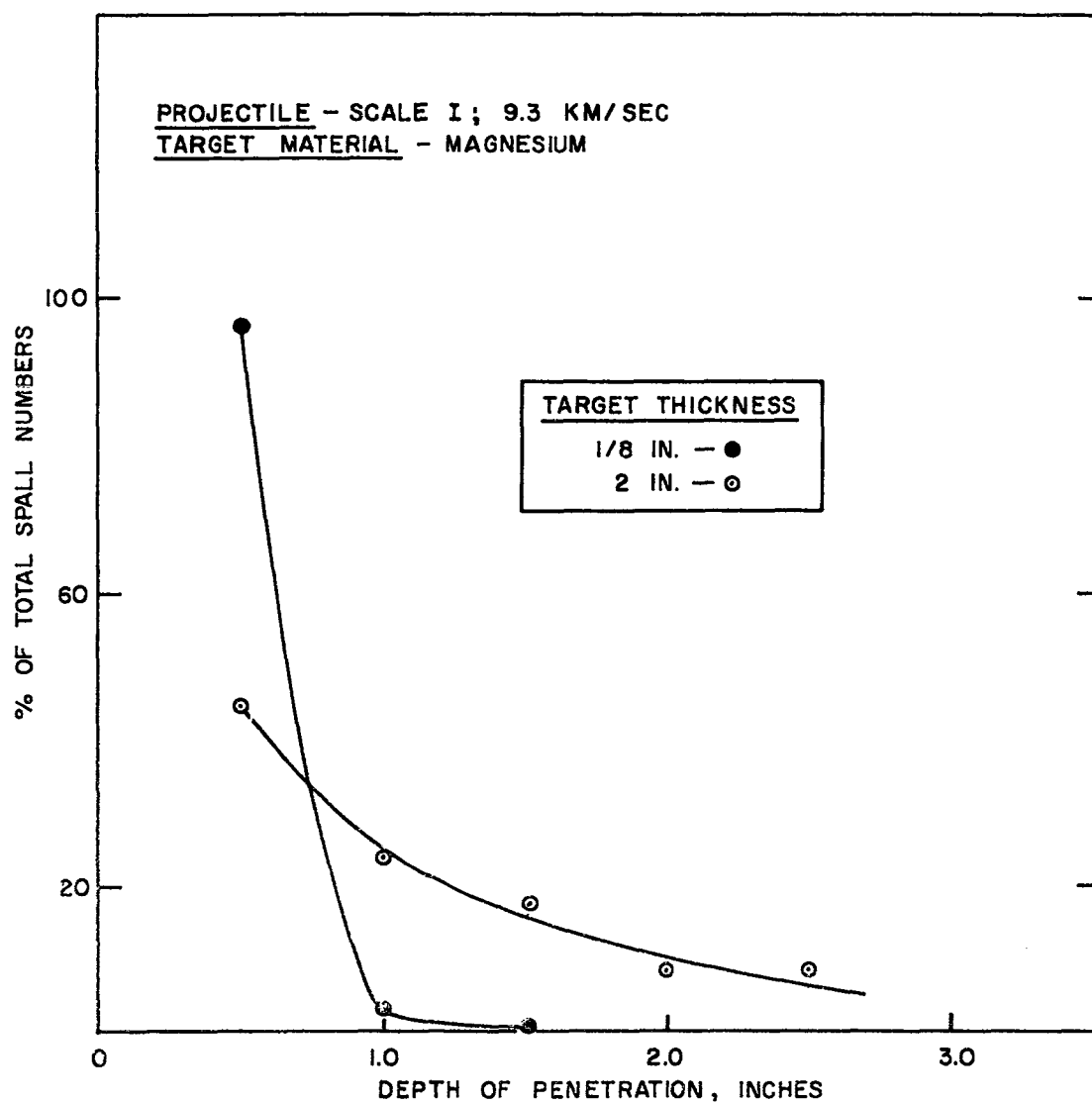


FIGURE 34 - NUMBERS OF MAGNESIUM SPALL PARTICLES DISTRIBUTED
ACCORDING TO DEPTH OF PENETRATION INTO FIBERBOARD

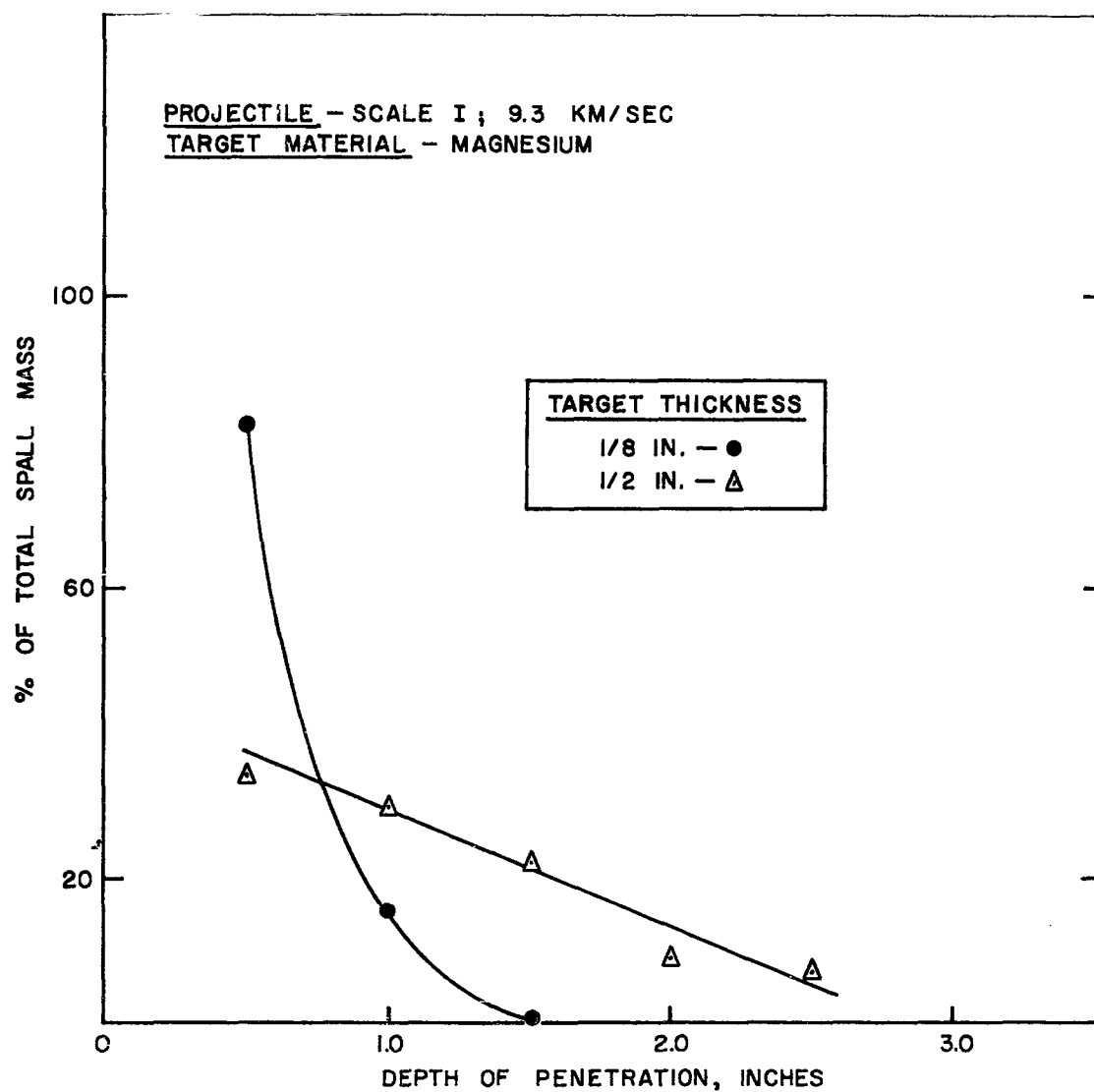


FIGURE 35 - MASSES OF MAGNESIUM SPALL PARTICLES DISTRIBUTED
ACCORDING TO DEPTH OF PENETRATION INTO FIBERBOARD

SECRET

NRL Memorandum Report 1492

HYPERVELOCITY KILL MECHANISMS PROGRAM
ARPA ORDER NO. 149-60

Impact Damage Phase

Annual Progress Report for Period
Ending 30 September 1963

J. J. Condon
S. M. Halperson

This research was supported by the Advanced Research Projects
Agency, Ballistic Missile Defense System Branch.

NOTE: This report is for inclusion in the overall HKM Report.
The page designation for this Section of the report is the
letter "B"

DDC AVAILABILITY NOTICE

All distribution of this report is controlled. Qualified DDC
users shall request through Director, U.S. Naval Research
Laboratory, Washington, D. C. 20390.

Further distribution of this report or of an abstract or
reproduction thereof may be made only with approval of
the Director, U.S. Naval Research Laboratory, Wash-
ington, D. C. 20390, or of the activity sponsoring the research
reported herein as appropriate.

U. S. NAVAL RESEARCH LABORATORY
WASHINGTON, D. C.

SECRET

B

SECRET

CONTENTS

	<u>Page Number</u>
PROBLEM STATUS	ii
AUTHORIZATION	ii
IMPACT DAMAGE PHASE	B
Summary	B1
Introduction	B2
Progress	B2
Phenolic Refrasil	B3
Phenolic Nylon	B5
GE Series 124A	B6
Impacts of Missile Components	B7
Witness Plates	B8
Sabot Development	B9
Spaced Steel Plates	B11
Conclusions and Future Plans	B13
References	B14
Table I - Hole Dimensions of Previously Reported NRL Data	B16
Table II - Impact Characteristics in Ablative Structures	B17
Table III - Physical Properties of Ablative Materials	B21
Table IV - Impact Characteristics of Steel Plates	B22
FIGURES	B23
APPENDIX	B41

SECRET

Bi

SECRET

PROBLEM STATUS

This is an Annual Technical Progress Report.
Work on this Project is continuing.

AUTHORIZATION

NRL Problem 62 F04-11B
ARPA Order No. 149-60
Amendments 1-7

SECRET

Bii

SECRET

SUMMARY

In this reporting period emphasis was placed on the perforation characteristics of different types of ablative materials. The targets were flat ablative plates bonded to metal plates for simulation of R/V outer construction. The ablation materials impacted were laminated and random-chopped phenolic refrasil and nylon and G.E. Series 124A. The thickness varied from 2-inch to 0.5-inch. The majority of the materials used in these impact experiments were one-inch thick. For the phenolics the back-up materials were steel, aluminum and magnesium varying in thickness from 1/8-inch to 1/4-inch. For the G.E. Series 124A the back-up was a one-inch aluminum honeycomb. The projectiles were solid steel, aluminum and plastic spheres. The tests were made primarily with steel spheres. The projectile velocity ranged from 3 to 7 km/sec and angles of obliquity from 90° (normal impact) to 15°. Correlations of the hole size with target thickness and composition, projectile energy, velocity, size and density were examined for each of the composite targets. Some comparisons are made between impacts into an actual ablative structure and the simulated flat plate targets. Photographs of all impacted targets discussed in the text are shown in the Appendix. A brief description is given of a solid sabot and stripping device which was developed during this period for higher velocity impacts. Also included as a separate topic are data and discussion on steel into steel impacts. These data were gathered from materials used as targets in firings in the development of a sabot for firing dense projectiles.

SECRET

B1

SECRET

INTRODUCTION

The object of this work is to determine the impact results on ablative materials and re-entry vehicle structures from hypervelocity impact with compact projectiles of various densities. Analytical means will be used to explain the experimental results and to correlate significant parameters so that accurate and reliable impact predictions can be made. Relationships will be established for penetration, minimum perforation and complete perforation of the various composite materials used in missile structures. The majority of the impact experiments are accomplished using targets which closely approximate the outside structure of actual vehicles. A limited number of impacts are made into actual vehicle sections.

PROGRESS

In this report year emphasis has been on the perforation characteristics of ablative materials. These targets were ablative plates bonded to a metal plate to simulate the R/V outer structure. The projectiles were primarily steel spheres with some aluminum and plastic. The projectile velocity ranged from 3 to 7 km/sec and angles of obliquity from 90° (normal impacts) to 15°. The ablative thickness varied from 2-inch to 0.5-inch with 1-inch thickness making up the majority of the materials used in the impact experiments. The tolerance on the ablative thickness was 1/32-inch. The metal back-ups were steel, aluminum and magnesium varying in thickness from 1/8-inch to 1/4-inch.

Table I is a list of new measurements of previously reported data obtained from experiments completed prior to this year. The measurements are listed with the round numbers in order to provide identification of the impact data previously reported. Table II is a list of all targets impacted during this reporting period with the impact conditions and the data obtained. The targets listed in Table II are in the following general order: phenolic refracil, phenolic nylon, GE 124A and R/V's. For the two phenolic materials the laminated type is listed first and the random-chopped molded variety is listed second. For the same ablative material and projectile size the experiments are reported in the order of increasing velocity. The perforation areas reported in both Tables I and II were obtained by tracing the outline of the minimum hole size in the ablative and measuring the enclosed area with a polar planimeter. An equivalent diameter for a circular hole, D_a , was then calculated from this measurement.

SECRET

B2

SECRET

In Appendix A, photographs of each target are shown with the witness plates. The photographs for each target are listed separately in the Appendix and appear in the same order as in Table II. Ablative material properties are shown in Table III.

Graphical correlations are shown in Figures 1,2,3,4 for the phenolic refrasil and nylon and the 124A material. The correlations are the best that have been obtained so far. Attempts to fit a curve to these data were not satisfactory due to a lack of higher energy and higher velocity data and to the large scatter in the lower regions. The plots indicate that for the phenolic materials the hole size trend is not increasing at the same rate above energy/thickness ratios of 10 to 15 kilojoules per cm as it is below these values. The experiments that are planned in the next few months will provide additional data and it is felt that a curve can then be fitted to the data. In order to see how the data compare to previously reported results an expression given in Reference 1 is plotted on the same graph.

The impact experiments that were planned for the last quarter of this report year were postponed because of sabot development necessary for these experiments and for support of the large projectile mass experiments using the 8.2" - 2.5" light-gas gun.

PHENOLIC REFRASIL

The laminated and random-chopped refrasil phenolic materials that were impacted this year are listed in Table II along with the impact results obtained. The ablative thickness varied from 0.5-inch to 2-inches and the thickness of the steel and aluminum back-ups (when used) varied from 0.125-inch to 0.25-inch. The projectiles were primarily steel, with some aluminum and plastic (zelux), spheres and cylinders. All projectiles except the plastic were sabot. Impact angles were varied from 90° (normal impact) to 15°. Projectile velocities covered a range from approximately 3 to 7 km/sec; masses from 1 to 15 gm. This corresponds to a range of impact energies from 10 to 350 kilojoules.

SECRET

B3

SECRET

Figure I is a graph of the equivalent hole diameter D_a in the ablative vs impact energy per unit of ablative thickness for all the phenolic refrasil data that has been obtained at NRL for the cases where at least perforation of the ablative has occurred. The laminated and random-chopped molded types are designated by triangles (Δ) and circles (O) respectively. Although there is considerable scatter in the data, a large number of impact conditions are covered. Note that in some cases the back-up was not perforated and in other instances the hole in the metallic back-up material was not as large as the hole in the ablative material.

Consistent differences in the perforation diameters for the laminated and random-chopped squares ablatives are not apparent, however, there does appear to be some difference in the front spall characteristics in the two types of materials. As shown in the photographs of the Appendix (see, for example, round numbers 4-865 and 4-866) the front spall area in the laminated material is not much larger than the perforation area. The spall cavity in the random-chopped type is shaped differently and has a larger area than the perforation.

In the impact experiments with the phenolic refrasil material the back-ups usually came off the back of the ablative during the impact. The material was procured without back-ups and the bonding was made in-house. Two methods were used: (1) a thin layer of glue was put between the ablative and the metal and allowed to set overnight, with weights to provide sufficient pressure to keep the two in contact and (2) an epoxy bond with the ablative and metal plate pressed together under heat. When the metal plate came off during impact it pulled a very thin layer of ablative material with it. The phenolic nylon and 124A materials were procured with the back-ups already bonded to the ablative. The bonding was 1/16-inch thick rubbery-type for the phenolic nylon and 1/8-inch thick felt-type bond for the 124A. The back-ups for these latter two materials did not come off as a result of impact.

The steel and aluminum back-ups used with the phenolic refrasil always petalled when perforation of the metal occurred. A typical bulging and stretching of the metal around the perforation that occurs prior to separating into petals is shown by round number 1-1-65 where perforation of the back-up did not occur.

SECRET

B4

PHENOLIC NYLON

The impacted laminated and random-chopped phenolic nylon materials are listed in Table II along with the impact conditions and results. The back-up thickness was 0.25-inch and the material was aluminum for the laminated nylon and magnesium for the random-chopped type ablative. The 1 to 2 gm steel spheres impacted at 90° with velocities from 3 to 5 km/sec.

A correlation of the equivalent perforation diameter in the ablative vs energy per unit thickness of the ablative for all of the phenolic nylon data is shown in Figure 2. Also shown in this figure are several impacts into R/V structures. On the basis of this correlation these impacts are in approximate agreement with the impact results from the regular flat-plate target configuration. Analysis of this impact data has been particularly difficult due to the erratic results obtained. Whether this is due to different characteristics in the material coming from different batches or borderline transitions that occur at certain critical velocities is uncertain. Results for round numbers 4-851 and 4-852 shown in the Appendix are an example of this inconsistency. The projectiles in this case were 0.25-inch diameter, 1-gm steel spheres impacting at 90° with a velocity of 4.75 km/sec. As shown in the photographs (see Table II for actual measurements) the perforation diameters for the two impacts are considerably different although the front spall and hole in the magnesium back-up are approximately the same. Although other correlations, and modifications to the one used here have been tried, none have been as successful.

Within the energy range of this data a difference has been observed between the type of spall cavity formed in the laminated phenolic nylon as compared to the random-chopped type. The depth of the spall cavity in the random-chopped molded material varies in a gradually increasing amount from the outside edge of the spall cavity toward the center of the perforation. The depth of the cavity remaining in the laminated type is nearly constant from the outside edge of the cavity toward the center where the perforation is located. An example of this can be seen in the Appendix by comparing round number 4-871 and 4-867. The spall characteristics for the random-chopped phenolic re-frasil and nylon are very similar. The laminated types of these two materials have different spall cavities. An example of this can be seen in the Appendix by comparing round number 4-865 and 4-871.

SECRET

For lower energy impacts into the random-chopped material, large pieces of the front spall are often recovered after impact and can be placed back into the spall cavity. An example of this is shown in Figure 5 for round numbers 4-851 and 4-852. The small hole where the projectile entered the material is clearly discernible. The shock waves resulting from these impacts were not strong enough to disintegrate the material but were intense enough to fracture the material around the perforation and loosen large pieces of spall.

The majority of the impact experiments with phenolic nylon and refracil were made with targets of 1-inch thick ablative with 1/4-inch metal back-up. For the cases of complete perforation the hole in the metal back-up was as large or larger than the perforation in the ablative. An inconsistent result can be seen in Appendix A for round number 4-889. In this case the ablative material was 1/2-inch thick and the aluminum back-up was a 1/4-inch thick. As can be seen from Table II the diameter of the perforation in the back-up is only about 1/2 the diameter of the ablative hole. Comparing this result to other similar impact conditions, e.g. round number 4-871, where the ablative thickness is 1-inch shows that the hole in the back-up is larger than in the ablative. Whether the result shown by round number 4-889 is due to the physical difference in the thickness of the ablative or a ratio between the ablative to back-up thickness is not certain.

The aluminum back-up used with the phenolic nylon always petalled when perforation occurred whereas the magnesium always broke off in fragments.

GE SERIES 124A

A summary of the impacts into the 124A material with nylon and steel spheres is shown in Table II. The 0.25-inch diameter sabot nylon spheres (0.156gm) impacting at 90° did not perforate the composite target for velocities up to 6.58 km/sec (rounds 5-3-60 to 5-3-67). The 7/16-inch ablative material was perforated at a velocity of about 4.6 km/sec (see round number 5-3-64). The "projectile" was visible in the bottom of the crater after impact in round numbers 5-3-60, 61, 62 and after removal (round number 5-3-62) the weight of the nylon sphere was about the same as before impact.

SECRET

B6

SECRET

It could be seen from visual inspection that part of the "projectile" was composed of ablative material fused to the nylon. Although the nylon sphere did not perforate the entire back-up, the associated impact in rounds 5-3-66 and 67 did loosen the last aluminum plate in the honeycomb sandwich from the honeycomb for more than half the contact surface.

Comparison of the equivalent hole diameter in the ablative vs impact energy is shown in Figure 3 for all the steel sphere impacts. The results show that the impact effects for this material are more dependent on the impact angle than are the phenolic materials. For those materials, with the data obtained so far, the angle of impact did not make a large difference in the equivalent diameter of the perforation, provided the energies were above the minimum perforation value. In the 124A material both minimum perforation and hole diameter are dependent on the angle of impact. As can be seen in Figure 3 the 15° impact hole size compares favorably with the 90°. The 30°, 45° and 60° hole sizes are all larger than the 90°. It is interesting that the ablative material hole sizes for 15° and 90° do compare fairly well on an energy basis although the 15° impacts did not perforate the entire target. Figure 4 is a comparison of the equivalent hole diameter in the ablative material vs impact velocity for 90° impacts with 0.25-inch steel and nylon spheres. Round numbers 1-2-9 to 1-2-18 were impacts of this material with 0.25-inch steel spheres at velocities from 3.86 to 5.57 km/sec. The steel spheres completely perforated the target at all of the velocities in this range.

IMPACTS OF MISSILE SECTIONS AND COMPONENTS

Impact data on components of actual R/Vs are needed for two reasons: (1) To determine the damage to one of these components from an actual impact and (2) To be sure that the target configurations (sample sections approximating the actual vehicle skin) used in the impact studies are producing the same results as full scale vehicle impacts.

Round numbers 1-1-28, 1-1-31, 4-745 and CBA-1 listed in Table II are impact experiments on actual components where complete perforation occurred. A photograph of the impacted cylinder and flare of an early Mark IV R/V, that was used in Round Number CBA 1, is shown in Figure 6. The projectile was Lexan cylinder and weighed 253 gms. before launching.

SECRET

B7

SECRET

The projectile impacted with a velocity of 5.6 km/sec. The impact angle was 20° from the cylinder surface. The point of impact was just forward of the 7/8" by 3/4" steel flange shown in Figure 6.

Although none of the ablative and back-up structures of the sample targets correspond exactly to that of the vehicle, the resulting hole size based on damage to the back-up material compares favorably with the E/T correlation. It should be noted that extensive cracking and delamination occurred to both the ablative and metal structure of the R/V. A more complete discussion on structural damage produced during this experiment will appear in a forthcoming report on damage by large mass fragments by C.D. Porter.

WITNESS PLATES

For most of the experiments reported during this past year, a soft aluminum (1100F) witness-plate stack was spaced about 10-inches behind and parallel with the target (see Figure 7). This witness-plate stack was made up of a series of 1/8-inch, 1/4-inch, or 1/2-inch plates with zero spacing. For oblique impacts, an additional stack was placed perpendicular to the target. The purpose of the witness plate was to obtain an estimate of the severity of the damage caused by the spall emanating from the rear of the target after impact. From this information the expected damage to internal components of an R/V after an impact on the outer surface can be approximated. Initially it was planned to count the number of perforations in each one of the plates making up the witness-plate stack and to report this information. However, in most of the firings the force of the blast coming from the rear of the target mashed or welded the plates together making it very difficult to separate them. In the Appendix is shown a photograph of the first witness plate of the stack for each experiment where a witness plate was used. Included in the caption of each picture is the total number and thickness of the plates, the distance of the first plate from the target, and the depth of the deepest penetration measured normally from the surface of the first plate.

SECRET

B8

SECRET

SABOT DEVELOPMENT

In order to simulate in the laboratory the impact conditions that would exist during a fragment encounter with an R/V it is necessary to accelerate dense projectiles to velocities between 5 and 10 km/sec. Current interest is primarily in high-mass projectiles of steel and uranium. Initial attempts toward improving the design of split sabots utilizing stronger materials failed because the severe stresses imposed on the sabot during acceleration usually resulted in the projectile breaking through the rear of the sabot permitting the driver gases to escape resulting in a lower projectile velocity than expected. All projectiles used in the impact experiments reported in the tables were made with split sabots.

An improvement in saboting technique for dense projectiles at higher velocities was accomplished with a solid sabot which is separated from the projectile after it reaches maximum velocity. Of the various designs and materials used for solid sabots the best results were attained with a composite type of fibreglas and plastic. Figure 8 is a dimensional drawing of this type of sabot used in a 30-caliber launch tube. The outer cylindrical cup is Zelux and the inner core is Scotch Ply*, Type 1002 Crossply, which is a glass-reinforced epoxy resin. The glass fibers are oriented perpendicular to the longitudinal axis of the sabot. The dimensions have been scaled for successful firings in larger diameter launch tubes (up to 2.5-inch I.D.). The calculations for determining the maximum acceleration loading to which a given sabot and projectile combination can be subjected, without break-up of the sabot, were based on a simple shear-out calculation, using the shear strength of the sabot material, thickness of material under the projectile and the projectile diameter and mass. The expected values of maximum acceleration were provided by the NRL-Narec light-gas gun computer program.

The use of a solid sabot required that a means be found for separating the sabot from the projectile after accelerating and removing the sabot from the trajectory. A

* Trade name for this product made by the Minnesota Mining and Manufacturing Company.

SECRET

B9

SECRET

sabot stripping device consisting of a series of thin, spaced plates with drilled holes attached directly to the muzzle end of the launch tube was successfully tested for use with a 30-calibre launch tube. The 1/16-inch 1100F aluminum plates were spaced 1/2-inch apart with the first plate 1/8-inch from the muzzle. After further development the stripper, as currently used, consists of only two copper plates. The dimensions of the plates, holes and spacers have been scaled successfully for use with larger diameter launch tubes. The distance of the first stripper plate from the muzzle has been held to no greater than half the length of the sabot in order to insure that the projectile will be separated from the sabot while the launch tube is still guiding the sabot. With this arrangement, accurate trajectory will result. This stripping device has operated successfully for most of the firings. Figures 10 to 12 are a series of flash x-ray pictures taken from firing records which show the sequence of events that take place. Figure 10 is a picture of a solid sabot and steel sphere, several inches after leaving the muzzle, when a stripper was not used. The photographs shown in Figure 11 are taken at the same position after launch, as in Figure 10, when the stripper was used to separate the steel sphere from the same type of sabot. In the first picture a single copper plate was used and in the second picture two copper plates were used. In both cases the steel sphere was out of the field of view but is shown in another experiment in Figure 12. In this photograph a larger field of view is covered than in Figure 11, and both the steel sphere and the debris from the stripper can be seen.

Modifications to the sabot and sabot stripper are continually being made. It is expected that during the next year the hypervelocity impact data, from 6 to 9 km/sec using solid spheres of steel and uranium will be obtained.

SECRET

B 10

SPACED STEEL PLATES

This section deals with impacts of steel spheres into structures of specifically spaced steel plates, and these data were obtained from targets and firings used in the sabot development program. Targets were SAE 1020 or SAE 4340 steel. (Two impacts were also made into thick block targets of 1020 steel). The masses of the projectiles ranged from 1.05 to 100 grams, and impact velocities ranged from 6.26 km/sec to 4.48 km/sec. All impacts were at 90° to the surface of the target. Table IV shows the parameters and results of the experiments.

Phenomenologically, hypervelocity impact damage may be divided into two categories: thin plate and semi-infinite or thick plate. The former condition exists when the ratio of the plate thickness (t) to the projectile diameter (d) is much less than one. The critical ratio for this condition to commence is dependent on the plate and sphere materials involved, and impact velocity. The semi-infinite condition exists when the specimen is large enough to prevent disturbance of the crater by reflected waves from free boundaries. A third, transitional category showing some characteristics of the other two categories also exists. The different impact conditions are illustrated in Figure 13.

The most realistic case from the viewpoint of protecting vulnerable missile components from a hypervelocity kill is the thin plate condition (Figure 13a). In this impact situation the intense initial shock is modified not only by lateral rarefactions but by the release wave reflecting from the rear of the plate. The impact phenomena can be described in terms of compressible, inviscid, hydrodynamic flow, and material mechanical properties are not of prime importance. For a specific impact (known projectile and target and impact velocity) the resulting hole will decrease and should approach the diameter of the projectile as the thickness of the plate approaches zero. Figure 14 illustrates this type of impact.

The transitional impact category (Figure 13b) exhibits the characteristics of both thin plate (Figure 13a) and thick target (Figure 13c) impacts. Although the target is perforated, the hole is not as clearly defined as in the thin plate, lateral flow of the target material is evident as is spalling of the front and rear surfaces. Figure 15 is an example of this type of impact.

SECRET

The thick target case is merely an extension of the transitional impact category. The specimen's dimensions, however, are large enough to prevent crater distortion by reflected stress waves. Extensive discussion of thick target cratering can be found in the literature.

Measurements were made of hole dimensions in each plate of the structures under investigation. Depth of penetration, and crater diameter and volume in thick targets were also measured (Table 4). The ratios of minimum hole diameter to sphere diameter (D_h/d) where D_h is the hole diameter in the initial plate are included. Although limited data are presented, initial plate hole size may be predicted for an impact situation from the hole of another impact provided the materials are the same, and the ratio of plate thickness to sphere diameter, and velocity are equivalent.

Target ejecta and those portions of the projectile which pass through the first plate may possess a large damage potential. In the thin plate case, the velocity of small spall fragments can approach that of the projectile. With the impact of transitional target by a high-speed pellet, the spall will consist of fewer, larger fragments moving at low velocities, compared with impact velocity. The damage potential behind a semi-infinite target is zero.

Let us consider a structure composed of thin plates ($t/d < 1$) which is struck by a hypervelocity pellet. The initial plate impacted will have a clearly defined circular hole punched in it. A cloud of debris composed of projectile and target fragments will be projected from the initial plate. If the spall has sufficient energy density, a similar clearly defined perforation will occur in the second plate. This perforation will be larger than the first plate hole, since the spall bubble will be expanding both radially and axially. Bending and tearing frequently occur in successive plates. It should be noted that damage is extremely sensitive to plate spacing due to the rapidity with which the spall pattern changes shape. Figure 16 shows the damage to an array of 1/8-inch thick steel plates impacted by a 25-gram steel sphere at a velocity of 4.22 km/sec. Plate 1 is cleanly perforated, while plate 2 shows evidence of bending. Succeeding plates clearly show bending and tearing of the steel. At plate 7 the remaining energy density of the debris from plate 6 is sufficient to produce a 3.14 cm bulge.

Quantitative measurements of target impulse and spall momentum should be the next consideration in the investigation of impact damage to spaced plate structures. Pendulum techniques and pressure measurement devices which can be used to access these parameters are currently available or under development.

SECRET

CONCLUSIONS AND FUTURE PLANS

The graphical correlations shown in Figures 1 to 4 are the most satisfactory obtained so far. In order to fit a curve to the data reported it is necessary that information be obtained at higher velocities and energies. The expression, $D_a = K\left(\frac{E}{T}\right)^{0.36}$, obtained from Reference 1, when plotted on the graphs of Figures 1 to 3 does show fairly good agreement with the present data, except for oblique impacts of the GE 124A material. It should be noted that the expression from Reference 1 was derived from impacts where the hole in the back-up structure was \geq the hole in the ablative. The best correlation for normal impacts of GE 124A with 1/4-inch diameter steel and nylon spheres was found to be D_a (cm) = Velocity (km/sec) - 2.2. The few R/V impacts that have been obtained thus far show good agreement with the flat plate results when they are compared on the basis of energy/thickness of the ablative material. Within the range of the impact conditions covered in this work the laminated and random reinforced phenolics do not show any consistent difference in the hole sizes although the front spall characteristics do show differences. Oblique impacts, except for the 124A materials, do not appear to make significant difference in the equivalent perforation diameter provided the normal impact energy is above the minimum perforation requirement.

Impact data with higher velocity projectiles of various densities must be obtained in order to determine the validity of the hole size vs impact energy per unit thickness relation. Lower obliquity impacts (less than 15°) must be obtained and more impacts into actual R/V components. The effect of target thickness must be more carefully examined, particularly as it is related to projectile size. A comparison of the impact results will be made with aluminum, steel and uranium spheres when they impact a target with the same energy. Comparisons will also be made between the impact results obtained when different mass spheres of the same material impact a target at the same energy.

Flash radiographs will be taken of the front of the target during impact and the spall emanating from the rear. This will permit a determination of the time when the front of the target material starts to spall and when the back-up material starts to bulge prior to petalling.

Measurements will be made of the wave amplitude arriving at the rear surface of the target as a result of a hypervelocity impact. It is planned to make these measurements with

SECRET

B 13

SECRET

a carbon resistor gauge⁽²⁾, developed by the Bureau of Mines, Pittsburgh, Penna. This information, with an estimate of the impact pressure, will make it possible to determine the shock attenuation of the wave in an ablative material. If the minimum pressure that is needed to fracture and spall the metal back-up plate is known, it will then be possible to determine if a given composite target will be perforated, in terms of the initial projectile parameters.

REFERENCES

- (1) Persechino, M.A., "Hypervelocity Impacts Into Ablative Materials" Sixth Symposium on Hypervelocity Impact Vol IV, page 235 - May 1963.
- (2) Private Communication, R. Watson, Bureau of Mines, Pittsburgh, Pennsylvania.

SECRET

SECRET

LEGEND FOR TABLES #1 and 2

Ph. Ref	-	Phenolic Refrasil
Ph. Ny	-	Phenolic Nylon
R.C.M.	-	Random orientation of chopped squares
L	-	Reinforcing material is oriented parallel to surface of material
OTWPN	-	Oblique tape wound phenolic nylon (Fibers oriented at an angle of 20° to surface)
OTWR	-	Oblique tape wound phenolic refrasil
Perf	-	Perforated
A _a	-	Measured area of perforation in ablative
D _a	-	Diameter of equivalent circle calculated from measured A _a
R/V	-	Re-entry vehicle
Abl	-	Ablative
B-U	-	Back-up

SECRET

B 15

SECRET

TABLE I - PERFORATION DIMENSIONS FOR
PREVIOUSLY REPORTED NRL DATA *

Round No.	A_a cm ²	D_a cm	Round No.	A_a cm ²	D_a cm
1-1-18	54.045	8.30	4-787	40.452	7.18
1-1-19	34.258	6.60	4-426	33.290	6.51
1-1-20	33.516	6.53	1-1-39	10.200	3.60
1-1-21	19.400	4.97	4-797	6.35	2.52
1-1-13	12.226	3.95	4-755	16.258	4.55
1-1-16	15.626	4.46	4-792	15.664	4.47
1-1-32	30.645	6.25	4-793	16.452	4.58
4-779	12.832	4.04	4-730	3.419	2.09
4-425	28.258	6.00	4-734	4.45	2.38
5-3-16	1.48	1.37	5-3-4	5.82	2.72
5-3-18	3.35	2.07	5-3-7	2.7	1.86
5-3-20	1.35	1.31	4-748	10.323	3.63
5-3-24	25.55	5.70	4-421	6.23	2.82
5-3-25	31.16	6.30	4-749	12.226	3.95
5-3-28	29.74	6.15	4-750	9.581	3.49
4-784	26.32	5.79	4-751	0.419	0.73
4-785	28.13	5.98	4-778	113.98	12.05
4-786	45.161	7.58	4-782	12.606	4.01

* Addendum to NRL Report 5913, Progress Report No. 9 for period
ending September 20, 1962, Vol I.

SECRET

B 16

XX FIVE

[illegible]

Penetration depth measured to the top of the protective, normal to ablatative surface

*** Piece of abrasive material just about broken out. Large dia. measurement taken to edge of hole as if the piece had broken out.

IX

Sample Identification	Type of Material	Diameter (in.)	Length (in.)	Weight (lb.)	Volume (cu. in.)	Density (lb./cu. in.)	Tensile Strength (psi)	Yield Strength (psi)	Elongation (%)	Impact (ft.-lb.)	CHARACTERISTICS				Remarks	Round Number
											Beam	Spall	Diagonals	Drop		
17-12127/16"	Sphere	1.160	90	11.255	3.583	1.001	0.82 - 0.83 (creep)	0.61 - 0.91 (creep)	0.91 - 2.0 (creep)	0.91 - 2.0 (creep)	Not perf.	Not perf.	Not perf.	Agglutinated into the Abl.	5-3-61	
17-12127/16"	Sphere	1.160	90	11.255	3.583	1.138	0.7624 (creep)	0.71 (creep)	0.95 2.0 - 1.9 (creep)	0.95 2.0 - 1.9 (creep)	"	"	"	Slight bulge on the Abl.	5-3-63	
17-12127/16"	Sphere	1.160	90	11.255	3.583	1.302	2.04 (creep)	2.3 - 1.5 (creep)	2.84 1.90 3.6 - 3.1 (creep)	2.84 1.90 3.6 - 3.1 (creep)	"	"	"	Slight bulge on the Abl.	5-3-64	
17-12127/16"	Sphere	1.160	90	11.255	3.583	1.679	Perf. of 2.9 - 2.5 (creep)	2.4 5.01 2.72 4.3 - 3.8 (creep)	2.4 5.01 2.72 4.3 - 3.8 (creep)	2.4 5.01 2.72 4.3 - 3.8 (creep)	"	"	"	Slight bulge on the Abl.	5-3-65	
17-12127/16"	Sphere	1.160	90	11.255	3.583	1.939	Abl. only	Perf. of 2.6 - 2.1 (creep)	3.87 2.22 4.1 - 4.0 (creep)	3.87 2.22 4.1 - 4.0 (creep)	"	"	"	Slight bulge on the Abl.	5-3-66	
17-12127/16"	Sphere	1.160	90	11.255	3.583	3.489	Perf. of 6.0 - 3.2 (creep)	13.42 4.73 4.7 - 4.5 (creep)	13.42 4.73 4.7 - 4.5 (creep)	13.42 4.73 4.7 - 4.5 (creep)	"	"	"	Slight bulge on the Abl.	5-3-67	
17-12127/16"	Sphere	1.160	90	11.255	3.583	3.380	Abl. only	4.2 - 3.7 (creep)	13.87 4.20 5.4 - 5.4 (creep)	13.87 4.20 5.4 - 5.4 (creep)	"	"	"	Slight bulge on the Abl.	5-3-68	
17-12127/16"	Sphere	1.160	90	11.255	3.583	8.764	Complete	5.3 - 3.4 (creep)	2.4 17.08 4.66 13.3 - 12.4 (creep)	10.3 - 7.0 (creep)	11.7 - 7.6 (creep)	11.7 - 7.6 (creep)	11.7 - 7.6 (creep)	Slight bulge on the Abl.	5-3-69	
17-12127/16"	Sphere	1.160	90	11.255	3.583	2.665	3.71 (creep)	3.0 - 1.3 (creep)	3.605 2.15 19.5 - 15.6 (creep)	21.2 - 17.1 (creep)	1.1-55 (creep)	1.1-55 (creep)	1.1-55 (creep)	Slight bulge on the Abl.	5-3-70	
17-12127/16"	Sphere	1.160	90	11.255	3.583	2.653	19.644 (creep)	3.1 (creep)	13.7 - 12.0 (creep)	19.8 - 17.0 (creep)	1.1-51 (creep)	1.1-51 (creep)	1.1-51 (creep)	Slight bulge on the Abl.	5-3-71	
17-12127/16"	Sphere	1.160	90	11.255	3.583	77.900	Complete	8.5 - 5.5 (creep)	4.0 (creep)	7.0 12.8 - 7.9 (creep)	16.6 - 14.3 (creep)	16.6 - 14.3 (creep)	16.6 - 14.3 (creep)	Slight bulge on the Abl.	5-3-72	
17-12127/16"	Sphere	1.160	90	11.255	3.583	77.900	Complete	8.5 - 5.5 (creep)	4.0 (creep)	7.0 12.8 - 7.9 (creep)	16.6 - 14.3 (creep)	16.6 - 14.3 (creep)	16.6 - 14.3 (creep)	Slight bulge on the Abl.	5-3-73	
17-12127/16"	Sphere	1.160	90	11.255	3.583	77.900	Complete	8.5 - 5.5 (creep)	4.0 (creep)	7.0 12.8 - 7.9 (creep)	16.6 - 14.3 (creep)	16.6 - 14.3 (creep)	16.6 - 14.3 (creep)	Slight bulge on the Abl.	5-3-74	
17-12127/16"	Sphere	1.160	90	11.255	3.583	77.900	Complete	8.5 - 5.5 (creep)	4.0 (creep)	7.0 12.8 - 7.9 (creep)	16.6 - 14.3 (creep)	16.6 - 14.3 (creep)	16.6 - 14.3 (creep)	Slight bulge on the Abl.	5-3-75	
17-12127/16"	Sphere	1.160	90	11.255	3.583	77.900	Complete	8.5 - 5.5 (creep)	4.0 (creep)	7.0 12.8 - 7.9 (creep)	16.6 - 14.3 (creep)	16.6 - 14.3 (creep)	16.6 - 14.3 (creep)	Slight bulge on the Abl.	5-3-76	
17-12127/16"	Sphere	1.160	90	11.255	3.583	77.900	Complete	8.5 - 5.5 (creep)	4.0 (creep)	7.0 12.8 - 7.9 (creep)	16.6 - 14.3 (creep)	16.6 - 14.3 (creep)	16.6 - 14.3 (creep)	Slight bulge on the Abl.	5-3-77	
17-12127/16"	Sphere	1.160	90	11.255	3.583	77.900	Complete	8.5 - 5.5 (creep)	4.0 (creep)	7.0 12.8 - 7.9 (creep)	16.6 - 14.3 (creep)	16.6 - 14.3 (creep)	16.6 - 14.3 (creep)	Slight bulge on the Abl.	5-3-78	
17-12127/16"	Sphere	1.160	90	11.255	3.583	77.900	Complete	8.5 - 5.5 (creep)	4.0 (creep)	7.0 12.8 - 7.9 (creep)	16.6 - 14.3 (creep)	16.6 - 14.3 (creep)	16.6 - 14.3 (creep)	Slight bulge on the Abl.	5-3-79	
17-12127/16"	Sphere	1.160	90	11.255	3.583	77.900	Complete	8.5 - 5.5 (creep)	4.0 (creep)	7.0 12.8 - 7.9 (creep)	16.6 - 14.3 (creep)	16.6 - 14.3 (creep)	16.6 - 14.3 (creep)	Slight bulge on the Abl.	5-3-80	
17-12127/16"	Sphere	1.160	90	11.255	3.583	77.900	Complete	8.5 - 5.5 (creep)	4.0 (creep)	7.0 12.8 - 7.9 (creep)	16.6 - 14.3 (creep)	16.6 - 14.3 (creep)	16.6 - 14.3 (creep)	Slight bulge on the Abl.	5-3-81	
17-12127/16"	Sphere	1.160	90	11.255	3.583	77.900	Complete	8.5 - 5.5 (creep)	4.0 (creep)	7.0 12.8 - 7.9 (creep)	16.6 - 14.3 (creep)	16.6 - 14.3 (creep)	16.6 - 14.3 (creep)	Slight bulge on the Abl.	5-3-82	
17-12127/16"	Sphere	1.160	90	11.255	3.583	77.900	Complete	8.5 - 5.5 (creep)	4.0 (creep)	7.0 12.8 - 7.9 (creep)	16.6 - 14.3 (creep)	16.6 - 14.3 (creep)	16.6 - 14.3 (creep)	Slight bulge on the Abl.	5-3-83	
17-12127/16"	Sphere	1.160	90	11.255	3.583	77.900	Complete	8.5 - 5.5 (creep)	4.0 (creep)	7.0 12.8 - 7.9 (creep)	16.6 - 14.3 (creep)	16.6 - 14.3 (creep)	16.6 - 14.3 (creep)	Slight bulge on the Abl.	5-3-84	
17-12127/16"	Sphere	1.160	90	11.255	3.583	77.900	Complete	8.5 - 5.5 (creep)	4.0 (creep)	7.0 12.8 - 7.9 (creep)	16.6 - 14.3 (creep)	16.6 - 14.3 (creep)	16.6 - 14.3 (creep)	Slight bulge on the Abl.	5-3-85	
17-12127/16"	Sphere	1.160	90	11.255	3.583	77.900	Complete	8.5 - 5.5 (creep)	4.0 (creep)	7.0 12.8 - 7.9 (creep)	16.6 - 14.3 (creep)	16.6 - 14.3 (creep)	16.6 - 14.3 (creep)	Slight bulge on the Abl.	5-3-86	
17-12127/16"	Sphere	1.160	90	11.255	3.583	77.900	Complete	8.5 - 5.5 (creep)	4.0 (creep)	7.0 12.8 - 7.9 (creep)	16.6 - 14.3 (creep)	16.6 - 14.3 (creep)	16.6 - 14.3 (creep)	Slight bulge on the Abl.	5-3-87	
17-12127/16"	Sphere	1.160	90	11.255	3.583	77.900	Complete	8.5 - 5.5 (creep)	4.0 (creep)	7.0 12.8 - 7.9 (creep)	16.6 - 14.3 (creep)	16.6 - 14.3 (creep)	16.6 - 14.3 (creep)	Slight bulge on the Abl.	5-3-88	
17-12127/16"	Sphere	1.160	90	11.255	3.583	77.900	Complete	8.5 - 5.5 (creep)	4.0 (creep)	7.0 12.8 - 7.9 (creep)	16.6 - 14.3 (creep)	16.6 - 14.3 (creep)	16.6 - 14.3 (creep)	Slight bulge on the Abl.	5-3-89	
17-12127/16"	Sphere	1.160	90	11.255	3.583	77.900	Complete	8.5 - 5.5 (creep)	4.0 (creep)	7.0 12.8 - 7.9 (creep)	16.6 - 14.3 (creep)	16.6 - 14.3 (creep)	16.6 - 14.3 (creep)	Slight bulge on the Abl.	5-3-90	
17-12127/16"	Sphere	1.160	90	11.255	3.583	77.900	Complete	8.5 - 5.5 (creep)	4.0 (creep)	7.0 12.8 - 7.9 (creep)	16.6 - 14.3 (creep)	16.6 - 14.3 (creep)	16.6 - 14.3 (creep)	Slight bulge on the Abl.	5-3-91	
17-12127/16"	Sphere	1.160	90	11.255	3.583	77.900	Complete	8.5 - 5.5 (creep)	4.0 (creep)	7.0 12.8 - 7.9 (creep)	16.6 - 14.3 (creep)	16.6 - 14.3 (creep)	16.6 - 14.3 (creep)	Slight bulge on the Abl.	5-3-92	
17-12127/16"	Sphere	1.160	90	11.255	3.583	77.900	Complete	8.5 - 5.5 (creep)	4.0 (creep)	7.0 12.8 - 7.9 (creep)	16.6 - 14.3 (creep)	16.6 - 14.3 (creep)	16.6 - 14.3 (creep)	Slight bulge on the Abl.	5-3-93	
17-12127/16"	Sphere	1.160	90	11.255	3.583	77.900	Complete	8.5 - 5.5 (creep)	4.0 (creep)	7.0 12.8 - 7.9 (creep)	16.6 - 14.3 (creep)	16.6 - 14.3 (creep)	16.6 - 14.3 (creep)	Slight bulge on the Abl.	5-3-94	
17-12127/16"	Sphere	1.160	90	11.255	3.583	77.900	Complete	8.5 - 5.5 (creep)	4.0 (creep)	7.0 12.8 - 7.9 (creep)	16.6 - 14.3 (creep)	16.6 - 14.3 (creep)	16.6 - 14.3 (creep)	Slight bulge on the Abl.	5-3-95	
17-12127/16"	Sphere	1.160	90	11.255	3.583	77.900	Complete	8.5 - 5.5 (creep)	4.0 (creep)	7.0 12.8 - 7.9 (creep)	16.6 - 14.3 (creep)	16.6 - 14.3 (creep)	16.6 - 14.3 (creep)	Slight bulge on the Abl.	5-3-96	
17-12127/16"	Sphere	1.160	90	11.255	3.583	77.900	Complete	8.5 - 5.5 (creep)	4.0 (creep)	7.0 12.8 - 7.9 (creep)	16.6 - 14.3 (creep)	16.6 - 14.3 (creep)	16.6 - 14.3 (creep)	Slight bulge on the Abl.	5-3-97	
17-12127/16"	Sphere	1.160	90	11.255	3.583	77.900	Complete	8.5 - 5.5 (creep)	4.0 (creep)	7.0 12.8 - 7.9 (creep)	16.6 - 14.3 (creep)	16.6 - 14.3 (creep)	16.6 - 14.3 (creep)	Slight bulge on the Abl.	5-3-98	
17-12127/16"	Sphere	1.160	90	11.255	3.583	77.900	Complete	8.5 - 5.5 (creep)	4.0 (creep)	7.0 12.8 - 7.9 (creep)	16.6 - 14.3 (creep)	16.6 - 14.3 (creep)	16.6 - 14.3 (creep)	Slight bulge on the Abl.	5-3-99	
17-12127/16"	Sphere	1.160	90	11.255	3.583	77.900	Complete	8.5 - 5.5 (creep)	4.0 (creep)	7.0 12.8 - 7.9 (creep)	16.6 - 14.3 (creep)	16.6 - 14.3 (creep)	16.6 - 14.3 (creep)	Slight bulge on the Abl.	5-3-100	
17-12127/16"	Sphere	1.160	90	11.255	3.583	77.900	Complete	8.5 - 5.5 (creep)	4.0 (creep)	7.0 12.8 - 7.9 (creep)	16.6 - 14.3 (creep)	16.6 - 14.3 (creep)	16.6 - 14.3 (creep)	Slight bulge on the Abl.	5-3-101	
17-12127/16"	Sphere	1.160	90	11.255	3.583	77.900	Complete	8.5 - 5.5 (creep)	4.0 (creep)	7.0 12.8 - 7.9 (creep)	16.6 - 14.3 (creep)	16.6 - 14.3 (creep)	16.6 - 14.3 (creep)	Slight bulge on the Abl.	5-3-102	
17-12127/16"	Sphere	1.160	90	11.255	3.583	77.900	Complete	8.5 - 5.5 (creep)	4.0 (creep)	7.0 12.8 - 7.9 (creep)	16.6 - 14.3 (creep)	16.6 - 14.3 (creep)	16.6 - 14.3 (creep)	Slight bulge on the Abl.	5-3-103	
17-12127/16"	Sphere	1.160	90	11.255	3.583	77.900	Complete	8.5 - 5.5 (creep)	4.0 (creep)	7.0 12.8 - 7.9 (creep)	16.6 - 14.3 (creep)	16.6 - 14.3 (creep)	16.6 - 14.3 (creep)	Slight bulge on the Abl.	5-3-104	
17-12127/16"	Sphere	1.160	90	11.255	3.583	77.900	Complete	8.5 - 5.5 (creep)	4.0 (creep)	7.0 12.8 - 7.9 (creep)	16.6 - 14.3 (creep)	16.6 - 14.3 (creep)	16.6 - 14.3 (creep)	Slight bulge on the Abl.	5-3-105	
17-12127/16"	Sphere	1.160	90	11.255	3.583	77.900	Complete	8.5 - 5.5 (creep)	4.0 (creep)	7.0 12.8 - 7.9 (creep)	16.6 - 14.3 (creep)	16.6 - 14.3 (creep)	16.6 - 14.3 (creep)	Slight bulge on the Abl.	5-3-106	
17-12127/16"	Sphere	1.160	90	11.255	3.583	77.900	Complete	8.5 - 5.5 (creep)	4.0 (creep)	7.0 12.8 - 7.9 (creep)	16.6 - 14.3 (creep)	16.6 - 14.3 (creep)	16.6 - 14.3 (creep)	Slight bulge on the Abl.	5-3-107	
17-12127/16"	Sphere	1.160	90	11.255	3.583	77.900	Complete	8.5 - 5.5 (creep)	4.0 (creep)	7.0 12.8 - 7.9 (creep)	16.6 - 14.3 (creep)	16.6 - 14.3 (creep)	16.6 - 14.3 (creep)	Slight bulge on the Abl.	5-3-108	
17-12127/16"	Sphere	1.160	90	11.255	3.583	77.900	Complete	8.5 - 5.5 (creep)	4.0 (creep)	7.0 12.8 - 7.9 (creep)	16.6 - 14.3 (creep)	16.6 - 14.3 (creep)	16.6 - 14.3 (creep)	Slight bulge on the Abl.	5-3-109	
17-12127/16"	Sphere	1.160	90	11.255	3.583	77.900	Complete	8.5 - 5.5 (creep)	4.0 (creep)	7.0 12.8 - 7.9 (creep)	16.6 - 14.3 (creep)	16.6 - 14.3 (creep)	16.6 - 14.3 (creep)	Slight bulge on the Abl.	5-3-110	
17-12127/16"	Sphere	1.160	90	11.255	3.583	77.900	Complete	8.5 - 5.5 (creep)	4.0 (creep)	7.0 12.8 - 7.9 (creep)	16.6 - 14.3 (creep)	16.6 - 14.3 (creep)	16.6 - 14.3 (creep)	Slight bulge on the Abl.	5-3-111	
17-12127/16"	Sphere	1.160	90	11.255	3.583	77.900	Complete	8.5 - 5.5 (creep)	4.0 (creep)	7.0 12.8 - 7.9 (creep)	16.6 - 14.3 (creep)	16.6 - 14.3 (creep)	16.6 - 14.3 (creep)	Slight bulge on the Abl.	5-3-112	
17-12127/16"	Sphere	1.160	90	11.255	3.583	77.900	Complete	8.5 - 5.5 (creep)	4.0 (creep)	7.0 12.8 - 7.9 (creep)	16.6 - 14.3 (creep)	16.6 - 14.3 (creep)	16.6 - 14.3 (creep)	Slight bulge on the Abl.	5-3-113	
17-12127/16"	Sphere	1.160	90	11.255	3.583	77.900	Complete	8.5 - 5.5 (creep)	4.0 (creep)	7.0 12.8 - 7.9 (creep)	16.6 - 14.3 (creep)	16.6 - 14.3 (creep)	16.6 - 14.3 (creep)	Slight bulge on the Abl.	5-3-114	
17-12127/16"	Sphere	1.160	90	11.255	3.583	77.900	Complete	8.5 - 5.5 (creep)	4.0 (creep)	7.0 12.8 - 7.9 (creep)	16.6 - 14.3 (creep)	16.6 - 14.3 (creep)	16.6 - 14.3 (creep)	Slight bulge on the Abl.	5-3-115	
17-12127/16"	Sphere	1.160	90	11.255	3.583	77.900	Complete	8.5 - 5.5 (creep)	4.0 (creep)	7.0 12.8 - 7.9 (creep)	16.6 - 14.3 (creep)	16.6 - 14.3 (creep)	16.6 - 14.3 (creep)	Slight bulge on the Abl.	5-3-116	
17-12127/16"	Sphere	1.160	90	11.255	3.583	77.900	Complete	8.5 - 5.5 (creep)	4.0 (creep)	7.0 12.8 - 7.9 (creep)	16.6 - 14.3 (creep)	16.6 - 14.3 (creep)	16.6 - 14.3 (creep)	Slight bulge on the Abl.	5-3-117	
17-12127/16"	Sphere	1.160	90	11.255	3.583	77.900	Complete	8.5 - 5.5 (creep)	4.0 (creep)	7.0 12.8 - 7.9 (creep)	16.6 - 14.3 (creep)	16.6 - 14.3 (creep)	16.6 - 14.3 (creep)	Slight bulge on the Abl.	5-3-118	
17-12127/16"	Sphere	1.160	90	11.255	3.583	77.900	Complete	8.5 - 5.5 (creep)	4.0 (creep)	7.0 12.8 - 7.9 (creep)	16.6 - 14.3 (creep)	16.6 - 14.3 (creep)	16.6 - 14.3 (creep)	Slight bulge on the Abl.	5-3-119	
17-12127/16"	Sphere	1.160	90	11.255	3.583	77.900	Complete	8.5 - 5.5 (creep)	4.0 (creep)	7.0 12.8 - 7.9 (creep)	16.6 - 14.3 (creep)	16.6 - 14.3 (creep)	16.6 - 14.3 (creep)	Slight bulge on the Abl.	5-3-120	
17-12127/16"	Sphere	1.160	90	11.255	3.583	77.900	Complete	8.5 - 5.5 (creep)	4.0 (creep)							

	Ripped away
* From Existing Angle	
** Ablative Back-up Dimensions Here: 1/4 R/V (Cylinders & Flare)	
*** Ablative Thicknesses: 1/8" and 3/16"	
**** Thick Ast. Laminates parallel to surface. Top ply perpendicular to	
Cylinder	1/2" OVR
Flare	3/16" MG
***** Steel flange between cylinder and flare (see Fig. 6) broken	
***** Steel flange between cylinder and throat. About 30% of surface area of	
tension cone ripped open.	
③ Bulged and loosened last A-1 plate from the nosecone for about 1/2 the contact area. + Abrasive surfaces measured to the tip of the projectile, normal to the direction of travel.	

SECRET

SECRET

TABLE III.
PROPERTIES OF VARIOUS ABLATIVE MATERIALS

Material	Density gm/cc	Com- pressive Strength psi	Com- pressive Modulus psi	Tensile Strength psi	Tensile Modulus psi	Poisson's Ratio	Acoustic Velocity ft/sec - km/sec
Phenolic @75°F Nylon	1.2 (a)	13,150 (a)	4.4x10 ⁵ (a)	5,230 (a)	2.28x10 ⁵ (a)	0.4 (a)	11,583.3 (b) 3,531 (b) 11,500.0 3,505
Phenolic Refrasil laminated	1.6-1.7	42,000 to 55,000	-	10,000 to 15,000	2.3 x10 ⁶ to 3.2 x10 ⁶	-	14,500.0 4,420 10,583.3 3,226
GE 124A @75°F	1.2	4,500	2.7x10 ⁵	5,600	1.9 x10 ⁵	-	9,500.0 2,896
GE 126 @75°F	1.2	6,300	2.7x10 ⁵	6,300	2.7 x10 ⁵	-	9,166.7 2,794
GE 525 @75°F	0.8-0.9	5,000	2.3x10 ⁵	3,400	2.4 x10 ⁵	-	7,500 2,288
GE 223C-@75°F 15 ST	1.35	6,500	4.4x10 ⁵	6,500	4.4 x10 ⁵	-	- -

(a) random chopped
(b) laminated

The above table is a list of ablative material properties that was compiled from several sources. The acoustic velocities (room temperature) were determined by NRL. The data for the phenolic nylon (R.C.M.) and G.E. Series was supplied by the manufacturer as typical values. The data on the phenolic refrasil was obtained from actual test results performed by the manufacturer.

SECRET

B21

TABLE IV
RESUME OF HYPERVELOCITY IMPACTS
ONTO STEEL TARGETS BY STEEL SPHERES

TARGET Material and Size (in)	Vice Supporting Size (in)	Plate Thick. Sphere Dia. (in)	Diameter (in)	Material Hardness (GPa)	PROJECTILE Mass (Grams)	Velocity (in/Sec)	Impact Energy (in/Sec)	DAMAGE CHARACTERISTICS					Round Number
								1st Plate or Semi- Infinite Target	2nd Plate	3rd Plate	4th Plate	5th Plate	
1020 12"x12"x1/8"	3	1.625	1.00	0.375	Rc 41	3,506	70.34	H.D. 3.73cm Ø P.S. 4.58 R.S. 5.22	Pen. 1.42cm P.S. 5.19 Back Spalled	Slight dent from spall Ø2	---	---	3.92 1-1-75
1020 12"x12"x0.106"	4	0.255	0.278	0.375	Rc 41	1,506	5,054	H.D. 2.06 P.S. None	H.D. 2.46 P.S. None	H.D. 3.18 x 5.39	---	---	2.11 1-1-76
1020 12"x12"x0.106"	6	0.375	0.278	0.375	Rc 41	3,522	5,763	H.D. 2.54 P.S. None	H.D. 3.18 P.S. None	Coupled together P.S. None	Plate Bulge 1.27	---	2.06 1-1-74
4340 12"x12"x1/8"	2*	14.0	1.39	0.720	Rc 31	25.00	4,214	H.D. 6.01 F.S. 11.09 R.S. 10.18 1.27 & 0.95 small holes	Bulged and 2 small holes	---	---	---	3.286 1-1-80
4340 12"x12"x1/8"	9	1.0	0.347	0.72	Rc 41	25.00	4,215	H.D. 3.45 P.S. None	H.D. 4.99	8.84 x 7.56 9.98 x 9.32 9.63	8.78 Bulge Overlapped Hole (see Fig. 6)	---	1-1-81
4340 6"x8"x0.128"	4	0.125	1.01	0.125	Rc 65	0.132	6,946	H.D. 1.35 P.S. 2.30 R.S. 1.59	H.D. 0.951 Pen 0.61	Pen. 0.32 No Pen.	---	---	4.256 1-2-44
1020 8"x8"x4"	Seal- Infinite	16.0	0.250	Rc 30	1.045	6,329	20,929	Crater Diam: 2.68 Penetration: 1.35	Crater Diam: 2.68 Penetration: 1.35	Volume: 4.65cm ³	---	---	4-115
1020 8"x8"x4"	"	16.0	0.250	Rc 30	1.045	6,263	20,495	Crater Diam: 2.65 Penetration: 1.34	Crater Diam: 2.65 Penetration: 1.34	Volume: 4.30cm ³	---	---	4-216
4340 6"x8"x1/2"	2**	1.0	2.14	0.234	Rc 20	0.857	4,937	H.D. 1.51 P.S. None R.S. 2.97	H.D. 1.36	---	---	---	2.541 4-218
4340 6"x8"x1/2"	2***	1.0	2.67	0.234	Rc 20	0.857	3,540	H.D. 1.80 P.S. None R.S. 3.98	No Penetration	---	---	---	3.19 4-219
4340 24"x24"x1"	2	1.0	0.898	1.14	Rc 28	99.70	4,468	H.D. 8.50	Bulged Irregular spalling around front & rear surfaces	---	---	---	2.791 C84-2

* Second Plate: 4340 Steel, 12"x12"x1/4"

** Second Plate: 2024-T3 Al., 6"x6"x1/2"

*** Second Plate: 1020 Steel, 6"x6"x1/2"

SECRET

B23

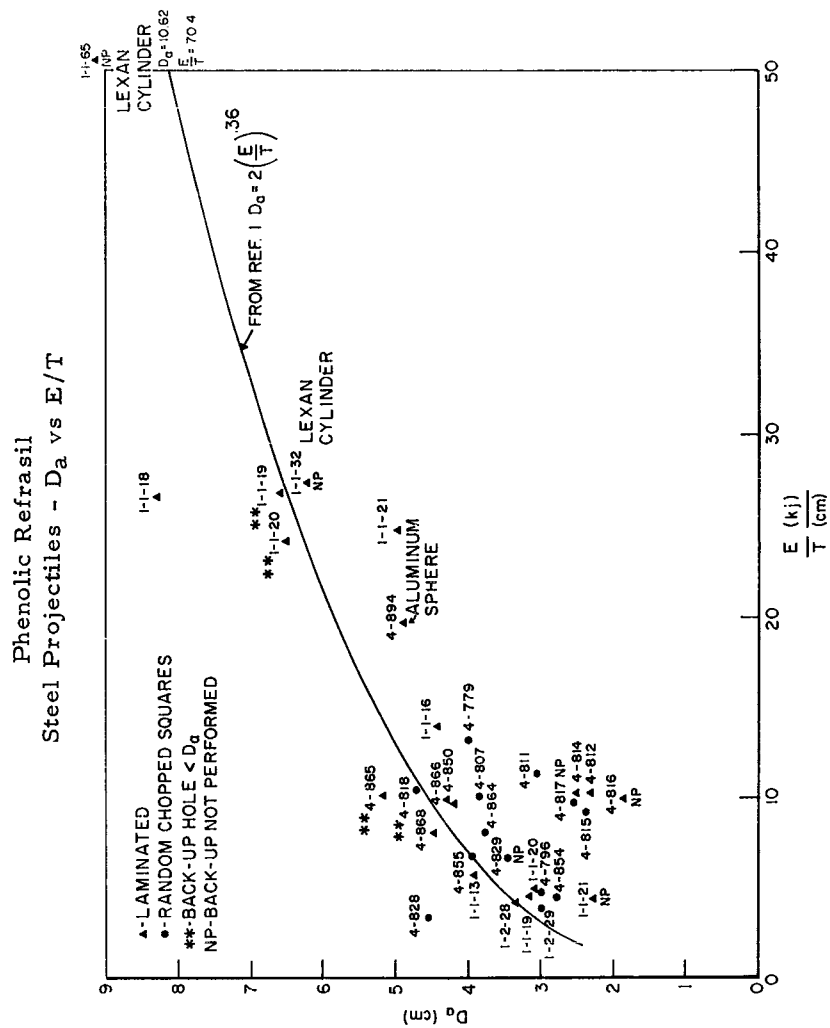


Fig. 1 - Hole size vs impact energy per unit of ablative thickness for phenolic refrasil

SECRET

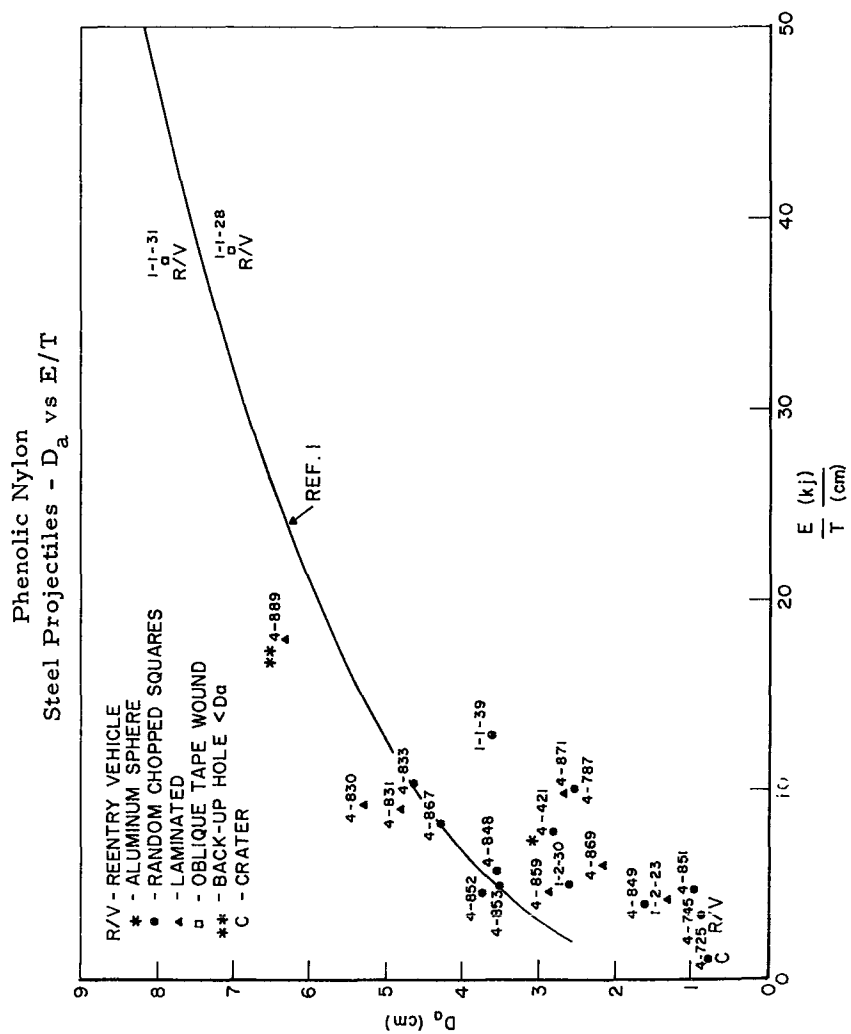


Fig. 2 - Hole size vs impact energy per unit of ablative thickness for phenolic nylon

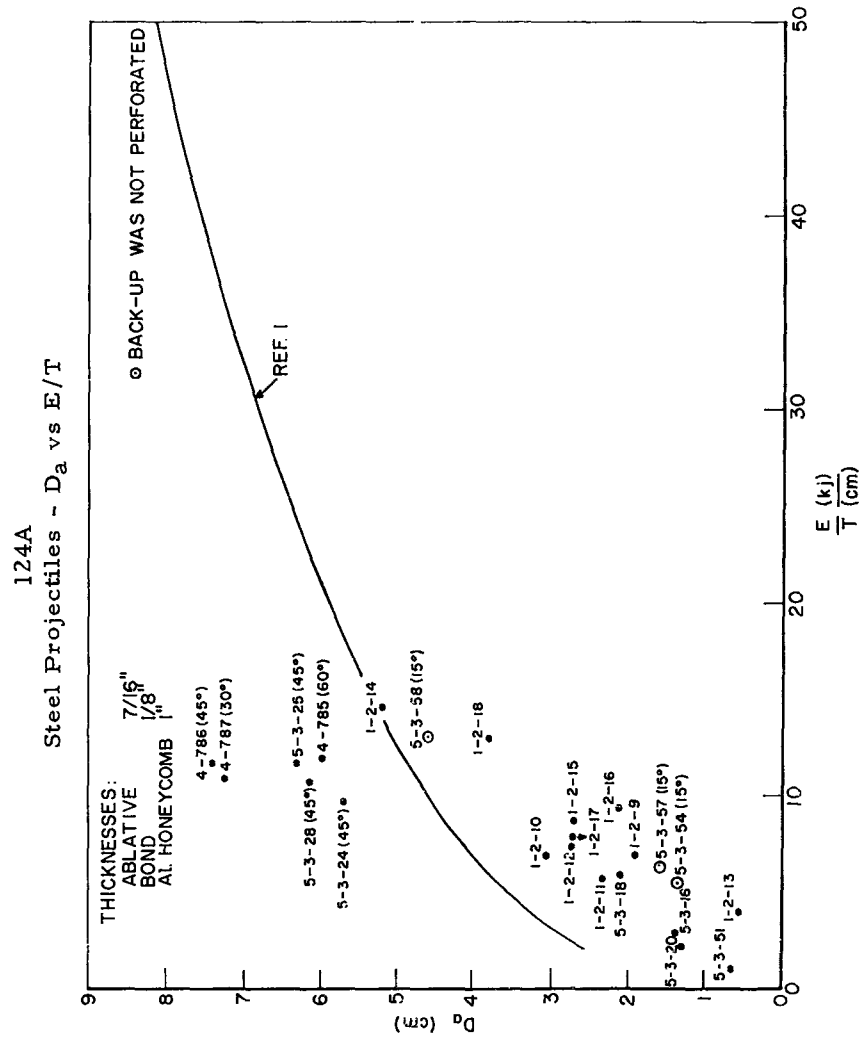


Fig. 3 - Hole size vs impact energy per unit of ablative thickness for GE 124A

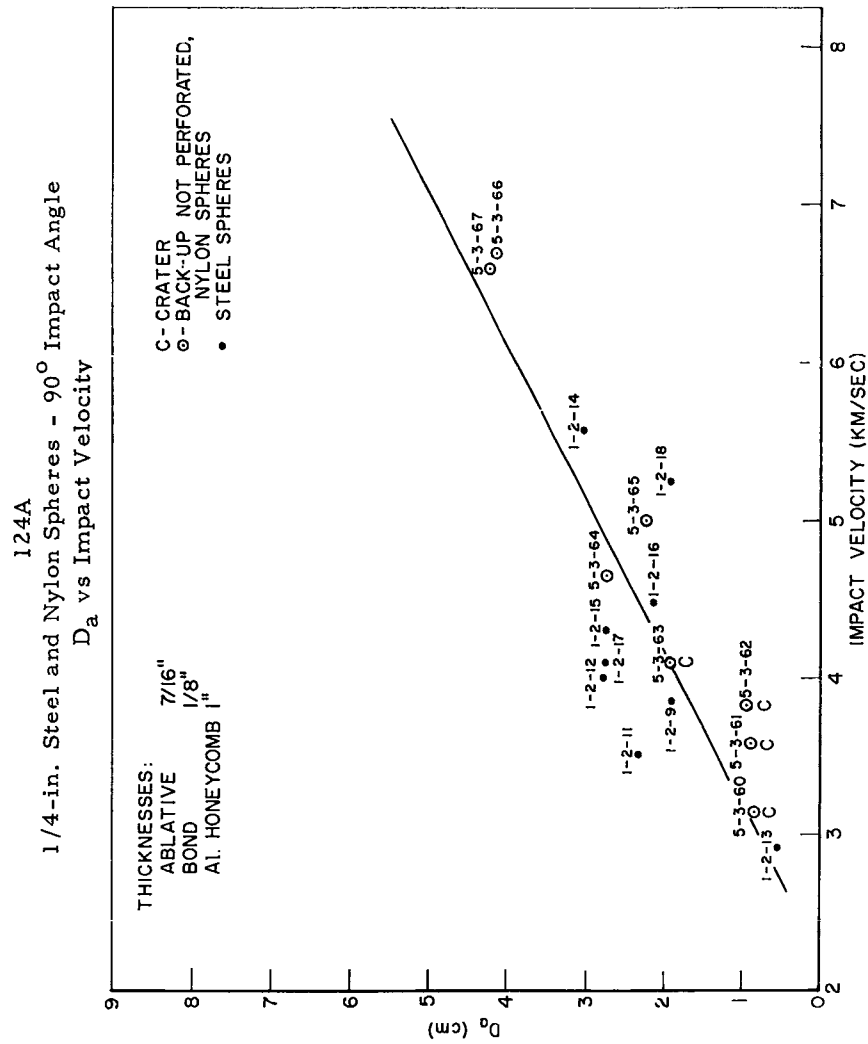
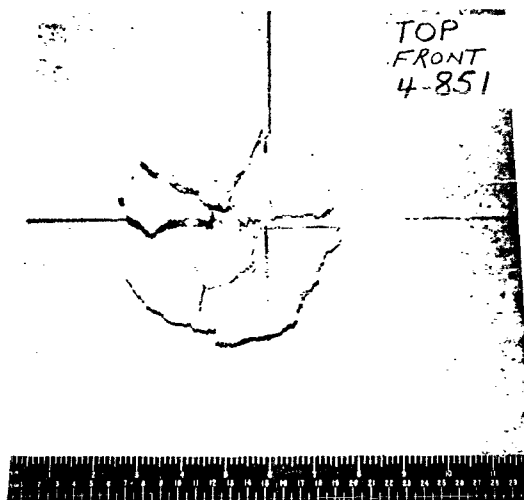
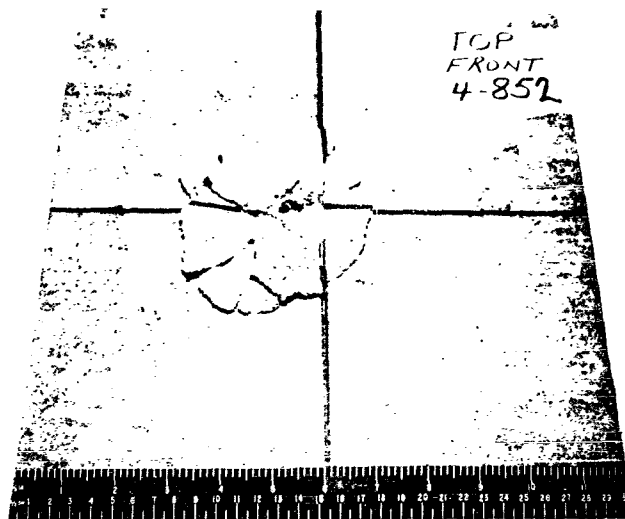


Fig. 4 - Hole size vs impact velocity (1/4-in. steel and nylon spheres)
for GE 124A

SECRET



ROUND NO. 4-851



ROUND NO. 4-852

Fig. 5 - Recovered front spall pieces placed back into spall cavity after impact

SECRET

B27

SECRET



Fig. 6 - Impact (250 grams Lexan @ 5.6 Km/sec) into early Mark IV R/V. OTWR with steel and laminated Mg liner. Impact angle 20° .

SECRET

B28

SECRET

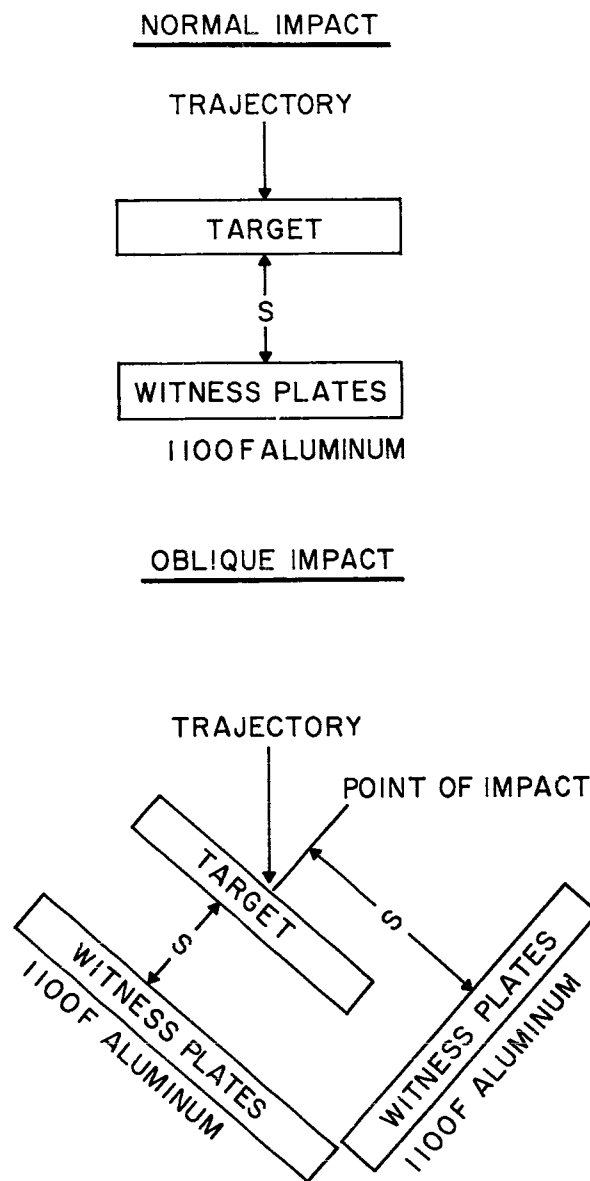


Fig. 7 - Layout of target plate and witness plates

SECRET

B29

SECRET

B 30

SECRET

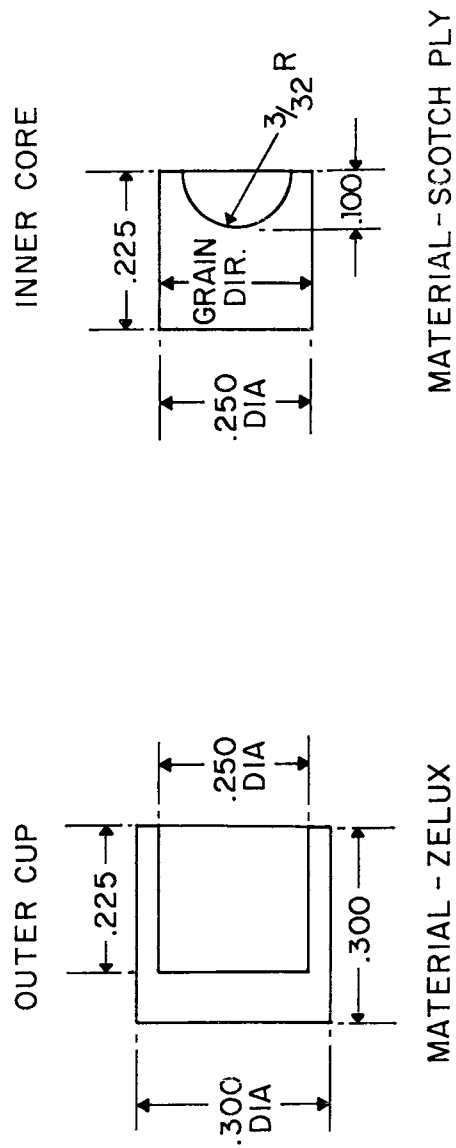


Fig. 8 - 30 Calibre composite sabot

SECRET

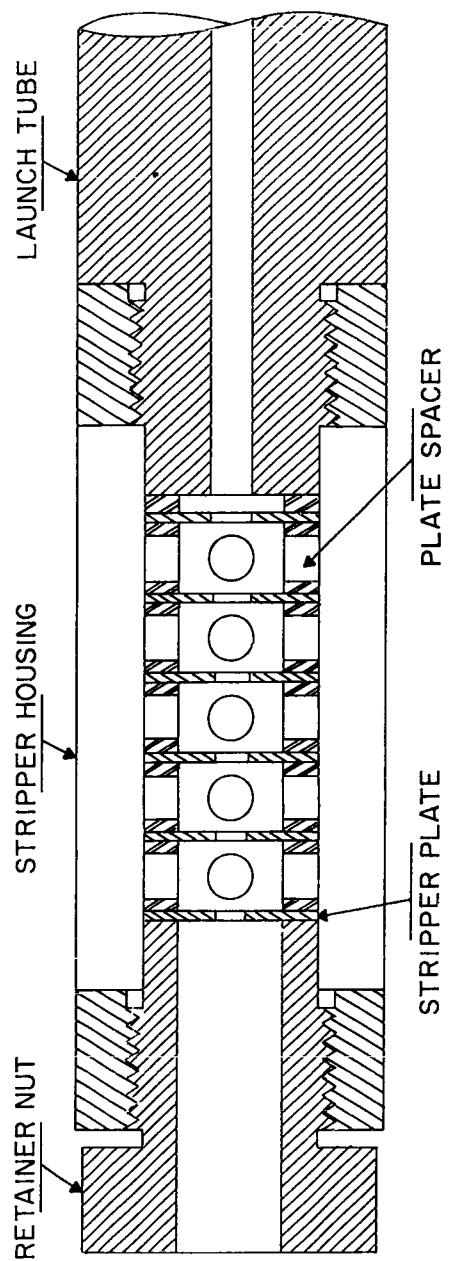


Fig. 9 - Spaced plate sabot stripper

SECRET

B31

SECRET

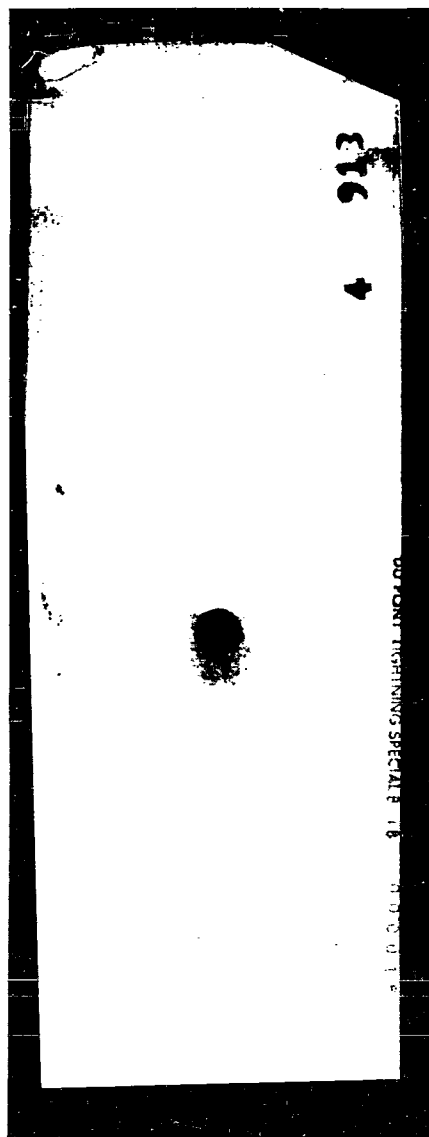


Fig. 10 - Flash X-ray photograph of steel sphere and solid sabot several inches after launch. (Sabot stripper not used.) Steel sphere set back 1/8 inch.

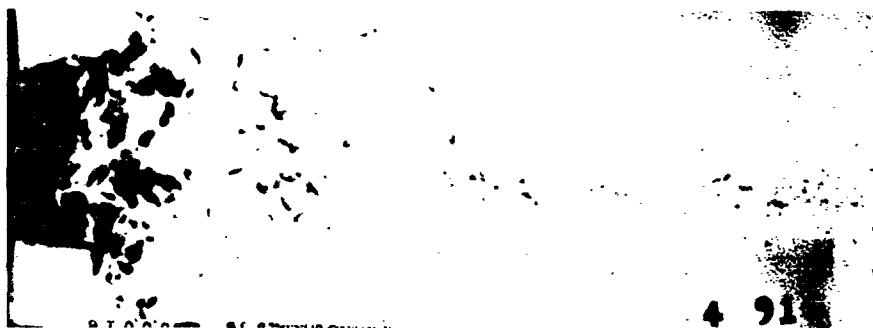
SECRET

E32

SECRET



SINGLE PLATE



TWO PLATES

Fig. 11 - Flash X-ray photographs of debris from stripper plates and sabot after impact

SECRET

B33

SECRET

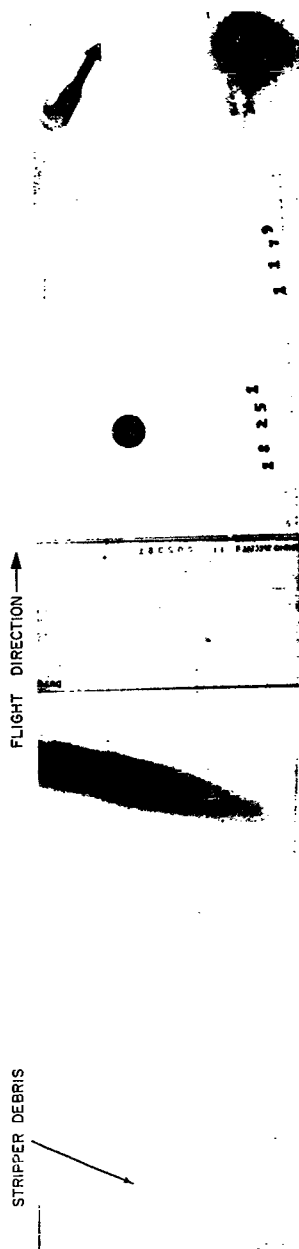


Fig. 12 - Flash X-ray photograph of steel sphere (≈ 1 ft. from muzzle)
and stripper plate debris

SECRET

B34

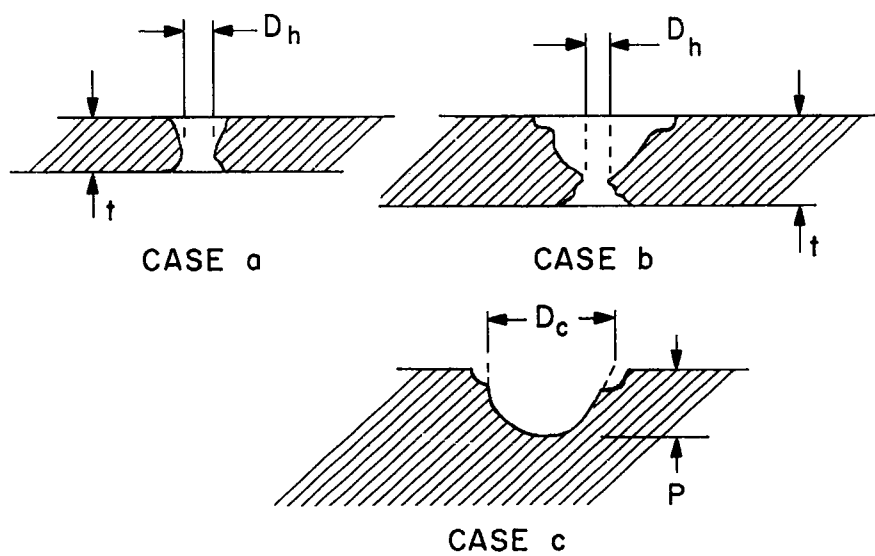


Fig. 13 - Hole and crater formation in finite and semi-infinite steel targets

SECRET

1-1-79

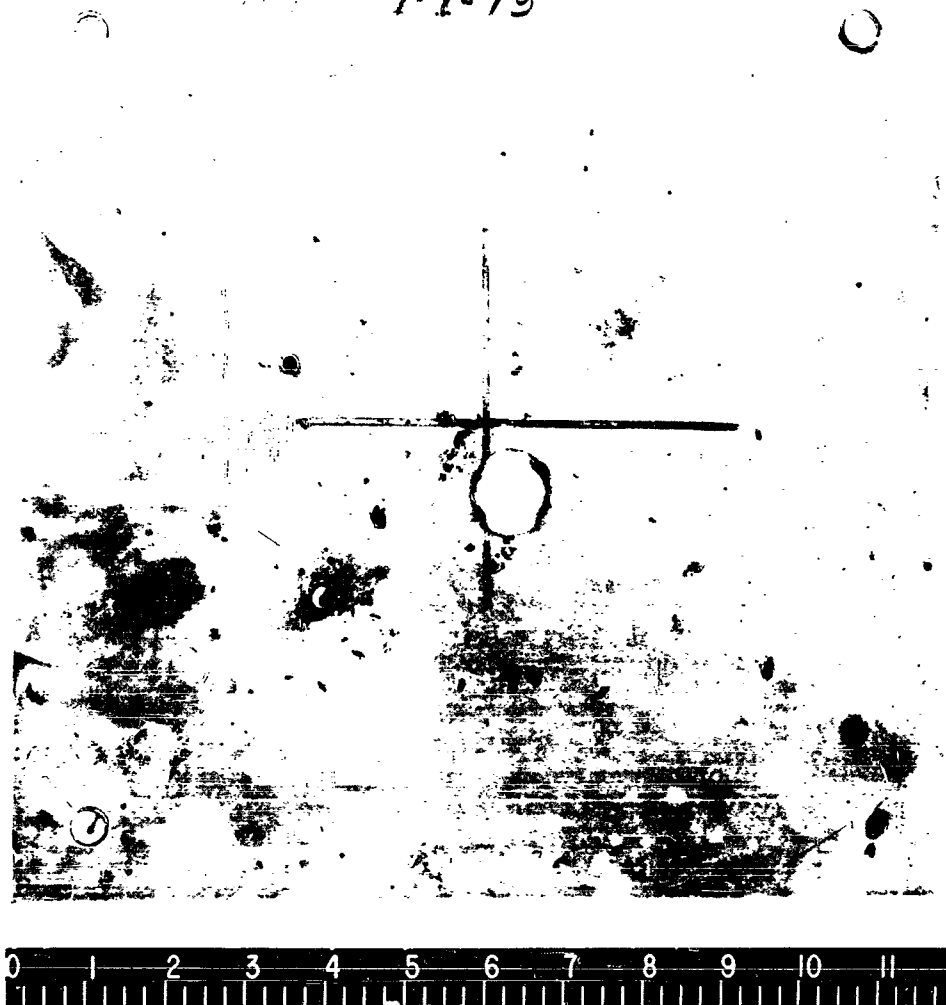


Fig. 14 - 1020 steel plate (0.104 inch thick) struck by 3.5-gram steel sphere at 5.56 km/sec, $t/d = 0.278$

SECRET

B36

SECRET

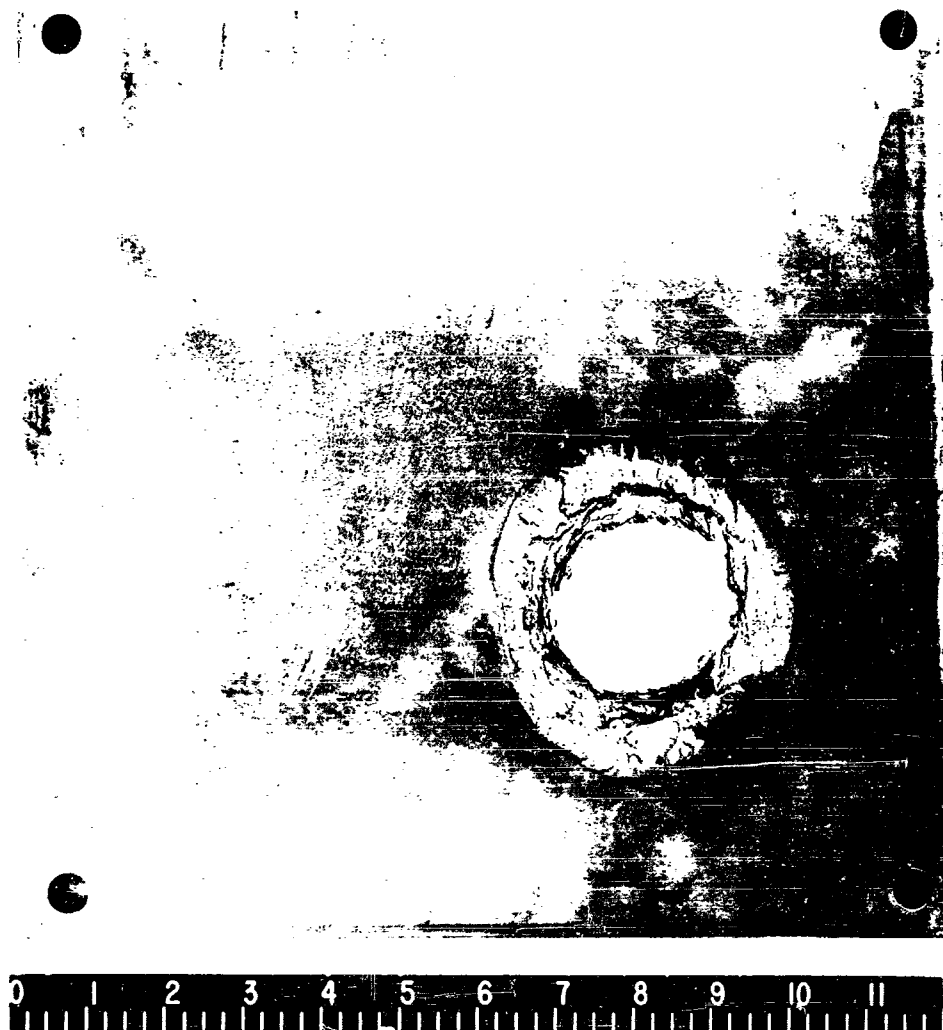


Fig. 15 - 4340 steel plate (1 inch thick) struck by 25.00 gram steel sphere at 4.21 km/sec, $t/d = 1.39$

SECRET

B37

SECRET

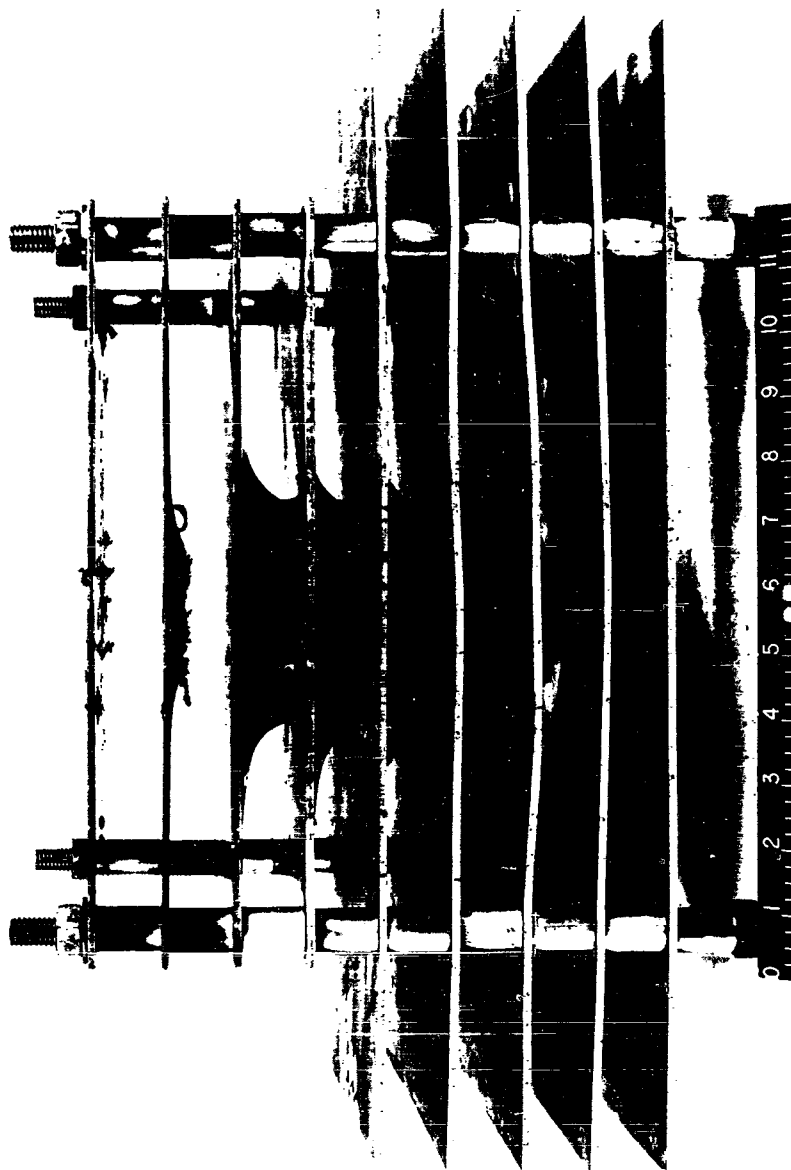


Fig. 16 - Post-impact condition of 1/8 inch thick 4340 steel plates impacted by 25.00 gram steel sphere at 4.22 km/sec. Plate spacing: 1 inch $t/d = 0.347$

SECRET

B38

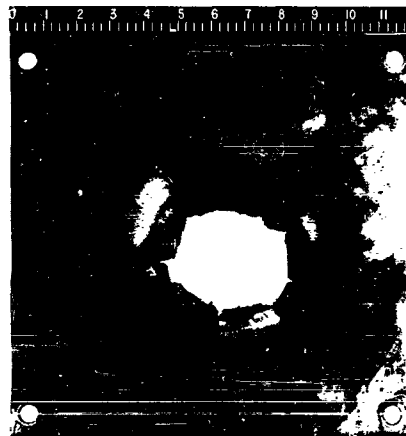
SECRET



(a)



(b)



(c)



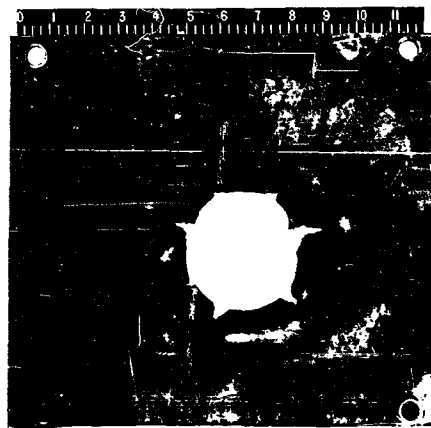
(d)

Fig. 16 - Separate views of impact damage to first four plates of steel plate array impacted by 25-gram steel sphere at 4.215 km/sec

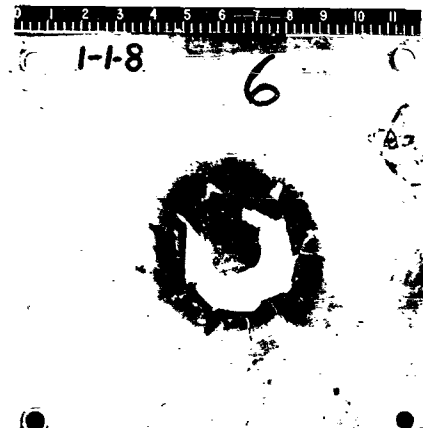
SECRET

B39

SECRET



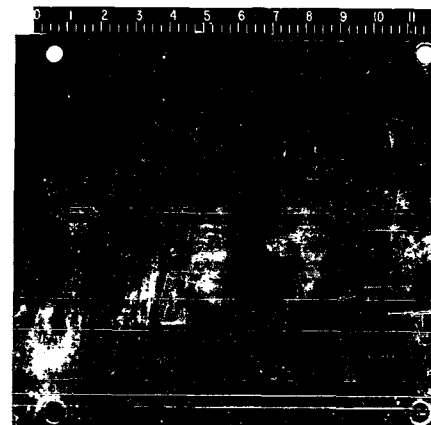
(e)



(f)



(g)



(h)

Fig. 16 - Separate views of impact damage to last four damaged plates in the steel target array impacted by 25-gram steel sphere at 4.215 km/sec

SECRET

B40

SECRET

APPENDIX

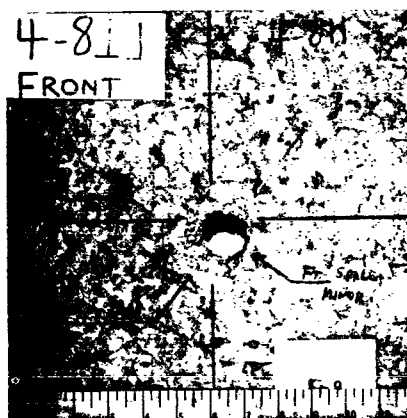
In this appendix photographs are shown of the front, rear and edge view of each target and, when perforation occurred, a front view of the first witness plate. The target pictures are shown in the same order as listed in Table II with the corresponding round number identifying each set of pictures. Along with the picture of the witness plate the following information is given: the number and thickness of the plates making up the stack, s = distance from the rear of the target to the front of the first witness plate and P_m = the depth of the maximum penetration into the witness plates. For normal impacts the witness plates were placed parallel to the rear of the target and about 10-inches behind, see Figure 7. For oblique impacts an additional stack of plates were placed 90° to the target. The distance recorded in this case was measured from the point of impact to the front surface of the first witness plate.

SECRET

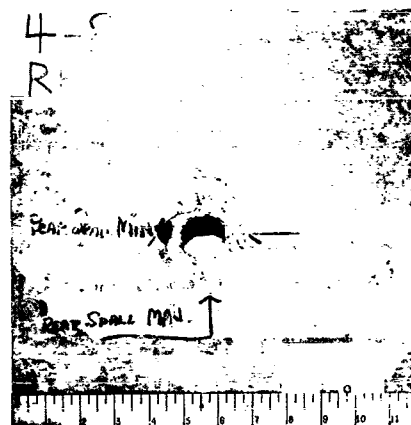
B41

SECRET

ROUND NO. 4-811

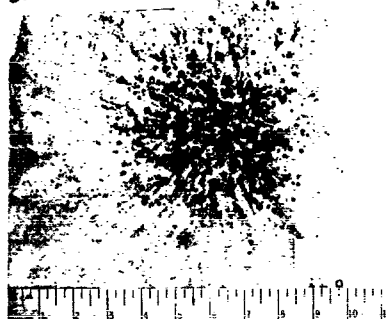


FRONT TARGET



REAR TARGET

4-811 FRONT
10" FROM
OF TARGET



W.P. 3-1/8" PLATES

s = 10"

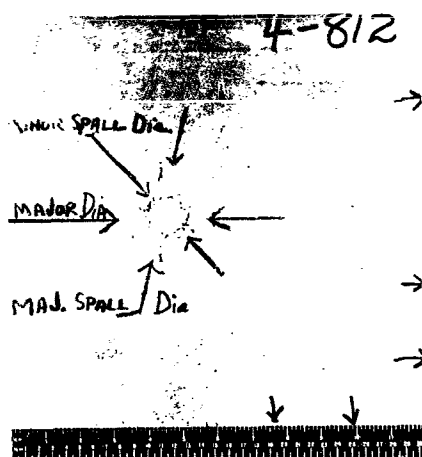
P_m = 0.86 cm

SECRET

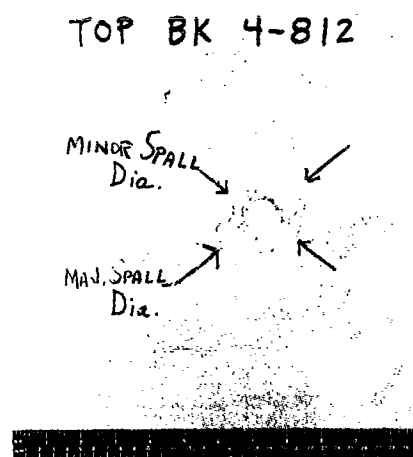
B42

SECRET

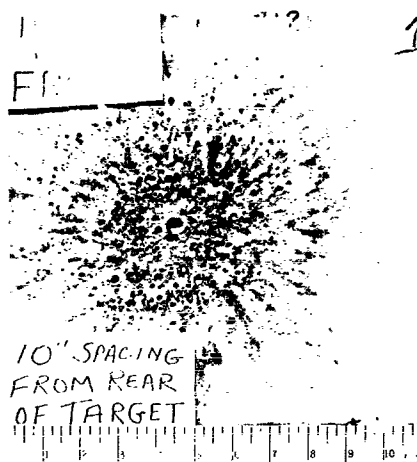
ROUND NO. 4-812



FRONT TARGET



REAR TARGET



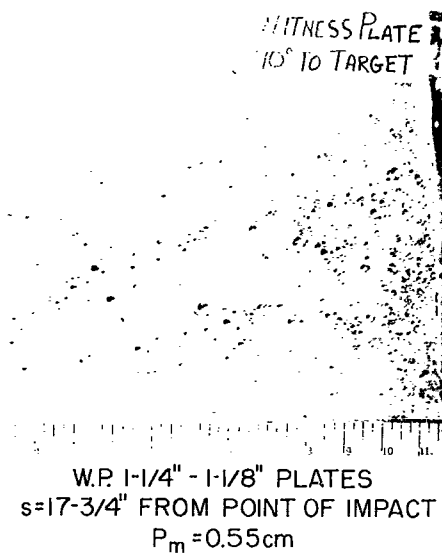
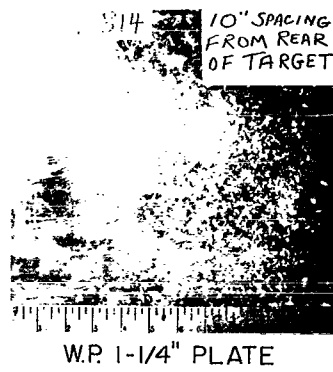
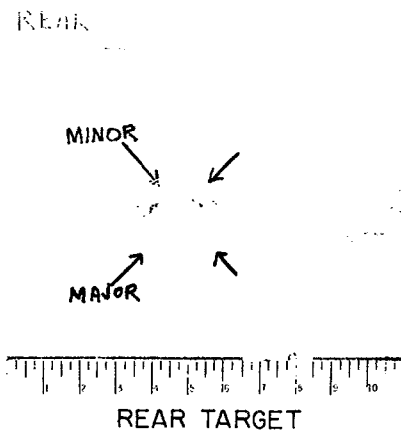
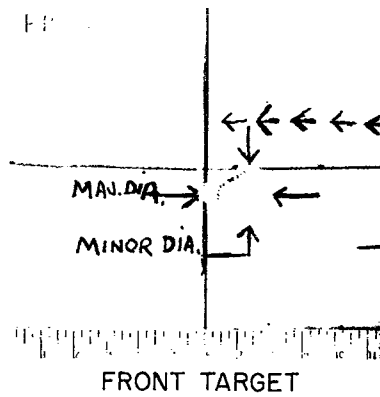
W.P 4-1/8" PLATES
s = 10"
P_m = 0.97cm

SECRET

B43

SECRET

ROUND NO. 4-814

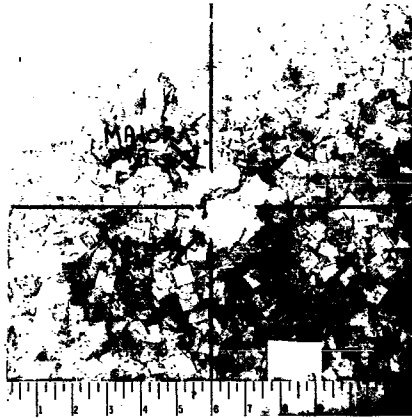


SECRET

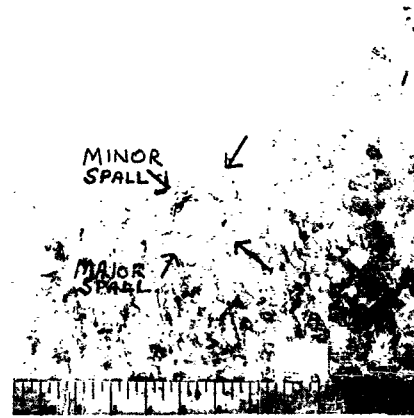
B44

SECRET

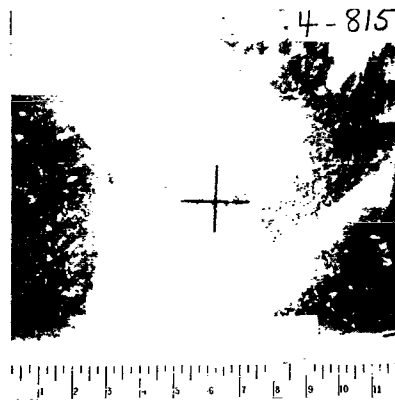
ROUND NO. 4-815



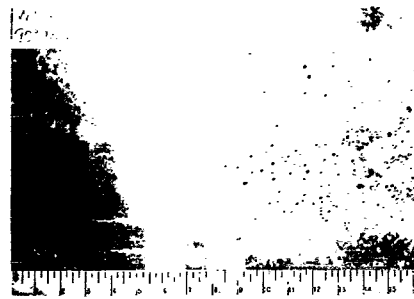
FRONT TARGET



REAR TARGET



W.P. 1-1/4" PLATE
 $s = 10"$
 $P_m = 0.03\text{cm}$



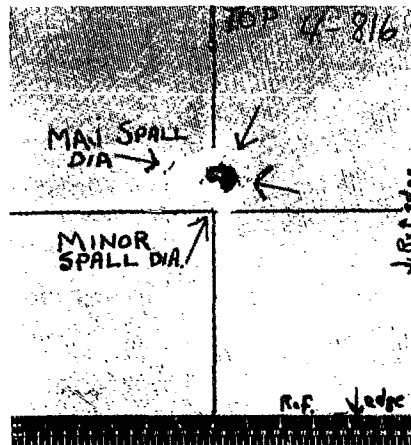
W.P. 1-1/4" PLATE
 $s = 17-1/2"$ FROM POINT OF IMPACT
 $P_m = 0.72\text{cm}$

SECRET

B45

SECRET

ROUND NO. 4-816



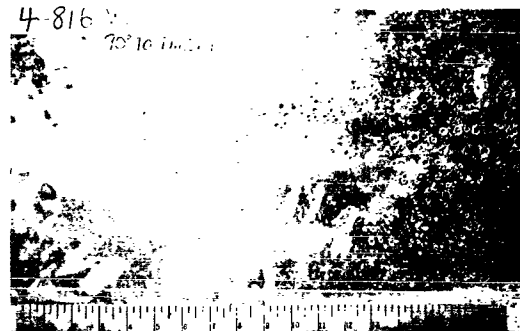
FRONT TARGET



REAR TARGET



EDGE TARGET



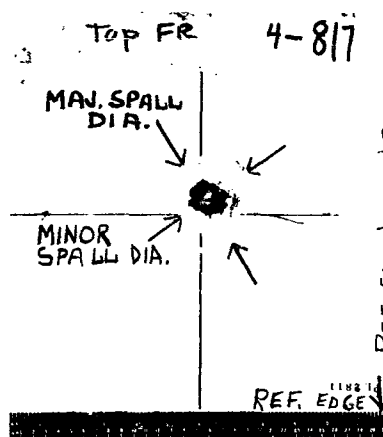
W. P. 1-1/4" PLATE
s = 17-1/4" FROM POINT OF IMPACT
 $P_m = 0.52\text{cm}$

SECRET

B46

SECRET

ROUND NO. 4-817



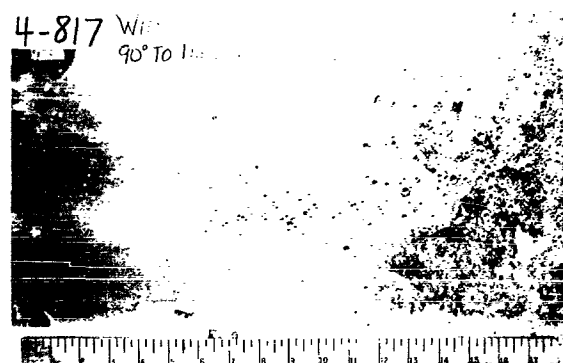
FRONT TARGET



REAR TARGET



EDGE
TARGET



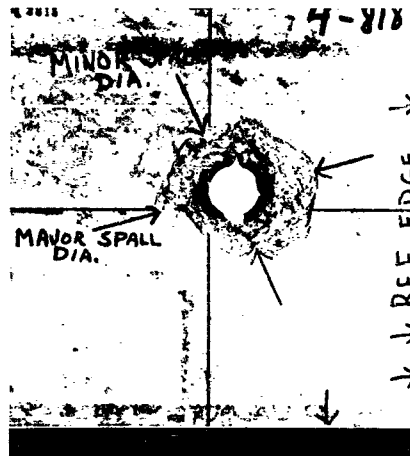
4-817 W.P. 1-1/4" PLATE
90° TO 100°
s=18" FROM POINT OF IMPACT
 $P_m = 0.67\text{cm}$

SECRET

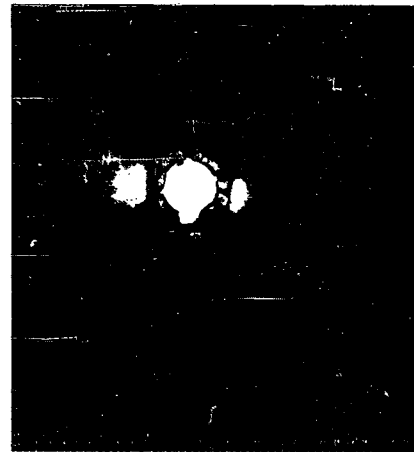
B47

SECRET

ROUND NO. 4-818



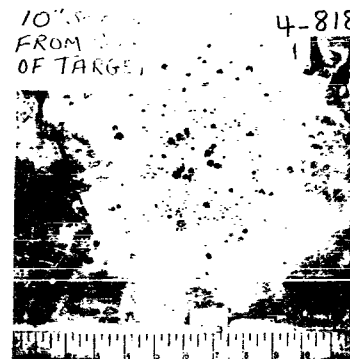
FRONT TARGET



REAR TARGET



EDGE
TARGET



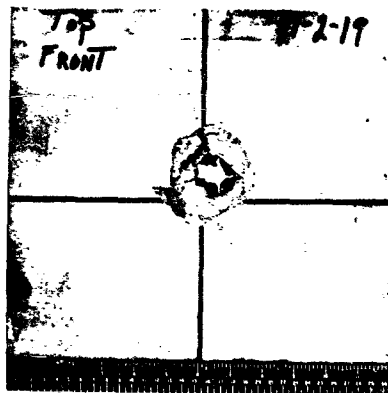
W.P. 3-1/4" PLATES
s = 10"
 $P_m = 0.81 \text{ cm}$

SECRET

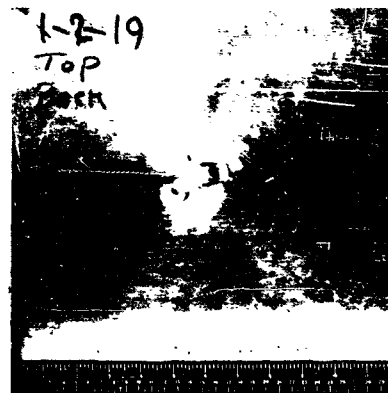
B48

SECRET

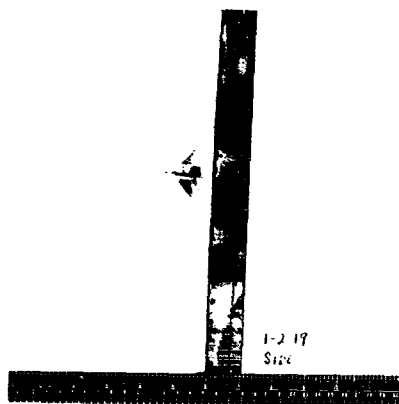
ROUND NO. 1-2-19



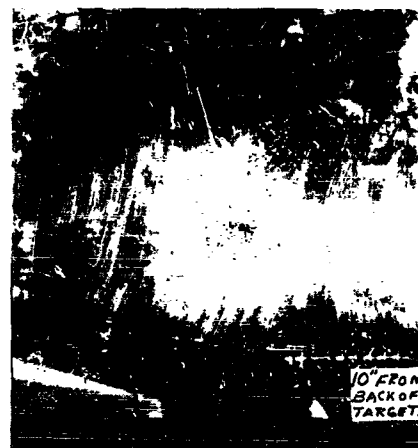
FRONT TARGET



REAR TARGET



EDGE TARGET



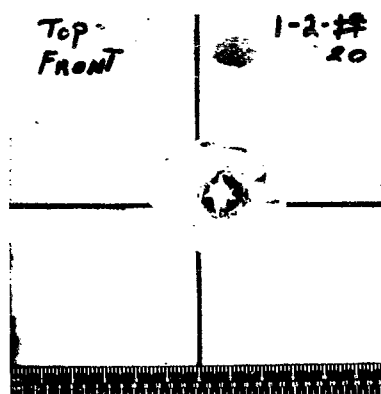
W.P. 4-1/4" PLATES
s=10"
P_m=0.04 cm

SECRET

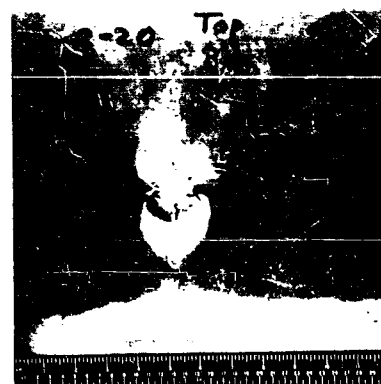
B50

SECRET

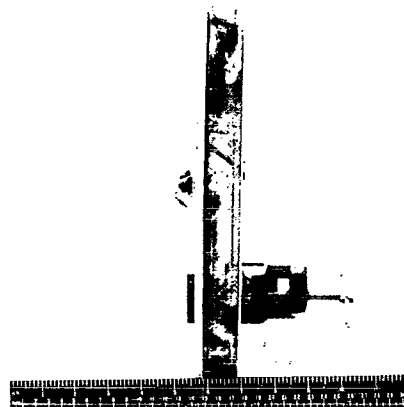
ROUND NO. 1-2-20



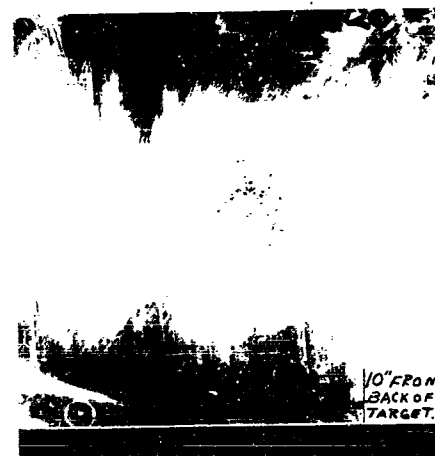
FRONT TARGET



REAR TARGET



EDGE TARGET



W. P. 4-1/4" PLATES
s = 10"
P_m = 0.3 cm

SECRET

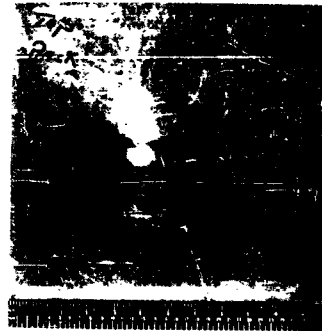
B51

SECRET

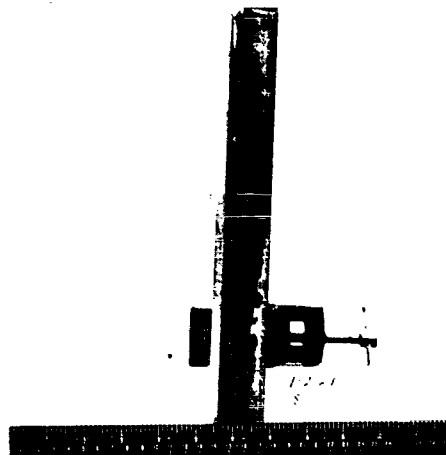
ROUND NO. 1-2-21



FRONT TARGET



REAR TARGET



EDGE TARGET

SECRET

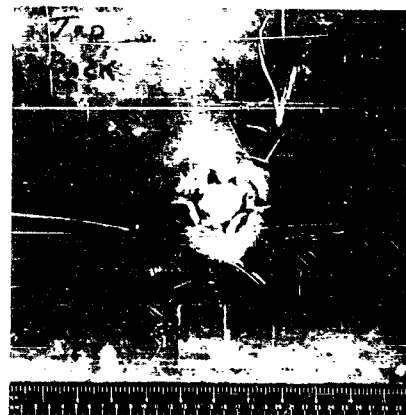
B52

SECRET

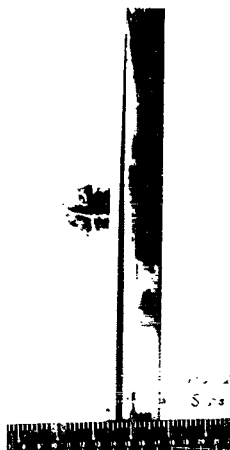
ROUND NO. 1-2-28



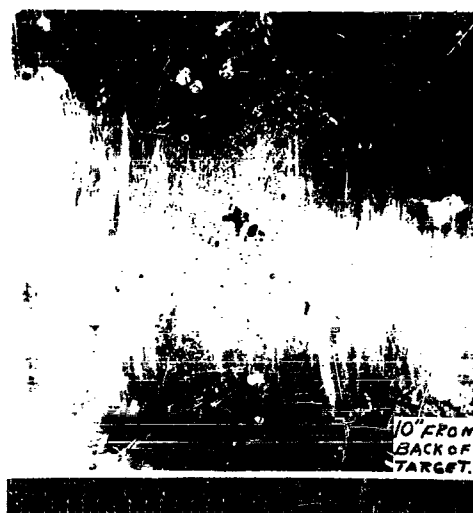
FRONT TARGET



REAR TARGET



EDGE TARGET



W. P. 1-1/2" PLATE
s=10"
 $P_m = 0.27 \text{ cm}$

SECRET

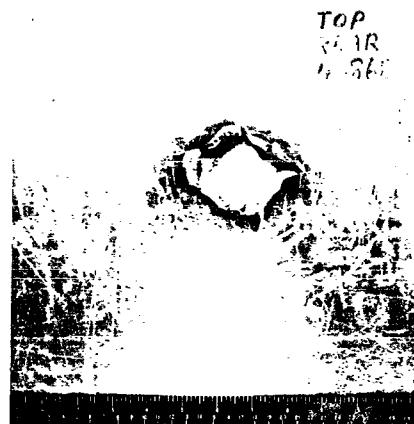
B53

SECRET

ROUND NO. 4-868



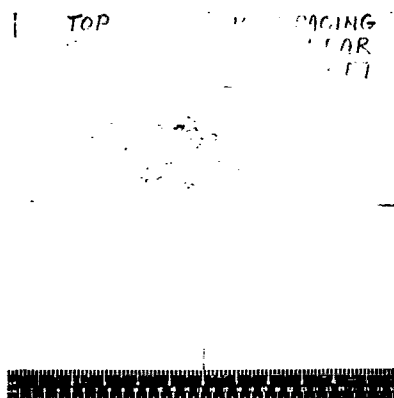
FRONT TARGET



REAR TARGET



EDGE TARGET



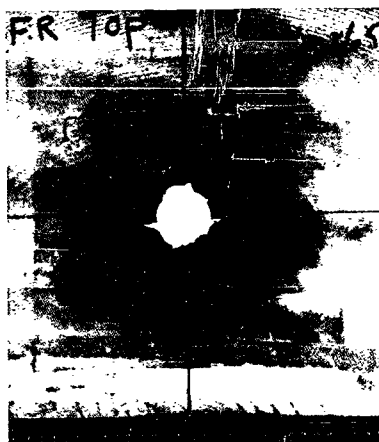
W.P. 1-1/4" PLATE
s=10"
PERFORATED PLATE

SECRET

B54

SECRET

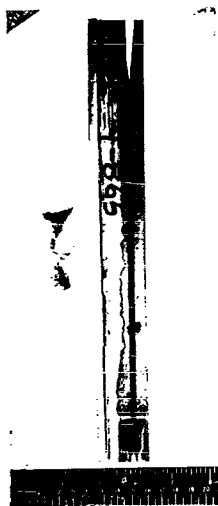
ROUND NO. 4-865



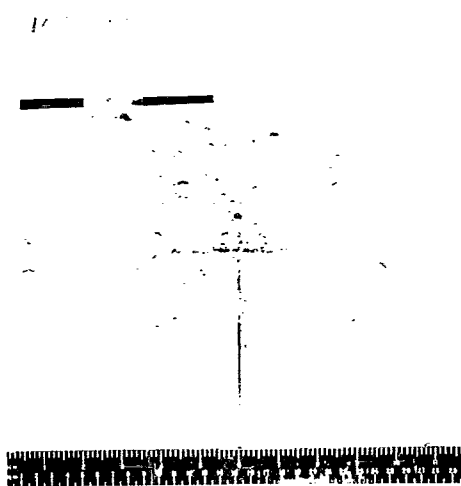
FRONT TARGET



REAR TARGET



EDGE TARGET



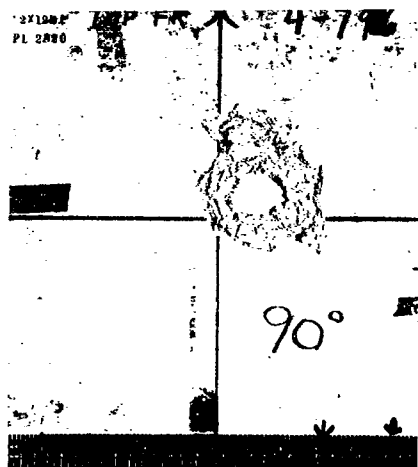
W.P. 2-1/4" PLATES
s = 10"
 $P_m = 0.58 \text{ cm}$

SECRET

B55

SECRET

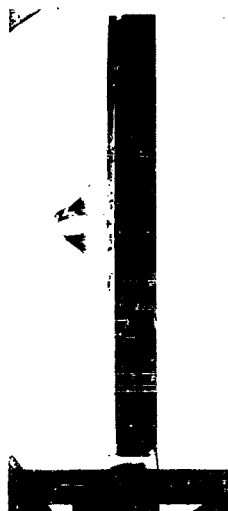
ROUND NO. 4-796



FRONT TARGET



REAR TARGET



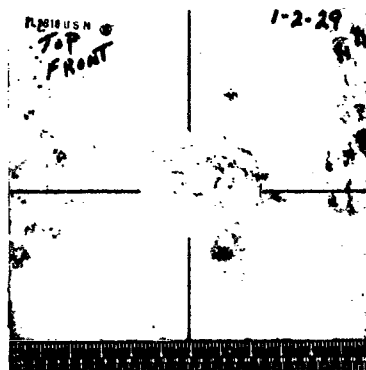
EDGE TARGET

SECRET

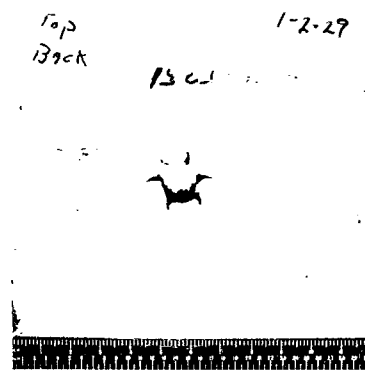
B56

SECRET

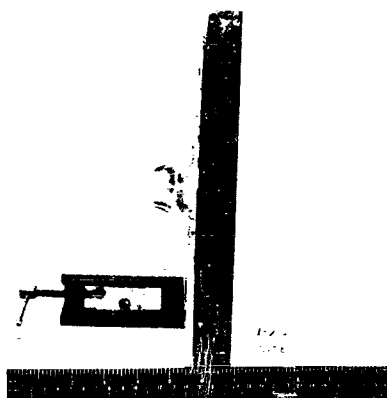
ROUND NO. 1-2-29



FRONT TARGET



REAR TARGET



EDGE TARGET



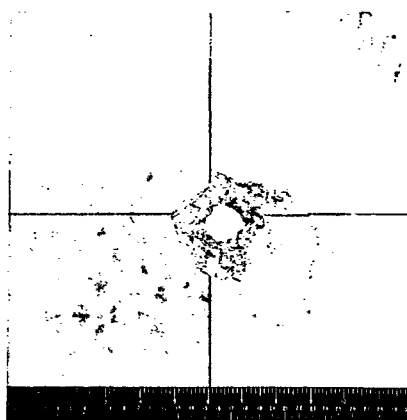
W.P. 1-1/2" PLATE
s = 10"
P_m = 0.18 cm

SECRET

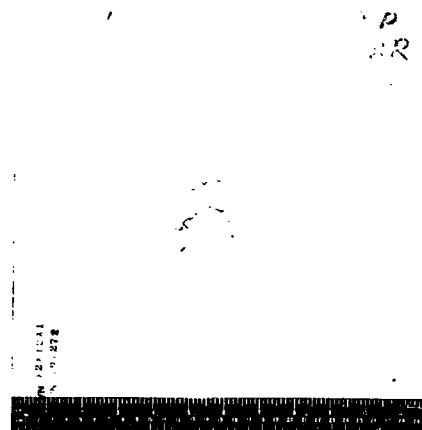
B57

SECRET

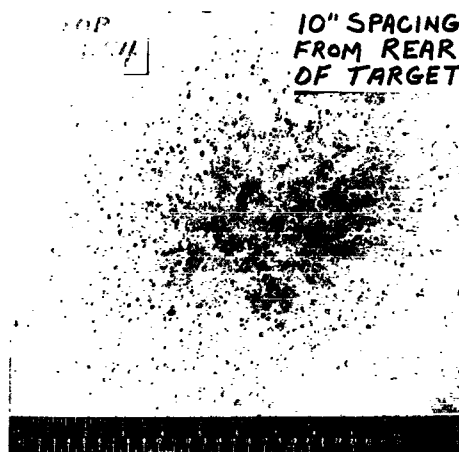
ROUND NO. 4-854



FRONT TARGET



REAR TARGET



W. P. 2-1/4" PLATES
 $s = 10"$
 $P_m = 1.37 \text{ cm}$

SECRET

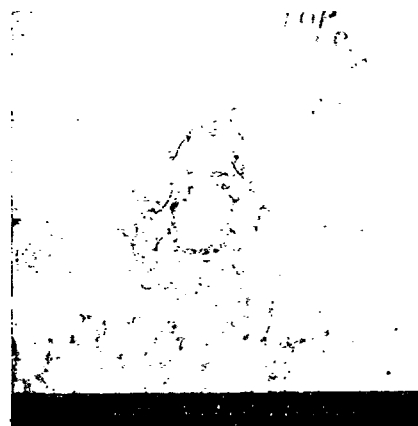
B58

SECRET

ROUND NO. 4-855



FRONT TARGET



REAR TARGET

F TOP
4-855

10" SPACING
FROM REAR
OF TARGET

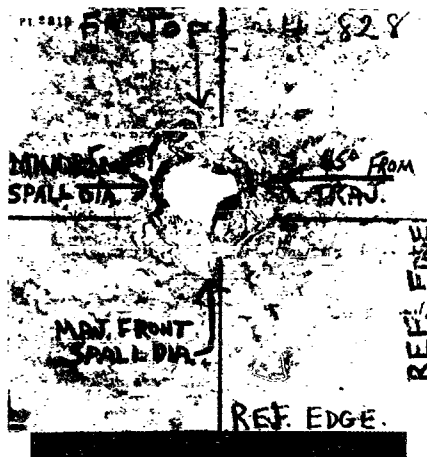
W. P. 2- 1/4" PLATES
s = 10"
P_m = 1.08 cm

SECRET

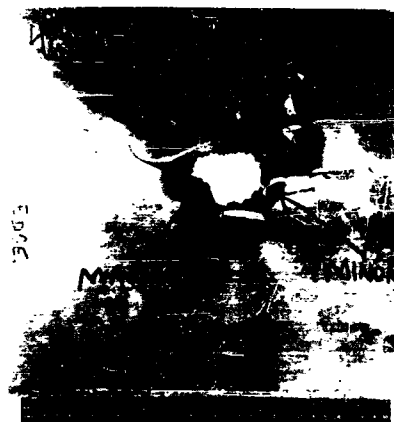
B59

SECRET

ROUND NO. 4-828



FRONT TARGET



REAR TARGET



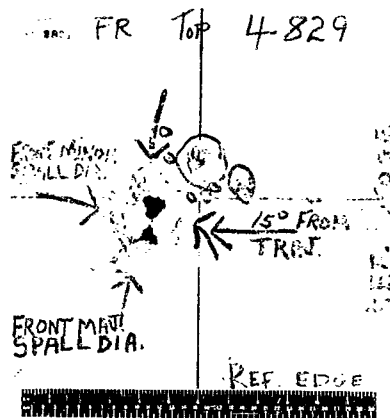
EDGE TARGET

SECRET

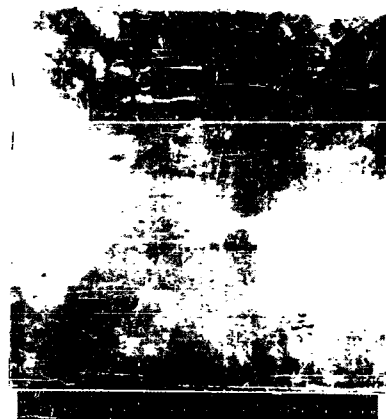
B60

SECRET

ROUND NO. 4-829



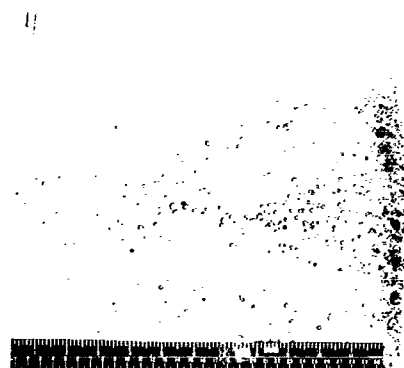
FRONT TARGET



REAR TARGET



EDGE TARGET



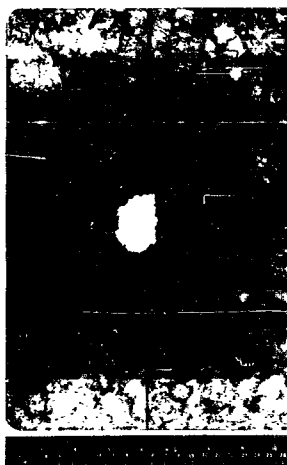
W. P. 1- 1/4" PLATE
s=16-1/2" FROM POINT OF IMPACT
PERFORATED PLATE

SECRET

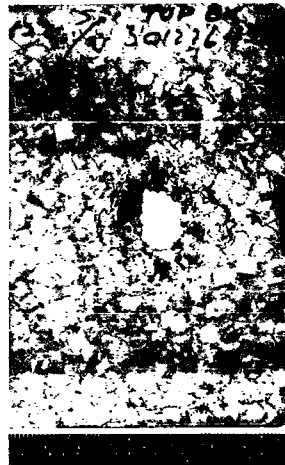
B61

SECRET

ROUND NO. 4-864



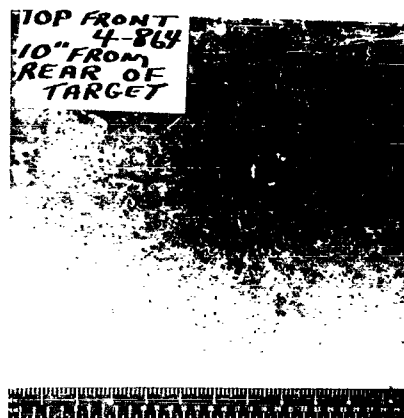
FRONT TARGET



REAR TARGET



EDGE TARGET



W. P. 3-1/4" PLATES

s=10"

$P_m = 1.0 \text{ cm}$

SECRET

B62

SECRET

ROUND NO. 4-866



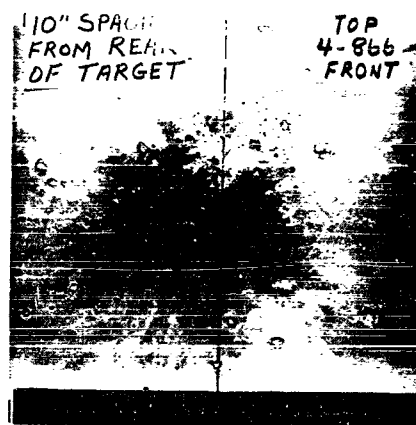
FRONT TARGET



REAR TARGET



EDGE TARGET



W.P. 2-1/4" PLATES
s = 10"
 $P_m = 0.47 \text{ cm}$

SECRET

B63

SECRET

ROUND NO. 4-807



FRONT TARGET



REAR TARGET



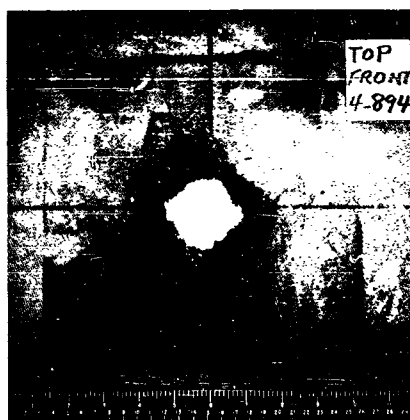
EDGE TARGET

SECRET

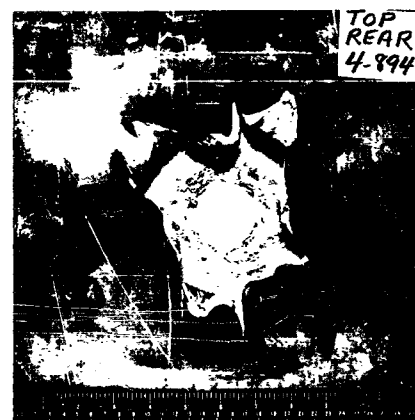
B64

SECRET

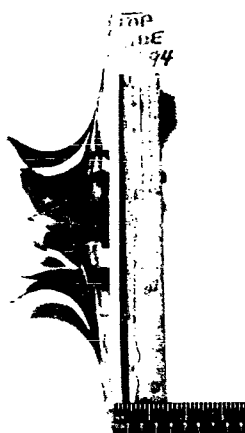
ROUND NO. 4-894



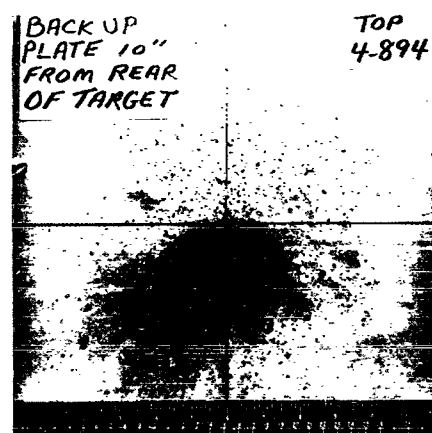
FRONT TARGET



REAR TARGET



EDGE TARGET



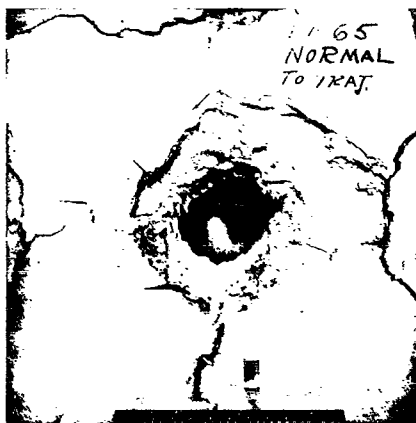
W.P. 2-1/2" PLATES
s = 10"

SECRET

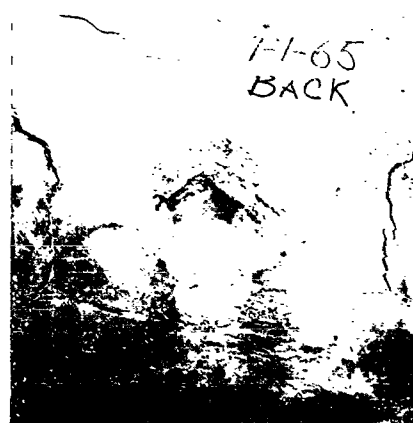
B65

SECRET

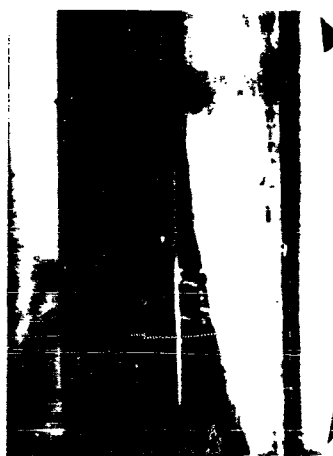
ROUND NO. 1-1-65



FRONT TARGET



REAR TARGET
(WITHOUT BACK-UP)



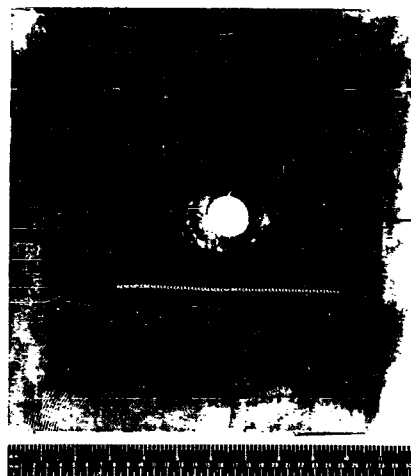
EDGE TARGET

SECRET

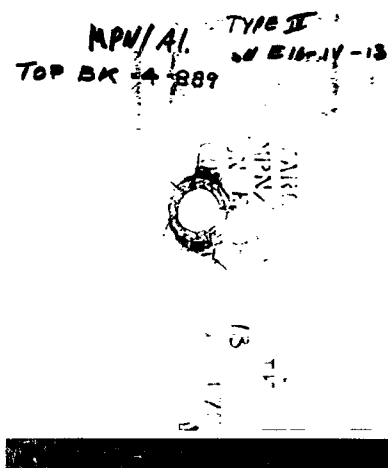
B66

SECRET

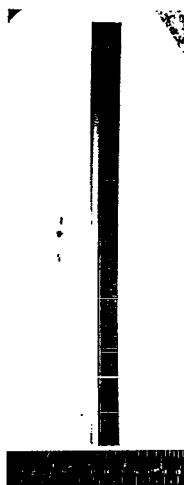
ROUND NO. 4-889



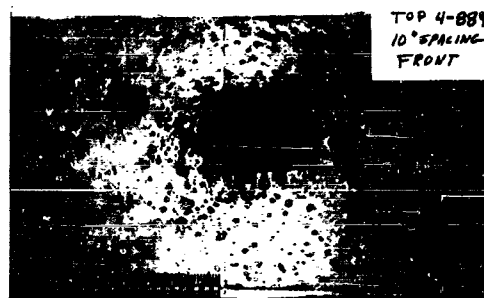
FRONT TARGET



REAR TARGET



EDGE TARGET



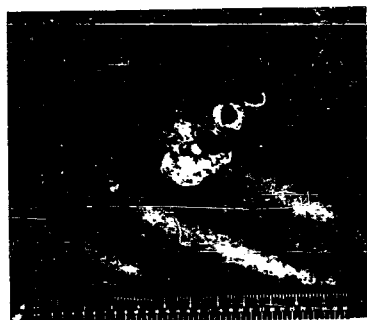
W. P. 1-1/2" PLATE
s=10"

SECRET

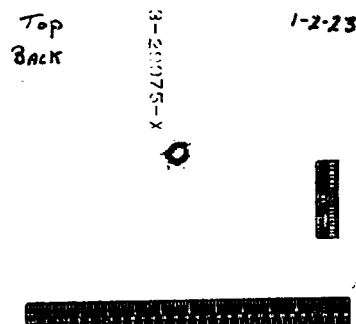
B67

SECRET

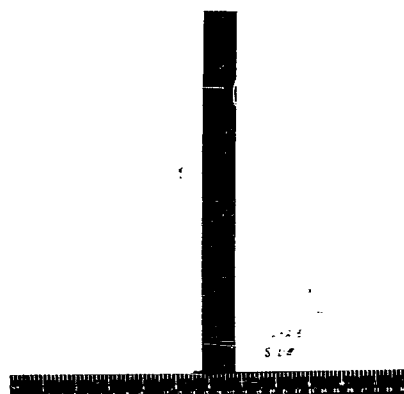
ROUND NO. 1-2-23



FRONT TARGET



REAR TARGET



EDGE TARGET



W.P. 1-1/4" PLATE
s = 10"
P_m = 0.67 cm

SECRET

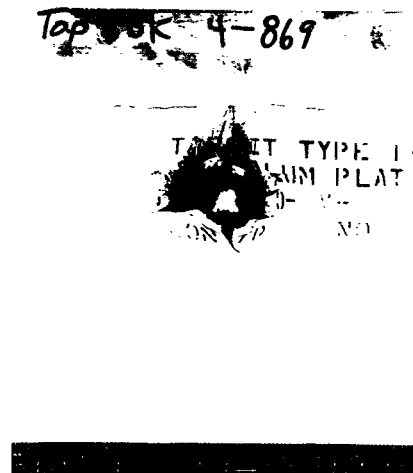
B68

SECRET

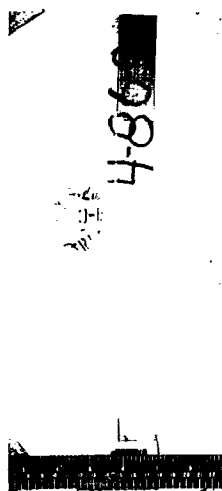
ROUND NO. 4-869



FRONT TARGET



REAR TARGET



EDGE TARGET



W.P. 2-1/4" PLATES
s = 10"
P_m = 0.39 cm

SECRET

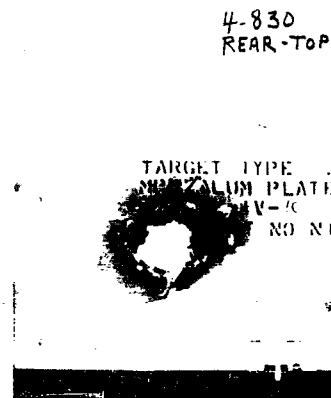
B69

SECRET

ROUND NO. 4-830



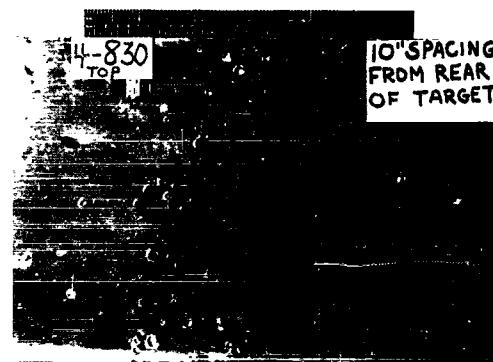
FRONT TARGET



REAR TARGET



EDGE TARGET



W. P. 2-1/4" PLATES
s = 10"
P_m = 0.91cm

SECRET

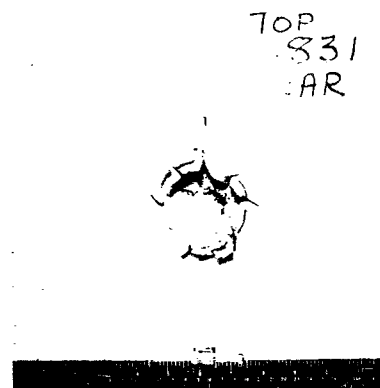
B70

SECRET

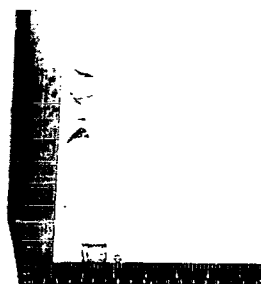
ROUND NO. 4-831



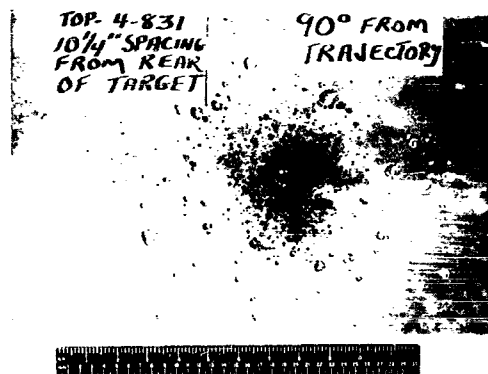
FRONT TARGET



REAR TARGET



EDGE TARGET



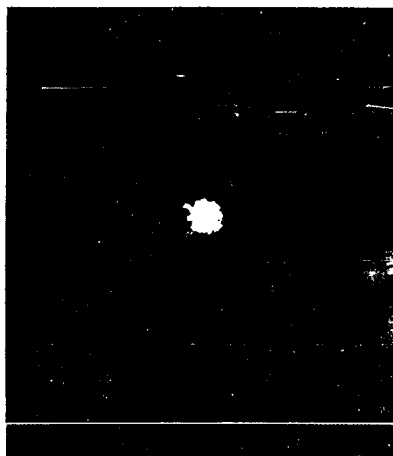
W.P. 2-1/4" PLATES
2-1/8" PLATES
s = 10-1/4"
P_m = 1.47 cm

SECRET

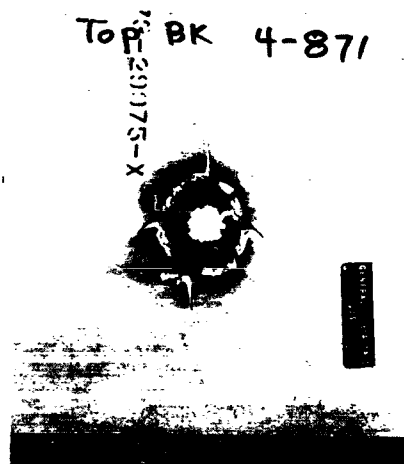
B71

SECRET

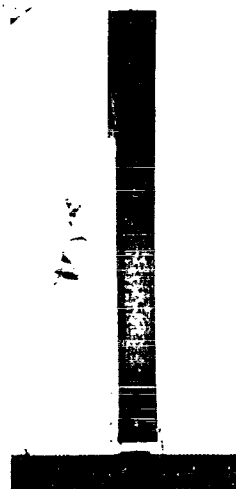
ROUND NO. 4-871



FRONT TARGET



REAR TARGET



EDGE TARGET



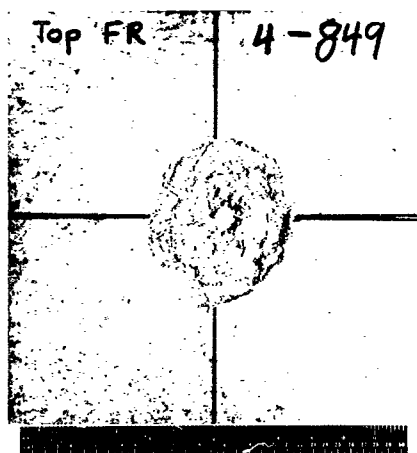
W.P. 4-1/8" PLATES
s=10"
P_m = 1.34 cm

SECRET

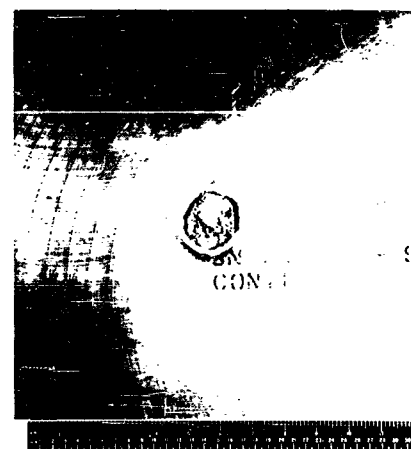
B72

SECRET

ROUND NO. 4-849



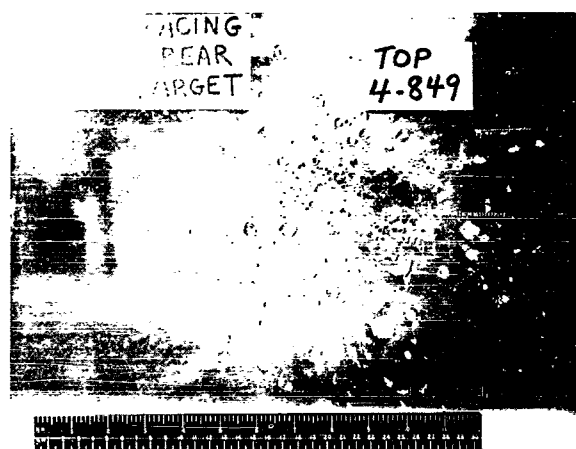
FRONT TARGET



REAR TARGET



EDGE TARGET



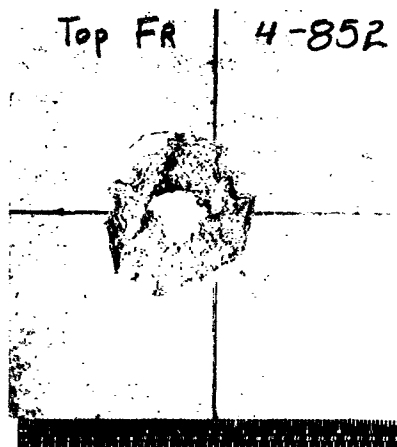
W.P. 1-1/4" PLATE
s = 10"
P_m = 0.34 cm

SECRET

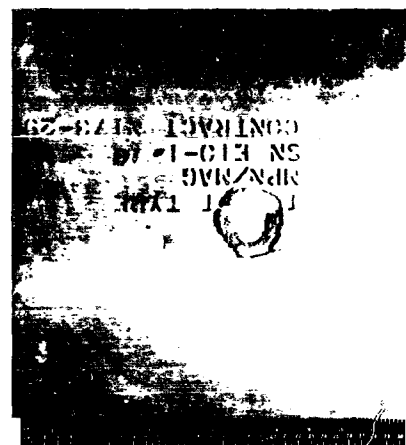
B73

SECRET

ROUND NO. 4-852



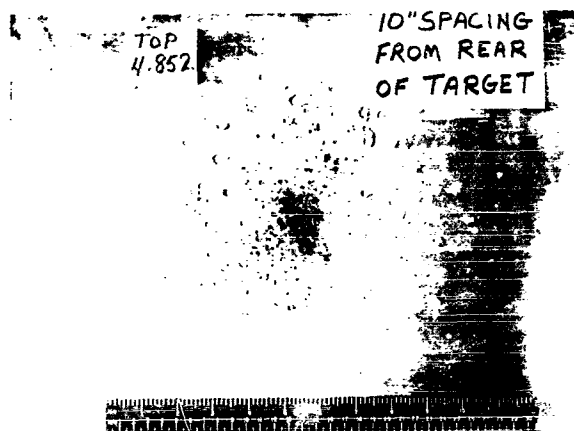
FRONT TARGET



REAR TARGET



EDGE TARGET



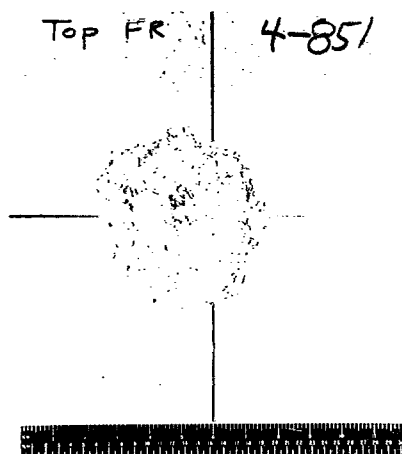
W.P. 2-1/4" PLATES
s = 10"
 $P_m = 0.78 \text{ cm}$

SECRET

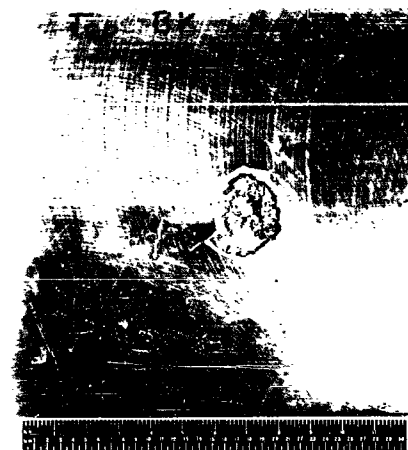
B74

SECRET

ROUND NO. 4-851



FRONT TARGET



REAR TARGET



EDGE TARGET



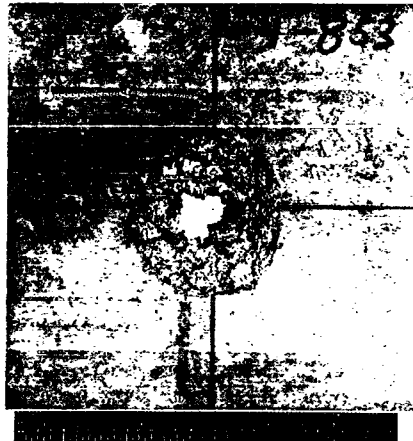
W.P. 2-1/4" PLATES
s = 10"
P_m = 0.69 cm

SECRET

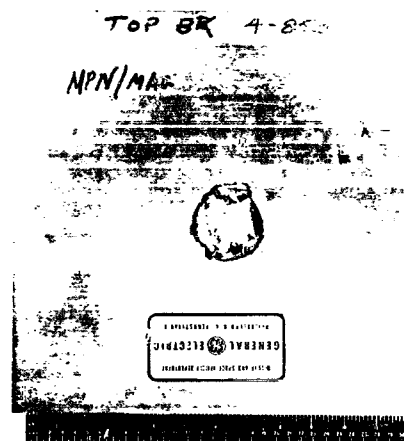
B75

SECRET

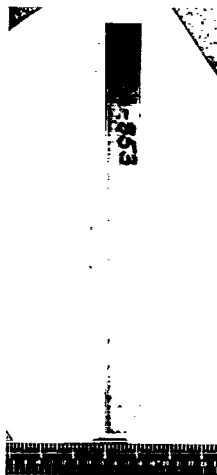
ROUND NO. 4-853



FRONT TARGET



REAR TARGET



EDGE TARGET



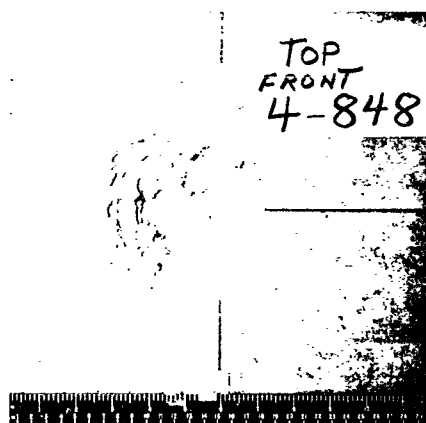
W.P. 2-1/4" PLATES
s = 10"
P_m = 1.24 cm

SECRET

B76

SECRET

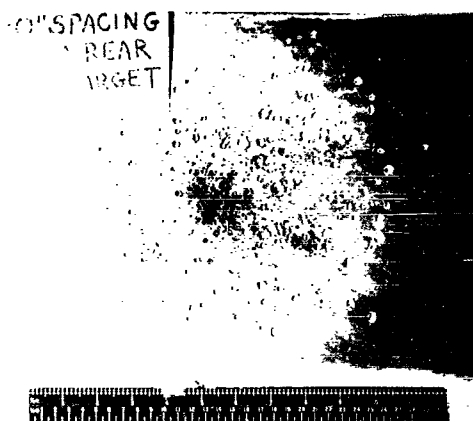
ROUND NO. 4-848



FRONT TARGET



REAR TARGET



W. P. 2 - 1/4" PLATES
s = 10"
P_m = 0.725 cm

SECRET

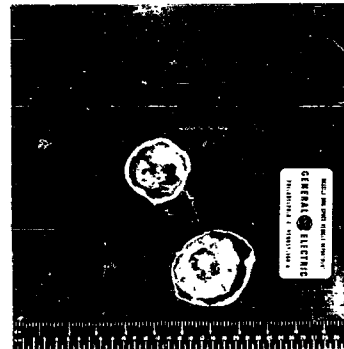
B77

SECRET

ROUND NO. 1-2-30



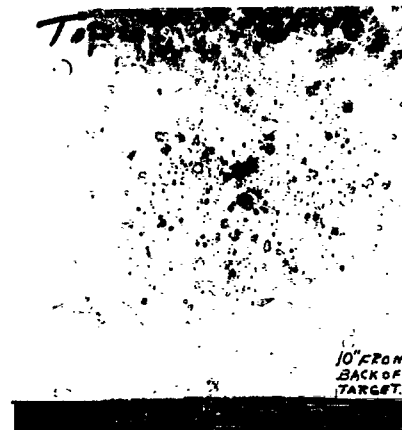
FRONT TARGET



REAR TARGET



EDGE TARGET



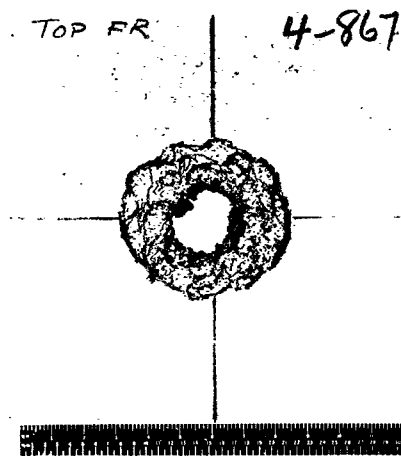
W.P. 1-1/2" PLATE
s = 10"
P_m = 1.32 cm

SECRET

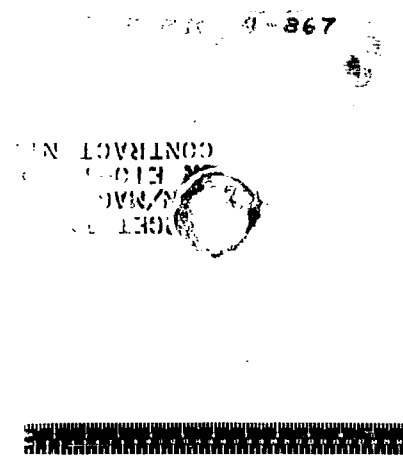
B78

SECRET

ROUND NO. 4-867



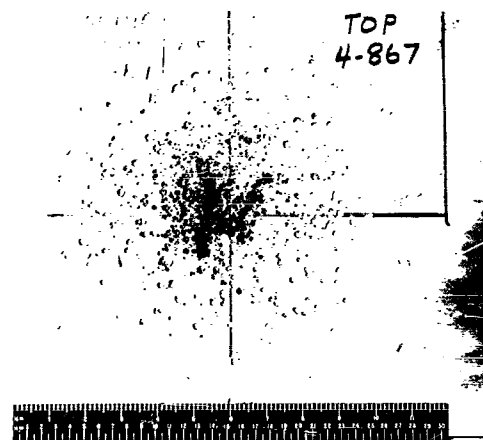
FRONT TARGET



REAR TARGET



EDGE TARGET



W.P. 2-1/4 PLATES
s = 10"
P_m = 1.09 cm

SECRET

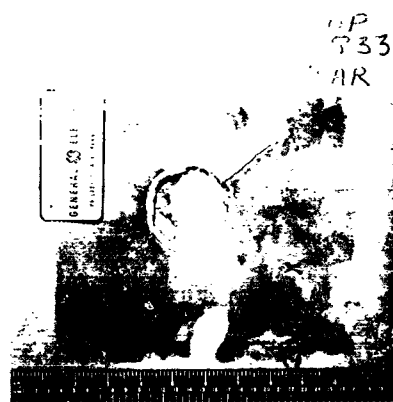
B79

SECRET

ROUND NO. 4-833

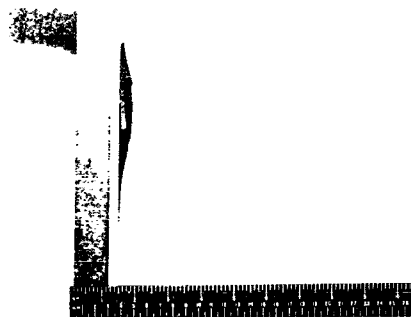


FRONT TARGET



REAR TARGET

4



EDGE TARGET



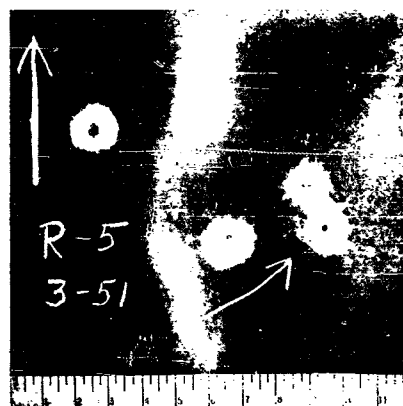
W.P. 3-1/4" PLATES
s = 10-1/4"
P_m = 1.1 cm

SECRET

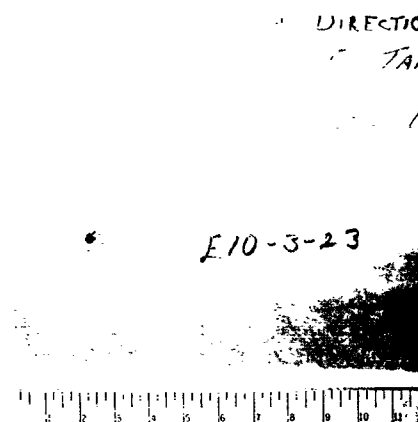
B80

SECRET

ROUND NO. 5-3-51



FRONT TARGET



REAR TARGET

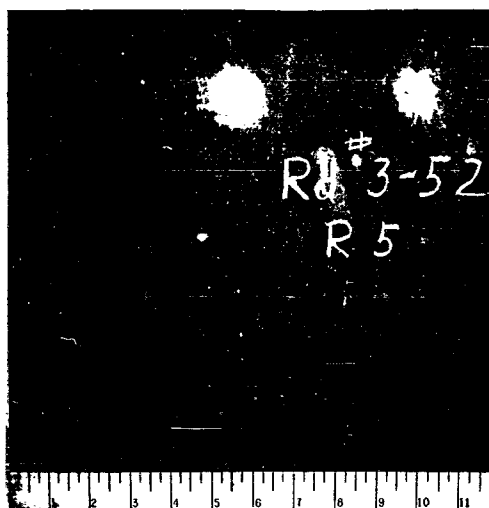
EDGE TARGET

SECRET

B81

SECRET

ROUND NO. 5-3-52



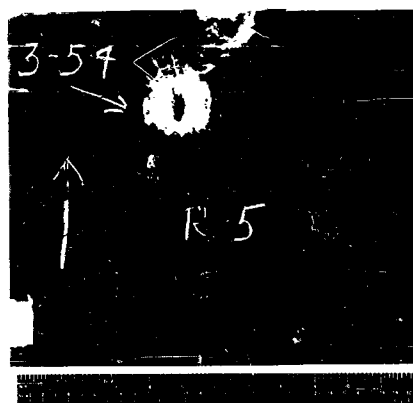
FRONT TARGET

SECRET

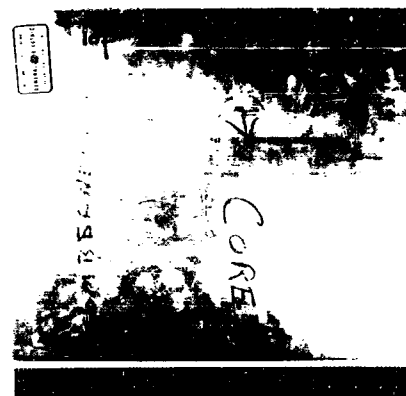
B82

SECRET

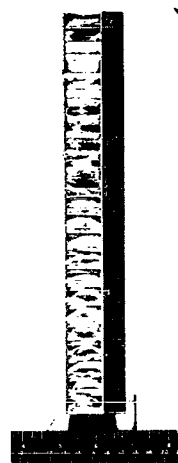
ROUND NO. 5-3-54



FRONT TARGET



REAR TARGET



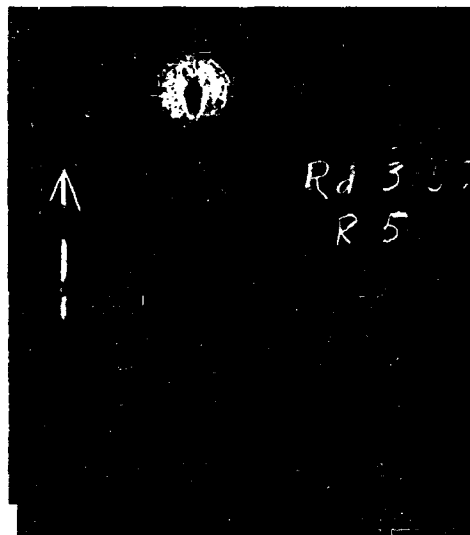
EDGE TARGET

SECRET

B83

SECRET

ROUND NO. 5-3-57



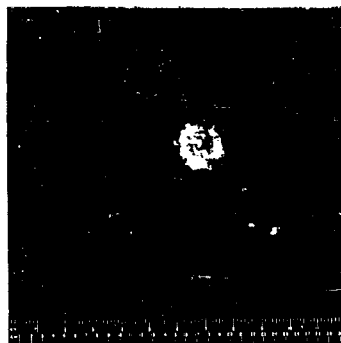
FRONT TARGET

SECRET

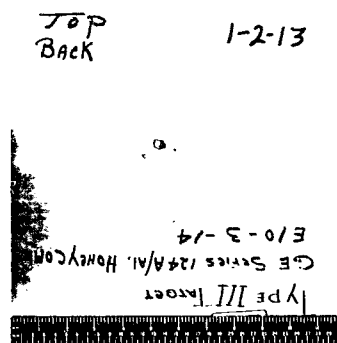
B84

SECRET

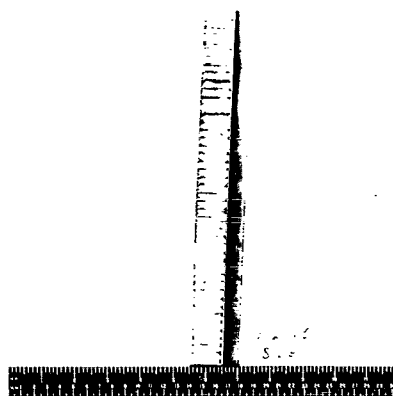
ROUND NO. 1-2-13



FRONT TARGET



REAR TARGET



EDGE TARGET



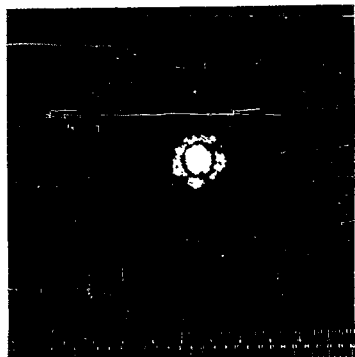
W.P. 4-1/4" PLATES
s = 10"
P_m = 1.1 cm

SECRET

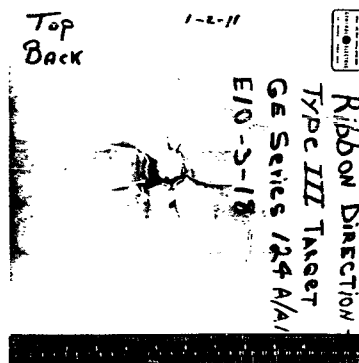
B85

SECRET

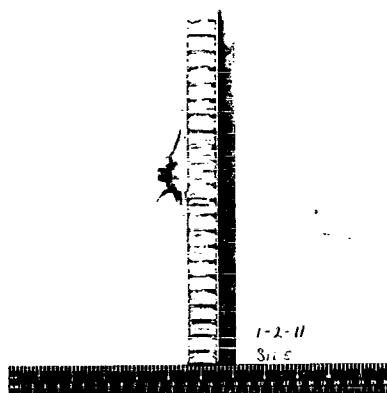
ROUND NO. 1-2-II



FRONT TARGET



REAR TARGET



EDGE TARGET



W.P. 4 - 1/4" PLATES

s = 10"

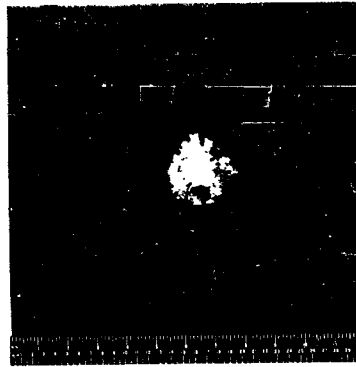
P_m = 0.98 cm

SECRET

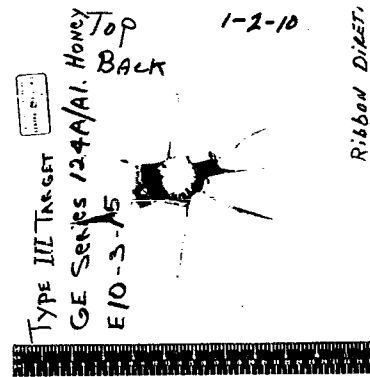
B86

SECRET

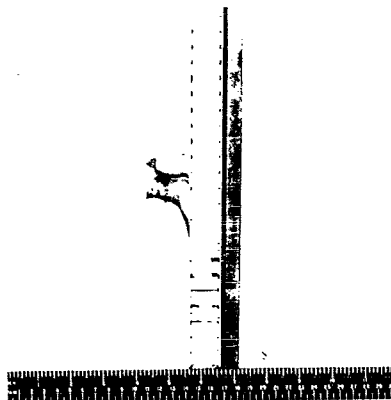
ROUND NO. 1-2-10



FRONT TARGET



REAR TARGET



EDGE TARGET



W.P. 2-1/4" PLATES
s = 10"
P_m = 0.78 cm

SECRET

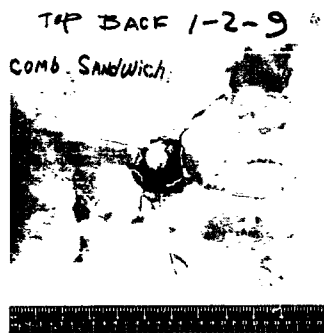
B87

SECRET

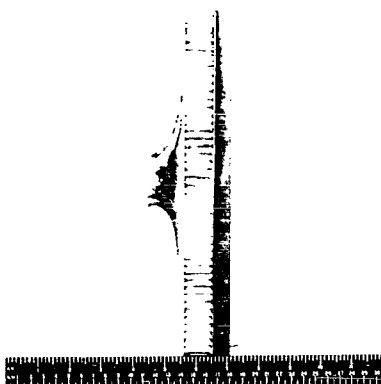
ROUND NO. 1-2-9



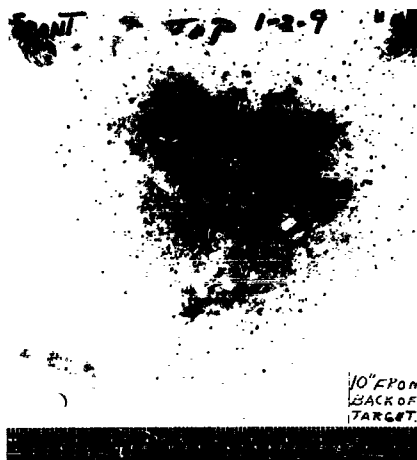
FRONT TARGET



REAR TARGET



EDGE TARGET



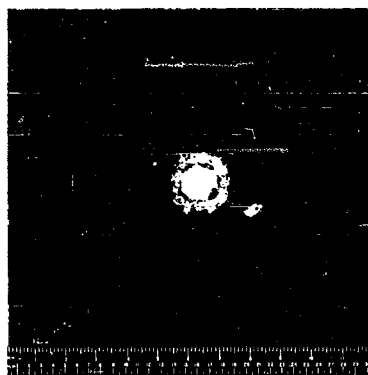
W.P. 4-1/4" PLATES
 $s = 10"$
 $P_m = 0.705 \text{ cm}$

SECRET

B88

SECRET

ROUND NO. 1-2-12



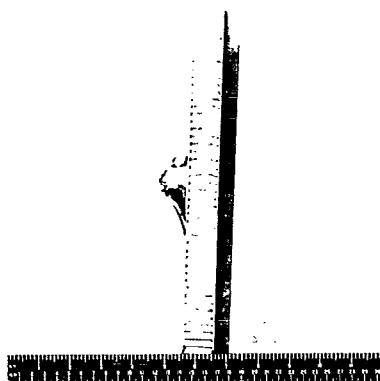
FRONT TARGET

Top
Back
Honeycomb Sandwich

1-2-12



REAR TARGET



EDGE TARGET



W.P. 2-1/4" PLATES
s = 10"
P_m = 0.81 cm

10" FROM
BACK OF
TARGET.

SECRET

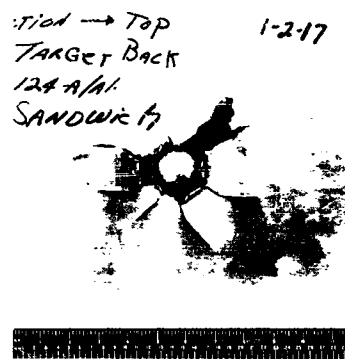
B89

SECRET

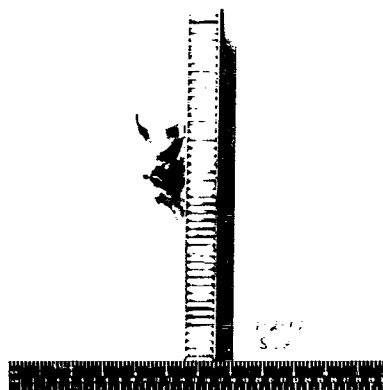
ROUND NO. 1-2-17



FRONT TARGET



REAR TARGET



EDGE TARGET



10" FROM
BACK OF
TARGET.

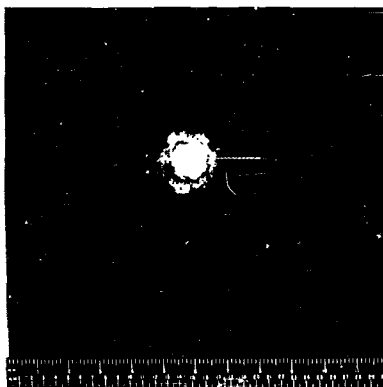
W.P. 4-1/4" PLATES
s = 10"
P_m = 0.94 cm

SECRET

B90

SECRET

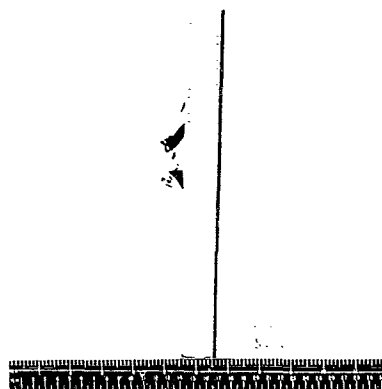
ROUND NO. 1-2-15



FRONT TARGET



REAR TARGET



EDGE TARGET



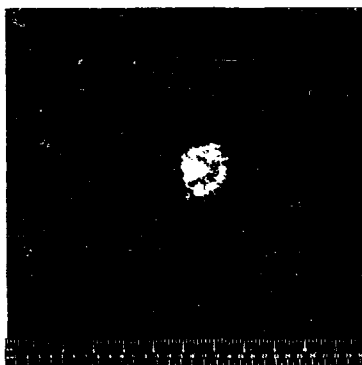
W.P. 4-1/4" PLATES
s = 10"
P_m = 0.5 cm

SECRET

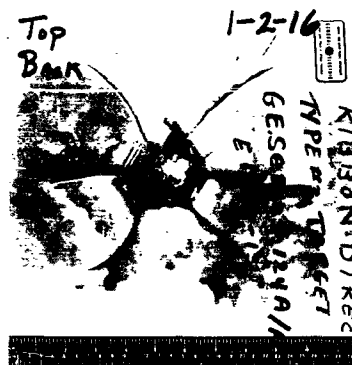
B91

SECRET

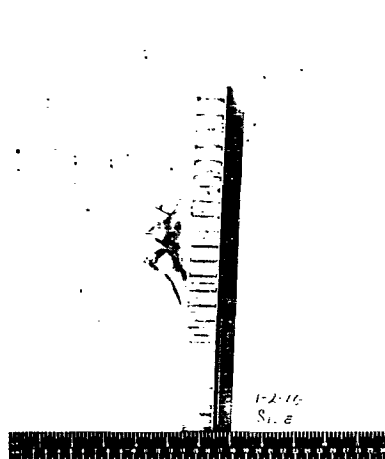
ROUND NO. 1-2-16



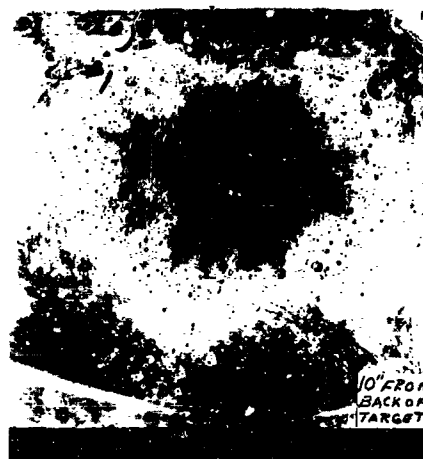
FRONT TARGET



REAR TARGET



EDGE TARGET



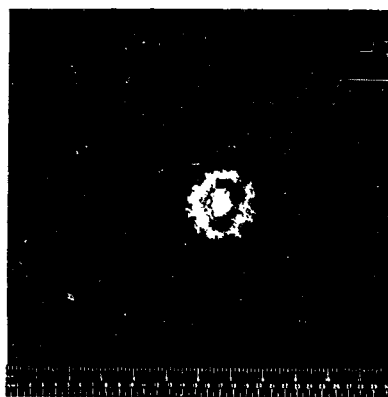
W.P. 4 - 1/4" PLATES
s = 10"
P_m = 1.0 cm

SECRET

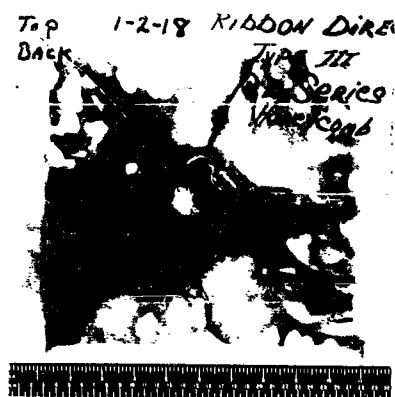
B92

SECRET

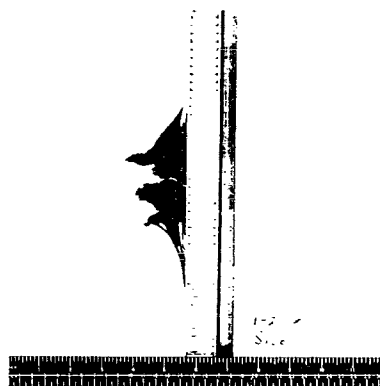
ROUND NO. 1-2-18



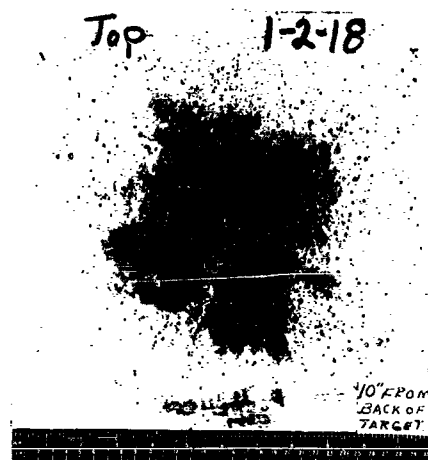
FRONT TARGET



REAR TARGET



EDGE TARGET



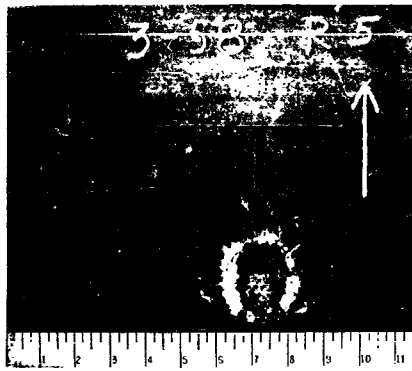
W.P. 4-1/4 PLATES
 $s = 10''$
 $P_m = 0.84 \text{ cm}$

SECRET

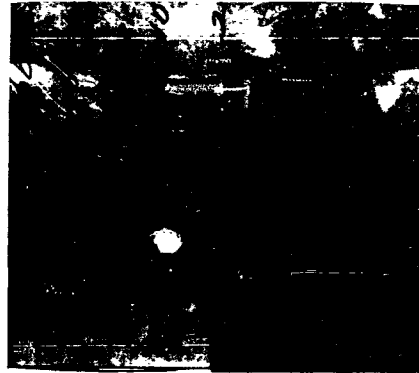
B93

SECRET

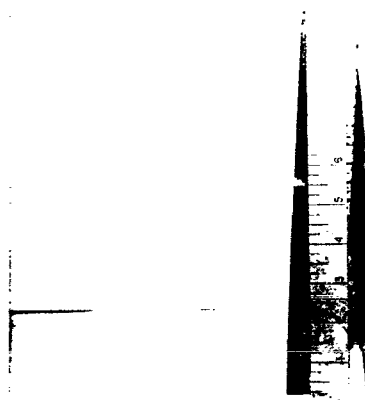
ROUND NO. 5-3-58



FRONT TARGET



REAR TARGET



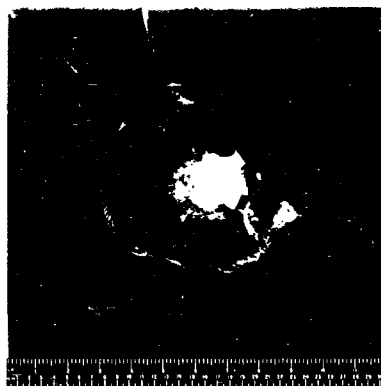
EDGE TARGET

SECRET

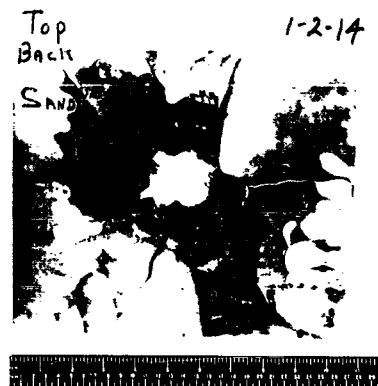
B94

SECRET

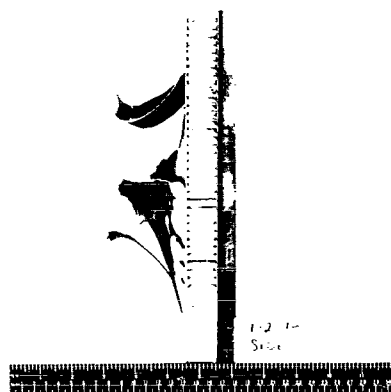
ROUND NO. 1-2-14



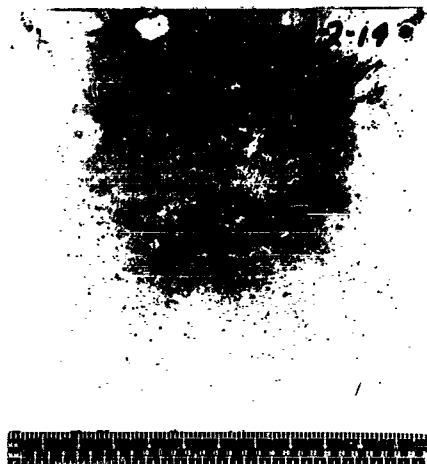
FRONT TARGET



REAR TARGET



EDGE TARGET



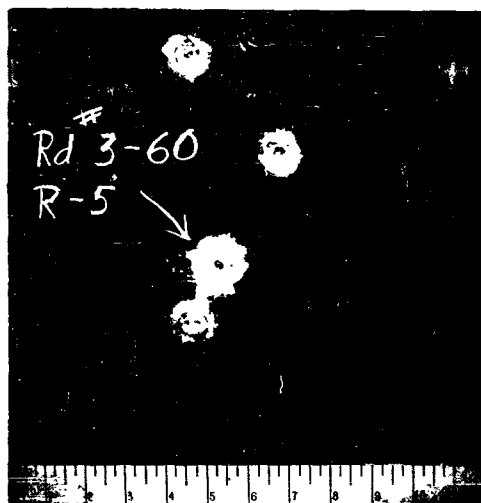
W.P. 4-1/4" PLATES
s = 10"
P_m = 0.90 cm

SECRET

B95

SECRET

ROUND NO. 5-3-60



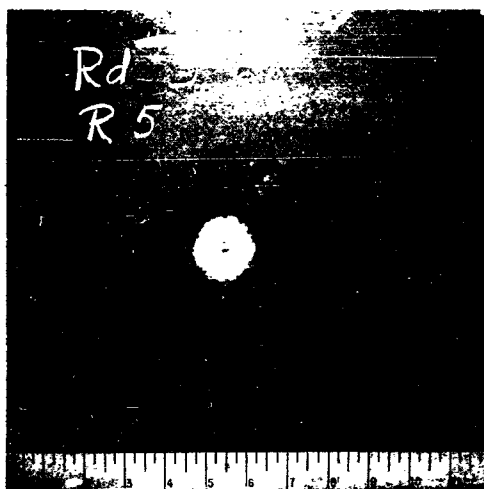
FRONT TARGET

SECRET

B96

SECRET

ROUND NO. 5-3-61



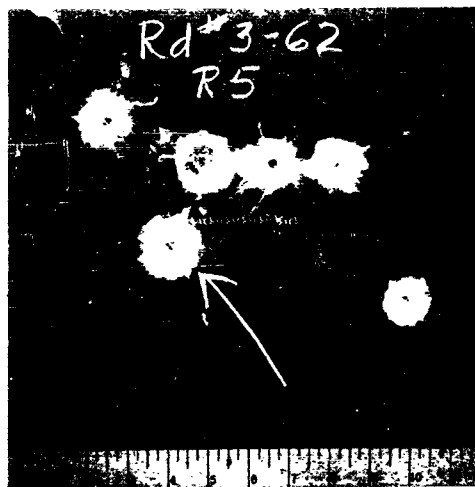
FRONT TARGET

SECRET

B97

SECRET

ROUND NO. 5-3-62



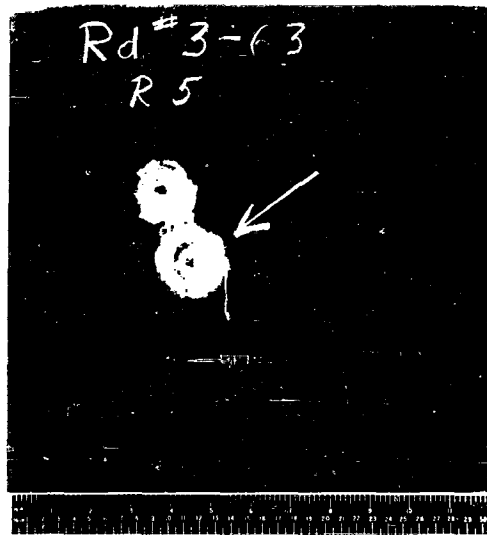
FRONT TARGET

SECRET

B98

SECRET

ROUND NO. 5-3-63



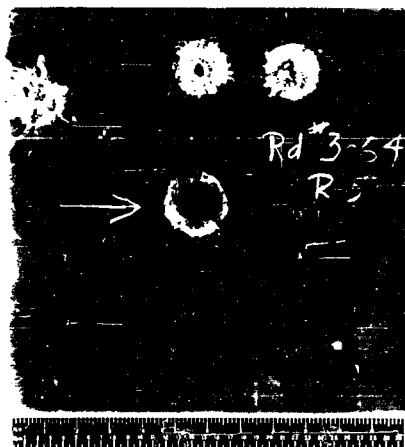
FRONT TARGET

SECRET

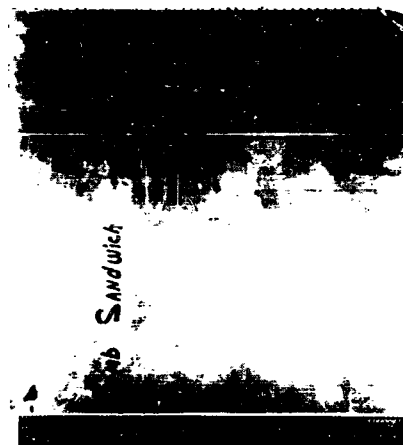
B99

SECRET

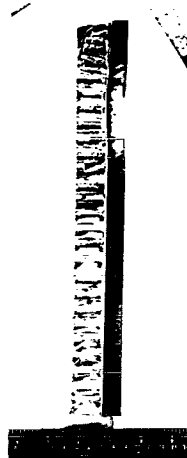
ROUND NO. 5-3-64



FRONT TARGET



REAR TARGET



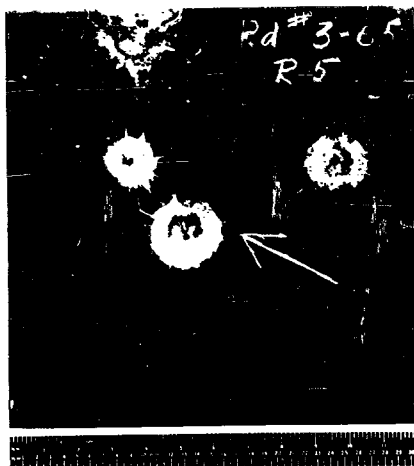
EDGE TARGET

SECRET

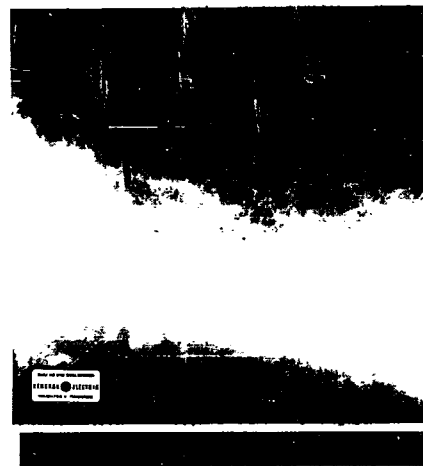
B100

SECRET

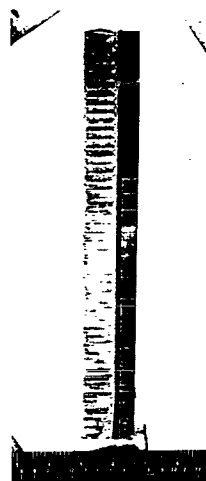
ROUND NO. 5-3-65



FRONT TARGET



REAR TARGET



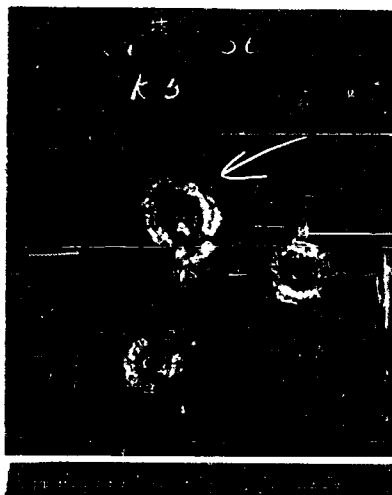
EDGE TARGET

SECRET

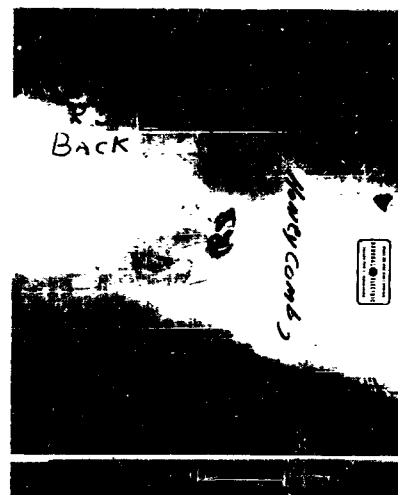
B101

SECRET

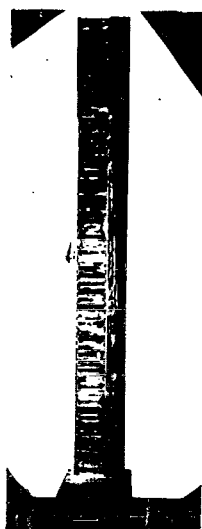
ROUND NO. 5-3-66



FRONT TARGET



REAR TARGET



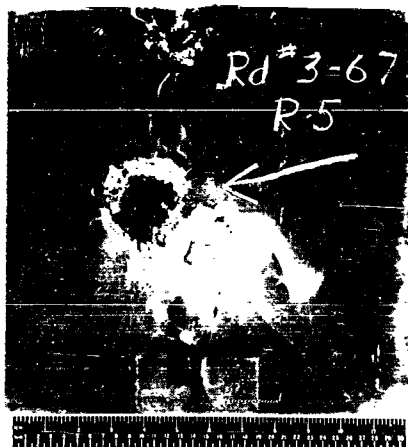
EDGE TARGET

SECRET

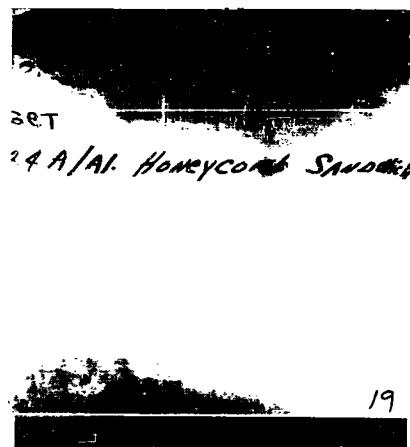
B102

SECRET

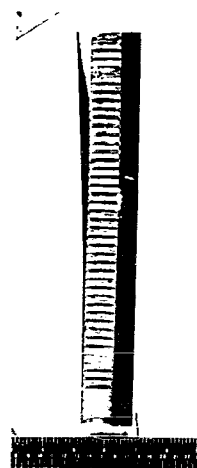
ROUND NO. 5-3-67



FRONT TARGET



REAR TARGET



EDGE TARGET

SECRET

B103

SECRET

ROUND NO. 4-795



FRONT TARGET



REAR TARGET



EDGE TARGET

SECRET

B104

SECRET

ROUND NO. 1-1-55



FRONT TARGET



REAR TARGET



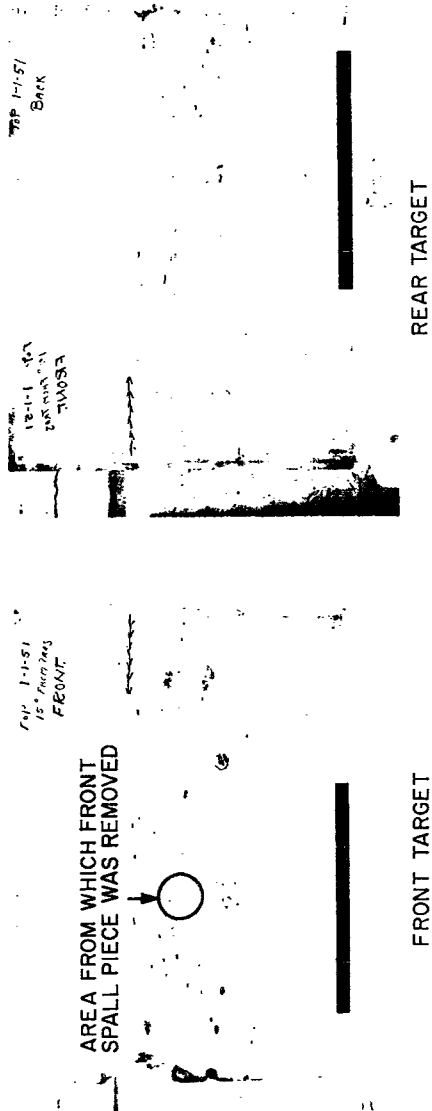
SECRET

B105

SECRET

B106

ROUND NO. 1-1-51



SECRET



SECRET

This document consists of 110 pages
Copy No. 24 of 179 copies, Series A

(UNCLASSIFIED TITLE)
HYPERVELOCITY KILL MECHANISMS PROGRAM

ARPA Order 149-60

Impact Damage Phase

Final Report
for Period Ending
31 May 1963

M. Rockowitz
C. A. Carey

16 July 1963

RESEARCH AND ADVANCED DEVELOPMENT DIVISION
AVCO CORPORATION
Wilmington, Massachusetts

SECRET

C

DOWNGRADED AT 3 YEAR INTERVALS
DECLASSIFIED AFTER 12 YEARS
DUD DIR. 5200.10

SECRET

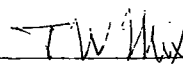
Project Code No. 7300

Contract NOmr 3307(00)

Status Report

RAD-SR-63-128

APPROVED


T. W. Mix
Project Director

This document contains information affecting the National Defense of the United States within the meaning of the Espionage Laws, Title 18, U.S.C., Sections 793 and 794, the transmission or revelation of which in any manner to an unauthorized person is prohibited by law.

C1

SECRET

DOWNGRADED AT 3 YEAR INTERVALS
DECLASSIFIED AFTER 12 YEARS
DOD DIR. 5200.10

SECRET

ACKNOWLEDGMENTS

The authors wish to express their gratitude to Mr. J. A. Hull and others of the Engineering Physics Section for their advice and overall assistance in carrying out this work. Special thanks is extended to Mr. H. Colby and Mr. D. DeChristoforo who labored tirelessly to obtain the data presented in this report. Finally, our thanks to Mr. J. Richards and Staff of the Physical Testing Section for their work on material property measurements.

C2

SECRET

SECRET

CONTENTS

I. Impact Damage Phase	C13
A. Objectives	C13
B. Experimental Procedure	C13
C. Results	C16
D. Interpretation of Results	C70
E. Perforation Energy Correlation	C74
F. Spallation Study.....	C81
G. Summary and Conclusions	C88
H. References	C90
I. Appendix 1, Summary of Impact Data	C92
J. Appendix 2, Summary of Spall Data	C99

SECRET

ILLUSTRATIONS

Figure 1	Firing Arrangement Used in the ARPA 149 Program	C14
2	Sectioned OTWR Target after Impact	C17
3	Sectioned Astrolite Target after Impact	C18
4	Sectioned RAD 60 HD Target after Impact	C19
5	Typical Cross Section of Perforated OTWR Target	C20
6	Approximate Puncture Profile Shown with Measured Parameters	C21
7	Inside Diameter versus Energy, 440 Steel on HITCO OTWR Bonded to Aluminum	C22
8	Inside Diameter versus Energy, 440 Steel on HITCO OTWR Bonded to Steel	C23
9	Inside Diameter versus Energy, 440 Steel Projectiles on Astrolite Bonded to Aluminum and Steel.....	C24
10	Inside Diameter versus Energy, 440 Steel Projectile on Scrap OTWR Bonded to 1/8-inch Aluminum.....	C25
11	Inside Diameter versus Energy, 440 Steel Projectile on RAD 60 HD Bonded to Aluminum	C26
12	Correlation of Constant, a , with Heat Shield Thickness for OTWR	C28
13	Correlation of Constant, a , with Heat Shield Thickness for All Heat Shield Materials	C29
14	Front Spall Area versus Projectile Energy, 440 Steel into First Batch of OTWR on Aluminum and Steel	C32
15	Front Spall Area versus Projectile Energy, 440 Steel into OTWR on Aluminum	C33
16	Front Spall Area versus Projectile Energy, 440 Steel into Astrolite on Aluminum and Steel.....	C34

ILLUSTRATIONS (Cont'd)

Figure 17	Front Spall Area versus Projectile Energy, 440 Steel into RAD 60 HD on Aluminum	C35
18	Back Spall Area versus Projectile Energy, 440 Steel into First Batch of OTWR on Aluminum and Steel	C39
19	Back Spall Area versus Projectile Energy, 440 Steel into Second Batch and Scrap OTWR on Aluminum and Steel	C40
20	Back Spall Area versus Projectile Energy, 440 Steel into Astrolite on Aluminum	C41
21	Back Spall Area versus Projectile Energy, 440 Steel into RAD 60 HD on Aluminum	C42
22	Front Spall Depth versus Projectile Energy, 440 Steel into First Batch of OTWR on Aluminum and Steel.....	C43
23	Front Spall Depth versus Projectile Energy, 440 Steel into Second Batch of OTWR on Aluminum and Steel	C44
24	Front Spall Depth versus Projectile Energy, 440 Steel into RAD 60 HD and Astrolite on Aluminum and Steel	C45
25	Back Spall Depth versus Projectile Energy, 440 Steel into OTWR on Aluminum and Steel	C46
26	Back Spall Depth versus Projectile Energy, 440 Steel into RAD 60 HD and Astrolite on Aluminum and Steel	C47
27	Characteristic Low Velocity Perforation of a Composite Target.....	C49
28	Condition 2 Fracture	C50
29	Condition 3 Fracture	C51
30	Condition 3a Fracture	C52
31	Condition 4 Damage Mode	C53
32	Condition 5 Damage Mode	C54
33	Condition 6 Damage Mode with Aluminum Backup	C55

SECRET

ILLUSTRATIONS (Cont'd)

Figure 34	Condition 6 Damage Mode with Steel Backup	C57
35	Backup Deformation Parameters	C58
36	Thickness Strain versus E/t_h^3 for OTWR on Aluminum	C59
37	Bulge Height versus Radial Distance and Impact Energy (1/2-in. OTWR on 1/4-in. Aluminum (2024-T3)	C61
38	Bulge Height versus Radial Distance and Impact Energy (1-in. HITCO OTWR on 1/4-in. Aluminum (2024-T3)	C62
39	Bulge Height versus Radial Distance and Impact Energy (1-1/2 in. OTWR on 1/4-in. Aluminum (2024-T3)	C63
40	Bulge Height versus Radial Distance and Impact Energy (1-1/2-in. OTWR on 3/8-in. Aluminum (2024-T3)	C64
41	Bulge Height versus Radial Distance and Impact Energy for 1/4-in. Steel Backups	C65
42	Bulge Height at $r = 0$ versus Impact Energy	C66
43	Mechanisms of Perforation	C67
44	One-Dimensional Interaction of Shock with Heat Shield Backup Interface after Reflection	C69
45	Pressure versus Particle Velocity Curves	C69
46	Total Target Thickness versus Perforation Energy	C75
47	Correlation of Perforation Parameter A with Effective Density Times Strength	C77
48	Plot Of Perforation Efficiency versus Target Effective Strength Times Density Parameter for Steel Projectile on Composite Targets	C78
49	Effect of Projectile on Perforation Energy for Steel Projectiles on Composite Targets	C79
50	Normalized Number Density versus Solid Angle (aluminum cases) ..	C82

SECRET

SECRET

ILLUSTRATIONS (Concl'd)

Figure 51	Normalized Number Density versus Solid Angle (steel cases)	C83
52	Normalized Number Density versus Solid Angle (total cases)	C84
53	Normalized Mass Density versus Solid Angle (aluminum cases)	C85
54	Normalized Mass Density versus Solid Angle (steel cases)	C86
55	Normalized Mass Density versus Solid Angle (total cases)	C87

SECRET

SECRET

TABLES

Table	1	Static Room Temperature Properties of Materials Used in ARPA 149 Program.....	C15
	2	Evaluation of Empirical Constant in the Effective-Inside Hole Diameter versus Energy Relationship ($d_I = a E^{2/3}$).....	C30
	3	Evaluation of Constants in Equation (2).....	C31
	4	Evaluation of Empirical Constant in the Effective Front Spall Diameter versus Energy Relationship ($d_f = KE^{1/2}$).....	C37
	5	Evaluation of Empirical Constant in the Effective Back Spall Diameter versus Energy Relationship ($d_b = KE^{1/2}$).....	C38
	6	Average Ratio of Spall Depths to Heat Shield Thickness.....	C38
	7	Impact Data for First Batch, HITCO OTWR on Aluminum....	C92
	8	Impact Data for First Batch of HITCO OTWR on Steel.....	C93
	9	Impact Data for Second Batch of HITCO OTWR.....	C94
	10	Impact Data on Scrap OTWR.....	C95
	11	Impact Data Astrolite on Aluminum and Steel.....	C96
	12	Impact Data, RAD 60 HD on 6061T6 AL.....	C98
	13	Shot No. 195.....	C100
	14	Shot No. 197.....	C101
	15	Shot No. 199.....	C102
	16	Shot No. 201.....	C103
	17	Shot No. 204.....	C104
	18	Shot No. 206.....	C105
	19	Shot No. 209.....	C106
	20	Shot No. 200.....	C107

SECRET

SYMBOLS

A	Area, cm^2
A_b	Back spall area, cm^2
d	Projectile diameter, cm
E	Projectile energy, joules
H_h	Heat shield ultimate compressive strength, dynes/cm^2
H_b	Backup ultimate tensile strength, dynes/cm^2
P	Pressure
p	Depth
p_b	Back spall depth
t	Thickness, cm
T	Total target thickness, cm
u	Particle velocity
U	Shock velocity
U'	Reflected shock velocity
ρ	Density, gm/cc
ϵ	Thickness strain, dimensionless
h	Bulge height, cm
r	Radial distance from center of impact, cm

Subscripts

b	Backup
f	Front spall
bs	Shocked backup

SECRET

SYMBOLS (Concl'd)

h	Heat shield
hs	Shocked heat shield
I	Inside
i	Interface
o	Original

C10

SECRET

SECRET

SUMMARY

This report presents the results of a study to determine the minimum impact conditions required to perforate a composite target consisting of a plate of ablative material bonded to a metallic backup structure. The heat shield materials consisted of Astrolite, Oblique Tape Wound Refrasil (OTWR) and RAD 60 HD, varying in thickness between 1/2 and 1-1/2 inch, and the backup materials consisted of aluminum and steel plates of thicknesses 1/4 and 3/8 inch. The Avco RAD light gas gun was used to launch steel projectiles varying in mass between 1/4 and 5 grams up to velocities of 5.5 km/sec.

Correlations are presented which allow a detailed description of the damage in the heat shield. The minimum perforation condition is defined as a bulge of the backup structure containing a fracture either partly or completely through the backup thickness. The results are correlated in terms of the projectile energy, target thickness, and an effective target strength times density factor weighted for thickness. The correlation allows a determination of the minimum perforation energy to within 20 percent.

C11

SECRET

SECRET

(NOT USED)

C12

SECRET

I. IMPACT DAMAGE PHASE

A. OBJECTIVES

The primary objectives of this study were to establish scaling laws required to predict the impact parameters needed to perforate ablative heat shield structures as a function of heat shield material, heat shield thickness, and backup structure thickness and material. A secondary objective was to determine the mass, velocity, and material distribution of fragments coming off the backface of a perforated target.

B. EXPERIMENTAL PROCEDURE

Figure 1 is a sketch of the firing arrangement. The light-gas gun using 0.22-, 0.28-, 0.31- and 0.60- caliber barrels, was used to launch 440 steel projectiles varying in mass between 0.250 and 5.00 grams at velocities which varied between 3 and 5.5 km/sec. The operation of the Avco RAD light-gas gun has been described in a previous paper.¹ Projectile velocity and integrity were obtained in flight using a pair of Kerr cell shadowgraph stations in conjunction with a 10-mc chronograph. This technique also has been described previously.² The accuracy of velocity determination is better than 1 percent. A pair of grids positioned down range from the shadowgraph stations were used in some cases as a backup velocity-measuring system. The targets were C-clamped on four corners to a portable rig which was stationed beyond the range, varying in distance from 1 to 12 inches from the end of the range. The C-clamping took place on the backup structure material and not the heat shield material, since the latter case seriously affected the results. All impacts were made under normal atmospheric conditions with the projectile trajectory being normal to the target surface.

The targets consisted of a 1-foot-square flat plate of ablative heat shield material varying in thickness between 1.27 cm (0.50 inch) and approximately 3.81 cm (1.5 inch). The ablative materials consisted of oblique tape-wound refrasil which is a high-purity silica tape refrasil wound in planes oriented at an angle of 22 degrees to the plate surface and impregnated in a phenolic resin. Other materials tested include Astrolite, also consisting of refrasil fibers wound in tape planes which are parallel to the target surface and impregnated in a phenolic resin and RAD 60 HD, which is an epoxy-novalic resin filled with silica resin and powder.

The backup structure materials consisted of a 16-inch square plate of aluminum (2024T3 and 6061T6) and steel (annealed 4140) having thicknesses of 0.635 cm (1/4 inch) and 0.953 cm (3/8 inch). These plates were bonded to the heat shield material with epoxy 5403. The bonding was checked ultrasonically to avoid the use of defective targets. Some of the mechanical properties of the target materials were measured at the physical testing laboratory at Avco RAD and are presented in table 1.

SECRET

From three to six impacts per target configuration were made to determine the minimum perforation conditions. The targets were analyzed after impact for degree of debonding, hole size data in the heat shield and backup structure when applicable, and backup structure deformation, fracture and spallation. The results are described in the following sections.

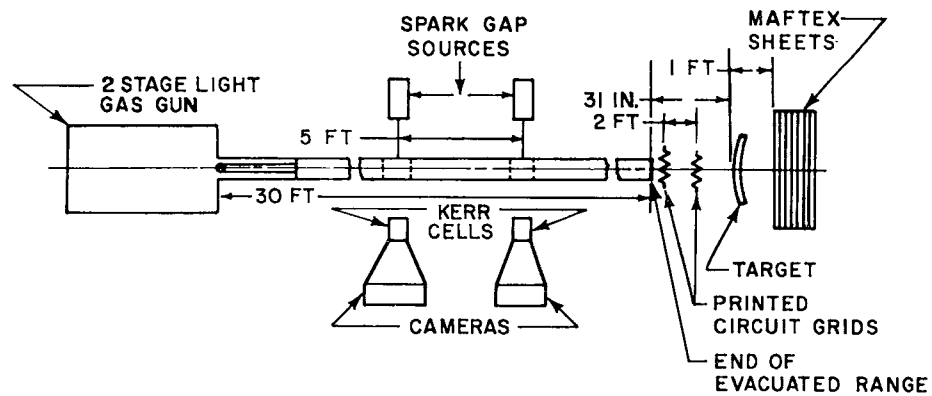


Figure 1 FIRING ARRANGEMENT USED IN THE ARPA 149 PROGRAM
62-3767

C14

SECRET

SECRET

TABLE I
STATIC ROOM TEMPERATURE PROPERTIES OF MATERIALS USED IN ARPA 149 PROGRAM

Material	Density (gm/cc)	Ultimate Tensile Strength (psi x 10 ⁻³)	Tensile Yield Strength (psi x 10 ⁻³) 0.2 percent offset	Ultimate Compressive Strength (psi x 10 ⁻³)	Modulus of Elasticity	
					Tensile (psi x 10 ⁻⁶)	Compressive (psi x 10 ⁻⁶)
GFR	1.55	Parallel to plate surface in direction of tapes - 6,684 Parallel to plate surface - 2,579 in direction of impact - 1,226	5,378 2,275 1,203	13,675 13,125 25,610	1,69 1,41 1,11	1,65 1,01 0,76
Astrolite	1.69	Parallel to plate surface in direction of warp - 16,300 Parallel to plate surface in direction of filling - 13,800 Direction of impact - 1,080	- - - -	26,400 25,000 51,200 16,000	2,31 2,09 - 1,61	2,21 2,12 1,50 1,42
AD 60 HD	1.45	Perpendicular to target surface, (direction of impact) - 3,580 Parallel to target surface - 4,500	- -	16,000 16,000	1,71	1,29
AL (2024 T3)	2.78	70	47,950	-	10,6	-
AL (6061 T6)	2.78	45	38	-	10,3	-
Steel (annealed 4140)	7.83	91	47	-	30,3	-
Steel (440C) ^a	7.75	285	275	-	29.0	-

^aMaterials in Design Engineering, November 1960.

SECRET

C. RESULTS

Figures 2 through 4 are representative photographs of OTWR, Astrolite and RAD 60 HD specimens after impact. The damage in the heat shield when target perforation occurs generally consisted of an inner hole surrounded above and below by a region of delaminated or spalled material extending from the inside hole to the top and bottom surfaces of the target. The backup structure damage generally consisted of either a bulge, or a bulge containing fractures, or a hole surrounded by a region of spallation of pedalling. The backup damage will be developed more fully later in the report.

Asymmetry in the puncture profile in OTWR targets arises from the interaction of the incident stress wave at the oblique refrasil tape plane boundaries. Spalling occurs when the stress wave travels nearly normal to the tape planes denoted in figure 5 by the letter N. Delamination occurs quite readily on this side of the crater. When the stress wave is travelling parallel to the tape planes (denoted as P) the spalling phenomena is not evident, and the material fails under the radial compression of the spherical stress wave. Astrolite and RAD 60 HD yield somewhat more symmetrically as shown in figures 3 and 4.

A sketch representing an approximate puncture profile for the three heat shield materials considered is shown in figure 6 along with the parameters which were measured. Spall diameters on the target front surface d_f and back surface d_b , and the inside hole diameter d_I , were obtained by measuring the areas enclosed on both surfaces and assuming circular symmetry, obtaining an effective diameter.

The area measurements were made with a planimeter. The limits of accuracy of the area measurements were $\pm 0.05 \text{ cm}^2$. Each area measurement was taken four times and averaged. The depth gauge was used to measure the spall depths p_f and p_b . The limits of accuracy of the depth measurements was $\pm 0.0001 \text{ cm}$. Heat shield thickness includes the bond thickness and was measured for each target plate with a vernier caliper. The results of all the impacts are presented in appendix 1. The following sections contain a detailed discussion of the results. (See reference 3 for further discussions of these results.)

1. Heat Shield Damage

The inside diameter (d_I) is the diameter of a circle with the same areas as the minimum hole (A_I) in the heat shield as shown in figure 6. Figures 7 through 11 are plots of d_I versus projectile energy. These figures show that d_I increases with increasing projectile energy and is independent of backup thickness (whether the backup is perforated or not) and ball size, since the data

SECRET

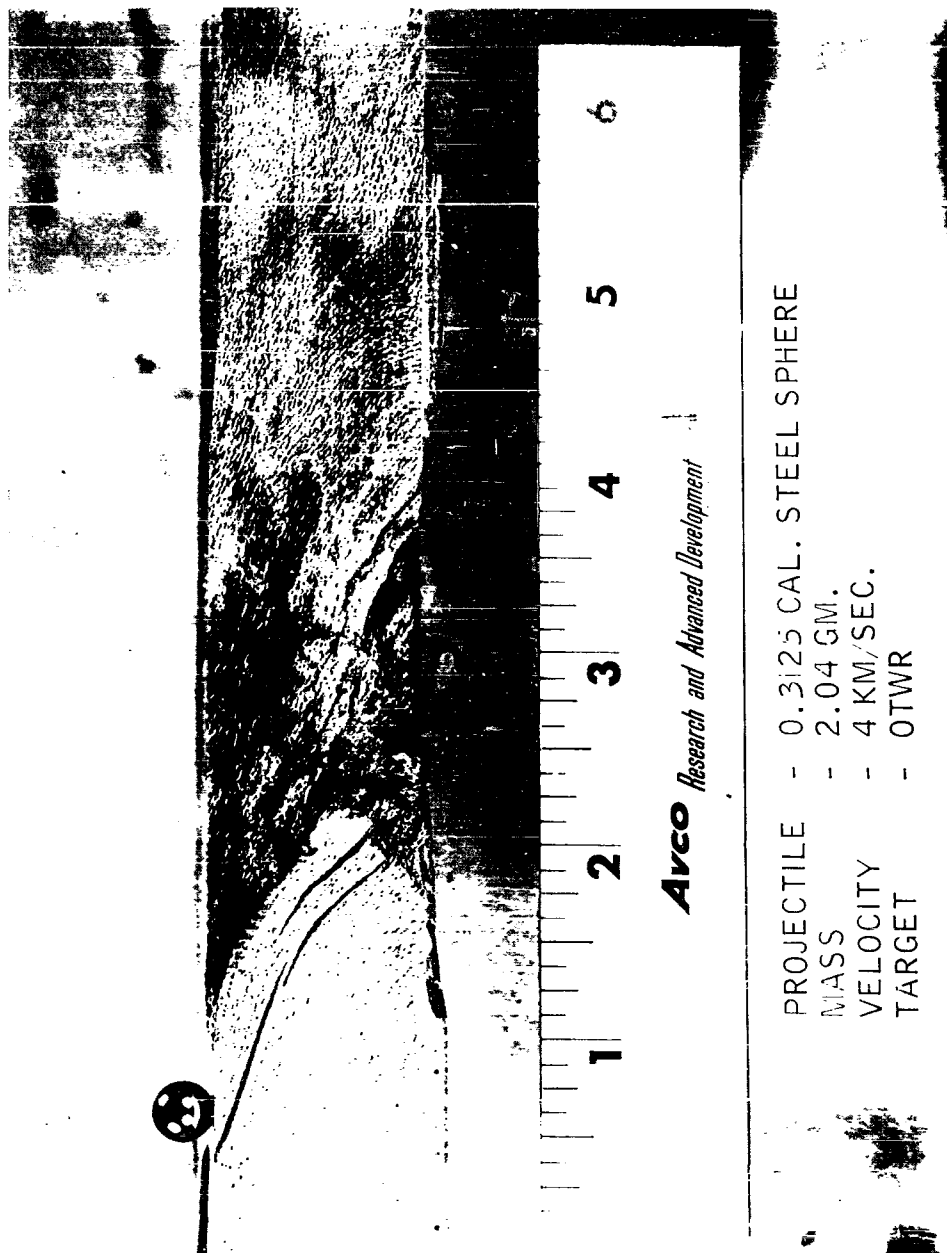
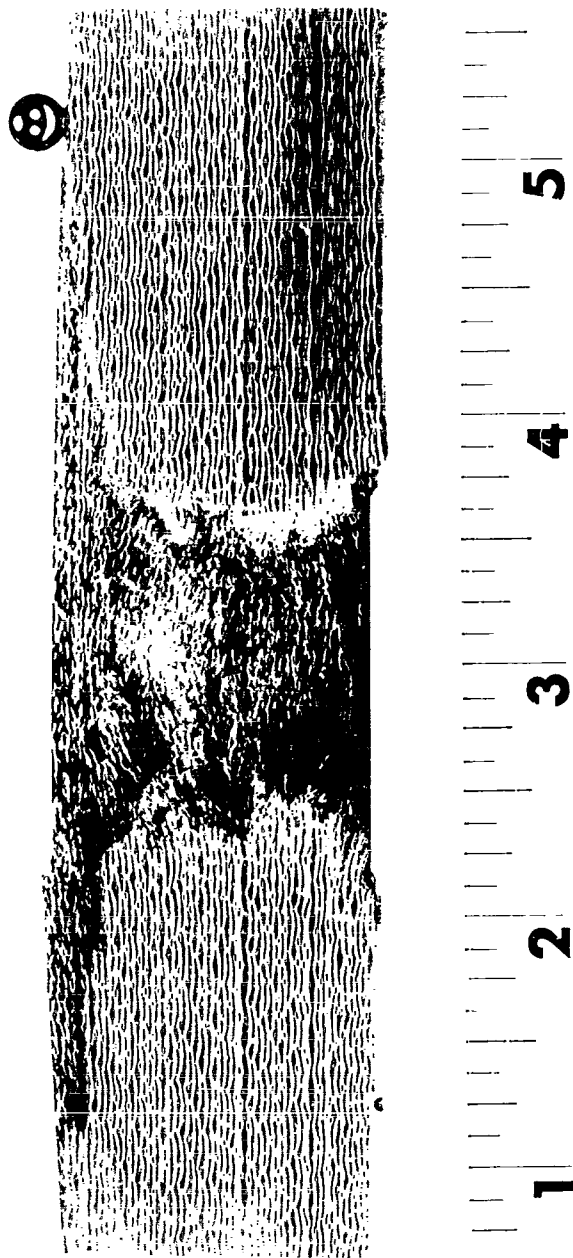


Figure 2 SECTIONED OTWR TARGET AFTER IMPACT
P9338

C17

SECRET

SECRET



Arco *Research and Advanced Development*

PROJECTILE - 0.2215 - CALIBER TUNGSTEN CARBIDE
MASS - 1.382 grams
VELOCITY - 4.9 km/sec
TARGET - ASTROLITE

Figure 3 SECTIONED ASTROLITE TARGET AFTER IMPACT

SECRET

SECRET



C19

SECRET

PROJECTILE - 0.28 - CALIBER STEEL SPHERE
MASS - 1.47 grams
VELOCITY - 4.7 km/sec
TARGET - RAD 60 HD

Figure 4 SECTIONED RAD 60 HD TARGET AFTER IMPACT

SECRET

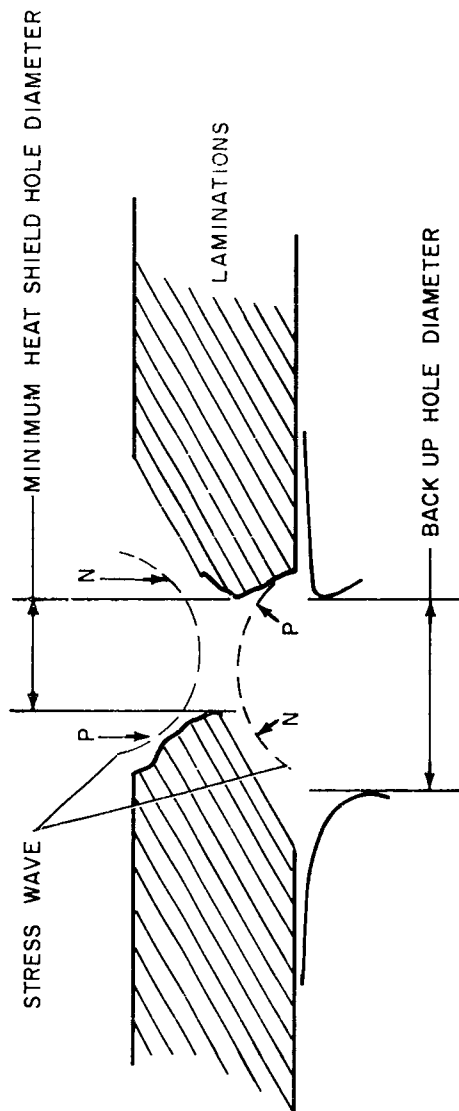


Figure 5 TYPICAL CROSS SECTION OF PERFORATED OTWR TARGET
62-4228

C20

SECRET

SECRET

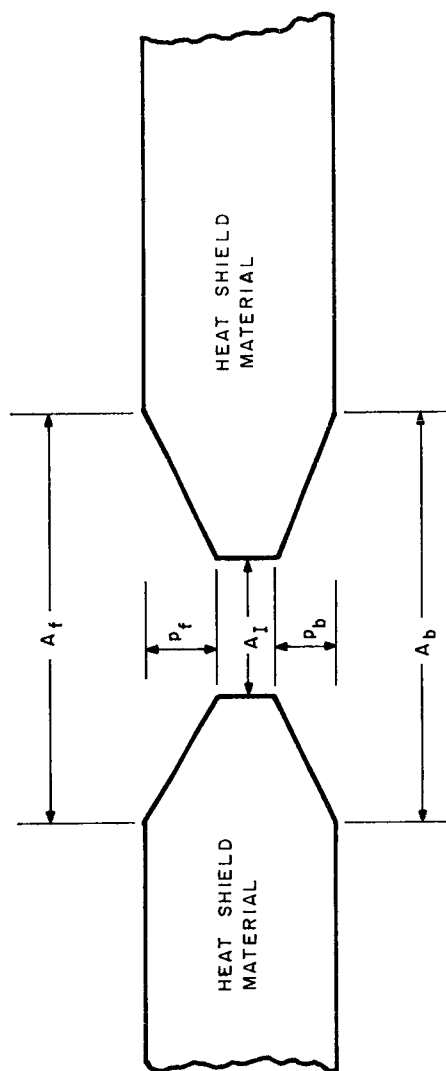


Figure 6 APPROXIMATE PUNCTURE PROFILE SHOWN WITH
MEASURED PARAMETERS

C21

SECRET

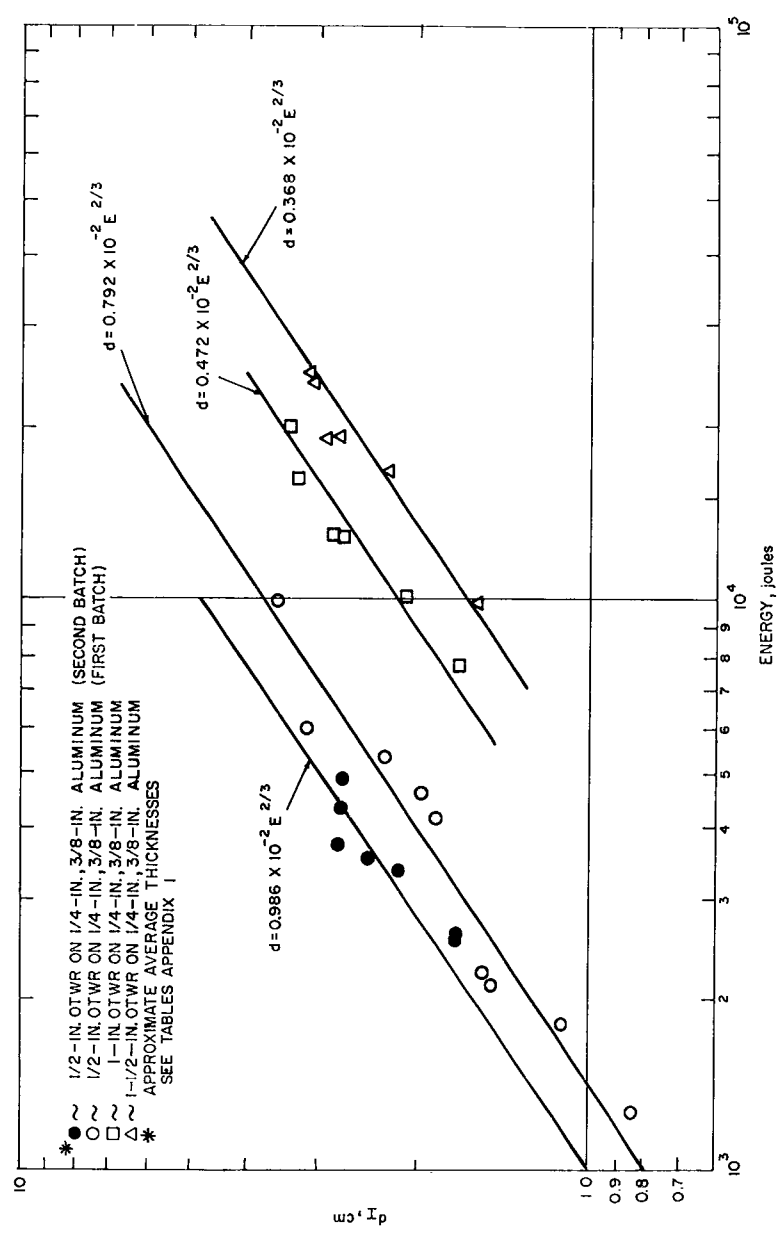


Figure 7 INSIDE DIAMETER VERSUS ENERGY, 440 STEEL ON HITCO OTWR BONDED TO STEEL 63-6260

SECRET

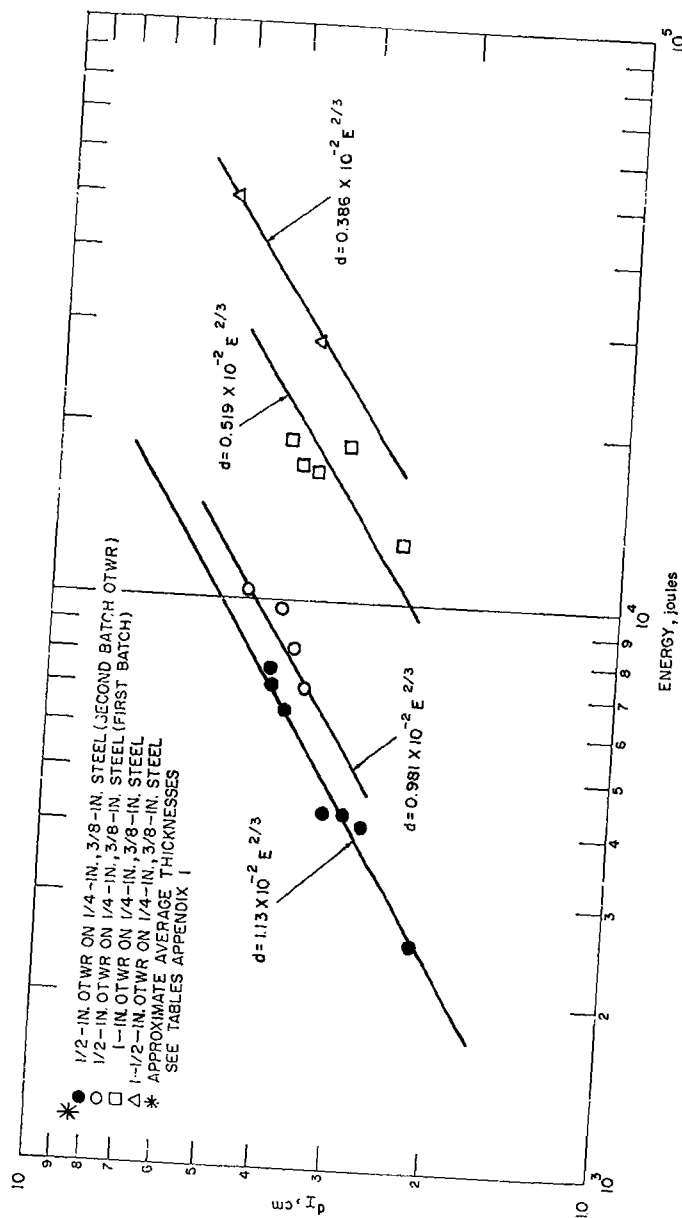


Figure 8 INSIDE DIAMETER VERSUS ENERGY, 440 STEEL ON HITCO OTWR
BONDED TO STEEL
63-6262

C23

SECRET

SECRET

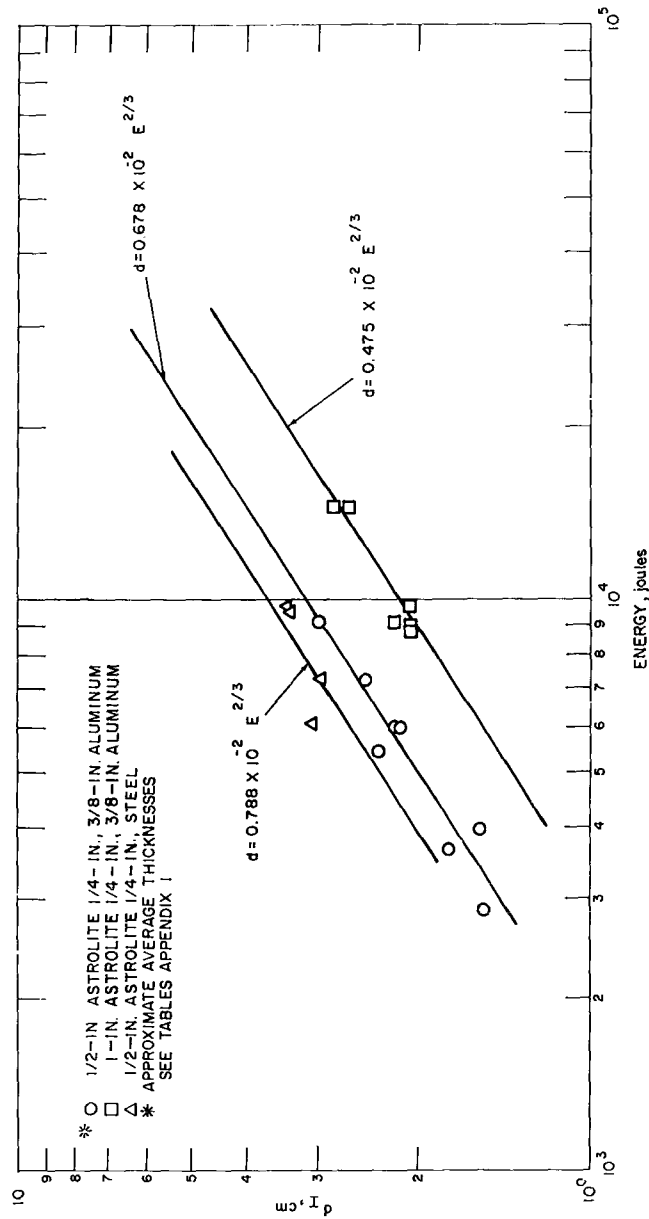


Figure 9 INSIDE DIAMETER VERSUS ENERGY, 440 STEEL PROJECTILES ON
ASTROLITE BONDED TO ALUMINUM AND STEEL
63-6264

SECRET

SECRET

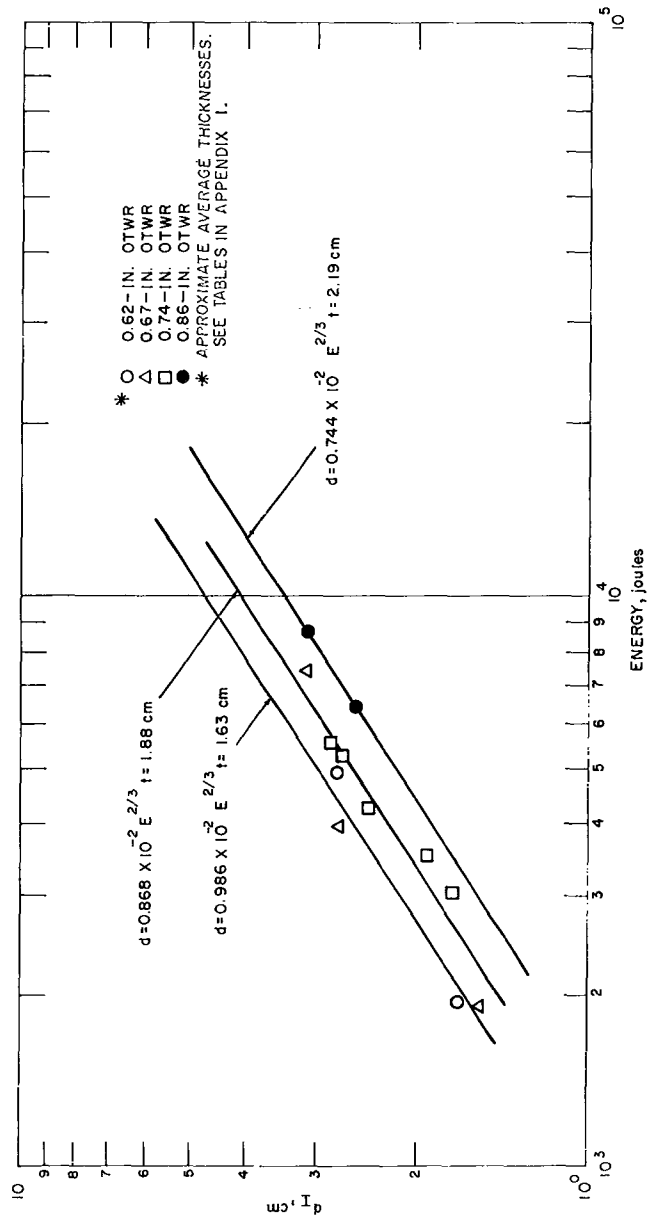


Figure 10 INSIDE DIAMETER VERSUS ENERGY, 440 STEEL PROJECTILE ON SCRAP OTWR BONDED TO 1/8-INCH ALUMINUM
63-6265

C25

SECRET

SECRET

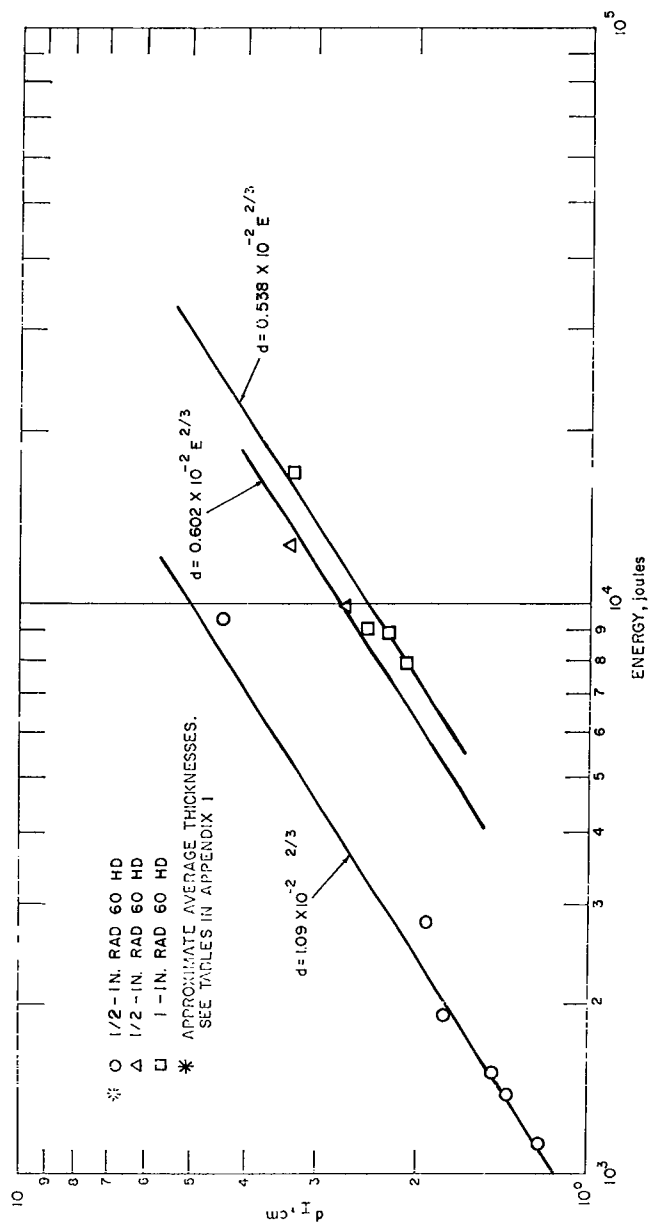


Figure 11 INSIDE DIAMETER VERSUS ENERGY, 440 STEEL PROJECTILE ON
RAD 60 HD BONDED TO ALUMINUM
63-6274

C26

SECRET

SECRET

points represent many variations of these parameters. For a given heat shield material of a given thickness, the relationship between inside hole diameter and projectile energy is of the form, $d_I = aE^{2/3}$ where, a depends on heat shield material, thickness and backup material.

The effect of heat shield material is evident in table 2. There were two shipments of OTWR received from the H. I. Thompson Company (HITCO). The plates in the second shipment were of 1/2-inch thickness. There were differences in the data obtained from the two batches of material that may be attributed to differences in the material. The inside hole sizes for the first batch of OTWR were about 25 percent smaller than the second batch of OTWR over a similar energy range. Scrap OTWR targets used in the study agree with the second batch of OTWR of the same thickness. The properties listed in table 1 refer to the first batch of OTWR.

Examination of table 2 reveals that for a given projectile energy the inside hole size for Astrolite on steel is 15 percent greater than Astrolite on aluminum; for OTWR on steel the holes are 25 percent greater than OTWR on aluminum. This phenomenon may be due to the fact that upon reflection of the target shock from steel the reflected pressures and energies are larger than for reflection from an aluminum backup (see section D. Interpretation of Results). The stronger shock in the case of steel interacts with the crater from cavitation causing a larger hole. Thus, to correlate the hole size data to within better than 25 percent, the shock properties or Hugoniot of the backup and heat shield must be known.

Finally, the effect of heat shield thickness is found by correlating the values of the constant a (see equation (1) in table 2) with heat shield thickness. The con-

stant a represents the average $\langle \frac{d_I}{E^{2/3}} \rangle$ for each heat shield thickness.

There are between 2 and 10 data points for each value of a . Plots of a versus heat shield thickness are shown in figures 12 and 13. The correlation which best fits the data is of the form,

$$d_I = a \frac{E^{2/3}}{t_h^n} \quad (2)$$

Since the deviation in a versus t_h is negligible (see figures 12 and 13) the values of n were obtained directly from the graphs. The values of a and n along with the standard deviation are presented in table 3.

SECRET

SECRET

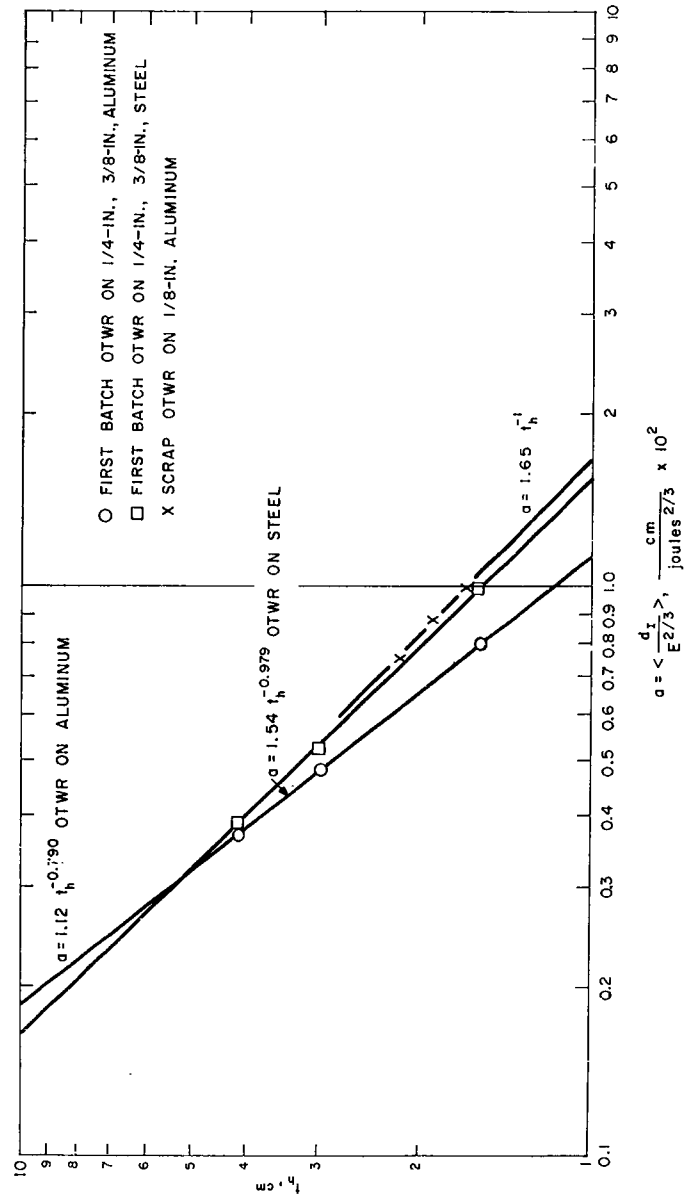


Figure 12 CORRELATION OF CONSTANT, a , WITH HEAT SHIELD THICKNESS
FOR OTWR
63-6258

SECRET

SECRET

C29

SECRET

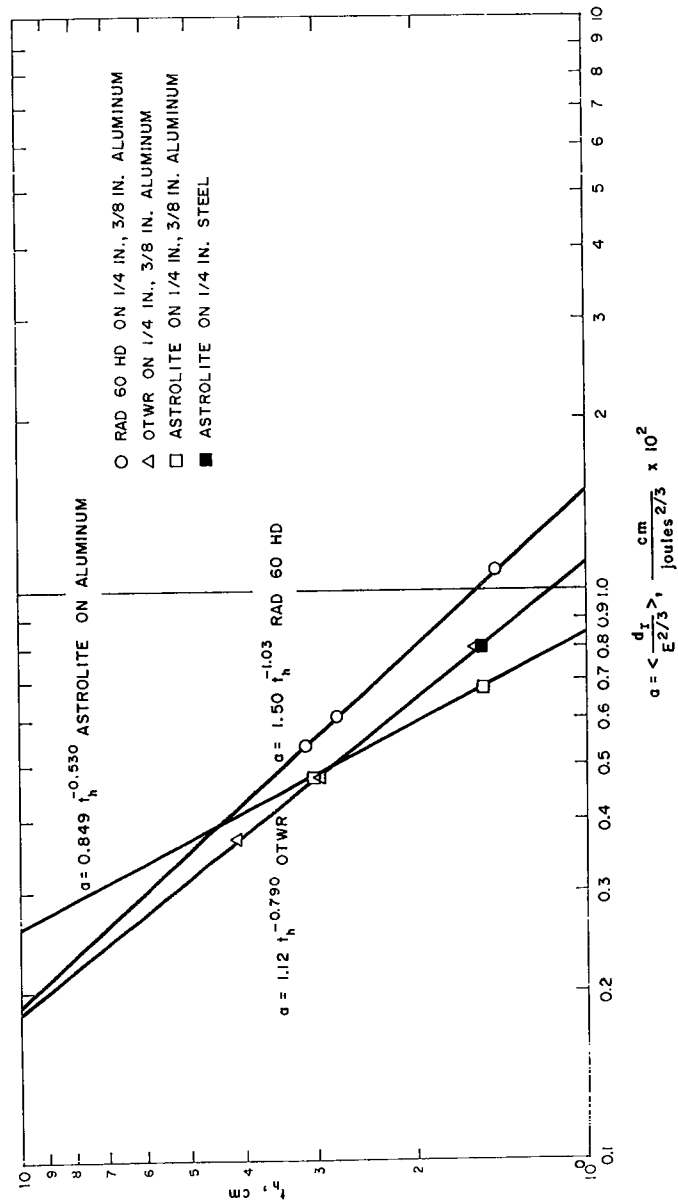


Figure 13 CORRELATION OF CONSTANT, a , WITH HEAT SHIELD THICKNESS
FOR ALL HEAT SHIELD MATERIALS
63-6252

SECRET

TABLE 2

EVALUATION OF EMPIRICAL CONSTANT IN THE EFFECTIVE INSIDE HOLE
DIAMETER VERSUS ENERGY RELATIONSHIP

$$d_1 = aE^{2/3} \quad (1)$$

Backup Material	Heat Shield Material	$a, \left(\frac{\text{cm} \times 10^2}{\text{joules}^{2/3}} \right)$	Number of Data Points	σ (percent)	Heat Shield Material Thickness (cm)	Projectile Material
AL (6061 T6)	RAD 60 HD	1.09	6	6	1.44	steel
		0.602	2	-	2.79	steel
		0.538	4	-	3.15	steel
AL (2024 T3)	Astrolite	0.678	7	10	1.52	steel
		0.475	6	3	3.043	steel
		0.310	3	-	3.048	tungsten carbide
		0.785	10	4	1.52	steel
Steel (4140)	scrap	0.986	5	6	1.60	steel
	OTWR	0.868	5	6	1.89	steel
		0.744	2	-	2.19	steel
Steel (4140)	OTWR (first batch)	0.981	5	5	1.60	steel
		0.519	5	10	3.00	steel
		0.386	2	-	4.17	steel
		1.13	7	5	1.54	steel
AL (2024 T3)	OTWR (first batch)	0.792	10	10	1.56	steel
		0.472	6	0.6	2.98	steel
		0.368	6	0.4	4.15	steel
		0.986	7	14	1.55	steel

C30

SECRET

SECRET

TABLE 3
EVALUATION OF CONSTANTS IN EQUATION (2)

Target	$a, \left(\frac{\text{cm}^n}{\text{joules}^{2/3}} \right)$	n	σ (percent)
Astrolite on Aluminum (2024T3)	0.849×10^{-2}	0.530	8
OTWR on Aluminum (2024T3)	1.12×10^{-2}	0.790	5
OTWR on Steel (4140)	1.54×10^{-2}	0.979	3
RAD 60 HD on Aluminum (6061T6)	1.50×10^{-2}	1.03	6
*Scrap OTWR on Aluminum (6061T6)	1.65×10^{-2}	1.00	6

*Properties of OTWR are unknown.

A force fit of the form

$$d_f = b \left(\frac{E}{t_{hs}} \right)^n \quad (3)$$

was tried on the data, but introduced larger deviations (from 10 to 15 percent), so for the sake of accuracy, the results are left in form given by equation (2).

An attempt was made to relate the variation of a and n with target material static properties, but the effort proved fruitless. Thus the inside hole diameters are consistent to within 8 percent when correlated by expression (2).

Although the scrap OTWR on aluminum data were consistent within themselves, they differ from the known data of the standard or known OTWR on aluminum. The properties of the scrap OTWR were unknown and thus a complete understanding of the differences in the results is not understood.

The front spall area A_f is the area on the front surface of the heat shield which is blown off the target by the impact. Figures 14 through 17 are plots of the enclosed front spall area measured with the planimeter as a function of projectile energy. For a given heat shield thickness, the spall area increases with energy. Also, the spall area is independent of backup structure material and thickness. There was considerable difference in the measured spall areas between 1/2- and 1-inch thick heat shields at a given energy, as can be

C31

SECRET

SECRET

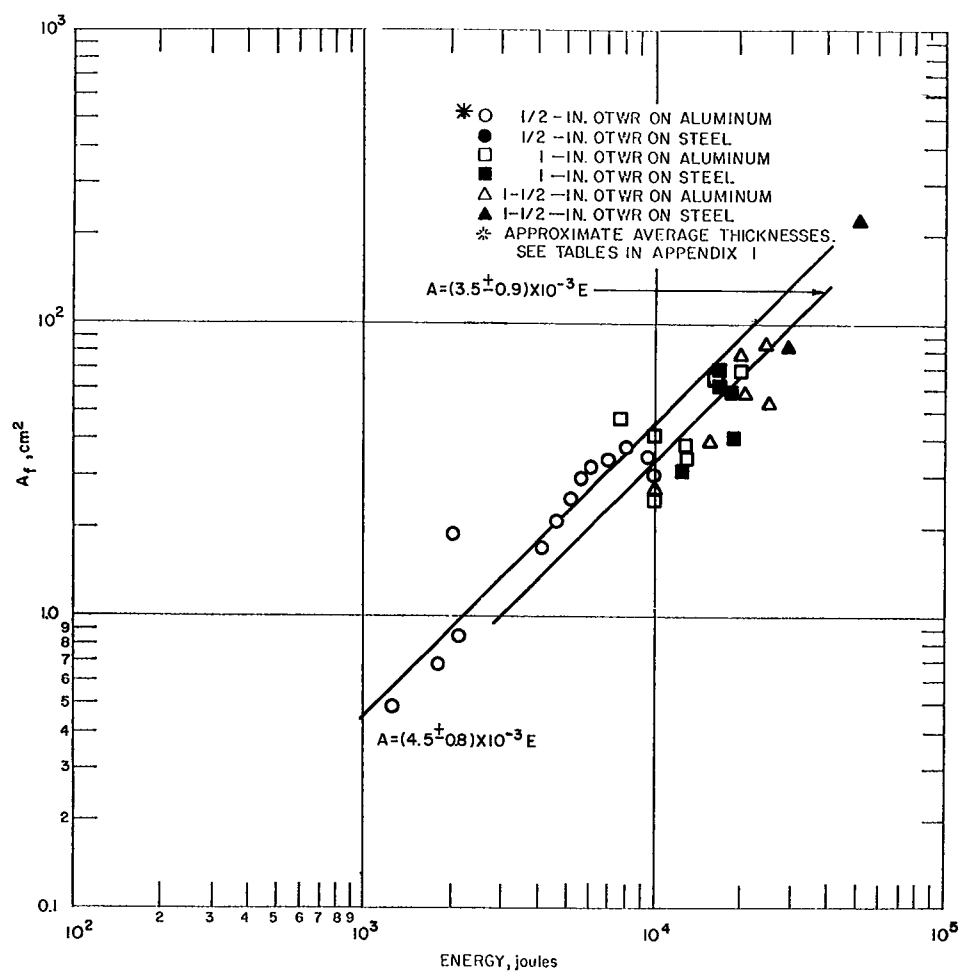


Figure 14 FRONT SPALL AREA VERSUS PROJECTILE ENERGY, 440 STEEL.
INTO FIRST BATCH OF OTWR ON ALUMINUM AND STEEL
63-6264

C32

SECRET

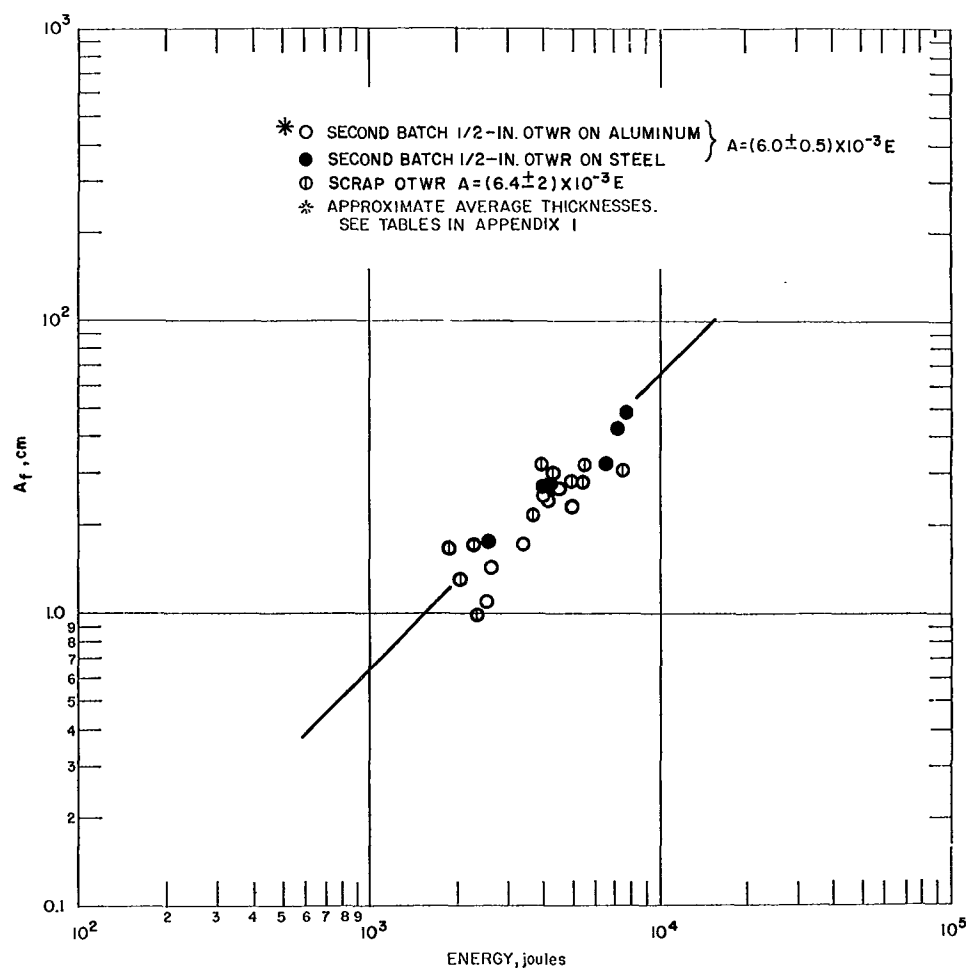


Figure 15 FRONT SPALL AREA VERSUS PROJECTILE ENERGY, 440 STEEL
INTO OTWR ON ALUMINUM
63-6255

SECRET

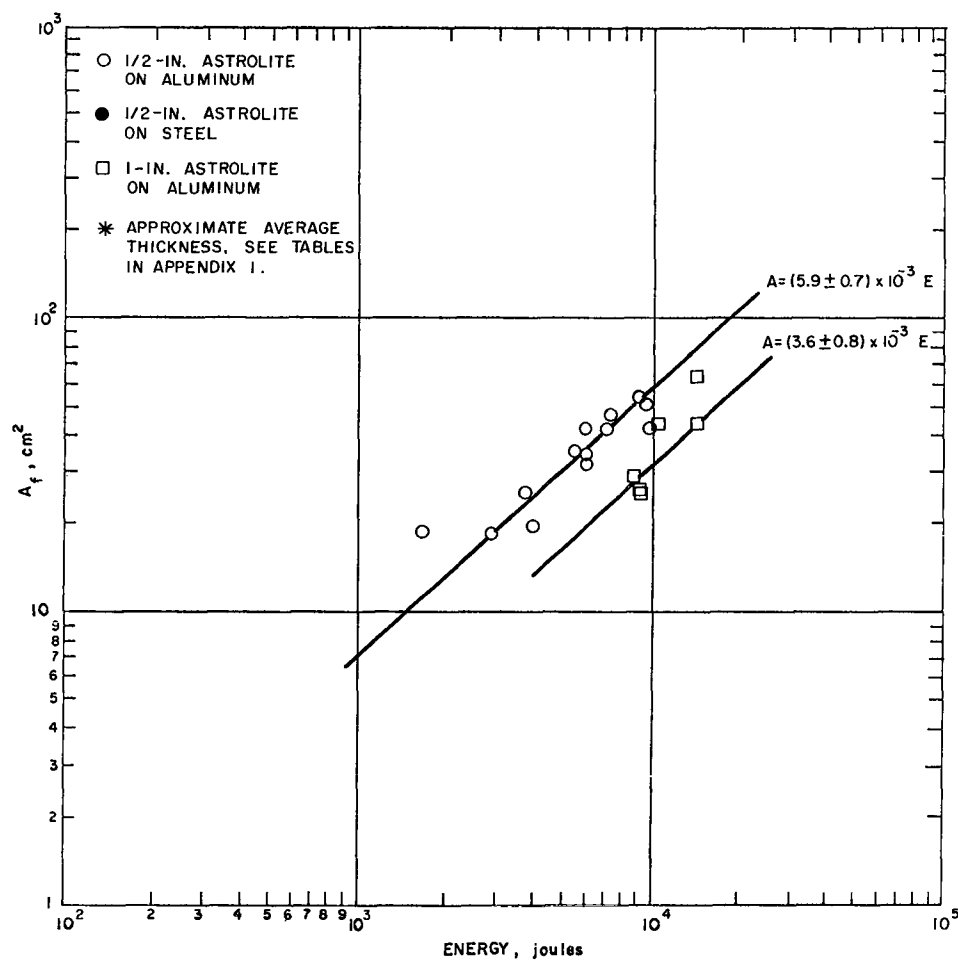


Figure 16 FRONT SPALL AREA VERSUS PROJECTILE ENERGY, 440 STEEL
INTO ASTROLITE ON ALUMINUM AND STEEL
63-6269

C34

SECRET

SECRET

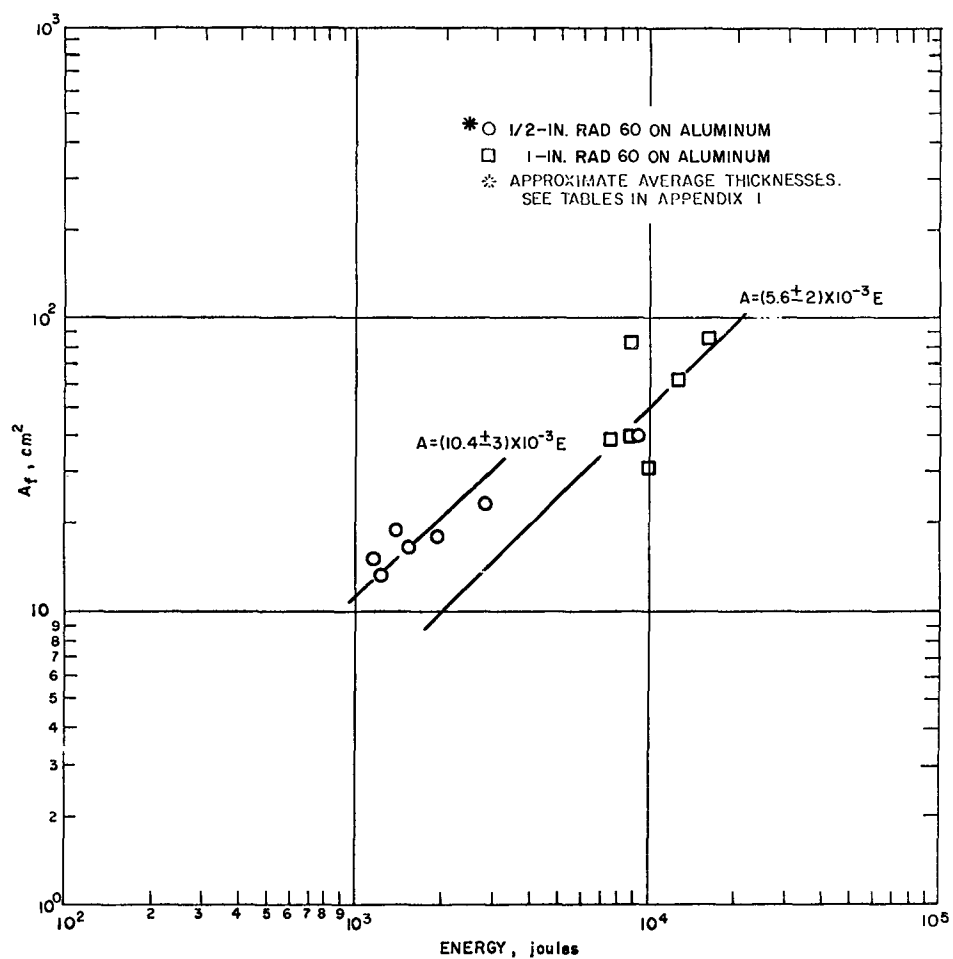


Figure 17 FRONT SPALL AREA VERSUS PROJECTILE ENERGY, 440 STEEL
 INTO RAD 60 HD ON ALUMINUM
 63-6256

C35

SECRET

SECRET

seen from the graphs. For a given energy, the spall area removed from the 1/2-inch thick heat shield is from 1.3 to about 2 times greater than the material removed from the 1-inch target. The thickness effect does not hold for the case of 1- and 1-1/2 inch OTWR on aluminum and steel as can be seen in figure 14. The data obtained on both these thicknesses falls closely together.

Also the differences between both shipments of OTWR can be observed from figures 14 and 15. There is a 30-percent variation in the measured spall areas between the first and second shipments of OTWR.

The best overall fit of front spall is a linear variation with projectile energy. However the statistics are poor since the phenomena is strongly dependent on how the heat shield fractures. For the sake of comparison, table 4 gives the correlation in terms of an equivalent diameter d_f , defined as the diameter having a circle having an equivalent area. From tables 2 and 4 it can be seen that the scatter in d_f is about twice as great as the scatter in d_I .

When the backup and heat shield separate, the heat-shield back surface spalls. The enclosed area of spalled heat shield is defined as the back spall area A_b . Figures 18 through 21 are plots of back spall area versus projectile energy. The back spall area is independent of heat shield and backup thickness, and backup material. The heat shield material and impact energy are sufficient to determine back spall area. With the exception of Astrolite, the back spall area was fitted to a linear function of impact energy. An effective diameter d_b similar to that defined previously is introduced, and table 5 presents the empirical correlation.

Finally the distances from the front surface of the heat shield and the bond-backup interface to the neck of the heat shield hole (figure 6) are called the front spall depth (p_f) and back spall depth (p_b) respectively. The spall depth is the average of four measurements taken at different places around the crater. In figures 22 through 26 the results of the front spall depth measurements versus impact energy are presented. No reasonable correlation is possible because of the complicated way in which spall depth varies and the scatter inherent in spall phenomena. However, it can be seen that spall depth depends only on heat shield material and thickness. The high energy shots in 1/2-inch thick heat shields show that back spall depth eventually disappears and the front spall extends the entire heat shield thickness. This fact also comes out of the correlations, since the inside hole diameter increases faster than the effective spall diameter with increasing projectile energy (e. g., $E^{2/3}$ versus $E^{1/2}$). Table 6 is the average spall depth over heat shield thickness ratio for each of the cases studied in this report.

SECRET

SECRET

TABLE 4

EVALUATION OF EMPIRICAL CONSTANT IN THE EFFECTIVE FRONT
SPALL DIAMETER VERSUS ENERGY
RELATIONSHIP

$$d_f = KE^{1/2*} \quad (4)$$

Heat Shield Thickness	K, $\left(\frac{\text{cm}}{\text{joules}^{1/2}} \times 10^2\right)$	Number of Data Points	σ (percent)
<u>First batch OTWR</u>			
1.60 cm	7.57	15	9
3.00 and 4.17 cm	6.67	11	12
<u>Second batch OTWR</u>			
1.54 cm	8.74	14	4.5
<u>Scrap OTWR</u>			
~ 1.80 cm	9.02	11	16
<u>Astrolite</u>			
1.52 cm	8.66	11	6
3.05 cm	6.77	6	11
<u>RAD 60 HD</u>			
1.44	11.5	7	14
~ 3.00	8.44	6	18

* d_f in cm, E in joules

C37

SECRET

SECRET

TABLE 5

EVALUATION OF EMPIRICAL CONSTANT IN THE EFFECTIVE
BACK SPALL DIAMETER VERSUS
ENERGY RELATIONSHIP

$$d_b = KE^{1/2*} \quad (5)$$

Target	$K, \left(\frac{\text{cm}}{\text{joules}^{1/2}} \times 10^2 \right)^*$	Number of Data Points	σ (percent)
<u>First batch</u>			
OTWR on steel and aluminum	4.80	32	14
Astrolite on aluminum	19.90	7	-
RAD 60 HD on aluminum	6.80	11	10
<u>Second batch</u>			
OTWR and scrap on steel and aluminum	5.53	20	8.5

*For Astrolite, $d_b = KE^{1/3}$

TABLE 6

AVERAGE RATIO OF SPALL DEPTHS TO
HEAT SHIELD THICKNESS

Material	t_h^* (inches)	p_f/t_h	p_b/t_h
OTWR	1/2	0.40	0.24
OTWR	1	0.59	0.43
OTWR	1-1/2	0.55	0.29
RAD 60 HD	1/2	0.40	0.28
RAD 60 HD	1	0.40	0.40
Astrolite	1-2**	-	-
	1	0.51	0.43

*Approximate average thickness

**Too much scatter in data

C38

SECRET

SECRET

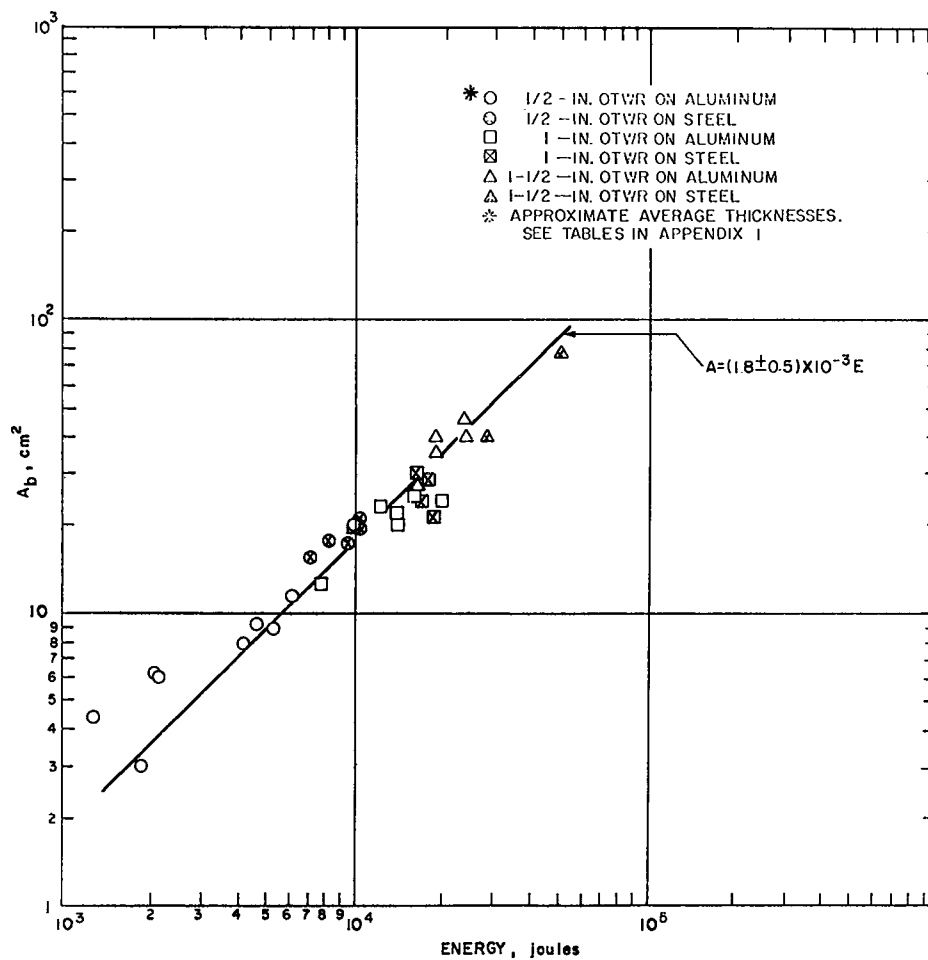


Figure 18 BACK SPALL AREA VERSUS PROJECTILE ENERGY, 440 STEEL INTO FIRST BATCH OTWR ON ALUMINUM AND STEEL
63-6270

C39

SECRET

SECRET

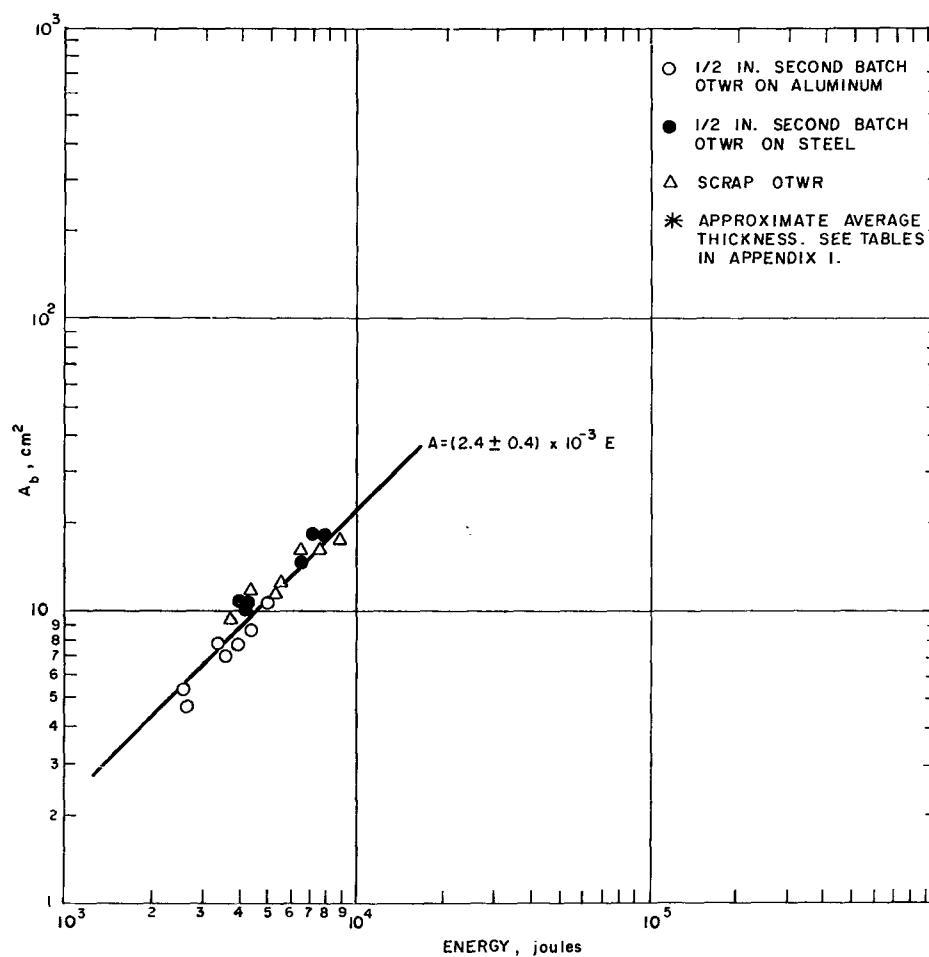


Figure 19 BACK SPALL AREA VERSUS PROJECTILE ENERGY, 440 STEEL INTO SECOND BATCH AND SCRAP OTWR ON ALUMINUM AND STEEL
63-6268

C-40

SECRET

SECRET

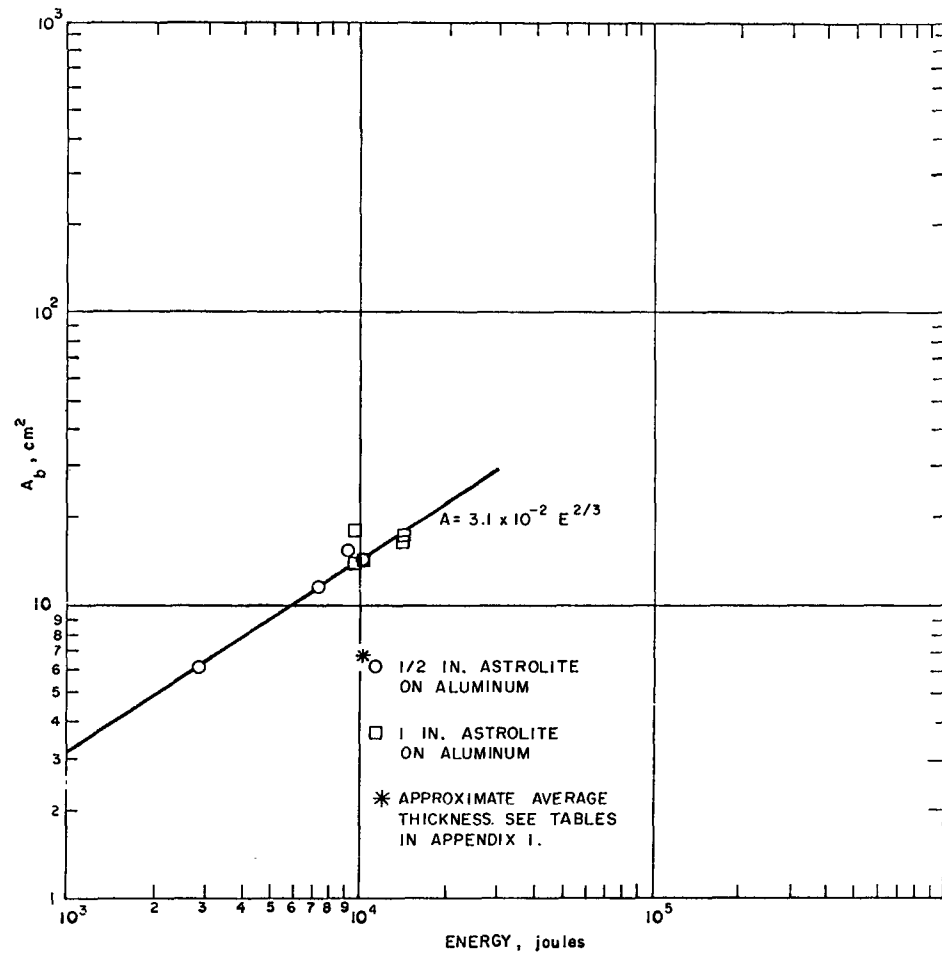


Figure 20 BACK SPALL AREA VERSUS PROJECTILE ENERGY, 440 STEEL
INTO ASTROLITE ON ALUMINUM
63-6261

C41

SECRET

SECRET

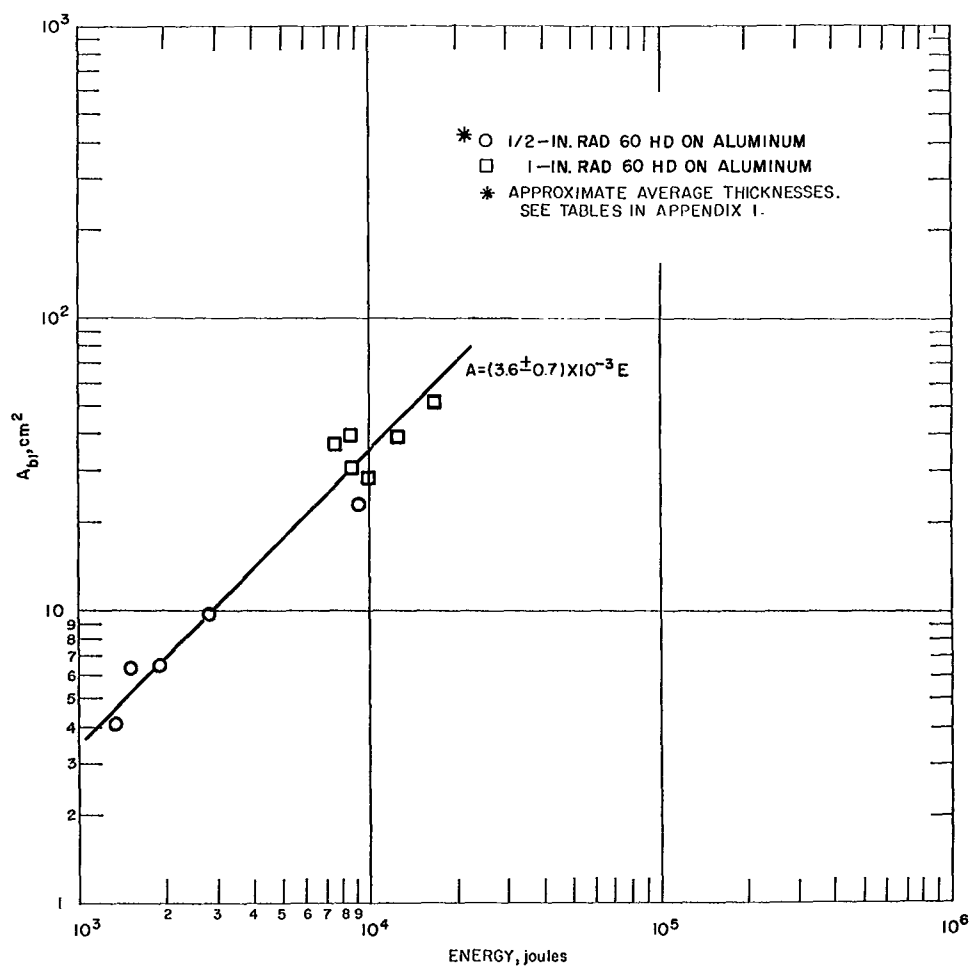


Figure 21 BACK SPALL AREA VERSUS PROJECTILE ENERGY, 440 STEEL
INTO RAD 60 HD ON ALUMINUM
63-6259

C42

SECRET

SECRET

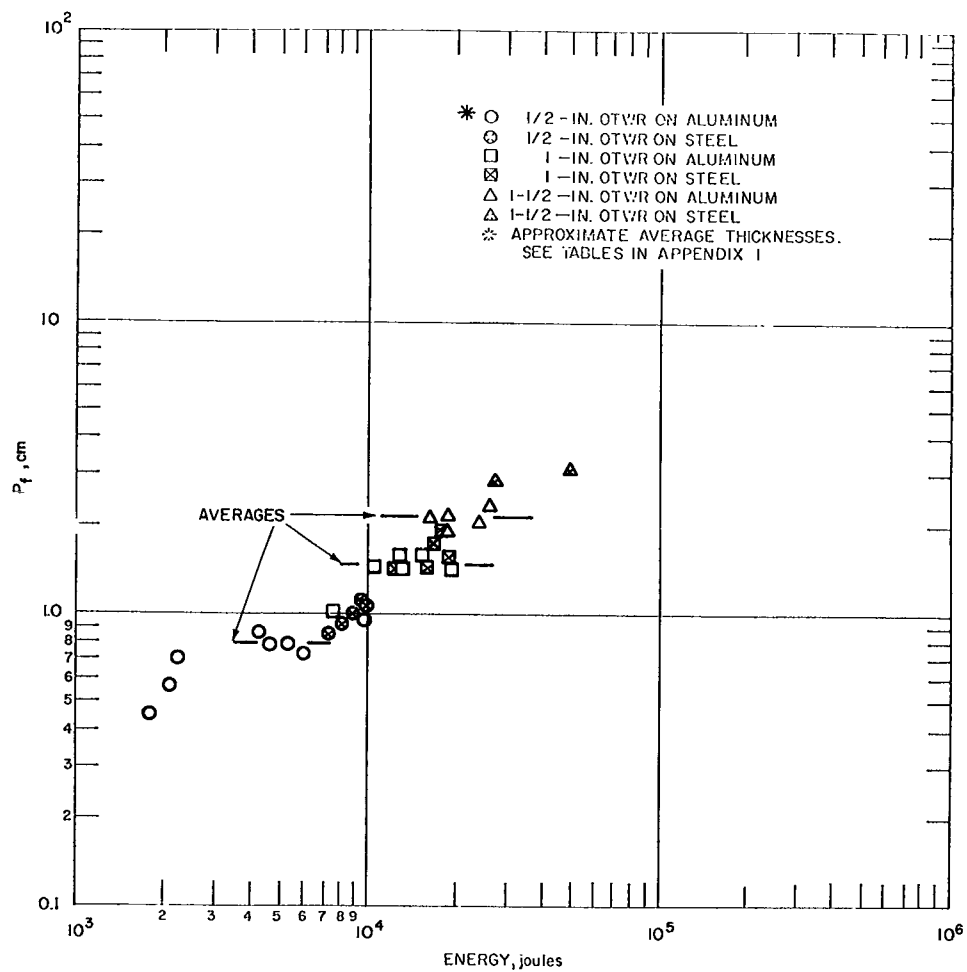


Figure 22 FRONT SPALL DEPTH VERSUS PROJECTILE ENERGY, 440 STEEL INTO FIRST BATCH OF OTWR ON ALUMINUM AND STEEL
63-6273

C43

SECRET

SECRET

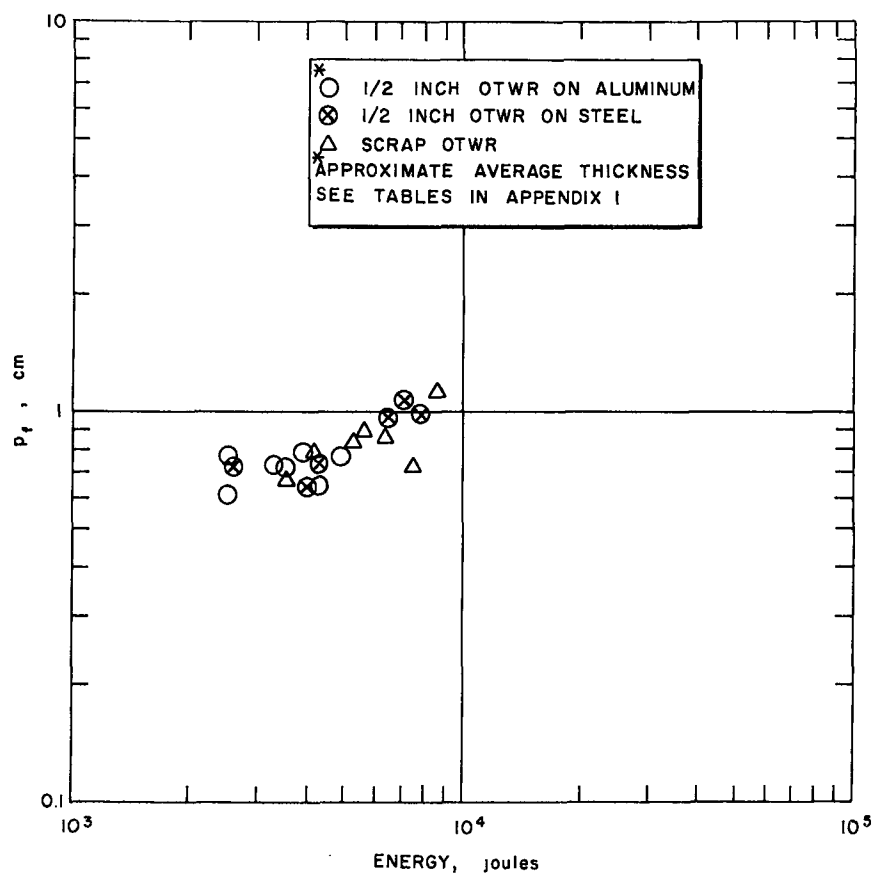


Figure 23 FRONT SPALL DEPTH VERSUS PROJECTILE ENERGY, 440 STEEL
INTO SECOND BATCH OF OTWR ON ALUMINUM AND STEEL
63-6243

C44

SECRET

SECRET

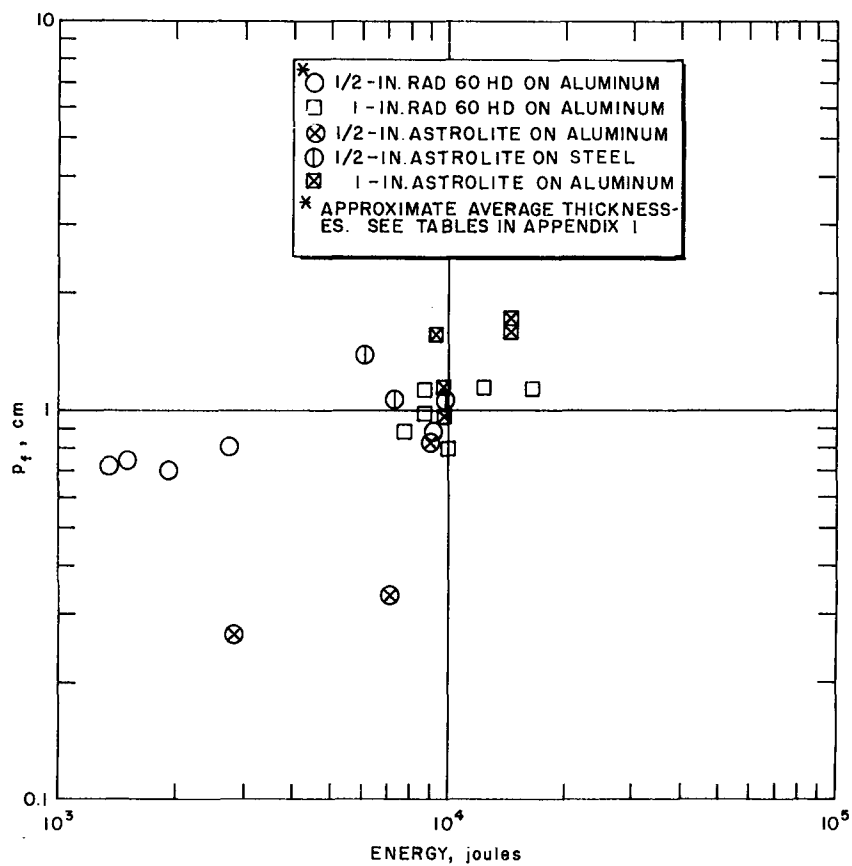


Figure 24 FRONT SPALL DEPTH VERSUS PROJECTILE ENERGY, 440 STEEL
INTO RAD 60 HD AND ASTROLITE ON ALUMINUM AND STEEL
63-6242

C45

SECRET

SECRET

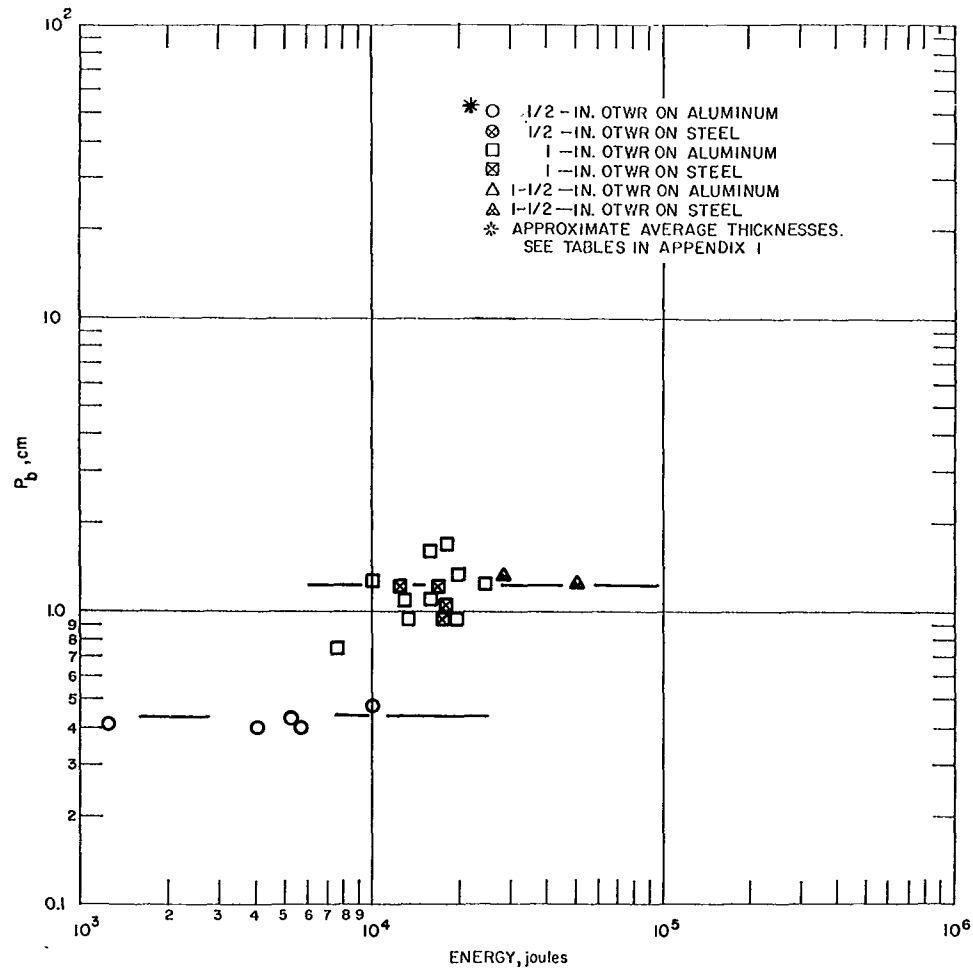


Figure 25 BACK SPALL DEPTH VERSUS PROJECTILE ENERGY, 440 STEEL
INTO OTWR ON ALUMINUM AND STEEL
63-6263

C46

SECRET

SECRET

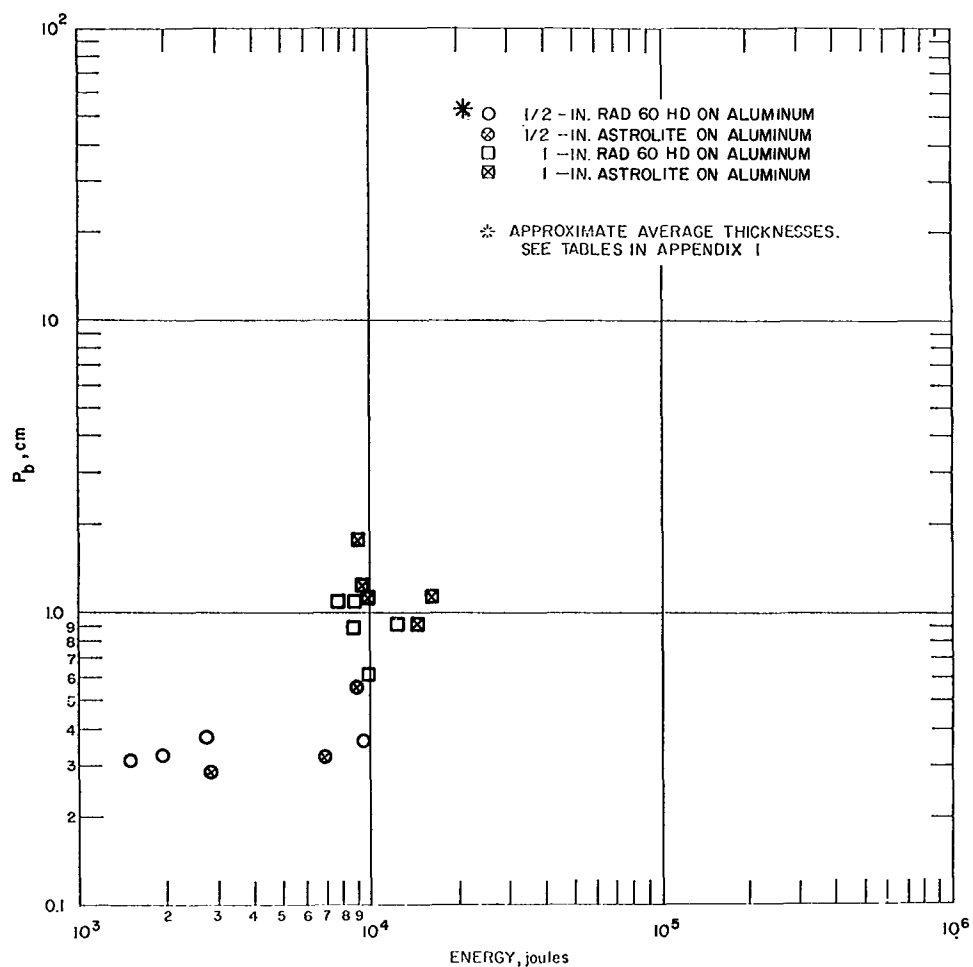


Figure 26 BACK SPALL DEPTH VERSUS PROJECTILE ENERGY, 440 STEEL
INTO RAD 60 HD AND ASTROLITE ON ALUMINUM AND STEEL
63-6272

C47

SECRET

SECRET

In summary, the damage to the heat shield material can be described by the measured parameters shown in the approximate puncture profile sketch in figure 6. Measurements have been made of the inside hole area, front and backface spall area, and front and back spall depths. These measurements have been correlated with the projectile energy, so that for steel projectiles, the damage profile can reasonably be described knowing the projectile energy.

At this point some justification must be given for the correlations presented, since in some cases insufficient data did not warrant a correlation. The characteristic spall areas, both front and back, will affect the aggravation effects, i. e., reentry heating on damage in the heat shield following impact. There is a noticeable lack of data in the literature which attempts to describe quantitatively the boundary effects resulting from particle impact on a finite thickness composite plate. Thus every effort was made to extract some reasonable way of quantitatively predicting the magnitude of the front and back spall areas and depths. It is suggested that all future studies concern themselves with measurements of this type to build up the knowledge and data in this area.

2. Backup Structure Damage

The backup structure materials consisted of aluminum (6061T6 and 2024T3) and steel (annealed 4140) varying in thickness between 1/8 and 3/8 inch. Several broad classifications of damage were observed which depended on projectile size and velocity and backup structure material and thickness. Figures 27 through 33 are representative photographs of the different types of damage observed, beginning with low-velocity perforation, where the projectile remains intact following perforation, to a high-velocity puncture, where the projectile is broken up and the result is an enlarged hole. Figure 27 is a photograph of a 1/4-inch aluminum (2024T3) backup which was bonded to a 1/2-inch Astrolite plate after impact with a 0.22-caliber steel sphere at a velocity of 2.2 km/sec. The projectile perforated the target intact and was recovered following its exit.

The backup hole is observed to be about the size of the projectile, which is characteristic of this type perforation. It was determined experimentally that projectile breakup for this combination of projectile and target took place between 2 and 3 km/sec. All perforation data to be discussed have been obtained in the velocity regime where the projectile breaks up on impact.

At low velocities the minimum-type damage observed was a bulge in the backup structure. The height of the bulge increases with increasing projectile velocity and size and decreasing target thickness. As one continues up the projectile-energy scale, the next type of damage observed is a fracture in the backup which generally does not extend through the backup structure thickness (see figure 28). This will be referred to as condition 2. This mode of damage occurred with all backup structure materials and thicknesses. Conditions 3

C48

SECRET

SECRET

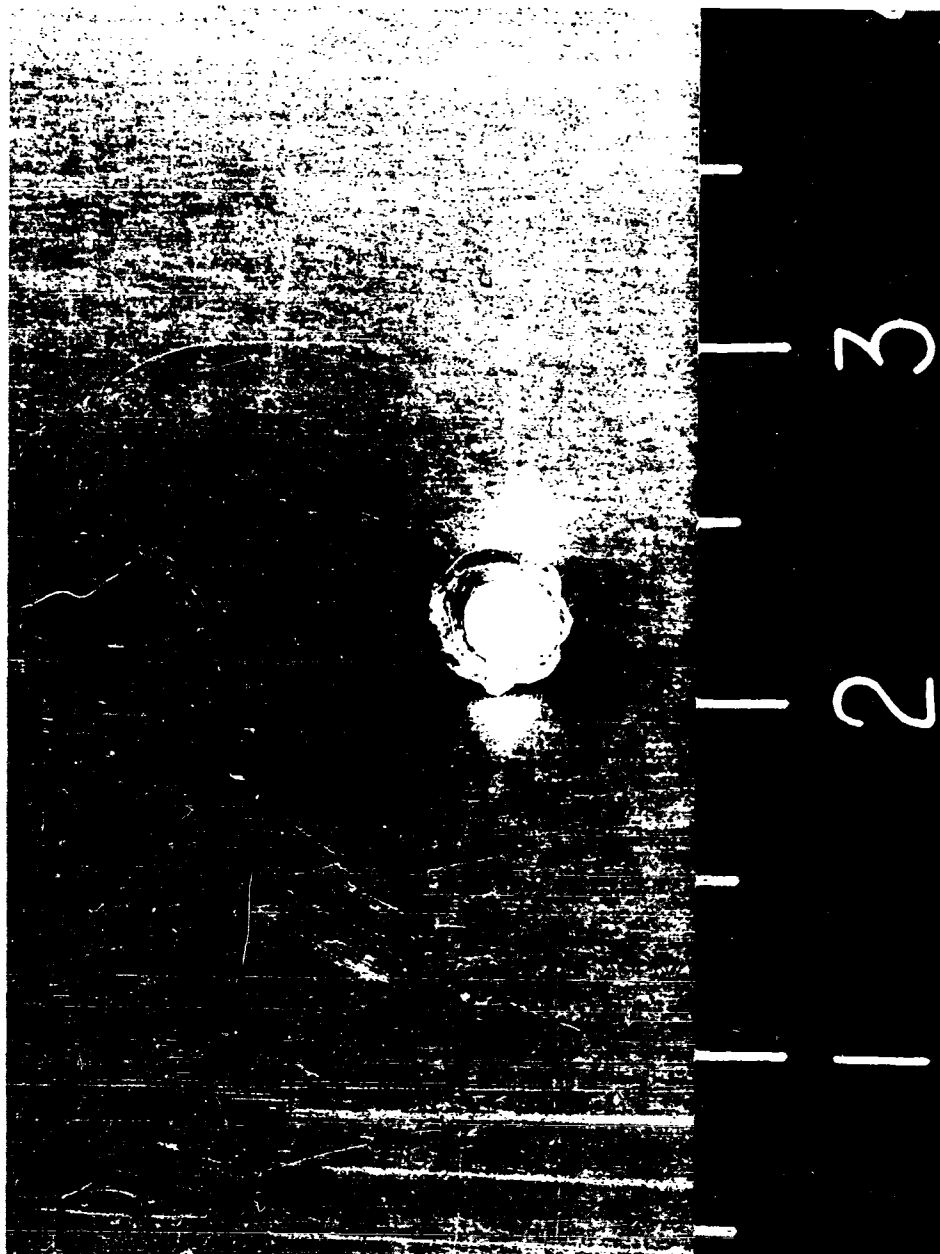
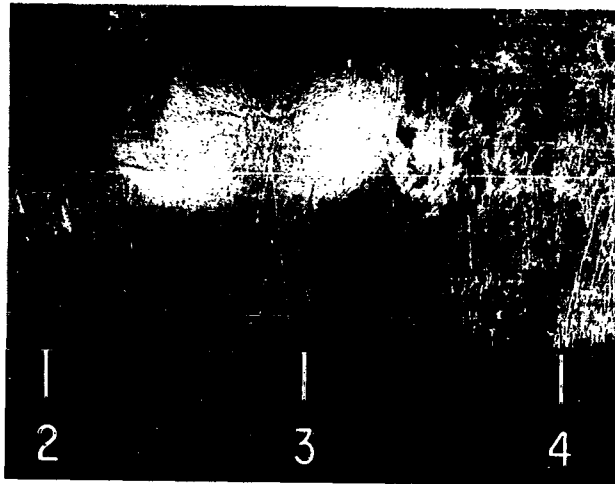


Figure 27 CHARACTERISTIC LOW VELOCITY PERFORATION OF A
COMPOSITE TARGET
P9340C

C49

SECRET

SECRET



a. Top View



b. Cross Section

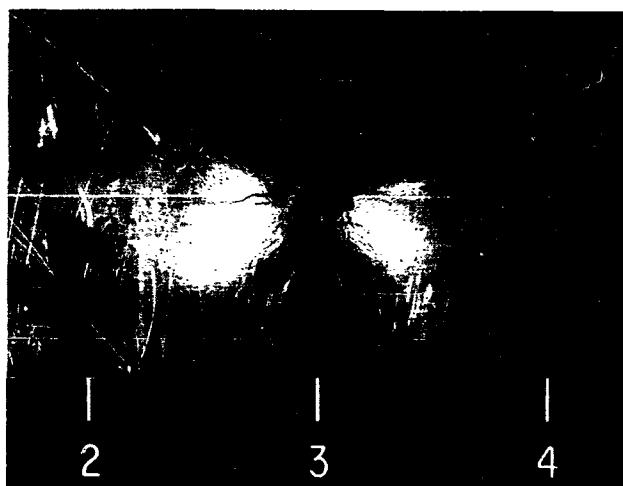
Arco *Research and Advanced Development*

Figure 28 CONDITION 2 FRACTURE
P9212A, P9311A

C50

SECRET

SECRET



a. Top View



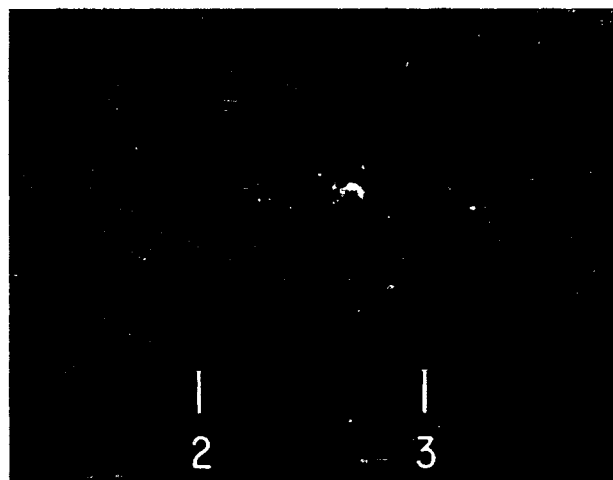
b. Cross Section

Figure 29 CONDITION 3 FRACTURE
P9212D, P9311Q

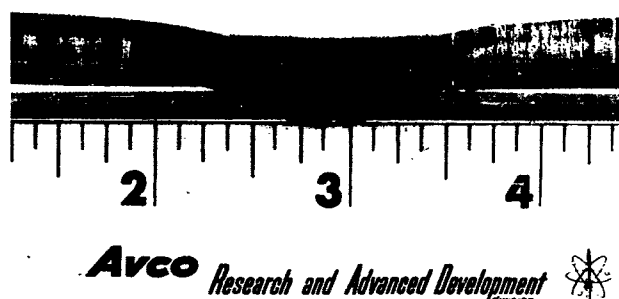
C51

SECRET

SECRET



a. Top View



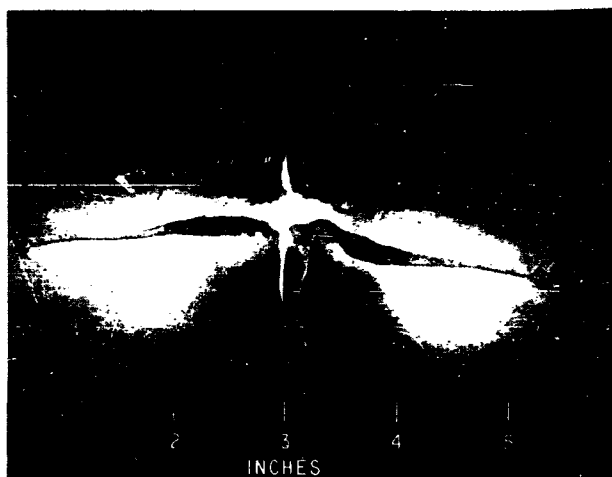
b. Cross Section

Figure 30 CONDITION 3a FRACTURE
P9212E, P9311O

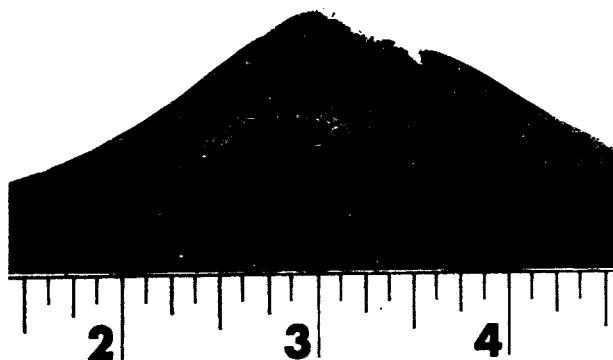
C52

SECRET

SECRET



a. Top View



Avco *Research and Advanced Development* 

b. Cross Section

Figure 31 CONDITION 4 DAMAGE MODE
P9212H, P9311M

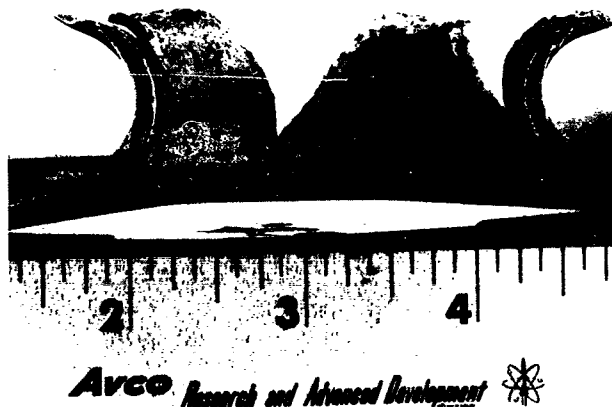
C53

SECRET

SECRET



a. Top View



b. Cross Section

Figure 32 CONDITION 5 DAMAGE MODE
P92121, P9311K

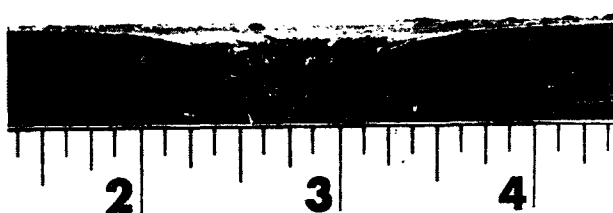
C54

SECRET

SECRET



a. Top View



Avco *Research and Advanced Development* 

b. Cross Section

Figure 33 CONDITION 6 DAMAGE MODE WITH ALUMINUM BACKUP
P9212M, P9311F

C55

SECRET

SECRET

and 3a shown in figures 29 and 30 are enhancements of condition 2, and required somewhat more projectile energy than condition 2. The difference between conditions 3 and 3a is that condition 3a is fractured through the thickness of the backup such that light can pass through, whereas 3 shows multiple fractures that do not pass light. Conditions 3 and 3a occurred with all backup materials and thicknesses except for 3/8-inch-thick steel. This point will be discussed later. As one continues up the energy scale, the mode of damage becomes more dependent on the heat shield thickness to backup-structure thickness ratio, as well as the type of backup structure material used. For the aluminum and steel structures, with the heat shield to backup-thickness ratio lying between 2.5 to 6.0 (the cases of thicker heat shields bonded to the 1/4-inch and 3/8-inch backup), the variation of damage mode with increasing projectile energy followed the directions illustrated by figures 31 and 32. A gaping crack (see figure 31) with the onset of petalling was observed at the next energy region, while at the higher energies a distinct pattern of petalling, as illustrated by the 1/8-inch-thick backup shown in figure 32 was seen. These conditions will be referred to as conditions 4 and 5. For aluminum and steel structures, with the heat-shield to backup-thickness ratio lying between the 1.35 and 2.00 (1.2-inch heat shield bonded to 3/8-inch and 1/4-inch backup respectively), the mode of damage is similar to that shown in figures 33 and 34. This will be referred to as condition 6. Here, material has spalled off the backup free surface and little bulging is evident surrounding the spall area. For the 3/8-inch-thick steel backup bonded to a 1/2-inch heat shield (OTWR) not enough data was taken to determine if the sequence of damage modes are the same as for the 1/4-inch backed target. At low energies, a bulge was obtained, and at high energies condition 6 was observed with the 3/8-inch-thick steel backup.

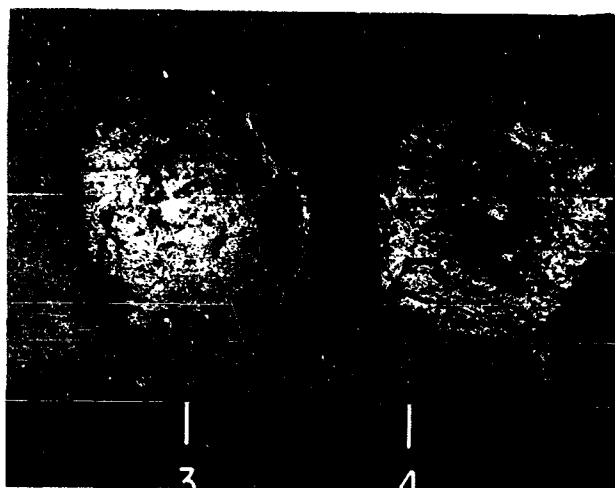
In addition to the mode of failure the strain in the backup is necessary to completely specify the backup damage. The backup deformation is defined by the bulge height and thickness strain as shown in figure 35. The purposes of the backup strain measurements are threefold. First, if the backup strain is given as a function of projectile energy and backup failure is associated with a critical strain, then the perforation energy can be calculated. Secondly, perturbations in the shape of the thickness strain and the bulge height versus radial distance show the impact effects of projectile fragments on the backup structure. Finally, the bulge height is significant in kill calculations.

The thickness strain for aluminum backups is a linear function of E/t_h^3 as shown in figure 36. The strain for the 1/4-inch backups increases with E/t_h^3 about twice as fast as the strain for 3/8-inch backups. A correlation such as that presented in figure 36 is possible only if projectile diameter/heat shield thickness is less than 0.250 ($d/t_h < 0.250$). For the steel backups no correlation with (E/t_h^3) is possible because the backup strain is strongly dependent upon d for $d/t_h > 0.250$ and most of the steel shots have a d/t_h about 0.300.

C56

SECRET

SECRET



a. Top View



Arco *Research and Advanced Development* 

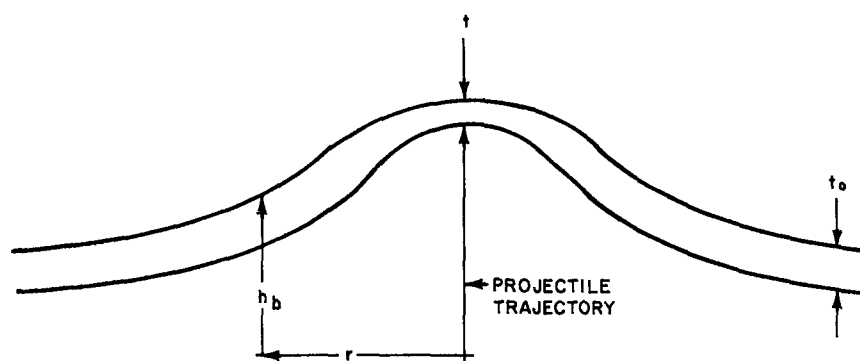
b. Cross Section

Figure 34 CONDITION 6 DAMAGE MODE WITH STEEL BACKUP
P9212F, P9311V

C57

SECRET

SECRET



BULGE HEIGHT AT DISTANCE r FROM CENTER OF IMPACT IS h_b .
THICKNESS STRAIN IS $\epsilon = \frac{t_0 - t}{t_0}$

Figure 35 BACKUP DEFORMATION PARAMETERS
62-6244

C58

SECRET

SECRET

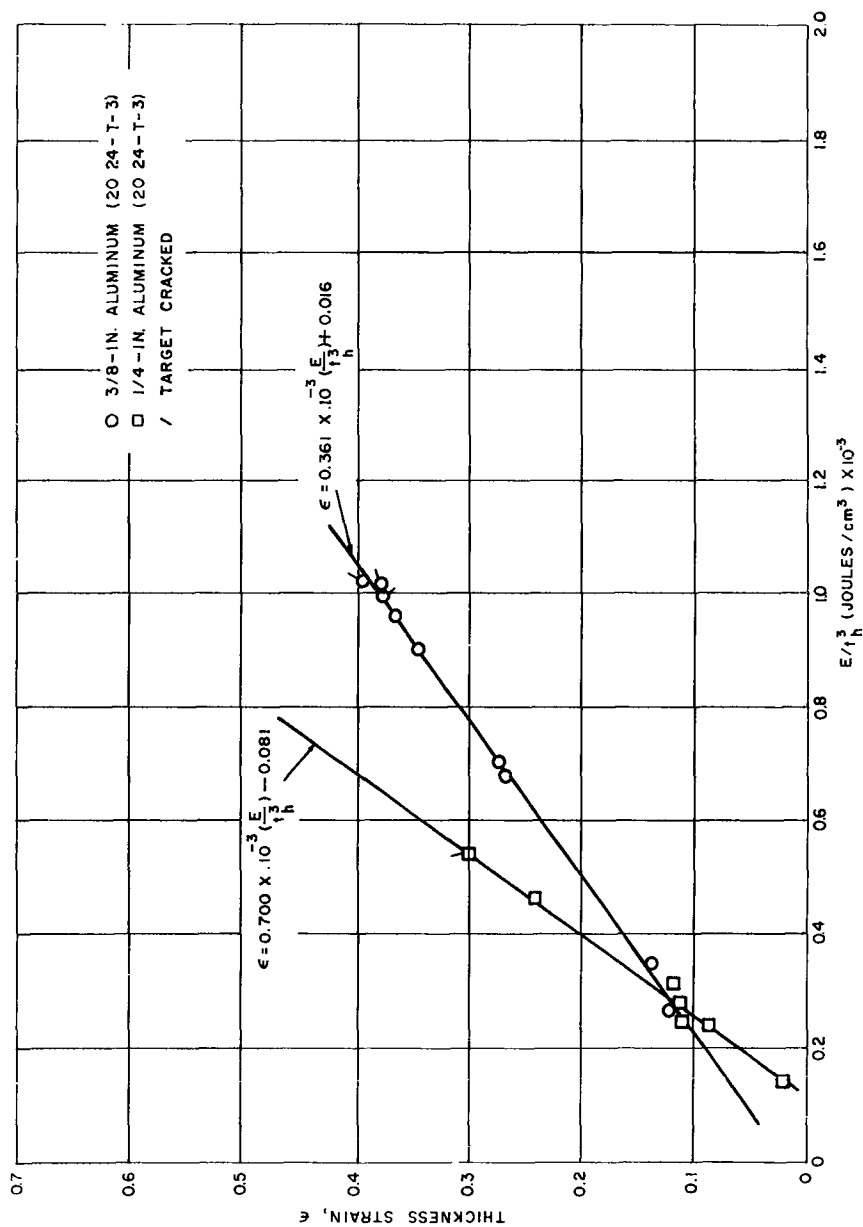


Figure 36 THICKNESS STRAIN VERSUS E/t_h^3 FOR OTWR ON ALUMINUM
 63-6266

C59

SECRET

SECRET

For the OTWR on 1/4-inch aluminum backups a critical thickness strain corresponding to a condition (2) failure may be taken to be $\epsilon_c = 0.250$. Substitution of ϵ_c into the equation

$$\epsilon_c = 0.700 \times 10^3 \left(\frac{E}{t_h^3} \right) - 0.081 \quad (6)$$

from figure 36, gives perforation energies which agree well with those values obtained experimentally. For the shots with 3/8-inch aluminum and 1/4-inch steel backups the critical thickness strain is a strong function of t_h/t_b , and d/t_h so that further analysis is necessary to evaluate ϵ_c as a function of impact parameters and target geometry.

Finally the significance of the backup bulge in kill calculations can be seen from an example. In Shot No. 212-3 (1-1/2-inch OTWR on 1/4-inch steel) the target is not perforated and the heat shield hole has a radius of 2.3 cm, while at a radius of 5.5 cm the backup is bulged 2 cm. The backup bulge and back spall combine to form a large volume in which hot gases may circulate.

For kill calculations typical bulge height versus radial distance curves are plotted in figures 37 through 44. Correlation of bulge height with impact parameters and target geometry has not been carried out because of lack of time. The bulge height for any given target geometry is a linear function of impact energy as shown in figure 42 for the 1/2-inch OTWR on 1/4-inch and 3/8-inch aluminum. For $d/t_h > 0.250$ the bulge height becomes a strong function of d in the same way as the thickness strain; additional work is required to understand this effect. The following sections will attempt to interpret what was observed; a correlation of the results is presented.

C60

SECRET

SECRET

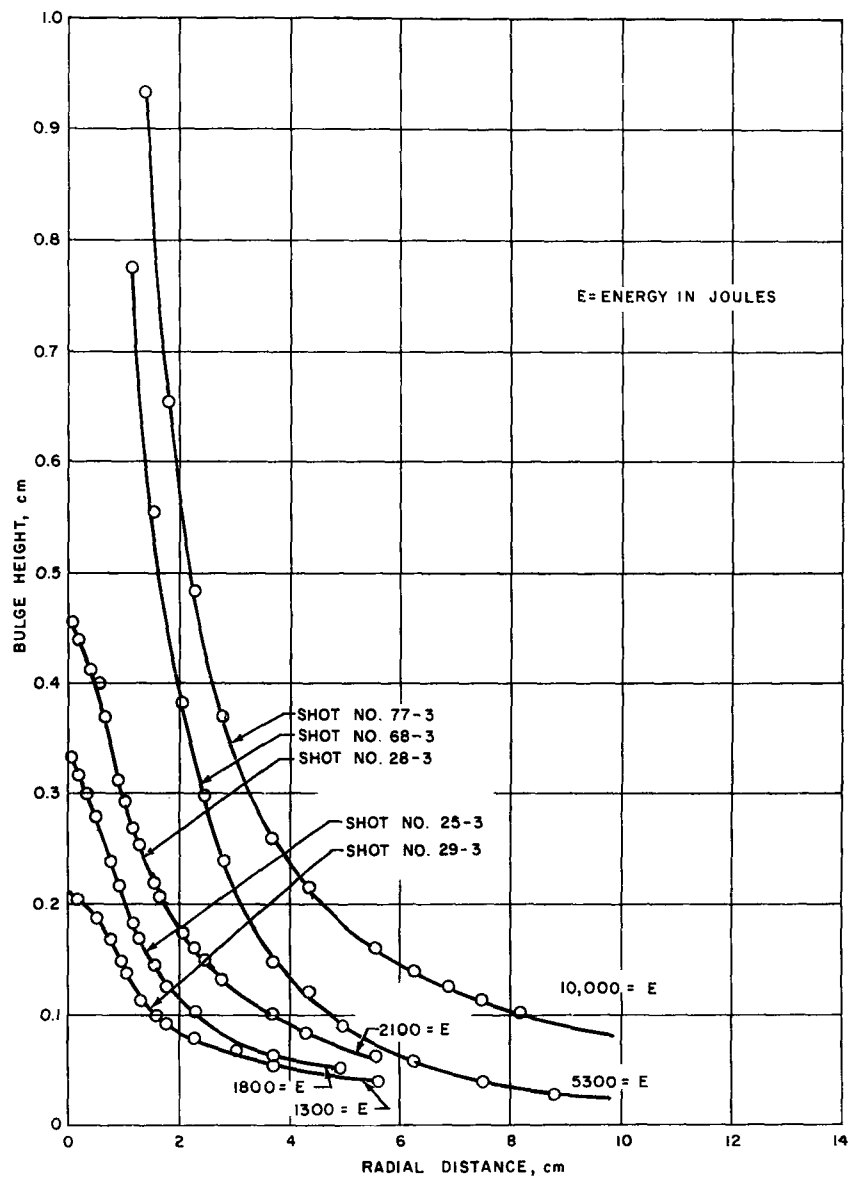


Figure 37 BULGE HEIGHT VERSUS RADIAL DISTANCE AND IMPACT ENERGY
(1/2-IN. OTWR ON 1/4-IN. ALUMINUM (2024-T3))
63-6236

C61

SECRET

SECRET

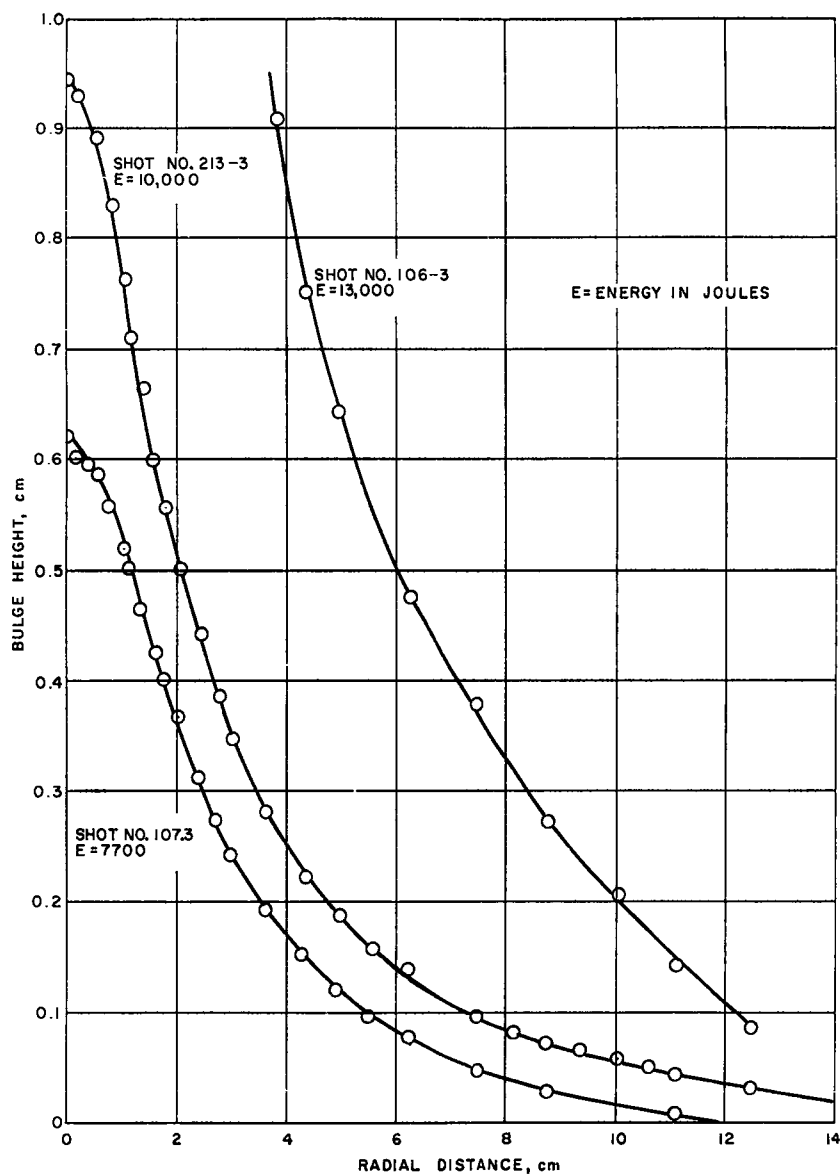


Figure 38 BULGE HEIGHT VERSUS RADIAL DISTANCE AND IMPACT ENERGY
(1-IN. HITCO OTWR ON 1/4-IN. ALUMINUM (2024-T3)
63-6239

C62

SECRET

SECRET

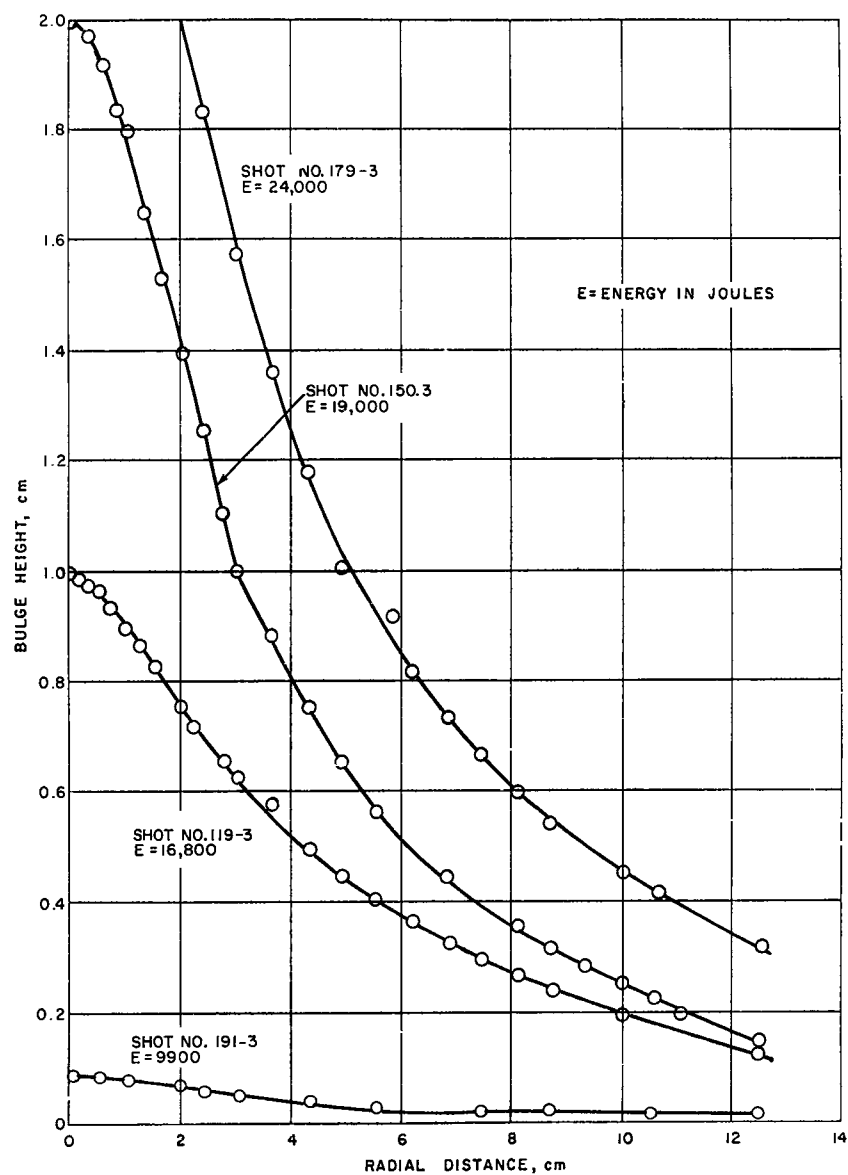


Figure 39 BULGE HEIGHT VERSUS RADIAL DISTANCE AND IMPACT ENERGY
(1-1/2-IN. OTWR ON 1/4-IN. ALUMINUM (2024-T3)
63-6237

C63

SECRET

SECRET

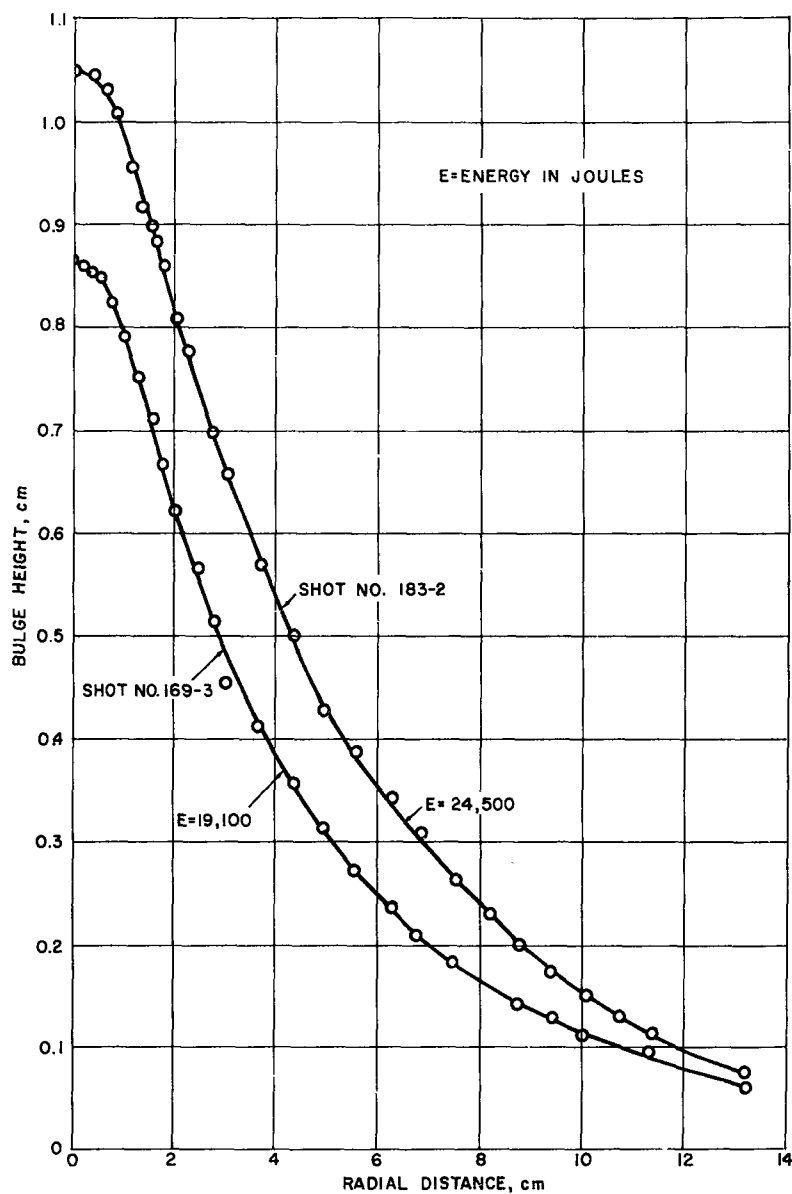


Figure 40 BULGE HEIGHT VERSUS RADIAL DISTANCE AND IMPACT ENERGY
(1-1/2-IN. OTWR ON 3/8-IN. ALUMINUM (2024-T 3))
63-6267

C64

SECRET

SECRET

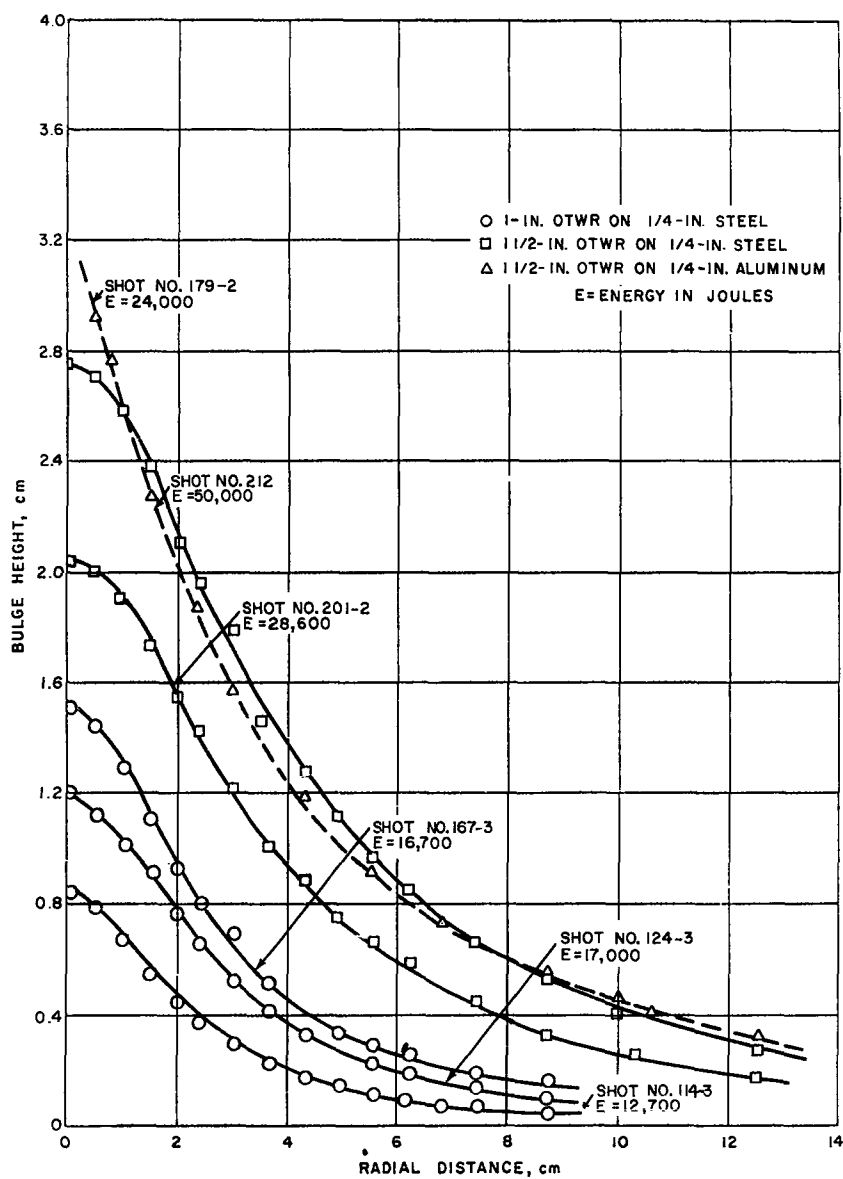


Figure 41 BULGE HEIGHT VERSUS RADIAL DISTANCE AND IMPACT ENERGY
FOR 1/4-IN. STEEL BACKUPS
63-6238

C65

SECRET

SECRET

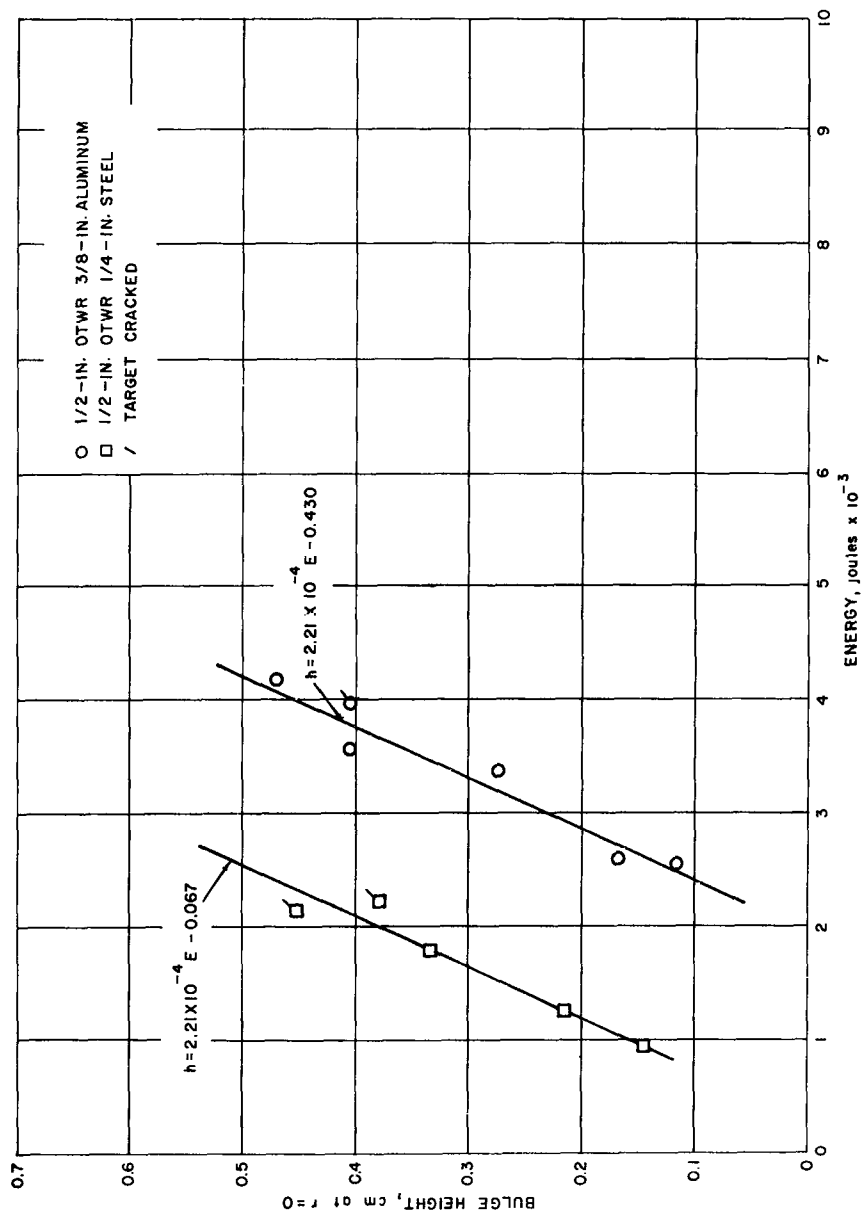


Figure 42 BULGE HEIGHT AT $r = 0$ VERSUS IMPACT ENERGY
63-6271

C66

SECRET

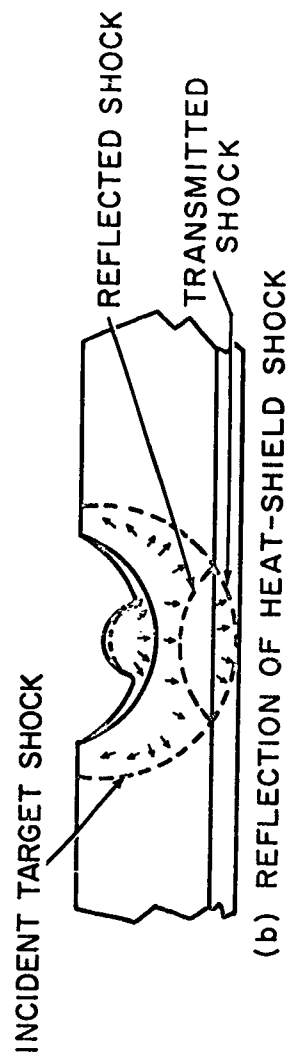
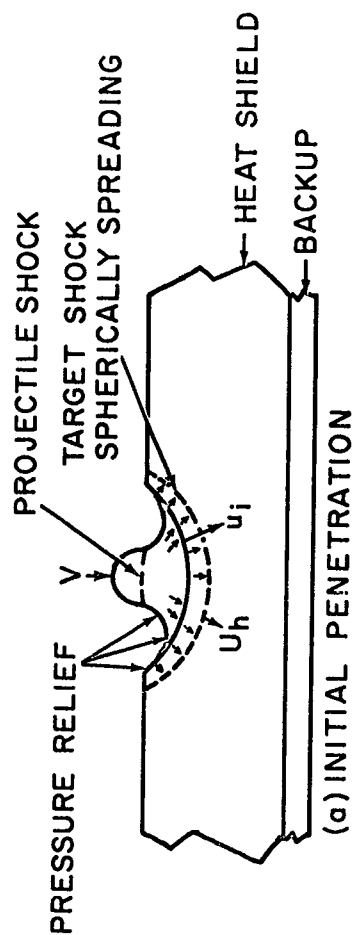


Figure 43 MECHANISMS OF PERFORATION (a) INITIAL PENETRATION (b) REFLECTION OF HEAT SHIELD SHOCK (c) BULGE FAILURE (d) SPALL FAILURE (e) EFFECT OF PROJECTILE FRAGMENTS
63-3931

C67

SECRET

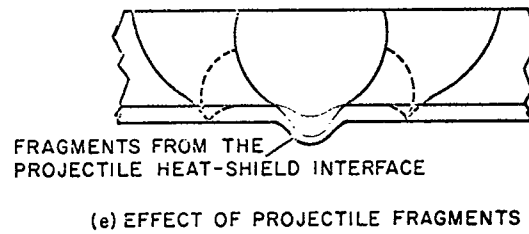
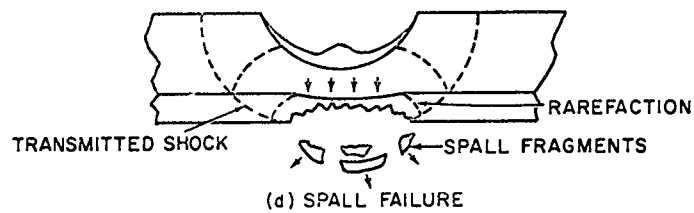
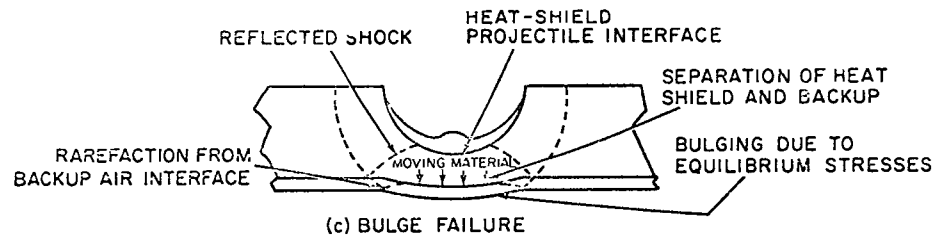


Figure 43 (Concl'd)

C68

SECRET

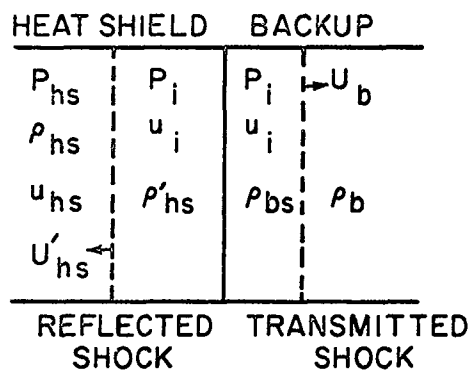


Figure 44 ONE-DIMENSIONAL INTERACTION OF SHOCK WITH HEAT SHIELD
BACKUP INTERFACE AFTER REFLECTION
63-3933

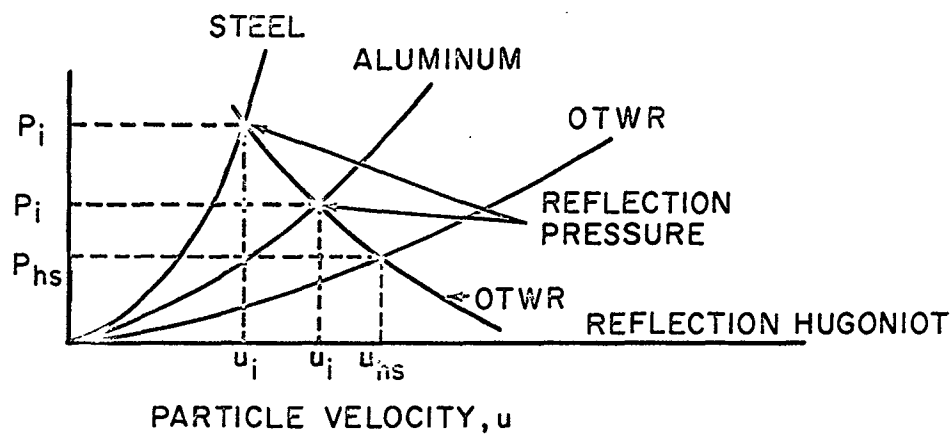


Figure 45 PRESSURE VERSUS PARTICLE VELOCITY CURVES
63-3933

SECRET

D. INTERPRETATION OF RESULTS

In recent years, the impact model proposed by Gehring, Eichelberger, and Bjork has been experimentally verified by observations with high-speed photography,^{4, 5, 6} flash X-ray, and wire grid experiments.⁷ An impact into a semi-infinite target is viewed in four parts. First is a transient stage where shocks are generated in the target and projectile, but pressure release and propagation have not had time to influence the impact (figure 43a). The pressure in this phase of the impact can be calculated from the one-dimensional shock relations^{8, 9} applied to the projectile shock and the target shock. After about $0.1 \mu\text{sec}$, an equilibrium flow pattern is established where the projectile is in the process of breaking up. About $1.0 \mu\text{sec}$ after the impact begins, the projectile is completely consumed by the flow and the cratering continues by cavitation, as described by Bjork¹⁰ and Davis, Huang, and Jaunzemis.¹¹ Finally, the stresses fall to the level of the elastic-plastic strength of the target. Cracking, spalling, and even shrinkage of the crater have been observed in this final phase.

In finite composite structures the target shock and target-projectile interface are intercepted by the heat-shield-backup interface and the backup free surface before the target comes to rest. Thus, the mechanism of perforation depends on the time sequence of arrival and energy content of the target shock and the materials moving behind the shock when they reach the heat shield-backup interface. Upon impact, the target-projectile interface moves into the target at a lower speed than the shock, as shown in figure 43 (a and b). When the shock transmitted to the backup is reflected from the backup free surface, a rarefaction is generated and the backup begins to bulge, as in figure 43c, or spalls, as in figure 43d. At some later time, the material from the projectile-target interface reaches the backup and does additional work, as shown for an extreme case in figure 43e.

Thus, for a complete description of the perforation, it is necessary to know: (1) the shock and projectile-target interface separation, (2) spreading and damping of target shock, (3) reflection of shock at heat shield-backup interface, (4) backup structure free-surface motion, (5) interaction of reflected shock with the projectile-target interface, and (6) interaction of the interface material with the backup.

The first thing the backup sees is the target shock. A qualitative description of what takes place at the heat shield-backup interface may be obtained by graphical solution of the pressure-particle velocity functions as described by Duvall.¹² A sketch of a one-dimensional interaction of an incident shock on the backup structure after reflection is shown in figure 44. Let the incoming shock in the heat shield have a pressure P_{hs} , density ρ_{hs} and particle velocity u_{hs} . Upon interaction with the backup, a reflected shock with pressure P_i , density ρ'_{hs} and particle velocity u_i will travel into the incident shock with a

SECRET

SECRET

shock velocity U'_{hs} . The transmitted shock will travel into the backup with pressure P_i , density ρ_{bs} and shock velocity U_b . The region between the reflected and transmitted shock will be at a uniform pressure and particle velocity or the interface will separate. From the conservation of mass and momentum equations written across the reflected and transmitted shock,

$$P_i - P_{hs} = \rho_{hs} (u_i - u_{hs}) (U'_{hs} - u_{hs})$$

$$P_i = \rho_b u_i U_b. \quad (7)$$

From shock-compression experiments on solids, a relation between shock velocity and particle velocity is obtained for heat-shield¹³ and backup materials

$$U'_{hs} - u_{hs} = a_h (u_i - u_{hs}) + b_h$$

$$U_b = a_b u_i + b_b. \quad (8)$$

where the constants a and b are determined experimentally. Combining equations (7) and (8), the conditions which must hold at the interface are

$$P - P_{hs} = \rho_{hs} (u_i - u_{hs}) [a_h (u_i - u_{hs}) + b_h] \quad (9a)$$

$$P_i = \rho_b u_i (a_b u_i + b_b). \quad (9b)$$

Figure 45 shows the plots of equation (9b) for aluminum, steel, and OTWR, and the plot of equations (9a), which is called the reflection Hugoniot, for OTWR. The intersection of equations (9a) and (9b) gives the solution of the equations, that is, the interface pressure and particle velocity. Since the $p - u$ curves for aluminum and steel lie above the OTWR line, the material in the reflected shock is under a higher pressure and lower particle velocity; and the transmitted shock is thinner and under a higher pressure than the material in the incoming shock.

The transmitted shock reflects as a rarefaction from the backup free surface. The backup free surface begins to move after the first reflection, bulges, and sometimes spalls. If the backup spalls, the spall acts as a momentum trap (figures 33a and 34a), and little bulging occurs. On the other hand, if the backup does not spall, it may bulge to the fracture point under the influence of the initial shock and the material behind the shock (figures 29, 30 and 31).

SECRET

SECRET

The second impulse that the backup receives is from the moving zone of shocked heat shield and broken-projectile material. The energy contained in this zone is a function of zone thickness and concentration of broken-projectile material. As can be seen from figure 45, the passage of the reflected shock through the heat shield has the effect of raising the pressure and lowering particle velocity. For the case of small (d/t_h) ball-diameter, heat-shield-thickness ratio, the projectile is completely consumed and the cavity free surface acts as a source of pressure relief for the heat shield material in front of the backup, which tends to reduce the energy content of this zone. In this case, the second impulse does not do significant work against the backup. For the case of large (d/t_{hs}) the projectile still is feeding energy into the interface when it encounters the backup, and may receive additional acceleration toward the backup under the influence of rarefaction caused by separation of heat shield and backup. Various stages of pitting due to steel fragments impacting the backup can be seen in figures 29a, 30a, 33a, and 34a. Figures 29a and b are photographs of a sectioned 3/8-inch-thick aluminum backup which was bonded to a 1/2-inch-thick Astrolite plate. The target was impacted with a 0.22-caliber steel sphere at a velocity of 3.93 km/sec. These photographs illustrate some of the points made in the preceding paragraphs. Observable are: (1) tensile fracture on the free surface, (2) spall fracture through the sample center parallel to the bulge-free surface, and (3) deformation and pitting at the center of the bulge at the bottom surface due to the interaction of the backup with the projectile-target interface.

Finally, the mechanism of perforation depends on the backup thickness and toughness. Consider first the case of a thin backup where the ratio of heat shield thickness to backup is large. The large heat shield thickness spreads the energy in the shock over a relatively large area. Since the backup is thin, it takes less energy to bulge it, and it ultimately rips and petals, as in figure 32. As the backup is made thicker, it takes a stronger shock to supply the energy necessary to bulge it, until the required shock is so strong it spalls the backup (figures 33a and 34a), leaving less energy for bulging. The 3/8-inch aluminum with 1/2-inch heat shield fails by a condition 3 fracture shown in figure 29 at some minimum energy; but, however, as the energy is increased, it begins to spall, as shown in figure 33a. When the heat shield thickness is increased to 1-1/2-inch the 3/8-inch aluminum backup petals, as in figure 32.

In summary, the various effects on perforation mechanisms may be outlined for steel projectiles as follows:

1. The Effect of d/t_h
 - a. For small d/t_h (~ 0.2), the target shock does most of the work.
 - b. For large d/t_h (~ 0.5), the moving projectile-heat-shield material does most of the work.

C72

SECRET

SECRET

2. The Effect of Backup Material

- a. The higher the $P/u \left(\frac{\text{pressure}}{\text{particle velocity}} \right)$ ratio of the backup, the smaller the energy entering the backup (in general, P/u increases with ρc).
- b. The higher the static ultimate tensile strength, the less likely the back will fail by cracking.

3. The Effect of Heat Shield Thickness to Backup-Thickness Ratio t_h/t_b

- a. For large t_h/t_b the target fails by bulging and ultimately petals
- b. For small t_h/t_b the target fails by spallation.

C73

SECRET

SECRET

E. PERFORATION ENERGY CORRELATION

The procedure described here is used to correlate the results into a form which would allow a prediction of something defined as perforation. The program plan consisted of making from three to six impacts into a given target configuration to determine minimum perforation conditions. Obviously, it was impossible to define perforation arbitrarily from one of the different backup-structure-damage modes and exactly determine what impact conditions would result in the chosen damage mode. Nevertheless, backup fracture similar in nature to conditions 2 and 3 was obtained with every configuration except the 1/2-inch OTWR with 3/8-inch steel case. This target failed by spallation (see figure 34) with the spalled fragment showing a condition 3 fracture. Thus, conditions 2 and 3 were arbitrarily defined as the backup-structure-fracture modes under minimum perforation conditions. Figure 46 is a log-log plot of total target thickness as a function of projectile energy for all cases. The points represent perforation energies to within 2 percent. For the four combinations of target materials impacted, the results can be correlated by an expression of the form

$$T = AE^{1/3} \quad (10)$$

where A is an empirical constant dependent on heat shield and backup-structure properties. An attempt then was made to reduce the data to a single expression by finding the functional dependence of A on the heat shield and backup-structure properties. It would be correct physically to define A in terms of some dynamic properties of these materials, but little information is available pertaining to dynamic properties of these materials at the impact pressures of interest. Thus, the solution seems to be a correlation in terms of static properties of materials. The work of Herman and Jones suggested a possible direction. They have correlated the penetration from high-velocity impact in terms of the projectile energy and the inverse product of target density and Brinell hardness, for a given projectile material. Thus, an effective density times strength term was defined as follows,

$$(\rho H)_{\text{eff}} = \frac{\rho_h H_h t_h + \rho_b H_b t_b}{T} \quad (11)$$

which essentially is an effective density times strength term weighted according to thickness. The data (figure 46) shows that for the laminated fiber reinforced phenolic resin materials (OTWR and Astrolite) bonded to aluminum structure, OTWR targets are somewhat easier to perforate than Astrolite. Table 1 shows that the ultimate compressive strength of these materials in the direction of impact follows this order. Thus, H_h refers to this parameter. The backup-structure fracture results from tensile stresses set up between the bulged region and the adjacent stationary region, thus H_b refers to the backup ultimate tensile strength.

SECRET

SECRET

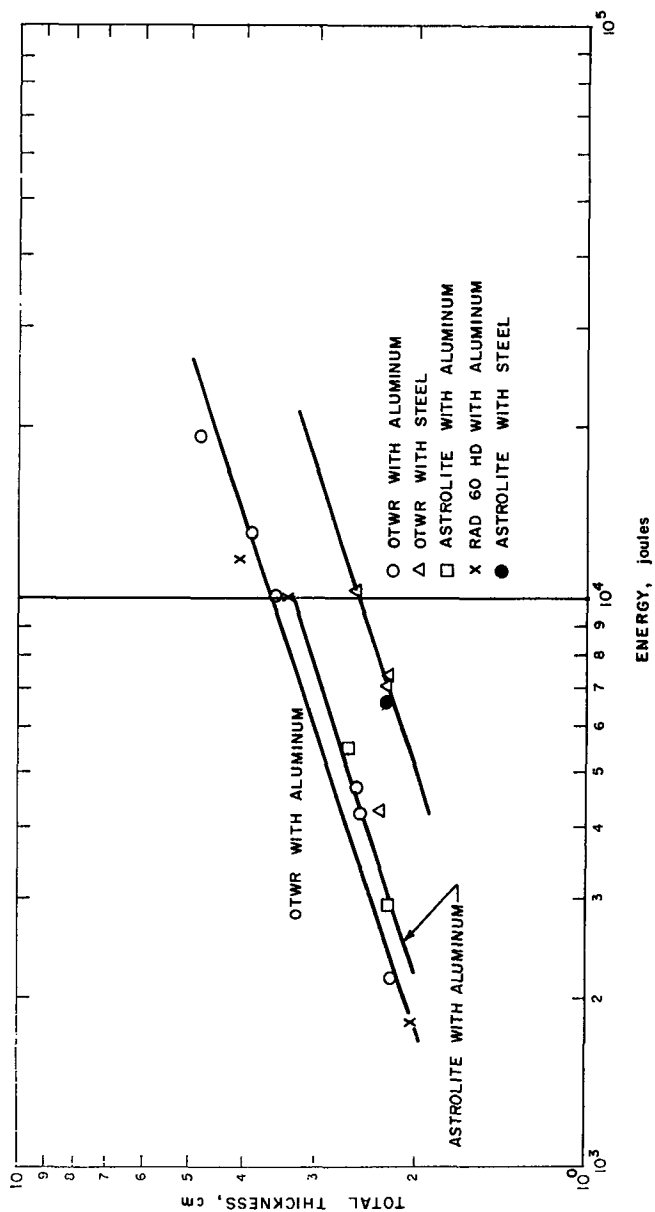


Figure 46 TOTAL TARGET THICKNESS VERSUS PERFORATION ENERGY
63-6253

C75

SECRET

SECRET

The constant A was plotted against $\left(\frac{1}{\rho H}\right)_{\text{eff}}$ and the result is shown in figure 47. This plot suggests a relationship of the form

$$T = B(1/\rho H)_{\text{eff}}^{1/3} E^{1/3} \quad (12)$$

One can rewrite this expression,

$$\frac{E}{T^3} = \frac{1}{B^3} (\rho H)_{\text{eff}} \quad (13)$$

The constant $C = \frac{1}{B^3}$ was determined by the method of least squares, and its value found to be,

$$C = (4.10 \pm 0.82) \times 10^{-8}$$

for E in joules, T in cm, and $(\rho H)_{\text{eff}}$ in $\frac{\text{gm}^2}{\text{cm}^4 \cdot \text{sec}^2}$. A plot of expression (13) is shown in figure 48 with the data.

At this point, it is important to insert some remarks pertaining to the above correlation. The minimum perforation energy for all configurations has been obtained with generally only one size projectile for each target configuration. This correlation has been obtained for the range of conditions

$$0.1 \leq d/t_h \leq 0.5$$

$$1.3 \leq t_h/t_b \leq 6$$

A limited number of tests were made on two targets with projectiles of varying mass to determine if the same mode of damage to the backup occurred at the same levels of projectile energy. The two configurations studied consisted of a 1/2-inch OTWR bonded to 1/4-inch steel and 3/8-inch aluminum (2024T3). The perforation damage mode was achieved with 0.22-caliber steel projectiles at energies of 7000 joules for the steel backed target and 4620 joules for the aluminum backed target. Impacts were then made with 0.25 caliber and 3/16-inch diameter projectiles into the steel backed target and a 3/16-inch diameter projectile into the aluminum backed target. The results are plotted in figure 49. For the steel backed target, a condition 3 damage mode occurred at about 5 percent more energy for the 0.25-caliber ball, and about 40 percent less energy for the 3/16-inch diameter ball than occurred for the 0.22-caliber projectile. This last shot was duplicated for verification. One of the contributing factors in this reduction might be due to differences in the heat shield materials for the 0.22-caliber and 3/16-inch diameter ball cases. Also it was observed

C76

SECRET

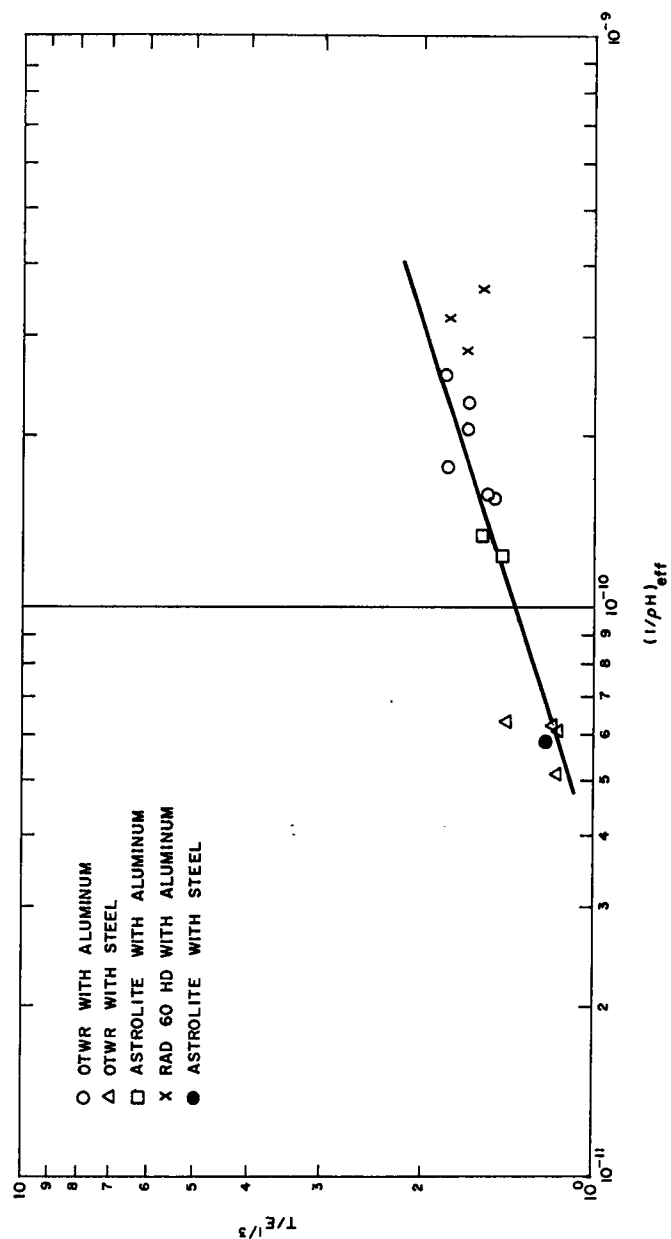


Figure 47 CORRELATION OF PERFORATION PARAMETER A WITH EFFECTIVE DENSITY TIMES STRENGTH
63-6251

SECRET

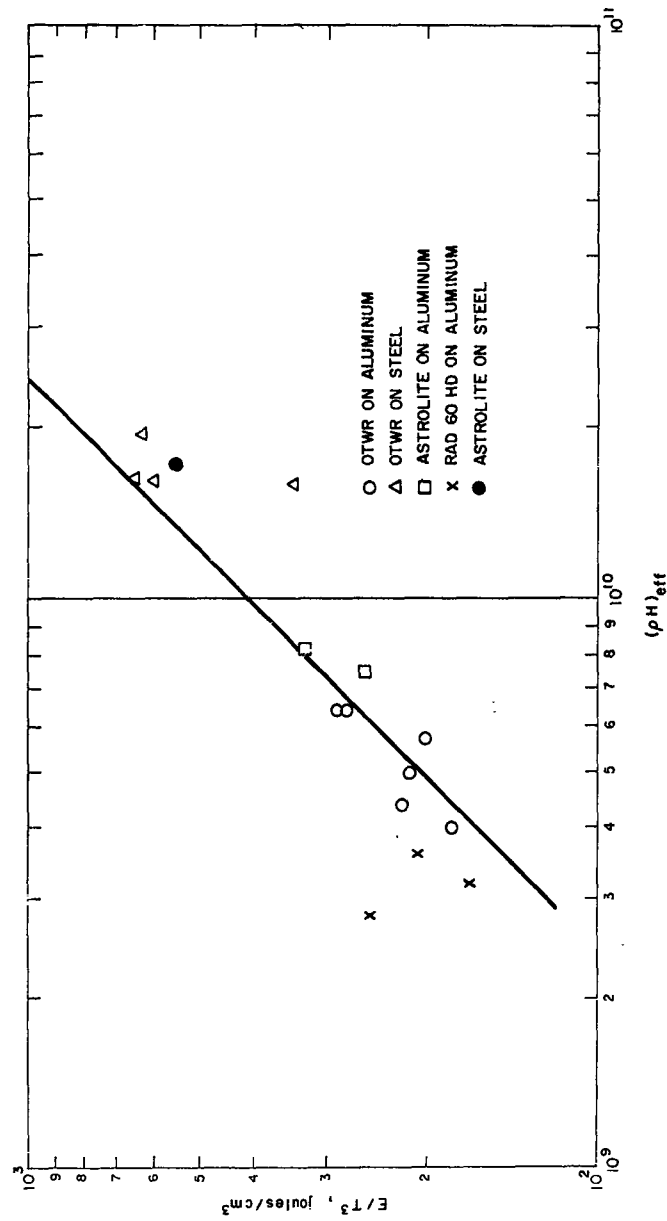


Figure 48 PLOT OF PERFORATION EFFICIENCY VERSUS TARGET EFFECTIVE STRENGTH TIMES DENSITY PARAMETER FOR STEEL PROJECTILES ON COMPOSITE TARGETS
63-6257

SECRET

SECRET

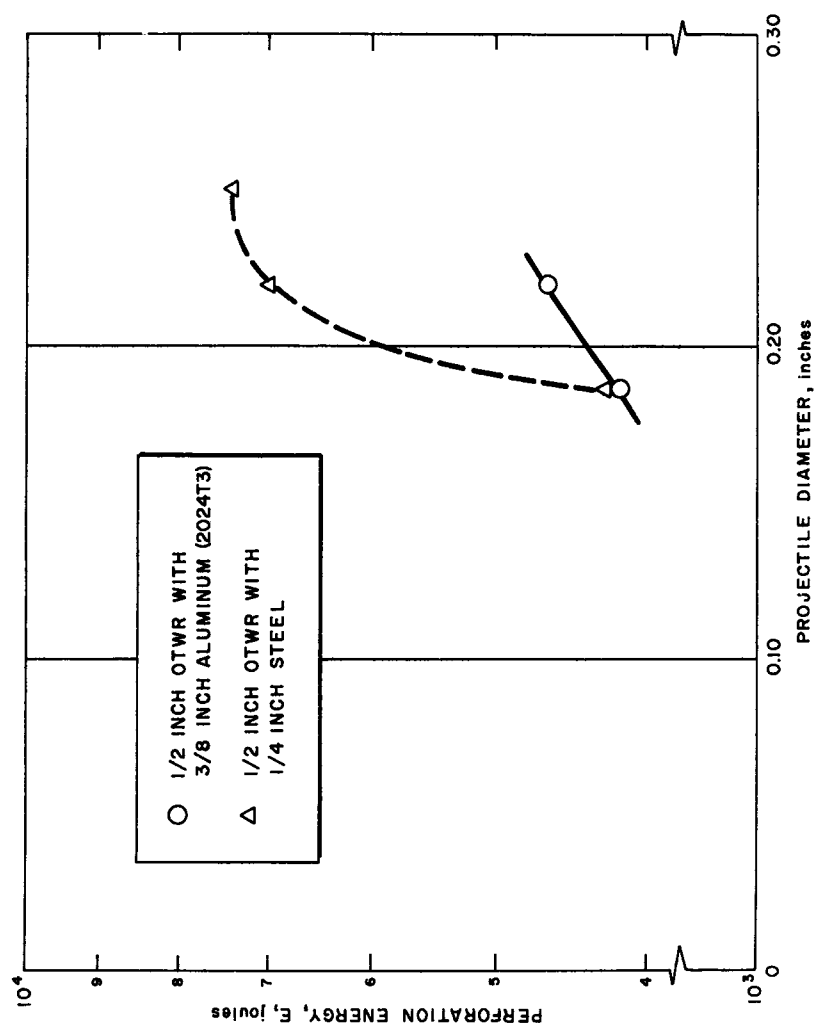


Figure 49 EFFECT OF PROJECTILE ON PERFORATION ENERGY FOR STEEL
PROJECTILES ON COMPOSITE TARGETS
63-6241

C79

SECRET

SECRET

for the 3/16-inch diameter case, that about 20 percent of the original projectile mass was lodged in the backup structure at the base of the fracture. To observe whether projectile velocity (proportional to impact pressure) was chiefly responsible for the observed effect, a 3/16-inch diameter ball was ground down on one face to a reduced mass of 0.354 gram (from 0.410 gram) and fired into the same target at about the same velocity. The resulting damage was only a bulge of the backup and not a fracture. The conclusion is that the secondary impact of the projectile fragments following the shocked material into the backup plays an important role at these velocities (4 to 5 km/sec).

With the aluminum backed target, the same damage mode was observed at a reduced energy level of 4160 joules for the 3/16-inch diameter case, or a reduction of 10 percent. Thus the perforation energy appears to decrease somewhat with decreasing ball size. This effect should be studied further to substantiate the correlation. The overall conclusion concerning perforation as defined in this report and projectile impact parameters is that perforation is caused by a complex combination of shock effects and the secondary impact of the broken projectile material on the backup structures. Over the realm of ball size to heat shield thickness ratios, heat shield to backup structure ratios, and projectile velocities, covered in this study, projectile energy is a meaningful term which correlates the results to within reasonable limits of accuracy.

It is also observed from figure 43 that the correlation better fits the data on the phenolic resins reinforced with the laminated fibers than the RAD 60 HD material which is a resin filled randomly with silica fibers and powder. The RAD 60 HD material is essentially another class of materials, and fails differently under impulsive loading than the laminates. Since RAD 60 HD was only given a cursory investigation, it should be studied further to extend the correlation into this class of ablative material.

Finally, since only steel projectiles were used in this study, the study should be extended to other projectile materials to extend the correlation.

C80

SECRET

F. SPALLATION STUDY

Earlier in the program, a study was carried out to determine the mass and spatial distribution of the fragments coming off the backface of a composite target which is perforated. The targets used were scrap-curved OTWR targets of targets of thicknesses 0.615-inch, 0.690-inch and 0.812-inch bonded Epoxy 5403 to 1/8-inch thick aluminum (6061T6) plates. The radii of curvature of the plates varied between 17 and 20 inches. The projectiles used were 0.22-caliber 440 steel spheres of mass 0.72 gram and the impact velocities varied between 2 and 4.5 km/sec.

A modified technique originated by the Ballistic Research Laboratory was used to capture the residual fragments. Briefly, it consists of placing sheets of insulation board (Maftex) at a known distance behind the target and normal to the particle trajectory (see figure 1). The residual fragments are caught in the Maftex, and then, recovered, counted and weighed, and their position recorded. From calibration data obtained by BRL¹⁴, expressing the particle depth of penetration in the Maftex, in terms of the mass, angle of impact and velocity of the fragment, one can determine the fragment velocity. The relationship between these variables for dural and steel are the following:

$$\text{Dural } V = 2035t^{0.736} m^{-0.255} (\sec \theta)^{0.711}$$

$$\text{Steel } V = 1276t^{0.736} m^{-0.255} (\sec \theta)^{0.711}$$

where V is the particle velocity in ft/sec, t is the Maftex thickness in inches, and m is the fragment mass in grains and θ is the angle between the fragment trajectory and the normal to the target surface.

A determination was made of the normalized mass and number density distributions per unit solid angle about the particle trajectory (with the apex of the cone originating from the exit hole of the perforation). Figures 50 to 55 show the results of these determinations. Appendix 2 presents the tabulated data which were used to make these composite plots. In general, both the number and mass densities decrease with increasing solid angle. The shape of the mass and number distributions are insensitive to impact velocity variations over the range of 2 and 5 km/sec. Insufficient variation in target thickness has prevented any correlation with this parameter. Some of the details of the masses and velocities of the recovered particles are shown in figures 5 to 55.

About midway through the program, the fragment distribution work was stopped. The technique adopted within the program to evaluate residual particle effects following perforation consisted of placing a 1/2-inch thick aluminum plate 10 inches behind the ablative target. Perforation of this witness plate was regarded as lethal. Perforation of this witness plate did not occur in any case following initiation of this procedure.

SECRET

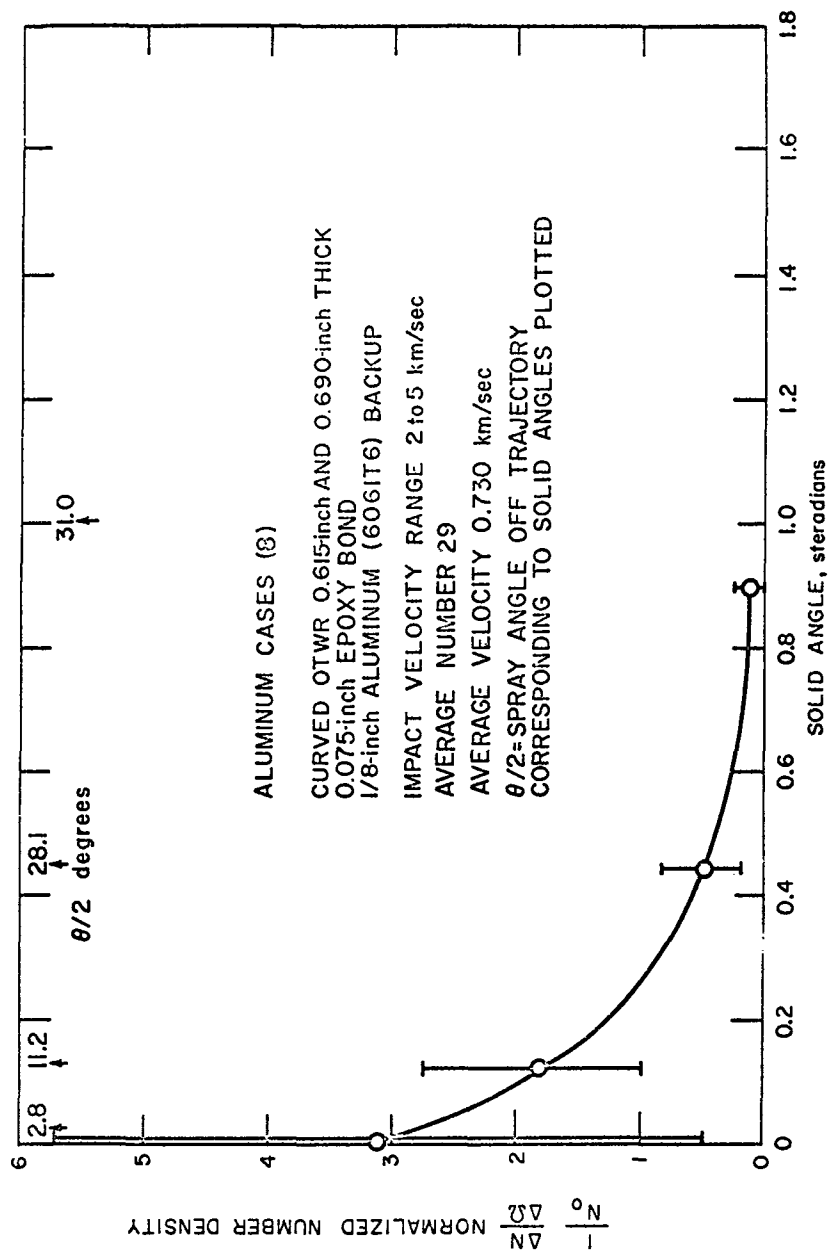


Figure 50 NORMALIZED NUMBER DENSITY VERSUS SOLID ANGLE
 (ALUMINUM CASES)

SECRET

SECRET

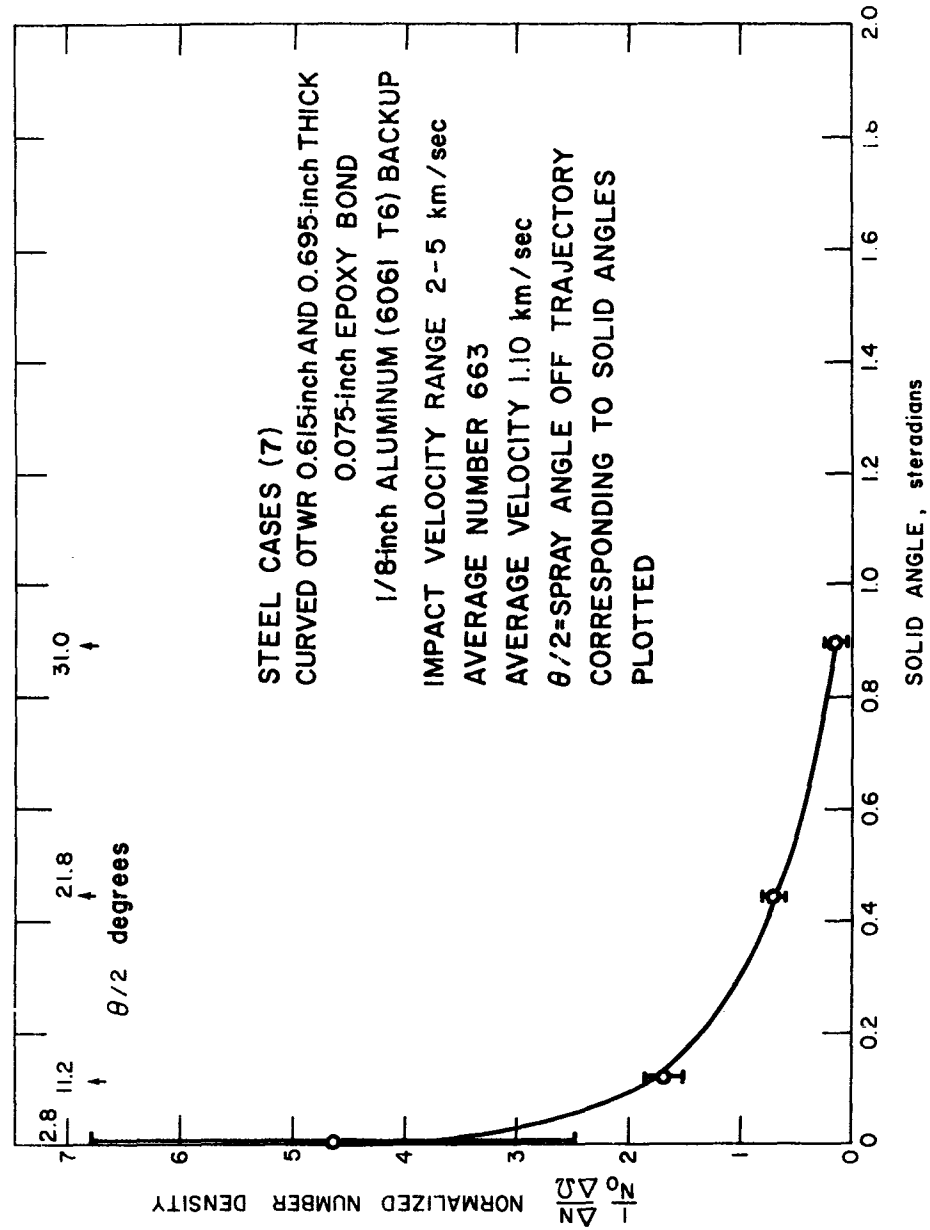


Figure 51 NORMALIZED NUMBER DENSITY VERSUS SOLID ANGLE
 (STEEL CASES)
 62-9895

C83

SECRET

SECRET

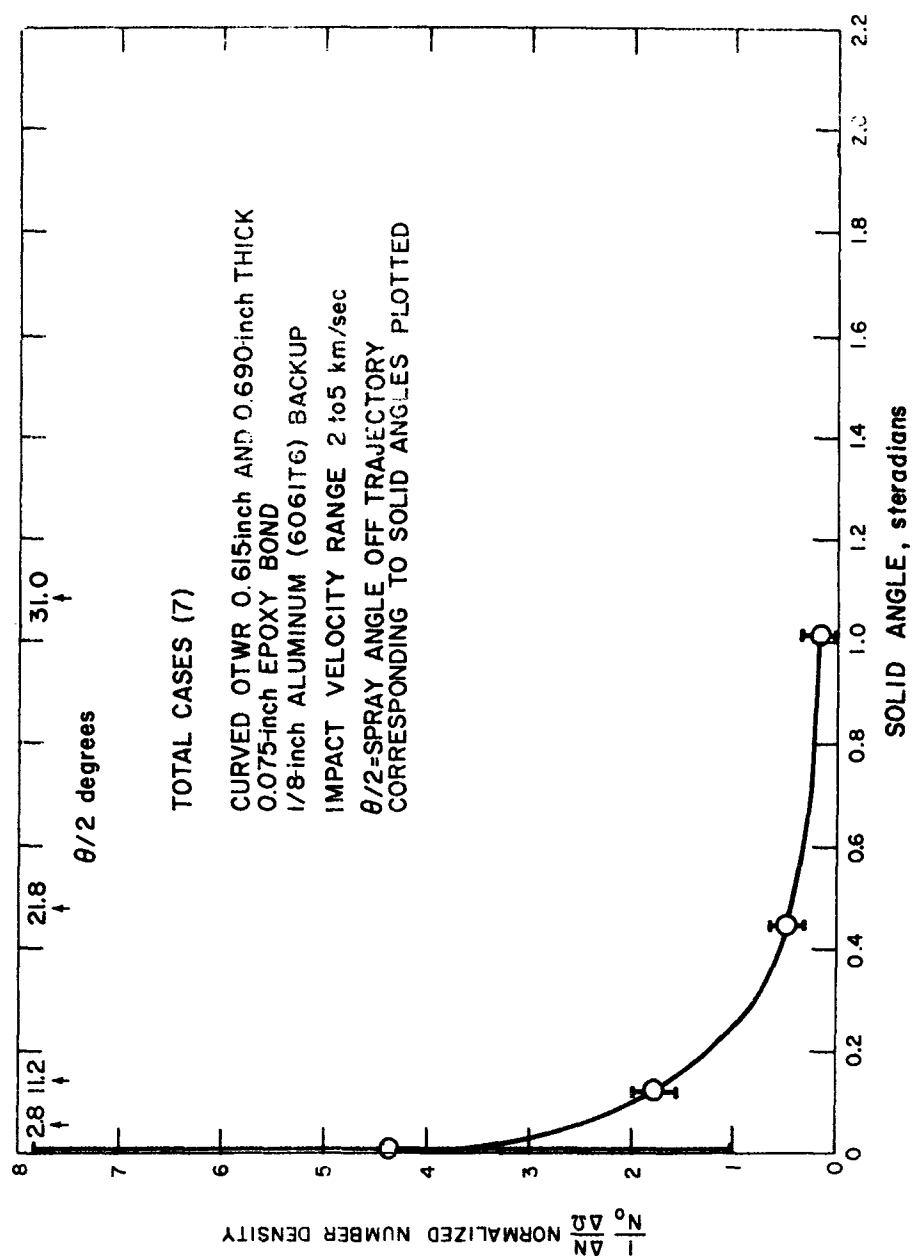


Figure 52 NORMALIZED NUMBER DENSITY VERSUS SOLID ANGLE
(TOTAL CASES)
62-9893

C84

SECRET

SECRET

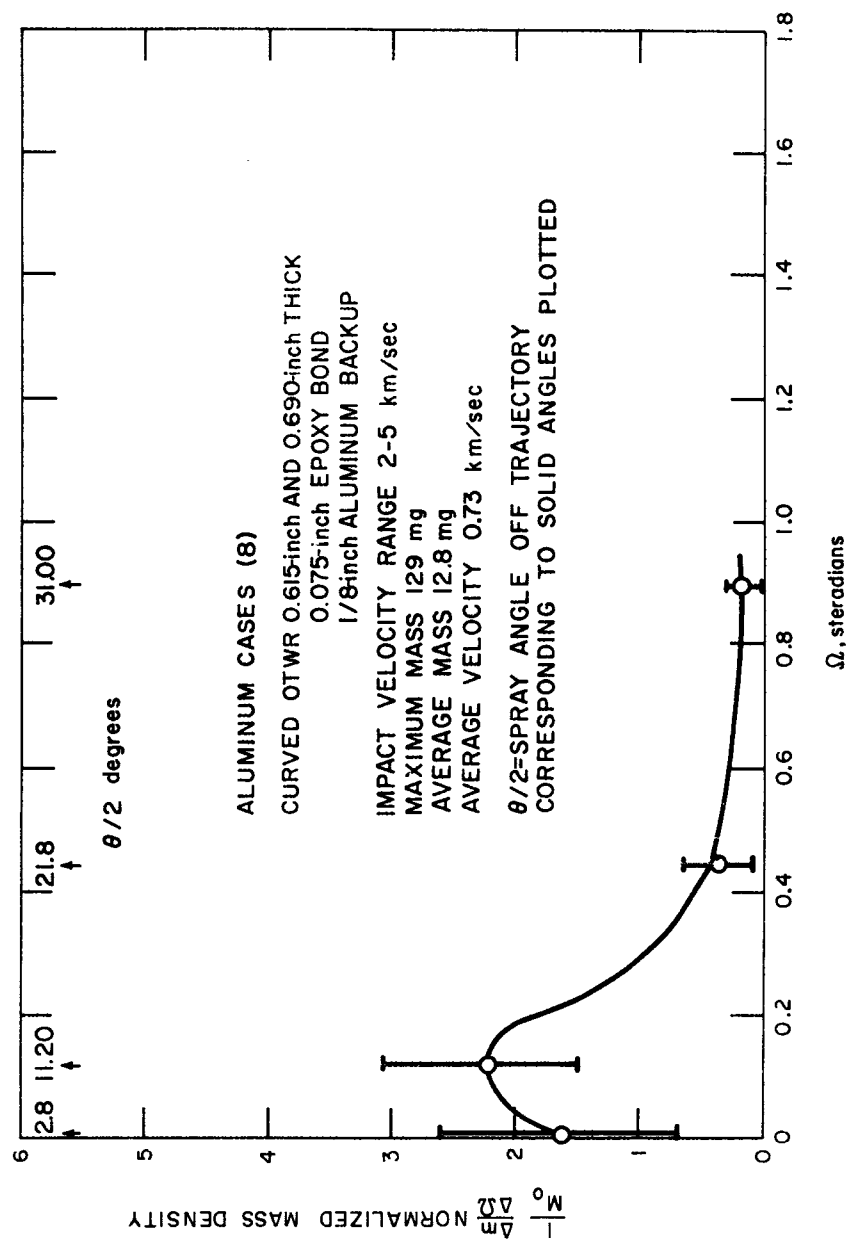


Figure 53 NORMALIZED MASS DENSITY VERSUS SOLID ANGLE
(ALUMINUM CASES)
62-9897

C85

SECRET

SECRET

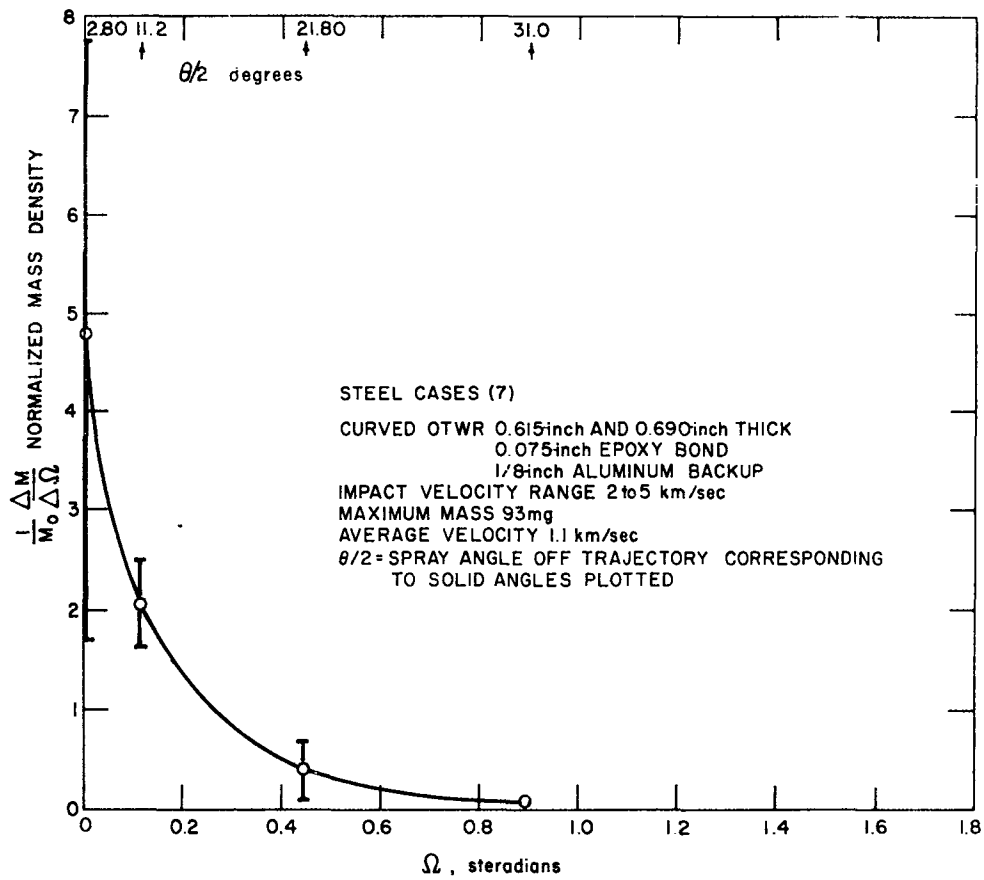


Figure 54 NORMALIZED MASS DENSITY VERSUS SOLID ANGLE
 (STEEL CASES)
 62-9898

C86

SECRET

SECRET

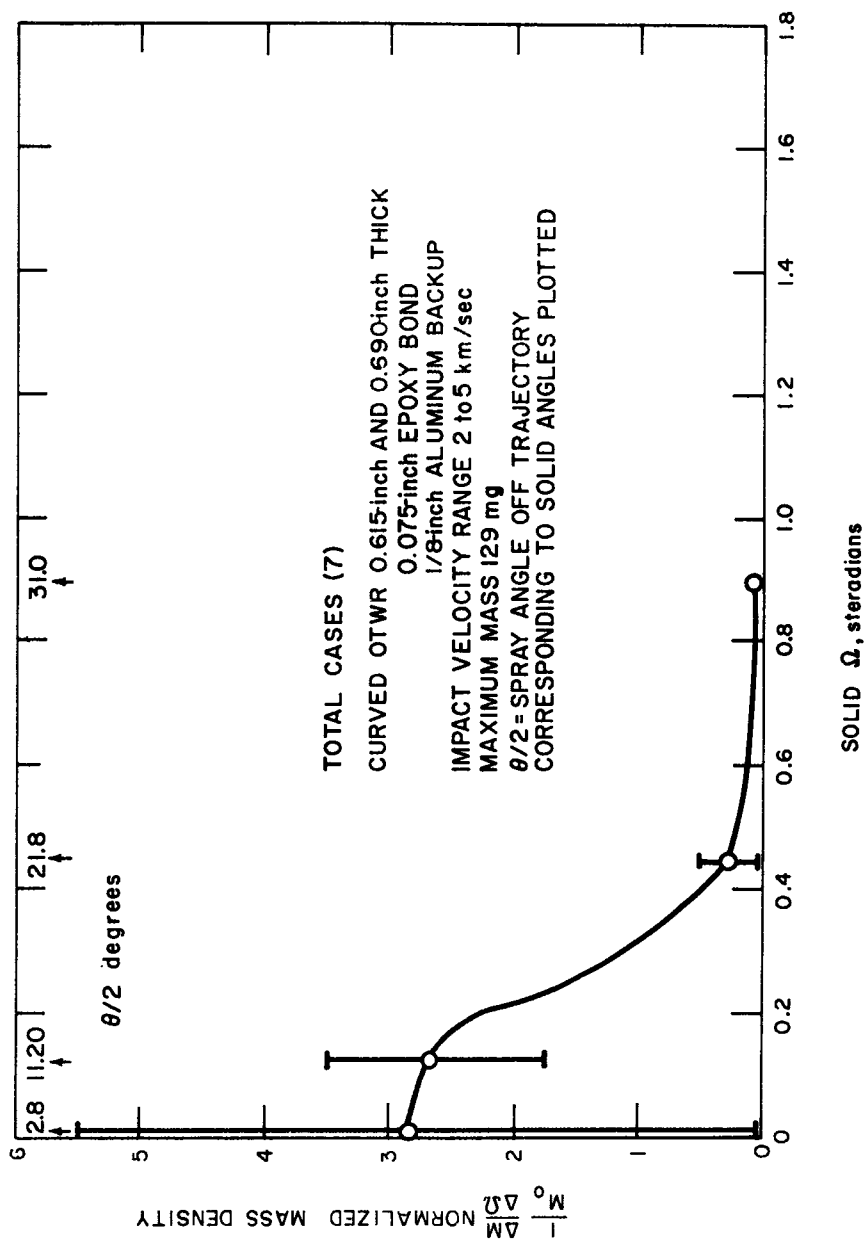


Figure 55 NORMALIZED MASS DENSITY VERSUS SOLID ANGLE
(TOTAL CASES)
62-9890

C87

SECRET

SECRET

G. SUMMARY AND CONCLUSIONS

The results of an investigation to determine the minimum impact conditions required to perforate a composite target are presented. The composite targets consisted of a flat plate of ablative heat shield material varying in thickness between 1/2 and 1-1/2 inches, bonded to either an aluminum or steel plate of 1/4- and 3/8-inch thicknesses. Steel projectiles varying in mass between 0.25 and 5.00 grams were launched with the Avco RAD light-gas gun at velocities up to 5.5 km/sec. All impacts were made normal to the target surface.

The impact of ablative material generally results in an irregular shaped crater or puncture consisting of an inner hole surrounded at the top and bottom surfaces of the heat shield plate by a region of spalled material. Measurements of front and back spall area, inside hole area, and the front and back spall depths (i.e., the depths from the front and back surfaces of the heat shield to the top and bottom of the inside hole) were made and correlated with the projectile energy, so that a reasonable description of the puncture profile in the heat shield material, can be given. The justification for such a detailed analysis is that a description of the heat shield damage is essential in analyzing the reentry heating effects on an impacted reentry vehicle subsequent to impact.

The various types of backup structure failure are described. The results indicate that the mechanism of perforation depends on projectile diameter to heat shield thickness ratio, as well as the heat shield to backup structure thickness ratio. For $d/t_h \approx 0.2$, the shock preceding the projectile target interface appears to do most of the damage, with little effect resulting from the broken projectile fragments. For $d/t_h \approx 0.5$ the moving projectile heat shield material behind the shock contributes strongly to the backup structure failure. For $t_h/t_b \approx 4$, the backup fails by bulging and petalling, whereas for smaller t_h/t_b (≈ 1.3) the target fails by spallation.

The minimum perforation condition is defined as a bulged backup containing a fracture either partly or completely through the thickness. It is shown that the minimum perforation condition can be described in terms of the projectile energy. The results have been correlated in terms of the projectile energy, target total thickness, and an effective target strength times density parameter, weighted according to heat shield and backup thickness. The correlation enables a determination of the minimum perforation energy to within 20 percent.

Several impacts were made with projectiles of varying mass on two targets to determine if the same mode of damage to the backup occurred at the same levels of projectile energy. The results showed that for the steel-backed target, a 3/16-inch diameter steel sphere having about 40 percent less kinetic energy than a 0.22-caliber sphere, produced the same damage mode (a minimum perforation condition) in the backup structure, for identical target configurations. For the aluminum-backed target, the 3/16-inch diameter sphere caused minimum

SECRET

SECRET

perforation at about 10 percent less energy than 0.22-caliber projectile. The indication is that the perforation energy appears to decrease somewhat with decreasing ball size. This effect should be examined further to substantiate the correlation presented. The overall conclusion concerning perforation as defined in this report and projectile impact parameters is that perforation is caused by a complex combination of shock effects and the secondary impact of the broken projectile material on the backup structure. Over the realm of ball size to heat shield thickness ratios, heat shield to backup structure ratios, and projectile velocities covered in this study, projectile energy is a meaningful term which correlates the results to within reasonable limits of accuracy.

Finally it is recommended that more controlled studies of this nature be carried out to further build up the knowledge of the complex phenomena associated with high velocity impact of ablative materials, as well as expand the data available to empirically predict heat shield damage and minimum perforation conditions. Studies should include projectiles other than steel, and other heat shield and backup structure materials.

C89

SECRET

SECRET

H. REFERENCES

1. Eckerman, J., W. McKay, Internal Ballistics of a Two-Stage Light Gas Gun, Avco RAD TM-60-62 (30 September 1960). Confidential
2. Carnevale, E., W. McKay, and J. A. Hull, Hypervelocity Impact Effects on Ablative Materials, Avco RAD TM-60-66 (10 October 1960). Secret
3. Perschino, M. and M. Rockowitz, Hypervelocity Impact into Ablative Materials, 6th Hypervelocity Impact Symposium, 30 April through 2 May 1963, Cleveland, Ohio.
4. Gehring, J. W., Observations of the Phenomena of Hypervelocity Impact, 4th Hypervelocity Impact Symposium, Eglin AFB (1960).
5. Kineke, J. H., Observations of Crater Formation in Ductile Materials, 5th Hypervelocity Impact Symposium, Denver, Colorado (1961).
6. Eichelberger, R. J., J. W. Gehring, Effects of Meteoroid Impacts on Space Vehicles, ARS Journal, 32, 10. p 1583 (October 1962).
7. Frasier, I. T., B. G. Korpor, Hypervelocity Impact Studies in Wax, 5th Hypervelocity Impact Symposium, Denver, Colorado (1961).
8. Herrmann, W., and A. H. Jones, Survey of Hypervelocity Impact Information, ASRL Report 991 (MIT) (September 1961).
9. Olshaker, A. E., R. L. Bjork, Hydrodynamics Applied to Hypervelocity Impact: Scaling Laws for Dissimilar Materials, 5th Hypervelocity Impact Symposium, Denver, Colorado (1961).
10. Bjork, R. L., Numerical Solutions to the Axially Symmetrical Hypervelocity Impact Process Involving Iron, RAND Corporation 3rd Hypervelocity Impact Symposium, II, (1958). Secret
11. Davids, W., Y. K. Huang, W. Jounzemis, Some Theoretical Models of Hypervelocity, 5th Hypervelocity Impact Symposium, Denver, Colorado (1961).
12. Duvall, G. E., Some Properties and Applications of Shock Waves, Response of Metals to High Velocity Deformation (AIME) Interscience Publications, New York (1961).

SECRET

SECRET

13. Wagner, M. H., N. A. Louie, Determination of Hugoniot Equations of State for Polymers and Reentry Vehicle Materials and Investigations of Fracture Phenomena, AFSWC TDR-62-66, I and II (August 1962).
Confidential
14. Bernier, R., The Calibration of a Collection Medium for the Determination of Particle Velocity, Preliminary Report, Ballistics Research Laboratory (1 June 1962).

C91

SECRET

SECRET

1. APPENDIX 1, SUMMARY OF IMPACT DATA

TABLE 7

IMPACT DATA FOR FIRST BATCH, HITCO OTWR ON ALUMINUM

Shot Number	Heat Shield Thickness (cm)	Backup Thickness (cm)	Velocity (m/sec)	Inside Diameter (cm)	Front Spall Area (cm ²)	Back Spall Area (cm ²)	Front Spall Depth (cm)	Back Spall Depth (cm)	Projectile Mass (grams)	Backup Fracture Mode	Bulge Height (cm)	Exit Diameter (cm)
26.3	1.56	0.635	4234	1.54	8.71	6.06	0.711	-	0.251	(2)	0.379	-
28.3	1.56	0.648	4147	1.49	14.9	6.39	0.572	-	0.251	(2)	0.454	-
25.3	1.56	0.640	3815	1.11	6.90	3.03	0.455	-	0.251	(1)	0.352	-
29.3	1.56	0.648	3175	0.89	4.96	4.45	0.449	0.414	0.251	(1)	0.214	-
30.3	1.59	0.648	2809	0.74	2.70	-	-	-	0.251	(1)	0.244	-
77.3	1.56	0.648	5301	3.53	30.7	20.6	0.980	0.480	0.7115	(6)	-	1.95
18.3	1.59	0.648	3862	2.27	25.2	8.97	0.810	0.442	0.7115	(6)	-	1.50
410.3	1.58	0.940	4086	3.12	32.5	11.5	0.757	-	0.7115	(6)	-	1.63
80.3	1.59	0.940	3605	1.96	21.5	9.23	0.805	0.409	0.7115	(3)	0.864	-
411.3	1.59	0.940	3425	1.86	17.2	7.94	0.858	0.409	0.7115	(3)	0.471	-
213.3	2.91	0.648	5325	2.10	26.3	19.74	1.49	1.23	0.7115	(3)	0.940	-
107.3	3.01	0.643	4643	1.69	48.0	12.52	1.02	0.762	0.7115	(1)	0.623	-
106.3	3.00	0.648	4190	2.67	37.9	22.4	1.60	1.10	1.485	(4)	-	1.97
108.3	2.98	0.942	4188	2.77	36.4	21.4	1.42	0.998	1.485	(3)	1.19	-
142.3	3.00	0.940	4432	3.35	69.8	23.87	1.46	0.937	2.038	(4)	-	1.13
141.3	2.98	0.937	4006	3.23	62.2	25.62	1.58	1.18	2.038	(3a)	1.92	-
179.3	4.14	0.655	4857	3.05	87.4	45.3	2.30	1.31	2.038	(4)	-	0.825
150.3	4.17	0.648	4322	2.90	60.5	39.9	1.94	1.35	2.038	(3a)	2.03	-
119.3	4.25	0.650	4763	2.24	39.0	27.7	2.13	1.79	1.485	(1)	0.995	-
191.3	4.12	0.645	5281	1.59	28.4	Just to Backup	-	-	0.7115	(1)	0.088	-
183.2	4.14	0.953	4907	3.09	54.8	41.1	2.03	1.27	2.038	(1)	1.05	-
169.3	4.14	0.953	4328	2.72	70.1	35.3	2.17	1.57	2.038	(1)	0.867	-

SECRET

SECRET

TABLE 8
IMPACT DATA FOR FIRST BATCH OF HICO OTWR ON STEEL

Shot Number	Heat Shield Thickness (cm)	Backup Thickness (cm)	Velocity (m/sec)	Inside Diameter (cm)	Front Spall Area (cm ²)	Back Spall Area (cm ²)	Front Spall Depth (cm)	Back Spall Depth (cm)	Projectile Mass (grams)	Backup Fracture Mode	Budge Height (cm)	Exit Diameter (cm)
413-1	1.62	0.678	5152	4.08	36.3	17.61	1.03	-	0.7115	6	-	0.785
412-1	1.60	0.678	4798	3.78	38.3	17.74	0.945	-	0.7115	(3a)	0.930	0
414-1	1.59	0.678	4439	3.60	34.3	15.61	0.866	-	0.7115	(3a)	0.858	0
90-3	1.59	0.940	5396	1.65	43.0	20.9	1.16	-	0.7115	6	-	0.195
70-3	1.59	0.940	5385	4.64	43.4	19.7	1.11	-	0.7115	6	-	0.150
114-3	3.02	0.673	4133	2.49	31.4	23.4	1.44	1.24	1.485	(1)	0.842	-
124-3	2.997	0.673	4088	3.81	64.4	24.5	1.71	1.21	2.038	(1)	1.20	-
167-3	3.061	0.638	4046	3.55	79.8	29.7	1.46	1.11	2.038	(1)	1.51	-
116-3	3.010	0.940	5036	3.13	40.7	20.7	1.33	0.963	1.485	(1)	0.495	-
126-3	2.997	0.940	4223	3.97	58.2	29.0	1.95	0.907	2.038	(1)	0.698	-
212-2	4.178	0.686	4542	5.95	227.3	77.7	3.11	1.36	4.861	(1)	2.75	-
201-2	4.161	0.686	3433	3.87	84.9	38.1	2.90	1.27	4.861	(1)	2.05	-

C93

SECRET

SECRET

TABLE 9
IMPACT DATA FOR SECOND BATCH OF HITCO OTWR

Shot Number	Heat Shield Thickness (cm)	Backup Thickness (cm)	Velocity (m/sec)	Inside Diameter (cm)	Front Spall Area (cm ²)	Back Spall Area (cm ²)	Front Spall Depth (cm)	Back Spall Depth (cm)	Projectile Mass (grams)	Backup Fracture Mode	Bulge Height (cm)	Exit Diameter (cm)
I. Aluminum Backups												
282-3	1.55	0.943	4721	2.75	23.4	10.6	0.762	-	0.4401	(6)	-	0.800
284-3	1.56	0.943	4458	2.73	26.2	8.71	0.943	-	0.4401	(3)	0.733	-
286-3	1.57	0.943	4248	2.79	25.5	7.81	0.795	-	0.4401	(2)	0.401	-
293-3	1.58	0.943	4578	1.73	14.9	4.71	0.759	-	0.251	(1)	0.168	-
292-3	1.54	0.943	4507	1.70	11.0	5.55	0.622	-	0.251	(1)	0.117	-
298-3	1.54	0.943	4499	2.41	24.4	7.09	0.719	-	0.354*	(1)	0.405	-
296-3	1.58	0.943	4348	2.17	17.98	7.87	0.739	-	0.356*	(1)	0.274	-
II. Steel Backups												
269-3	1.54	0.686	3851	4.13	49.3	18.6	0.986	-	1.037	(4)	-	1.14
266-3	1.54	0.698	3690	4.13	42.5	18.7	1.07	-	1.037	(1)	0.960	-
268-3	1.54	0.686	3537	3.85	32.5	15.0	0.952	-	1.037	(6)	-	1.11
290-3	1.54	0.652	4407	3.21	26.2	10.9	0.754	-	0.440	(2)	0.520	-
291-3	1.54	0.673	4392	2.98	28.5	10.3	0.756	-	0.440	(2)	0.395	-
295-3	1.54	0.676	4504	2.19	18.0	-	0.759	-	0.2505	(1)	0.142	-
297-3	1.54	0.673	4738	2.75	27.1	11.0	0.653	-	0.313*	(1)	0.363	-

*3/16-inch spheres with one flat side

SECRET

SECRET

TABLE 10
IMPACT DATA ON SCRAP OT WR

Shot Number	Heat Shield Thickness (cm)	Backup Thickness (cm)	Velocity (m/sec)	Inside Diameter (cm)	Front Spall Area (cm ²)	Back Spall Area (cm ²)	Front Spall Depth (cm)	Back Spall Depth (cm)	Ball Mass (grams)	Backup Fracture Mode	Bulge Height (cm)	Exit Diameter (cm)
192-3	1.57	0.318	4938	2.77	25.5	-	-	-	0.7112	5	-	4.06
6-2-61	1.57	0.318	3977	1.66	13.2	-	-	-	0.251	4	-	-
197	1.70	0.318	4572	3.12	32.7	26.5	0.734	0.498	0.7115	6	-	4.23
195	1.70	0.318	3353	2.74	33.2	-	-	-	0.7115	6	-	3.63
97-3	1.70	0.318	3945	1.55	17.6	-	-	-	0.251	5	-	-
2-28-62	1.89	0.318	4941	1.75	17.2	-	-	-	0.251	5	-	-
199-3	1.89	0.318	3962	2.82	32.6	12.4	0.892	0.688	0.7115	6	-	4.13
206-3	1.89	0.318	3840	2.73	28.4	11.5	0.830	0.612	0.7115	6	-	3.86
201-3	1.89	0.318	3475	2.49	30.1	11.9	0.777	0.439	0.7115	6	-	3.23
200-3	1.89	0.318	3188	1.92	21.9	9.48	0.663	0.716	0.7115	6	-	2.62
333-1	2.19	0.318	4947	3.15	22.3	17.8	1.12	0.612	0.7115	6	-	4.99
209-3	2.19	0.318	4257	2.57	21.8	16.5	0.861	0.554	0.7115	6	-	3.81

C95

SECRET

SECRET

TABLE 11
IMPACT DATA, ASTROLITE ON ALUMINUM AND STEEL

Shot Number	Heat Shield Thickness (cm)	Backup Thickness (cm)	Velocity (m/sec)	Inside Diameter (cm)	Front Spall Area (cm ²)	Back Spall Area (cm ²)	Front Spall Depth (cm)	Back Spall Depth (cm)	Ball Mass (grams)	Backup Fracture Mode	Bulge Height (cm)	Exit Diameter (cm)
I. Aluminum Backup-Steel Projectiles												
276-3	1.524	0.648	4812	1.52	19.35	6.13	0.226	0.287	0.2505	2	0.457	-
28-2	1.524	0.648	4099	2.12	34.39	-	-	-	0.7112	6	-	1.48
23-2	1.524	0.648	4099	2.16	32.97	-	-	-	0.7112	6	-	1.43
29-2	1.524	0.648	3328	1.55	19.87	-	-	-	0.7112	6	-	1.11
24-2	1.524	0.648	2633	1.02	8.08	-	-	-	0.7112	6a	-	0.914
25-2	1.524	0.648	2410	0.998	12.00	-	-	-	0.7112	6a	-	0.826
27-2	1.524	0.648	2238	0.787	2.97	-	-	-	0.7112	6a	-	0.571
26-2	1.524	0.648	2240	0.909	10.00	-	-	-	0.7112	6a	-	0.558
32-2	1.524	0.963	5080	2.95	54.47	15.42	0.831	0.561	0.7112	6	-	1.39
33-2	1.524	0.963	4501	2.45	42.68	11.81	0.335	0.325	0.7112	6	-	1.07
34-2	1.524	0.963	3928	2.34	36.00	-	-	-	0.7112	3	0.742	-
30-2	1.524	0.963	3212	1.76	25.68	-	-	-	0.7112	2	0.449	-
323-1	3.048	0.648	5174	2.07	44.26	14.45	1.13	1.22	0.7112	1	0.893	-
288-3	3.048	0.648	5094	2.06	26.00	14.98	0.909	1.79	0.7112	1	-	-
35-2	3.048	0.648	5038	2.17	29.81	17.86	1.55	1.19	0.7112	1	0.759	-
20-2	3.048	0.648	4958	2.06	-	-	-	-	0.7112	1	0.606	-
287-3	3.048	0.648	4422	2.80	44.07	16.97	1.63	0.925	1.485	5	-	2.89
289-3	3.048	0.648	4367	2.67	65.36	17.47	1.69	0.952	1.485	5	-	2.39

SECRET

SECRET

TABLE 11 (Concl'd)

Shot Number	Heat Shield Thickness (cm)	Backup Thickness (cm)	Velocity (m/sec)	Inside Diameter (cm)	Front Spall Area (cm ²)	Back Spall Area (cm ²)	Front Spall Depth (cm)	Back Spall Depth (cm)	Ball Mass (grams)	Backup Fracture Mode	Bulge Height (cm)	Exit Diameter (cm)
II. Steel Backups-Steel Projectiles												
170-3	1.524	0.686	5293	3.32	43.04	-	1.15	none	0.7112	6	-	0.615
277-3	1.524	0.686	5225	3.32	51.57	-	1.16	none	0.7112	6	-	0.660
182-3	1.524	0.686	4535	2.96	47.87	-	1.07	none	0.7112	3a	1.042	-
278-3	1.524	0.686	4119	3.03	42.80	-	1.40	none	0.7112	1	0.658	-
III. Aluminum Backups-Tungsten Carbide Projectiles												
38-2	3.048	0.686	4877	2.13	-	-	-	-	1.382	1	-	-
36-2	3.048	0.686	3679	1.47	-	-	-	-	1.382	5	-	2.11
37-2	3.048	0.963	3680	1.27	19.94	-	-	-	1.382	5	-	1.26

SECRET

SECRET

TABLE 12
IMPACT DATA, RAD 60 HD ON 6061T6 AL

Shot Number	Heat Shield Thickness (cm)	Backup Thickness (cm)	Velocity (m/sec)	Inside Diameter (cm)	Front Spall Area (cm ²)	Back Spall Area (cm ²)	Front Spall Depth (cm)	Back Spall Depth (cm)	Ball Mass (grams)	Backup Fracture Mode	Bulge Height (cm)	Exit Diameter (mm)
220-3	1.44	0.615	4795	1.50	16.19	6.58	0.749	0.312	0.1304	1	0.189	-
228-3	1.44	0.615	4605	1.37	19.16	4.25	0.732	-	0.1304	1	0.174	-
240-3	1.44	0.615	4348	0.989 ^a	13.81	-	-	-	0.1304	1	0.150	-
227-3	1.44	0.615	4185	1.22	15.64	-	-	-	0.1304	1	0.144	-
241-3	1.44	0.615	4701	1.96	23.87	9.94	0.808	0.376	0.2505	4	-	0.694
242-3	1.44	0.615	3908	1.80	18.52	6.77	0.703	0.328	0.2505	2	0.494	-
281-3	1.46	0.615	5134	4.25	42.26	23.68	0.894	0.363	0.7112	6	-	2.48
212-3	2.77	0.615	5307	2.68	31.94	29.03	0.800	0.610	0.7112	3	1.15	-
207-3	2.82	0.615	4110	3.36	64.5	40.7	1.14	0.730	1.485	4	-	1.09
206-3	3.15	0.615	4983	2.28	42.71	32.91	0.980	0.998	0.7112	1	0.725	-
204-3	3.16	0.615	4689	2.10	40.2	37.5	0.889	1.17	0.7112	1	0.665	-
214-3	3.16	0.953	5006	2.46	84.91	39.55	1.13	1.02	0.7112	1	0.254	-
215-3	3.11	0.953	4728	3.32	96.19	52.51	1.10	1.17	1.485	4	-	1.00

^a Backup not exposed.

SECRET

SECRET

J. APPENDIX 2, SUMMARY OF SPALL DATA

To understand the spall data requires comment about the meaning of the numbers in the tables and the methods used to collect them. For each particle in the table, mass, velocity, and angle distributions with respect to the axis of impact are listed. Most of the particles have been individually weighed. In the case of iron dust composed of particles with mass of less than 0.1 milligram, the weight of 10 particles has been measured and the number of particles in the dust has been found by dividing the total mass by the mass of 10 and multiplying by 10. In such cases, the number given under mass in the tables is the total mass of dust, and the number in parentheses is the number of dust particles making up the mass.

Two methods of collecting the particles were used. First, the easily accessible particles were picked, and the distance from the impact axis was determined to the nearest 1/4 inch, and the penetration determined to the nearest 1/4 (1/8 inch) sheet. In such cases, the numbers would be exact. After the sheets were picked, they were ruled into 2-inch-wide circular zones about the center of impact, and the zones cut out of each sheet. Each zone was burned to ash separately. The iron was removed with a magnet, and the charcoal washed away leaving the aluminum particles.

For the particles recovered after burning, the angle represents the angle to the midpoint of the zone, and the penetration is taken as the midpoint of the Maftex sheet for each particle. This is the reason for the repeated angles in the tables. The particles are assumed to be found symmetrically about the center of impact.

The distance between the back face of the target and the first Maftex sheet in all cases is 10 inches.

C99

SECRET

SECRET

TABLE 13

SHOT NO. 195

OTWR 0.615-INCH THICK

(Projectile 0.221-caliber Steel Sphere, Mass 0.72 gram
Velocity 3353 m/sec)

	Mass (10 ³ grams)	Spray Angle (degrees)	Velocity (m/sec)		Mass (10 ³ grams)	Spray Angle (degrees)	Velocity (m/sec)
I. Aluminum	14.2	5.3	619	II. Steel	131.5	0	522
	0.7	6.3	1335		10.0	3.9	769
	25.7	7.9	534		7.1	5.1	841
	4.0	7.9	858		1.6	5.6	407
	3.8	8.3	522		5.2	5.6	301
	42.9	13.7	384		11.7	6.6	551
	34.8	16.4	409		12.1	7.6	796
	50.0	16.8	544		10.2	10.6	574
	2.2	20.4	624		5.6	10.6	669
	1.1	20.4	745		7.1	10.6	630
	2.5	20.4	604		5.2	10.6	682
	2.6	20.4	598		6.2	10.6	652
	2.3	20.4	617		7.4	10.6	623
	4.5	20.4	520		8.6	10.6	600
	6.3	20.4	477		(20) 58.2	10.6	791
	19.4	21.3	360		(100) 24.1	10.6	1493
	12.2	21.3	404		(100) 149.0	10.6	938
	0.8	21.3	811		6.7	11.1	384
	0.7	21.3	839		5.0	11.1	414
	1.1	21.3	748		7.6	13.1	623
	8.2	21.3	448		(160) 55.9	20.4	625
	71.2	21.8	846		(30) 11.7	20.4	608
	20.4	21.6	799				
Total	331.8			Total	547.7		
Minimum	0.7	5.3	360	Minimum	0.24	0	301
Maximum	71.2	21.8	1335	Maximum	131.5	20.4	1493
Average	14.4		637	Average	1.3		907
Number	23			Number	427		

C100

SECRET

SECRET

TABLE 14

SHOT NO. 197

OTWR 0.615-INCH THICK

(Projectile 0.221-caliber Steel Sphere, Mass 0.72 gram
Velocity 4572 m/sec)

	Mass (10 ³ grams)	Spray Angle (degrees)	Velocity (m/sec)		Mass (10 ³ grams)	Spray Angle (degrees)	Velocity (m/sec)
I. Aluminum	109.9	6.6	554	II. Steel	(26) 71.8	2.8	793
	38.6	7.3	1209		38.9	7.0	756
	16.9	9.7	483		(6) 14.1	10.1	1215
	30.6	10.1	1007		(50) 161.	10.5	823
	2.6	10.5	1298		(280) 137.6	11.1	555
	2.3	10.5	1339		(300) 49.6	21.3	761
	5.9	10.5	1053		(80) 19.1	30.3	731
	8.0	10.5	974				
	25.8	10.5	723				
	47.7	10.5	618				
	51.2	10.5	607				
	(11) 22.9	11.1	613				
	(6) 16.0	21.3	597				
	44.6	30.3	414				
	28.1	30.3	756				
	25.3	30.3	797				
	42.5	31.2	787				
	90.2	33.0	588				
	12.4	33.0	586				
Total	621.5			Total	492.		
Minimum	2.1	6.6	414	Minimum	0.017	2.8	555
Maximum	109	33.0	1209	Maximum	161	30.3	1215
Average	18.3		708	Average	0.662		653
Number	34			Number	743		

C101

SECRET

SECRET

TABLE 15

SHOT NO. 199

OTWR 0.690-INCH THICK

(Projectile 0.221-caliber Steel Sphere, Mass 0.72 gram
Velocity 3962 m/sec)

	Mass (10 ³ grams)	Spray Angle (degrees)	Velocity (m/sec)		Mass (10 ³ grams)	Spray Angle (degrees)	Velocity (m/sec)
I. Aluminum	1.7	2.8	2083	II. Steel	8.2	2.8	874
	0.7	2.8	799		(6) 14.5	2.8	634
	(3) 1.7	2.8	800		(19) 10.9	2.8	1183
	22.6	3.1	1306		(5) 9.9	2.8	862
	20.7	9.3	854		5.4	2.8	668
	29.3	10.1	1018		8.5	2.8	595
	3.2	10.1	1791		5.9	2.8	653
	(7) 4.7	10.1	968		4.6	2.8	696
	4.1	10.5	515		3.6	3.1	639
	11.1	10.5	399		9.60	7.6	782
	8.9	10.5	412		31.7	10.1	626
	0.8	10.5	781		10.0	10.1	840
	0.1	10.5	1327		11.5	10.1	811
	(15) 5.1	10.5	971		6.6	10.1	934
	29.1	11.8	1024		(4) 10.5	10.1	1182
	5.7	12.0	2093		(12) 20.3	10.5	405
	110.3	13.1	563		9.7	10.5	445
	43.5	19.2	729		(80) 22.8	10.5	634
	4.4	20.4	523		93.6	12.0	642
	1.9	20.4	648		2.7	12.0	1584
	52.9	24.9	637		5.1	12.0	1347
	67.9	34.9	291		3.5	13.7	339
					(11) 6.9	13.7	525
					1.3	13.7	436
					1.5	13.7	421
					(100) 8.4	13.7	2890
					(14) 53.9	20.4	565
					(15) 18.1	20.4	760
					17.7	20.4	385
					9.2	20.4	453
					7.3	20.4	480
					5.6	20.4	514
					(10) 12.1	20.4	456
					8.2	20.4	915
					(160) 33.9	20.4	711
					1.2	30.5	465
					0.8	30.5	538
					1.4	30.5	466
					(300) 65.2	30.5	750
Total	430.4			Total	562		
Minimum	0.34	2.8	291	Minimum	0.084	2.8	405
Maximum	110.3	34.9	2093	Maximum	93.6	30.5	2890
Average	9.8		972	Average	0.75		1001
Number	44			Number	762		

C102

SECRET

SECRET

TABLE 16

SHOT NO. 201

OTWR 0.690-INCH THICK

(Projectile 0.221-caliber Steel Sphere, Mass 0.72 gram
Velocity 3475 m/sec)

	Mass (10 ³ grams)	Spray Angle (degrees)	Velocity (m/sec)		Mass (10 ³ grams)	Spray Angle (degrees)	Velocity (m/sec)
I. Aluminum	6.3	2.8	456	II. Steel	46.3	2.8	562
	2.5	2.8	577		28.2	2.8	638
	(2) 1.5	2.8	799		4.9	2.8	997
	4.1	2.8	2131		(10) 0.4	2.8	3398
	42.6	7.0	468		16.7	2.8	5001
	129.6	10.5	478		(35) 0.9	2.8	2630
	11.1	11.1	399		16.1	2.8	252
	6.5	11.1	458		4.0	2.8	321
	3.2	11.2	549		(25) 3.0	2.8	785
	103.1	15.6	637		(3) 2.2	2.8	2703
	8.3	17.6	732		(50) 1.7	2.8	454
	33.7	18.9	417		3.3	2.6	687
	49.5	20.4	783		83.2	7.3	662
	58.6	21.4	366		11.9	8.3	330
	14.9	21.4	385		11.7	9.3	684
	9.8	21.4	428		12.6	9.7	791
	2.6	21.4	601		11.4	9.7	812
	2.2	21.4	627		7.9	9.7	891
	1.5	21.4	691		6.1	9.7	951
					(2) 3.8	9.7	1281
					(100) 12.9	9.7	2544
					(50) 1.3	9.7	4904
					(7) 32.5	10.5	704
					12.4	10.5	546
					8.0	10.5	607
					8.2	10.5	619
					7.6	10.5	610
					(4) 5.2	10.5	971
					(20) 1.3	10.5	2085
					(6) 24.3	11.0	324
					(100) 63.2	11.0	521
					9.3	11.0	262
					2.6	13.7	1531
					14.3	17.6	400
					26.3	20.4	467
					(90) 3.4	20.4	1378
					5.8	21.4	286
					(100) 30.1	21.4	532
					(3) 3.3	30.5	496
					(200) 34.0	30.5	798
Total	491.6			Total	582.3		
Minimum	0.75	2.8	799	Minimum	0.038	2.8	252
Maximum	129.6	21.4	366	Maximum	83.2	30.5	3398
Average	24.6		639	Average	0.79		1631
Number	20			Number	828		

C103

SECRET

SECRET

TABLE 17

SHOT NO. 204

OTWR 0.615-INCH THICK

(Projectile 0.221-caliber Steel Sphere, Mass 0.72 gram
Velocity 2020 m/sec)

	Mass (10 ³ grams)	Spray Angle (degrees)	Velocity (m/sec)		Mass (10 ³ grams)	Spray Angle (degrees)	Velocity (m/sec)
I. Aluminum	0.9	0.8	748	II. Steel	(50) 0.7	2.8	1358
	8.2	7.0	574		702.0*	0	701
	1.6	7.0	871		2.5	11.1	367
	0.3	7.0	1335		(6) 1.1	11.1	714
	(4) 23.9	11.1	463		(50) 5.4	11.1	817
	(5) 13.5	11.1	573		0.4	21.3	607
	(5) 7.0	11.1	678		(3) 0.3	21.3	846
	(5) 3.1	11.1	834		(50) 5.9	21.3	829
	13.2	11.1	383				
	9.1	11.1	421				
	11.3	11.1	398				
	10.0	21.3	426				
	3.5	21.3	557				
Total	105.6			Total	718.3		
Minimum	0.3	0.8	398	Minimum	0.014	2.8	367
Maximum	13.2	21.3	1335	Maximum	702.0	21.3	1358
Average	3.8		643	Average	4.4		982
Number	28			Number	162		

* The sphere came through intact.

C104

SECRET

SECRET

TABLE 18

SHOT NO. 206

OTWR 0.690-INCH THICK

(Projectile 0.221-caliber Steel Sphere, Mass 0.72 gram
Velocity 3840 m/sec)

	Mass (10 ³ grams)	Spray Angle (degrees)	Velocity (m/sec)		Mass (10 ³ grams)	Spray Angle (degrees)	Velocity (m/sec)
I. Aluminum	18.7	2.8	346	II. Steel	4.7	2.8	1008
	38.0	10.1	953		(30) 0.4	2.8	4526
	49.9	10.5	537		(22) 42.9	2.8	865
	110.5	10.5	589		(40) 6.5	2.8	1638
	5.6	10.5	475		5.0	2.8	681
	8.1	10.5	433		7.3	2.8	618
	2.9	10.5	562		4.3	2.8	707
	3.0	10.5	557		7.0	2.8	278
	2.5	10.5	480		5.2	2.8	300
	(3) 2.7	10.5	757		3.2	2.8	340
	7.3	11.0	445		(100) 18.1	2.8	708
	9.3	11.0	418		4.5	5.4	312
	22.8	17.6	458		2.2	5.4	842
	47.5	18.1	380		31.7	5.4	621
	0.9	18.1	1050		13.7	5.4	769
	8.9	20.4	437		14.7	5.4	755
	4.8	20.4	511		(4) 26.6	5.4	925
	1.0	20.5	763		(200) 22.3	5.4	2631
	10.0	29.2	446		(50) 1.4	5.7	4780
	(6) 1.4	29.2	1210		18.8	8.9	662
					3.7	9.3	1080
					(10) 38.1	10.1	738
					(2) 6.9	10.1	756
					(18) 28.4	10.1	924
					(50) 15.4	10.1	1400
					(17) 36.5	10.5	380
					(200) 71.3	11.5	603
					11.9	13.7	753
					51.5	20.2	175
					(300) 76.4	20.4	717
Total	355.8			Total	580.6		
Minimum	0.9	2.8	340	Minimum	0.028	2.8	175
Maximum	110.5	29.2	1210	Maximum	51.5	20.4	4780
Average	12.7		781	Average	0.68		1466
Number	27			Number	1059		

C105

SECRET

SECRET

TABLE 19

SHOT NO. 209

OTWR 0.812-INCH THICK

(Projectile 0.221-caliber Steel Sphere, Mass 0.72 gram
Velocity 4257 m/sec)

	Mass (10 ³ grams)	Spray Angle (degrees)	Velocity (m/sec)		Mass (10 ³ grams)	Spray Angle (degrees)	Velocity (m/sec)
I. Aluminum	101.7	7.9	443	II. Steel	(20) 20.0	2.8	457
	105.5	8.3	224		4.4	2.8	313
	183.8	8.9	588		(100) 15.4	2.8	737
	1.1	10.1	1614		0.6	2.8	1703
	130.3	10.5	536		(40) 0.2	2.8	5770
	6.0	10.5	1174		(10) 39.1	2.8	725
	12.9	10.5	384		6.2	2.8	644
	1.6	10.5	654		(8) 3.1	2.8	1307
	1.2	12.4	707		(50) 2.1	2.8	1281
	32.7	20.4	314		9.3	4.2	349
	2.6	20.4	598		35.4	5.0	558
	0.5	20.4	911		7.8	5.3	752
	0.4	20.4	964		17.7	7.3	1021
	12.7	30.4	423		(5) 0.1	10.1	2718
	22.4	30.4	366		20.1	10.1	702
	2.2	30.4	662		(200) 5.8	10.1	2014
					(7) 38.5	10.6	672
					(5) 7.0	10.6	953
					(200) 15.3	10.6	2004
					(30) 43.9	10.6	317
					(9) 31.6	10.6	336
					9.4	10.6	693
					(600) 73.7	10.6	791
					(30) 0.5	19.6	4475
					(5) 6.1	19.6	1017
					(4) 26.2	19.6	663
					(2) 21.5	19.6	489
					(60) 5.2	19.6	2000
					(11) 28.7	21.3	376
					9.8	21.3	269
					10.6	21.3	263
					(9) 7.3	21.3	-
					(600) 58.6	21.3	-
					(500) 40.9	30.4	-
Total	617			Total	622.1		
Minimum	0.4	7.9	224	Minimum	0.005	2.8	263
Maximum	183.8	30.4	1614	Maximum	35.4	30.4	5770
Average	38.5		660	Average	0.240		1333
Number	16			Number	2597		

C106

SECRET

SECRET

TABLE 20

SHOT NO. 200*

OTWR 0.690-INCH THICK

(Projectile 0.221-caliber Steel Sphere, Mass 0.72 gram
Velocity 3188 m/sec)

	Mass (10 ³ grams)	Spray Angle (degrees)	Velocity (m/sec)
Aluminum	81.5	5.3	660
	9.9	5.3	1130
	3.7	5.3	1453
	16.1	8.3	487
	18.5	11.1	585
	65.9	11.8	705
	23.4	13.7	449
	8.2	17.6	594
	21.2	22.6	477
	6.0	21.3	485
	7.0	21.3	467
	4.6	21.3	519
	1.9	21.3	651
	64.2	23.7	268
	32.8	30.3	448
	9.3	34.4	473
	93.8	35.3	356
Total	468		
Minimum	1.9	5.3	268
Maximum	93.8	38.3	1453
Average	27.5		600
Number	17		

*Steel data not recorded.

C107

SECRET

SECRET

(NOT USED)

C108

SECRET

SECRET

DISTRIBUTION

<u>Addressee</u>	<u>Copy No.</u>
Director, U.S. Naval Research Laboratory (Code 1570)	1-150
Central File	151
Document Control	152-176
Research Library	177-178
Yellow File	179

C109

SECRET

SECRET

(NOT USED)

C110

SECRET

SECRET

DOCUMENT NO. 63SD823

This document contains 99 pages

Copy number 24 of 198 copies

HYPERVELOCITY KILL MECHANISMS PROGRAM (U)

Aerothermal Phase

Annual Progress Report

For Period Ending

30 September 1963

SPONSORED BY

Advanced Research Projects Agency
Ballistic Missile Defense Systems Branch
ARPA Order No. 149-60
Program Code No. 3730

This research was supported by the Advanced Research Projects Agency, Ballistic Missile Defense Systems Branch, and was monitored by the U. S. Naval Research Laboratory (Code 6240) under Contract No. Nonr 3295-(00)(X).

CONTRACTOR, GENERAL ELECTRIC COMPANY RE-ENTRY SYSTEMS DEPARTMENT

D. E. Nestler, Technical Director

G. S. Badders, Program Manager

NOTICE: This document contains information affecting the national defense of the United States within the meaning of the Espionage Laws, Title 18 U.S.C., Sections 793 and 794. Its transmission or the revelation of its contents in any manner to an unauthorized person is prohibited by law.

DOWNGRADED AT 12 YEAR INTERVALS;
NOT AUTOMATICALLY DECLASSIFIED.
DOD DIR. 5200.10

Reproduction of this report in whole or in part is
permitted for any purpose by the United States Government

GENERAL  ELECTRIC

L.A.N: 4148-30-1

RE-ENTRY SYSTEMS DEPARTMENT
A Department Of The Missile and Space Division
3128 Chestnut Street, Philadelphia 4, Penna.

SECRET

H-i

SECRET

SECRET

H-11

SECRET

CONTENTS

Section	Page
SUMMARY	H-1
I WALLOPS ISLAND FLIGHT PROGRAM	H-3
A. General Discussion	H-3
B. Detailed Analysis of Flight One Results	H-5
C. Detailed Analysis of Flight Two Results	H-8
D. Results of Malta Rocket Exhaust Tests of Flight Models	H-10
E. Comparison of Flight and Ground Test Results	H-14
II INTERNAL HEATING TESTS IN THE C. A. L. WAVE SUPER- HEATER HYPERSONIC TUNNEL	H-15
III WIND TUNNEL ORIFICE FLOW TESTS	H-17
IV MALTA INTERNAL PERFORMANCE TESTS	H-18
V PARAMETRIC COMPUTATIONS	H-19
A. Internal Heating Computer Program	H-19
B. Thermal Kill Study - C-1 Target Model	H-22
VI STRUCTURAL STUDIES	H-23
A. Introduction	H-23
B. Summary	H-24
C. Future Work Required	H-27
D. C-1 Vehicle Studies	H-27
E. Shells with Cut-Outs	H-31
F. Mark 3 Studies	H-32
G. Aerostructural Kill	H-34
VII ICBM FLIGHT EXPERIMENTS	H-35
APPENDIX A. Discharge Coefficients into Supersonic Free Stream.	H-36
APPENDIX B. External Viscous Effects on Internal Heating	H-36
APPENDIX C. Compressible Shear Layer Analysis of Internal Heat Transfer Downstream of Perforation	H-37
APPENDIX D. Coupled Flow Heating	H-41
APPENDIX E. Improved Correlation of Axial Velocity Decay of Compressible Jets	H-44
REFERENCES	H-45
NOMENCLATURE	H-49

SECRET

SECRET

SECRET

H-iv

SECRET

ILLUSTRATIONS

Figure		Page
1	Wallops Island Flight Model	H-53
2	Inlet and Exit Orifice Designs, Configuration One	H-53
3	Inlet Orifice Design, Configuration Two	H-54
4	Malta Test M1A Instrumentation Location	H-54
5	Malta Test M2A Instrumentation Location	H-54
6	Recovered Experiment Section, Flight One	H-55
7	Recovered Experiment Section, Flight Two	H-55
8	Wallops Island Flight Test Trajectories	H-56
9	Internal Pressure History, Flight One	H-56
10	Typical Thermocouple Responses, Flight One	H-57
11	Heat Flux Map for Flight One at 88 Seconds	H-58
12	Heat Flux Map for Flight One at 94 Seconds	H-58
13	Distribution of Heat Flux away from Impingement Point, Configuration One	H-59
14	Internal Pressure History, Flight Two	H-59
15	Typical Thermocouple Responses, Flight Two	H-60
16	Heat Flux Map for Flight Two at 88 Seconds	H-61
17	Heat Flux Map for Flight Two at 91 Seconds	H-61
18	Map of Heat Flux Distribution for Malta Test M1A $\theta = 4$ Seconds, $\dot{q} \sim \text{BTU/ft}^2\text{sec}$	H-62
19	Map of Heat Flux Distribution for Malta Test M2A $\theta = 4$ Seconds, $\dot{q} \sim \text{BTU/ft}^2\text{sec}$	H-62
20	Radial Distribution of Heat Flux away from Impingement Point	H-63
21	Internal Heating Model, Cornell Aeronautical Laboratory Tests	H-63
22	Internal Heating Model, with 6 inch Diameter Insert Installed	H-64
23	Internal Calorimeter-Thermocouple and Pressure Locations	H-64
24	Structural Cone Thermocouple and Pressure Locations	H-65
25	Impact Target to be Used in Orifice Flow Tests	
	(a) Front Surface	H-66
	(b) Back Surface	H-66
26	Schematic Diagram of Orifice Flow Tests	H-67
27	Probe Rake for Orifice Flow Tests	H-67
28	Block Diagram of the HKM Internal Heating Computer Program	H-68
29	Wallops Island Flight One Stagnation and Internal Pressures for Variation in f_w	H-68
30	Wallops Island Flight One Heat Flux to Back Plate for Variations in f_w	H-69
31	Wallops Island Flight One Stagnation and Internal Pressures for Variations in Vent Flow Coefficients	H-69
32	Wallops Island Flight One Heat Flux to Back Plate for Variations in Vent Flow Coefficient	H-70
33	Perforation Diameter Required for Thermostructural Kill of C-1 Type Targets (Based on $A/V^{2/3} = 0.05$)	H-70
34	Altitude of Kill vs Altitude of Hit, Forecone Perforation, C-1 Target (Monocoque Structure), Thermostructural Kill ..	H-71

SECRET

SECRET

ILLUSTRATIONS (Cont'd)

Figure		Page
35	Altitude of Kill vs Altitude of Hit, Payload or Aft Cone Perforation, C-1 Target (Monocoque Structure) Thermostructural Kill	H-71
36	Maximum Structure Thickness Which Can Be Melted by a Specified Altitude, C-1 Target (Monocoque Structure)	H-72
37	Failure Regime; Nose Impact, Aluminum Monocoque Forecone	H-72
38	Failure Regime; Nose Impact, Stainless Steel Monocoque Forecone	H-72
39	Failure Regime; Nose Impact, Inconel Monocoque Forecone . .	H-73
40	Hit vs Kill Altitude; Aluminum Monocoque Forecone	H-74
41	Hit vs Kill Altitude; Stainless Steel Monocoque Forecone . . .	H-74
42	Hit vs Kill Altitude; Inconel Monocoque Forecone	H-75
43	Effect of Hole Size; Cone Impact, Aluminum Monocoque Forecone	H-75
44	Effect of Hole Size; Cone Impact, Stainless Steel Monocoque Forecone	H-76
45	Effect of Hole Size; Cone Impact, Inconel Monocoque Forecone	H-76
46	Effect of Construction; Cone Impact, Aluminum Honeycomb Sandwich Forecone	H-77
47	Effect of Construction; Cone Impact, Stainless Steel Honeycomb Sandwich Forecone	H-77
48	Effect of Construction; Cone Impact, Inconel Honeycomb Sandwich Forecone	H-78
49	Effect of Construction; Cone Impact Ring Stiffened Shell Forecone	H-78
50	Critical Moment Ratio vs Cutout Angle	H-79
51	Trajectory Data, Mark 3 IOC	H-79
52	Forecone Geometry and Pressure Distribution	H-80
53	Failure Regime; Cone Impact	H-80
54	Forecone Temperature Rise, Coupled Flow ($A = .05 V^{2/3}$) . .	H-81
55	Hit vs Kill Altitude; Forecone	H-81
56	Influence of Temperature Change	H-82
57	Effect of Hole Size on Melting Altitude	H-83
58	Effect of Hole Size on $T = 0^\circ\text{F}$ Failure Condition	H-83
59	Material Comparison, Vehicle No. 4 ($W/C_D A = 4375$)	H-84
60	Construction Comparison, Vehicle No. 4 ($W/C_D A = 4375$) . .	H-84
61	Vehicle ($W/C_D A$) Comparison, Monocoque Structure	H-85
62	WAC/HKM Experiment Configuration	H-85
A-1	Discharge Coefficients into Free Stream of $M = 3.25$ (Vick, Reference 12)	H-86
A-2	Effect of External Mach Number on Discharge into Free Stream (Vick, Reference 12)	H-86
B-1	Variation of Relative Inlet Flow Rate with Inlet and Exit Orifice Diameters	H-87
C-1	Shear Layer Flow Past a Perforation	H-88
C-2	Laminar Shear Layer Profiles for C. A. L. Internal Heating Tests, $D = 3$ Inches	H-88
C-3	Effect of Mach Number on Turbulent Mixing Parameter	H-89

SECRET

SECRET

Figure	ILLUSTRATIONS (Cont'd)	Page
C-4	Turbulent Shear Layer Profiles for C. A. L. Internal Heating Tests, D = 3 Inches	H-89
E-1	Comparison of Experimental Axial Velocity Jet Decay to Adjusted Kleinstein Method	H-90
E-2	Comparison of Experimental Axial Velocity Decay with Theoretical and Empirical Predictions, Chicago Midway Arc Jet, M = .74	H-91
E-3	Comparison of Experimental Axial Velocity Decay with Theoretical and Empirical Predictions; Bezmenov Data (Reference 49)	H-91

TABLES

Table		Page
1.	Tabulation of Wall Thicknesses, Heat Fluxes, and Front Surface Temperatures at $\theta = 4$ Seconds	H-11
2.	Summary of Analysis of Malta Rocket Exhaust Test Results. .	H-12
3.	Summary of Flight and Ground Test Results	H-15
4.	Nominal Test Conditions for Cornell Aeronautical Laboratory Internal Heating Tests	H-16
5.	Test Agenda for Cornell Aeronautical Laboratory Internal Heating Tests	H-16
6.	Orifice Flow Test Agenda	H-18
7.	Malta Rocket Exhaust Test Schedule	H-19
8.	Material Comparison	H-25
9.	Mark 3 Forecone Performance	H-26
10.	Location of Hit Comparison	H-28
11.	Hole Sizes, C-1 Study	H-29
12.	Effect of Hole Size	H-29
13.	Configuration Comparison	H-30
14.	Hole Sizes, Mark 3 Study.	H-34
15.	Design Load Conditions	H-34
16.	Induced Trim	H-35

SECRET

SECRET

SECRET

H-viii

SECRET

SUMMARY

Under the Aerothermal Phase of the program, GE-RSD has continued thermal and structural studies designed to develop the technology required to assess the potential of thermostructural kill (during re-entry) of a re-entry vehicle which has been damaged by hypervelocity impact.

Significant progress has been achieved in flight and ground tests of vented models containing relatively small perforations. A two-flight program was conducted jointly with NASA Langley Research Center which resulted in successful telemetry of data and recovery of experiment payloads for both flights. As part of this program, rocket exhaust tests were conducted using models identical to the flight models. Analysis of the results thus far has indicated general agreement of internal heating patterns from flight and ground tests. However, unexplained anomalies exist between flight and ground results in internal pressure and impingement heat flux during the later portion of the first flight.

In order to pursue the "coupled flow" regime associated with relatively large perforations in unvented vehicles, an internal heat transfer model was designed, built, and tested in Cornell Aeronautical Laboratory's Wave Superheater Hypersonic Tunnel. Relatively low internal fluxes were measured for all orifices tested, for a range of $A/V^{2/3}$ from .01 to 0.20. These results were in reasonable agreement with a relation for energy influx through a single perforation developed by Donaldson, which predicts large internal heating for higher pressure environments typical of ICBM re-entry. Further testing of the model has been proposed at higher pressures in AEDC Tunnel C.

An analysis of two C.A.L. tests in which the model was vented disclosed the importance of external viscous effects on internal energy influx. Measured internal heat fluxes were an order of magnitude lower than predicted by theory using inviscid flow relations, whereas proper allowance for approach boundary layer velocity and enthalpy profiles yielded good agreement of theory and experiment.

An orifice flow test program is under way to determine flow characteristics of orifices having supersonic tangential approach flow. Flow rate, jet velocity profiles, and jet direction will be determined over a Mach number range from 1.5 to 5.0, for various orifice diameters, wall thicknesses, and orifice pressure ratios. Two tests will include actual impacted sections. All hardware has been designed, fabricated, and shipped to AEDC. Testing is scheduled for October 1963.

A new program of ground tests has been initiated in which seven models will be tested in the GE Malta Rocket Exhaust Facility. The primary objective of the program is to determine the effect of relatively large perforations on thermostructural behavior of unvented re-entry vehicle models. These tests will provide a crucial comparison of the effects of drilled vs. actual impact perforations in typical ablative heat shield-metal backup structures. Fabrication of the models has begun, with initial testing scheduled for December 1963.

The internal heating digital computer program developed by General Electric's Re-entry Systems Department has been modified by the addition of several subroutines to increase its capability and reduce the IBM 7090 calculation time and costs. Parametric studies were conducted using the program to evaluate the internal heating of the first Wallops Island flight vehicle as a function of internal energy partition factor and vent flow coefficient.

SECRET

SECRET

Results are presented of a thermal kill study conducted on the C-1 Advanced Target Model. It was found that coupled flow conditions were required to cause melting of the toughest structure considered. A semi-empirical relation for coupled flow heating was used to determine altitude of structure kill as a function of hit for aluminum, stainless steel, and Inconel X structures. By requiring intercept at altitudes of 70,000 feet or above, structural thicknesses of from 2 to 3 times the normal design values could be melted by 30,000 feet.

Basic analytical developments in the thermal studies have included the development of a semi-empirical relation for coupled flow heating, an engineering analysis of internal heat transfer downstream of a perforation based on steady compressible shear layer flow, and an improved correlation of axial velocity decay of compressible jets.

Under the structural study phase of the program, estimates of structure temperature rise due to coupled flow heating have been used to determine failure altitudes for the C-1 target model and for the Mark 3 re-entry vehicle. It was concluded that the attainment of structure melting temperature can be used as the failure criterion if (a) the internal heating is uniform, and (b) if the unsupported thermal shield cannot withstand the loading environment. In order to relax these requirements, an investigation of the reduction in load-carrying capacity of shells with an arbitrary hole cutout has been initiated. A survey of existing literature revealed that the available experimental or analytical results from aircraft types of construction could not be readily extended to unsymmetric cutouts or other geometries, and were further restricted to pure bending loads. Therefore additional study is being pursued in this area to provide an analysis technique.

A description is given of two experiments to be conducted under the Air Force WAC Program on board a sharp-nosed high $W/C_D A$ re-entry vehicle flying an ICBM trajectory at the Atlantic Missile Range. Coupled and uncoupled flow heating will be studied by opening external holes into compartments at about an altitude of approximately 90,000 feet.

SECRET

SECRET

I. WALLOPS ISLAND FLIGHT PROGRAM (Including Associated Malta Rocket Exhaust Tests)

A. General Discussion

During the past year, a two-flight test program was conducted jointly with NASA Langley Research Center which resulted in successful telemetry of data and recovery of experiment payloads for both flights. As part of this program, rocket exhaust tests were performed at the General Electric Malta facility using models identical to the flight models.

The primary objective of the program was to determine whether flight and ground test results of identical configurations could be correlated for the case of the internal heating due to perforations in the "uncoupled flow" size regime. A secondary objective was to compare flight and ground test results of the external heat shield aggravation due to the presence of cavities.

The experiment payload section (shown in Figure 1) consisted of a blunt sphere-cone configuration. An external ablative heat shield was mechanically fastened to an Inconel structure which also served as a calorimeter to measure internal heat flux. Structure temperatures were monitored by 24 chromel-alumel thermocouples spot-welded to the backface of the metal (i.e., on the surface not exposed to internal flow). Internal pressure was monitored by 4 pressure taps in the backplate.

Each model had one inlet port in the nose cap and two diametrically opposite exit ports on the cone. The exit ports were inclined 30 degrees in a downstream direction, to reduce interaction heating effects. The port locations, throat diameters, and detailed port insert designs are shown in Figures 2 and 3. For Configuration One, graphite inserts were installed in order to minimize ablation of the inlet and exit ports. For Configuration Two, the inlet and exit port inserts were made of phenolic nylon, in order to investigate the rate of perforation ablation. The inlet and exit port diameters were sized to provide measurable internal structure temperature rises and yet not jeopardize the structural integrity of the model. As a result, the rather small inlet port diameters resulted in an $A/V^{2/3}$ ratio of .003 for both configurations.

In addition to the complete perforations, Configuration One contained two cylindrical cavities drilled in the nose cap 45 degrees from the stagnation point. Each cavity was 0.25 inch deep, with diameters of 0.25 and 0.50 inches, respectively.

Prior to the flight tests, models identical in design to the flight models were tested in Pit Four of the G. E. Malta Rocket Exhaust Facility. The results of these tests were presented by Nestler and Vanden Eykel in Reference 1, and are summarized later in this report. Instrumentation locations for these tests are shown in Figures 4 and 5, and were similar for the flight models.

Flight One took place on 18 March 1963. All telemetry channels transmitted from vehicle lift-off until parachute deployment. The payload was sighted near its calculated impact point within 13 minutes after launch and was retrieved by helicopter. The recovered experiment section is shown in Figure 6.

SECRET

SECRET

Flight Two took place on 7 May 1963, and again resulted in successful telemetry of data and recovery of payload. The recovered experiment section is shown in Figure 7.

A four-stage booster system consisting of the Honest John, Nike, Lance, and Recruit rockets was used in each flight to accelerate the experiment section to 10,600 ft/sec (Mach 11) at an altitude 71,000 feet. The final trajectories as supplied by NASA are shown in Figure 8. A more detailed description of the flight sequence was given in Reference 2.

The noteworthy features of Configuration One, illustrated in Figure 6 were as follows:

- The inlet port insert was completely gone; however, the relatively uncharred appearance of the exposed phenolic nylon surface below the insert suggests that the insert was present during most or all of the heating portion of the flight.
- The cavities in the nose cap had completely disappeared, indicating low ablation rates within the cavities.
- The nose cap char layer was quite thin (on the order of .005 inches thickness), while the conical frustum char layer was thick (\approx .075 inches) and intact over the entire surface.
- Ablation downstream of the exit ports was reduced, apparently due to the film cooling effect of the relatively cool exit flow. Negligible enlargement of the vent throat areas occurred.
- Nose cap ablation was more severe than expected, as shown by the exposed screw heads.

The noteworthy feature of Configuration Two illustrated in Figure 7 was as follows:

- Most of the conical frustum heat shield had been lost, apparently due to severe aggravation immediately downstream of the inlet port. Burn-through had occurred to the insulation space between shield and structure, causing hot gas to heat the shield from both sides. (Later analysis of thermocouple records indicated that several seconds of valid internal heating data were obtained prior to burn-through.) The pressure forces appeared to have torn sections of the shield apart, leading to progressive failure and eventually complete removal of the heat shield, either late in the flight or upon water impact. The inlet port throat diameter had increased from 0.375 inches to an effective diameter of 0.58 inches during the flight.

In the following paragraphs, synopses are given of the present status of the flight data analysis for each flight. The final results, including external heat shield ablation measurements, will be compiled in a separate report to be issued in November, 1963.

SECRET

SECRET

B. Detailed Analysis of Flight One Results

The measured internal pressure for Flight One are plotted in Figure 9 for three of the four pressure taps. (A fourth tap was plugged prior to the flight because of a leak.) Typical thermocouple responses are plotted in Figure 10 for the backplate and cone structure. Comparison of Figures 9 and 10 indicates that at about 92 seconds and again at 100 seconds, sudden increases occurred simultaneously in the slopes of the pressure and temperature records. Since the inlet sleeve had disappeared from Flight Model One, it is likely that progressive loss of portions of the sleeve was the cause of these sudden increases. (Increased inlet area for a given exit area causes higher internal pressure to satisfy mass conservation, and also causes higher internal heat flux due to the reduced amount of jet diffusion.) The apparent jump in pressure at 92 seconds corresponds to the increase which would be expected if the .010-inch thick pyrolytic graphite coating on the inlet orifice suddenly failed. The rate of divergence between slopes of internal and external pressures which occurs between 96 and 102 seconds corresponds to an ablation rate about 33 percent higher than that predicted for graphite using the method of Walker (Reference 3). The inner phenolic nylon sleeve presumably was lost at water impact due to excessive ablation of the retaining plug.

The thermocouple responses were used to determine the internal heat flux histories by a process of iteration using an IBM 7090 computer one-dimensional conduction program, assuming an adiabatic backface. The use of the thin-wall method would constitute a reasonable approximation for the 0.125 inch cone structure, but is unacceptable on the thicker backplate. Instead, an iterative technique was employed in which various heat flux histories were used as inputs to the program until the computed backface temperature response matched the measured temperature history. The heat fluxes computed in this manner are mapped in Figures 11 and 12 for 88 and 94 seconds after lift-off, during the high heating portion of the flight.

At this point, comparison of measured heat fluxes with theory and Malta ground test results requires a computation of inlet flow rate, energy influx, and internal air temperature, by use of the mass and energy balances derived in Reference 4. The external stagnation pressure was determined from the trajectory of Figure 8 and the real gas normal shock relations of Musser (Reference 5). A plot of the external pressure in Figure 9 indicates that the internal pressure crossed over the external pressure at about 96 seconds, and remained above it thereafter. Such an unexpected occurrence could be attributed to one of several possible causes:

- Plugged vent ports;
- Trajectory errors;
- Errors in internal pressure data; and,
- Unstable shock wave causing higher effective external pressures than predicted by steady flow shock relations.

Examination of the reserved model showed no indication of plugged vents; and a check by NASA verified the accuracy of the trajectory. Since all three pressure readings agreed closely throughout the flight, incorrect pressures seem unlikely.

SECRET

SECRET

Therefore the hypothesis of an unstable shock wave is tentatively advanced as a possible explanation of the apparent anomaly in external-internal pressure history shown in Figure 9.

Unstable shocks upstream of bodies having cavities at the stagnation point have been reported by Johnson (Reference 6). Large amplitude pressure oscillations in resonance tubes with accompanying temperatures higher than free-stream stagnation temperature were measured by Vrebalovich (Reference 7). In rocket exhaust tests reported by Mathias and Vikestad (Reference 8), an inlet port at the stagnation point of a sphere cone model caused violent vibrations for an $A/V^{2/3}$ ratio of .005, but not for $A/V^{2/3} = .0006$. Since $A/V^{2/3} = .003$ for the present test, unstable flow effects are regarded as possible.

It was decided that the best procedure to determine effective external stagnation pressure and inlet flow rate consisted of using the measured internal pressure and internal heat flux distribution in a simultaneous solution of the conservation equations of mass and energy. As derived in Reference 4, these equations are:

$$m_1 = m_2 + V \frac{d\rho}{d\theta} \quad (1)$$

$$m_1 h_s = m_2 h_2 + V \frac{d(\rho_2 i_2)}{d\theta} + \int_{A_s} \dot{q} dA_s \quad (2)$$

From the measured internal pressure and heat flux history, it was verified that the transient terms $V d\rho_2/d\theta$ and $V d(\rho_2 i_2)/d\theta$ could be neglected with less than 3 percent error. In this case, Equations (1) and (2) reduce to the quasi-steady result:

$$m_1 = m_2 \quad (3)$$

$$m_1 h_s = m_2 h_2 + \int_{A_s} \dot{q} dA_s \quad (4)$$

The value of the integral in Equation (4) was determined by graphical integration of heat flux distributions such as those of Figures 11 and 12. Assuming the simple orifice flow equation to apply to inflow and outflow, m_1 and m_2 can be written:

$$m_1 = \frac{C m_1 P_1 \phi_1 A_1}{T_s^{0.5}} \quad (5)$$

$$m_2 = \frac{C m_2 P_2 \phi_2 A_2}{T_2^{0.5}} \quad (6)$$

SECRET

SECRET

where $\phi_1 = \alpha(P_2/P_1)$ and $\phi_2 = \alpha(P_3/P_2)$, with the function ϕ_j given by:

$$\phi_j = \left[\frac{2\gamma g}{R(\gamma - 1)} \right]^{0.5} \left(\frac{P_{j+1}}{P_j} \right)^{\frac{1}{\gamma}} \left[1 - \left(\frac{P_{j+1}}{P_j} \right)^{\frac{\gamma-1}{\gamma}} \right]^{0.5} \quad (7)$$

Combining Equations (3), (5), and (6) gives the relation:

$$\frac{P_2}{P_s} = \frac{A_1}{A_2} \frac{\phi_1}{\phi_2} \frac{Cm_1}{Cm_2} \left(\frac{T_2}{T_s} \right)^{0.5} \quad (8)$$

while combining Equations (3) and (4) leads to:

$$\frac{h_2}{h_s} = 1 - f_w \quad (9)$$

in which f_w is defined as the fraction of energy influx which is absorbed by the internal surfaces:

$$f_w = \frac{\int_{A_s} \dot{q} dA_s}{m_1 h_s} \quad (10)$$

Equations (8) and (9) were solved simultaneously for P and T_2 , with the aid of "real gas" charts for air (Moeckel and Weston, Reference 9) which relate h , T , and P . The inlet flow rate m_1 was then computed from Equation (5), and the energy partition function f_w was computed from Equation (10). The resulting values are shown on Figures 11 and 12 for 88 and 94 seconds, respectively. For these computations, the orifice flow coefficients Cm_1 and Cm_2 were taken as 0.9, due to the large thickness-to-diameter ratio (Reference 10). Also, it was tacitly assumed that the stagnation temperature T_s and stagnation enthalpy h_s corresponded to steady state normal shock values for the trajectory conditions, despite the anomaly in stagnation pressure. The values of P_s computed from Equation (8) are plotted in Figure 9 for comparison with the values computed from the trajectory.

The heat flux distribution at 88 seconds is plotted in normalized form in Figure 13, using an experimental value of 165 BTU/ft²sec for $\dot{q}_{T_{max}}$ and a computed value of $r_{0.5}$ of 0.75 inches. (The abnormally high value of backplate heat flux of 270 BTU/ft²sec in Figure 11 has been discarded, as well as the values of 12, 63, and 100 on the cone.) The heat flux distribution obtained from the Malta test of the same configuration is also shown in Figure 13 for comparison with the flight results. Reasonable agreement is seen to exist, indicating no strong effects of the 10-g deceleration in flight on the distribution of heat flux at 88 seconds. There is a trend towards a more rapid decrease in heat flux in the flight results as wetted length r increases along the conical frustum.

SECRET

SECRET

A comparison of theoretical impingement region heat fluxes (calculated by the methods of Reference 2) with maximum measured values is shown below:

Time (seconds)	88	94
Theoretical heat flux, BTU/ft ² sec		
Laminar stag. point	115	140
Maximum turbulent	230	230
Maximum measured heat flux, BTU/ft ² sec	165	33

Although reasonable agreement between theory and experiment exists at 88 seconds, a drastic reduction of measured maximum heat flux occurred at 94 seconds which is not predicted by theory. At present, the cause of this reduction is not understood. A drop-off in heat flux is expected eventually as time elapses during the flight, due to the decrease in air stagnation enthalpy and increase in wall enthalpy. At 94 seconds, however, the internal static enthalpy h_2 required to give a value of diffused jet enthalpy sufficiently low to account for the low measured heat flux results in an unresolvable inconsistency in the mass and energy conservation equations (Equations (3) and (4)). Since the Malta rocket exhaust test of the same configuration verified the theoretical flow and energy relations being used in the analysis, the flight results at 94 seconds infer that an instability of some nature developed in the incoming jet, such that the usual axisymmetric jet diffusion did not result.

It should be noted that a similar effect would have resulted if the exit ports had become plugged. Since the pressure plots in Figure 9 also imply a plugged exit condition, a calculation was made to determine the maximum pressure difference expected during the later portion of the flight when the external pressure was decreasing. It was found that a maximum pressure difference of 0.3 psi could be expected for a completely plugged exit. However, Figure 9 shows a difference of 25 psi, which cannot be explained by plugged exit ports.

C. Detailed Analysis of Flight Two Results

The measured internal pressures for Flight Two are plotted in Figure 14 for the four pressure taps. Typical thermocouple responses are plotted in Figure 15. Rapid rises in temperature occur for many of the thermocouple records after 94 seconds due to hot gas flow through the shield burnthrough shown in Figure 7. The increase in pressure at 95 seconds may be indicative of a trim angle caused by partial shield removal, or could also be the result of a sudden increase in inlet flow area.

Heat flux maps are shown in Figures 16 and 17 for 88 and 91 seconds, respectively. Maximum heating occurs along the meridian 180° from the inlet meridian, as expected. Rapid reduction in heating rates away from the jet impingement area is evident; comparison with the Malta heat flux map (Figure 19) indicates a more rapid decay in flight than at Malta. Since the external pressure and enthalpy are lower in flight than at Malta, less energy is contained in the entering jet in flight, with more rapid quenching of the jet upon impingement with the cooler walls.

For the inlet port location of Flight Two, supersonic tangential approach flow ($M = 1.64$) exists. Therefore the simple orifice flow relation (Equation 5) is replaced by an equation derived from first order expansion theory:

SECRET

SECRET

$$m_1 = C_{m_1} (P_1 - P_2) \frac{\beta g A_1}{U_1} \quad (11)$$

Otherwise, the analysis proceeds as before for Flight One. The transient terms in Equations (1) and (2) can again be neglected for times from 88 to 94 seconds, due to the almost constant internal pressure during this time period. The local external pressure P_1 shown in Figure 14 was computed from the modified Newtonian relation:

$$\frac{P_1}{P_s} \approx \cos^2 \theta \quad (12)$$

where θ is the angle between the body axis and a normal to the surface ($\theta = 60$ degrees in this case). The stagnation pressure P_s was computed from the real gas normal shock charts of Musser (Reference 5). The local velocity U_1 approaching the inlet was determined by isentropic expansion from stagnation conditions to P_1 , using the Moeckel and Weston charts (Reference 9). An average pressure P_2 was determined from Figure 14. The local external pressure at the vent exit P_3 (plotted in Figure 14) was determined from correlations of real gas flow fields

(Reference 11). The integrated heat rate to the wall $\int_{A_s} \dot{q} dA_s$ was determined by

graphical integration of the heat flux maps of Figures 16 and 17. The exit flow m_2 was again computed by Equation (6). It was found that a consistent agreement of mass and energy balances, Equations (3) and (4), was obtained by the following choices of flow coefficients:

Time (seconds)	88	91
C_{m_1}	0.50	0.61
C_{m_2}	0.37	0.62

The value of C_{m_1} is expected to be reduced by the tangential approach and possible shock losses; however, the values shown for C_{m_1} are considerably less than the value of 0.98 which yielded consistent results for the Malta test of the same configuration. The value of C_{m_2} is known to be reduced significantly when discharging into a supersonic free stream at low pressure ratio. (See data of Vick, Reference 12, shown in Figures A-1 and A-2, Appendix A.) If Vick's data are used to determine C_{m_2} for the flight conditions, even lower values of C_{m_1} would be required than those listed above. The possibility that C_{m_1} is being reduced by the presence of the approach flow boundary layer is under investigation. The results of the AEDC orifice flow tests discussed later are expected to clarify the choice of expected values of C_{m_1} .

SECRET

SECRET

A comparison of theoretical impingement region heat fluxes with maximum measured values is shown below:

Time (seconds)	88	91
Theoretical heat flux (BTU/ft ² sec)		
Laminar stag. pt.	63	45
Maximum turbulent	78	64
Maximum measured heat flux ₂ (BTU/ft ² sec)	47	31

In computing the theoretical heat fluxes, the stagnation point velocity gradient was assumed to be $U_i/r_{0.5}$, and the effects of oblique impingement were assumed to be negligible.

D. Results of Malta Rocket Exhaust Tests of Flight Models

Each of the flight models had an identical counterpart which was tested in Pit Four of the General Electric Malta Rocket Exhaust Facility. The method used to convert thermocouple data to heat fluxes, as well as the internal flow and energy analysis, were the same as discussed above for the flight results.

The results of the heat flux computations are presented in the form of heat flux maps at 4 seconds run time for each test, in Figures 18 and 19, respectively. In addition, a tabulation of all heat fluxes and computed front surface temperatures is given in Table 1.

The general noteworthy features in the heat flux maps are as follows:

Test M1A (Figure 18)

The heat flux pattern displays circumferential symmetry, confirming the internal flow pattern concept of a stable jet which impinges at the center of the backplate, forms an axisymmetric wall jet flow radially outward on the backplate, and then forms a wall jet flow forward along the conical frustum.

Test M2A (Figure 19)

The heat flux pattern displays a highly three-dimensional nature, as expected. The maximum heat flux occurs in the region of jet impingement on the meridian displaced 180 degrees from the inlet port meridian. An asymmetric radial wall jet pattern develops thereafter, which exhibits a relatively uniform axial heat flux variation along all meridians other than the impingement meridian.

The experimental internal pressure, heat flux, and orifice ablation were compared to the predictions of the internal heating theory for vented compartments developed previously under the HKM program (References 2 and 10). The principal results are summarized in Table 2. In each case, results are shown for a time near the end of the run in order to minimize the effects of H₂O condensation. This choice of time also provides a better probability that most of the air initially present within the model will have exhausted through the vent ports. The internal gas properties were obtained from the work of Botje (Reference 14).

SECRET

SECRET

**TABLE 1. TABULATION OF WALL THICKNESSES, HEAT FLUXES,
AND FRONT SURFACE TEMPERATURES AT $\theta = 4$ SECONDS**

Thermo- couple Number	TEST M1A			TEST M2A		
	L* inches	\dot{q} Btu/Ft ² Sec	T _w OF	L** inches	\dot{q} Btu/Ft ² Sec	T _w OF
1	.294	200	1105	.120	6	95
2	.295	210	1165	.120	18	225
3	.292	190	1025	.120	16	210
4	.239	150	855	.120	17	210
5	.234	80	525	.120	26	290
6	.238	135	775	.120	40	595
7	.292	180	980	.120	17	210
8	.240	135	775	.120	17	210
9	.241	75	480	.120	30	330
10	.295	195	1050	.120	--	--
11	.247	140	780	.120	21	255
12	.102	135	1220	.110	16	205
13	.105	135	1230	.110	28	340
14	.103	135	1220	.110	53	545
15	.114	90	815	.107	20	265
16	.105	100	940	.107	12	215
17	.109	105	895	.107	29	340
18	.116	85	690	.107	36	440
19	.121	83	725	.103	19	250
20	.116	80	710	.103	30	370
21	.120	60	525	.100	11	170
22	.120	--	--	.100	15	235
23	.121	55	495	.100	25	320
24	.122	60	535	.100	27	345
25	.115	65	550	.250	14	155
26	.125	35	245	.300	20	195
27	.120	35	280	.300	38	290
28	--	--	--	.250	35	290
29	.118	70	580	--	--	--
30	.119	70	755	--	--	--

* Local Micrometer Measurements

** Interpolated from Vendor's
Measurements

SECRET

SECRET

TABLE 2. SUMMARY OF ANALYSIS OF MALTA ROCKET
EXHAUST TEST RESULTS

Model stagnation conditions:			
		$p_s = 170$ psia	
		$T_s = 5600^{\circ}\text{R}$	
		$h_s = 3250$ Btu/lb	
Test number Time during test, seconds Location of inlet orifice		M1A 4.0 stag. point	M2A 4.0 60 deg. from stag. point
p_1	External static pressure at inlet, psia	170	52
p_3	External static pressure at vents, psia	22	22
p_2	Internal static pressure, psia	113	38
$m_1 h_s$	Rate of energy influx, Btu/Sec	360	68.3
$m_2 h_2$	Rate of energy efflux, Btu/Sec	190	23.8
$dQ_w/d\theta$	Rate of energy absorption by internal surfaces, Btu/Sec	170	44.5
$1-f$	Fraction of energy influx absorbed by internal surfaces	0.47	0.65
h_2	Internal static enthalpy, Btu/lb	1710	1140
T_2	Internal static temperature, $^{\circ}\text{R}$; Energy	2350	750
	Continuity	2300	1540
	Maximum heat flux in jet impingement region, Btu/Ft ² -Sec		
$\dot{q}_{\text{exp.}}$	Experimental value	205	53.0
\dot{q}_s	Laminar stagnation point theory	139	38.5
$\dot{q}_{T\text{max}}$	Maximum turbulent theory	388	74.0
D_1	Inlet orifice throat diameter, inches		
	Initial	0.375	0.375
	At 4 seconds	0.375	0.53
D_2	Vent diameter, inches (initial and final)		
	Vent No. 1	0.265	0.317
	Vent No. 2	0.265	0.200
D_1^*	Internal jet initial diameter, inches	0.375	0.198
M_1^*	Internal jet initial Mach Number	0.79	1.36
X/D_1^*	Internal jet X/D at impingement	26	33.4
D_j	Internal jet diameter at impingement, inches	1.5	0.87
u_j/U_1	Internal jet axial velocity decay	0.25	0.16
	Inlet orifice ablation for entire test		
	Experimental value - ΔD , inches	0.29*	0.20**
	Theoretical value - ΔD , inches		
	Laminar boundary layer	0.23	0.08
	Turbulent boundary layer	0.62	0.13

* Phenolic nylon entrance section

** Preliminary measurement

SECRET

SECRET

In evaluating the inlet and exit flow rates, the following values of flow coefficients were assumed:

	Test M1A	Test M2A
Inlet flow coefficient C_{m_1}	0.90	0.98
Exit flow coefficient C_{m_2}	0.90	0.48

With the exception of C_{m_2} for Test M2A, the choice of flow coefficients was based on the data collected in Reference 10, and includes consideration of orifice thickness-to-diameter ratio, pressure ratio, and entrance rounding. For Test M2A, the data of Vick (Reference 12) indicate a drastic reduction in flow rate for discharge into a supersonic stream when P_2/P_3 is not sufficiently large. The appropriate data for inclined vent discharge are shown in Figure A-2, Appendix A. It is significant that the "continuity method" of determining T_2 would be in agreement with the "energy method" for Test M2A if C_{m_2} were equal to 0.33.

For Test M1A, excellent agreement in internal static temperature was obtained by the two different methods of determining T_2 . Graphical integration of the heat flux distribution showed that approximately one-half of the entering energy was absorbed by the walls. The maximum heat flux in the jet impingement region was about 30 percent lower than the theoretical maximum turbulent heat flux. This result is in qualitative agreement with the results reported by ARAP (Reference 13) for the effect of a cylindrical enclosure on stagnation point velocity gradient of a diffused jet.

For Test M2A, lack of agreement in internal static temperature from the two methods of computation could be due to one or more of the following causes:

- Uncertainty in inlet and exit flow coefficients.
- Uncertainty in rate of energy absorption by surfaces.
- Possible direct outflow of internal jet prior to thorough mixing with internal gas.

Approximately two-thirds of the entering energy was absorbed by the walls. The maximum heat flux was about 30 percent below the theoretical maximum turbulent heat flux. Since the jet impingement location is not known precisely, this agreement is quite acceptable considering the large amount of jet diffusion, oblique angle of jet impingement, and concavity of the impingement surface in the circumferential direction.

The inlet orifice ablation for Test M1A was computed for the phenolic nylon entrance section at a location 0.5 inches from the original external surface, and compared to the measured value. As seen in Table 1, a laminar boundary layer theory gives fair agreement of theory with experiment. Since the local Reynolds number Re_x is less than 10^5 at $x = 0.5$ inches, it is reasonable to use the laminar theory.

SECRET

SECRET

The inlet orifice ablation for Test M2A was computed at a location 0.6 inches from the original external surface, and compared to the measured test value. Although Re_x is well below 10^5 , the measured throat ablation exceeded even the turbulent prediction by 50 percent. The irregular convergent-divergent-convergent ablated cross-section of this orifice along its length suggests vortex action as a possible cause of the relatively large ablation.

A correlation of the radial distribution of heat flux away from the internal jet impingement point for both tests is presented in Figure 20. The radial distance r was measured as the shortest distance along the internal surface from the jet impingement point to the particular thermocouple location. The theoretical half-radius of the diffused jet ($r_{0.5}$) was used to normalize the radial co-ordinate, while the maximum measured heat flux ($\dot{q}_{T_{max}}$) was used to normalize the heat flux. It is seen that this empirical correlation technique achieves reasonable unification of the heat flux distributions of both tests taken together, despite the differing internal flow configurations. The principal discrepancy occurs on the back-plate of Test M2A, where unusually high values of $\dot{q}/\dot{q}_{T_{max}}$ occurred.

E. Comparison of Flight and Ground Test Results

In general, the results of the two flight tests have substantiated the internal heat flux patterns measured in the Malta rocket exhaust ground tests. The magnitude of the maximum impingement heat flux was predicted reasonably well by theory for flight and ground tests of both configurations, with the exception of the anomalies existing in the later portion of the Flight One heating period. The internal heat flux distributions were similar for flight and ground tests. However, certain differences from ground test results have appeared in the analyses of both flights, as follows:

Flight One

For an inlet orifice at the stagnation point, severe attenuation of impingement heating occurred during the later heating period. Simultaneous discrepancies occurred in the internal-to-external pressure ratio. Barring gross sensor calibration or trajectory errors, an unstable shock wave and internal jet instability are offered as possible explanations. Neither phenomenon was suggested by the ground test results.

Flight Two

Although no impingement heating attenuation or internal pressure discrepancy occurred for this configuration (inlet orifice 60 degrees from stagnation point), unusually low values of inlet flow coefficient were required to obtain compatible mass and energy conservation relations.

In addition, severe external aggravation occurred downstream of the inlet orifice, whereas only slight indications of such aggravation were present in the ground test.

The effects of cavities placed in the nose region (at 45 degrees from the stagnation point) were similar in flight and ground test. In the Malta test, the cavities were tending to disappear with time, with no downstream aggravation; in flight, the cavities disappeared completely, again with no downstream aggravation.

SECRET

SECRET

For convenience, a summary of some of the primary test parameters and results is given in Table 3.

TABLE 3. SUMMARY OF FLIGHT AND
GROUND TEST RESULTS

Configuration	1	2
$A/v^{2/3}$.003	.003
Inlet area (in ²)	0.11	0.11
Exit area (in ²)	0.11	0.11
Stagnation pressure (psia)		
Flight (max)	124	200
Malta	170	170
Stagnation enthalpy (BTU/lb)		
Flight (max)	2300	2300
Malta	3250	3250
Max. heat flux (BTU/ft ² sec)		
Flight	165	47
Malta	205	53
Fraction of energy to walls (f_w)		
Flight (at 88 sec.)	0.56	0.75
Malta	0.47	0.65
Max. internal surface temp. (°R)		
Flight	1350	1300
Malta	1800	1150

II. INTERNAL HEATING TESTS IN THE C. A. L. WAVE SUPERHEATER HYPER-SONIC TUNNEL

During the past year, an internal heat transfer model was designed, built, and tested in Cornell Aeronautical Laboratory's Wave Superheater Facility. The primary objectives of this program were:

- To determine the range of $A/v^{2/3}$ required for coupled flow for a single orifice in an unvented volume.
- To determine the magnitude and distribution of internal heating when coupled flow exists.

In addition, secondary objectives consisted of investigating the effects of two orifices in an unvented volume, and the effects of venting through the model base to wake pressure.

A schematic drawing of the model is shown in Figure 21, and a photograph of the model with the largest orifice insert is shown in Figure 22. Instrumentation consisted of a total of 34 thermocouples and 8 pressure taps on the calorimeter structure, as shown in Figure 23, and 9 thermocouples and 4 pressure taps on the external structure, as shown in Figure 24.

SECRET

SECRET

A summary of the nominal test conditions is given in Table 4, followed by a tabulation (Table 5) of the configurations which were tested. As noted in Table 5, the $A/V^{2/3}$ ratio was varied from .01 to 0.2 in an effort to locate the critical value required for the onset of "coupled flow".

TABLE 4. NOMINAL TEST CONDITIONS FOR CORNELL AERONAUTICAL INTERNAL HEATING TESTS

Reservoir pressure	100 atm
Reservoir temperature	7000 °R
Free-stream pressure	.05 psfa
Free-stream temperature	150 °R
Free-stream Mach number	17
Model stagnation pressure	20 psfa
Average run time	4.2 sec.

TABLE 5. TEST AGENDA FOR CORNELL AERONAUTICAL LABORATORY INTERNAL HEATING TESTS

Run No.	Nominal Orifice Diameters-Inches			$A/V^{2/3}$
	D_1	D_2	D_3	
1	1.5	-	-	.01
2	3.0	-	-	.05
3	4.5	-	-	.10
4	6.0	-	-	.20
5	3.0	3.0	-	.05/.05
6	3.0	6.0	-	.05/.20
7	3.0	-	1.5	.05/.01
8	6.0	-	1.5	.20/.01

The local cone surface Mach number was computed to be 8.5; the local cone surface Reynolds number was computed to be 70,000 (based on wetted length); and the local external laminar heat flux at the perforation location was measured to be about 1.0 BTU/ft² sec.

An analysis of the preliminary data which have been supplied by C. A. L. has led to the following conclusions, which strictly apply only to the configuration shown in Figure 21 when exposed to the environment indicated in Table 4:

For a single orifice in an unvented volume, configurations with $A/V^{2/3}$ of .01 and .05 resulted in internal heat fluxes which were less than 2 percent of the external cone heat flux. Configurations with $A/V^{2/3}$ of 0.10 and 0.20 caused maximum internal heat fluxes of only 7 percent of the external heat flux, with these maxima occurring on the meridian opposite the orifice. These results are in general agreement with the relation proposed by Donaldson in Reference 15 based on a turbulent shear layer energy transfer model, but are far below the predictions of the semi-empirical relation derived by Nestler in Appendix D based on an oscillating shear layer model and the BRL Malta rocket exhaust tests of Reference 16.

SECRET

SECRET

The configurations having two orifices diametrically opposite on the cone (Runs 5 and 6) caused little if any internal heating, with maximum heat fluxes being on the order of 2 or 3 percent of the external cone heat flux.

The configurations having venting (Runs 7 and 8) resulted in surprisingly low internal heat fluxes, with maximum heat fluxes on the order of 5 to 15 percent of the external cone heat flux. These values are an order of magnitude lower than expected from the analysis developed in Reference 4, but have been shown to agree with the analysis if allowance is made for viscous effects on the approach flow characteristics (see Appendix B).

Calorimeters located at the midpoint of the downstream edge of the orifice inserts for Runs 1 and 2 indicated heat fluxes on the order of the external cone heat flux. Theoretical predictions based on a stagnation heat flux "strip method" using Chapman's laminar shear layer profiles were in good agreement with the measured values (see Appendix C).

In summary, the C.A.L. tests have shown very low relative internal heating rates over the "coupled flow" region of $.05 < A/V^{2/3} < 0.20$. These results are in qualitative agreement with the relation presented by Donaldson in Reference 15 for energy influx through an orifice in an unvented volume. More accurate analysis of the C.A.L. results was hampered by low temperature rises, due in part to the short run time. (4 seconds vs 15 seconds for which the calorimeter structure was designed). Hence it has been recommended that the tests be re-run in the higher heating environment of AEDC Tunnel C at a Mach number of 10, where run times of 30 seconds or more can be obtained.

III. WIND TUNNEL ORIFICE FLOW TESTS

Tests will be conducted in Tunnel D of the AEDC to determine the flow characteristics of orifices having supersonic tangential approach flow. Flow rate, velocity profiles, and direction of the expended jet will be determined as functions of approach Mach number, orifice thickness-to-diameter ratio, and orifice pressure ratio. In addition, the effects of orifice diameter and obliquity on flow rate and jet direction will be determined for various orifice-to-thickness ratios at one approach Mach number, and the effects of orifice shape on flow rate and jet direction will be determined for one orifice thickness-to-diameter ratio at one approach Mach numbers. The study of shape effect will feature two test inserts of actual impacts into phenolic nylon targets with metal backup structures. One of these targets is shown in Figure 25.

Similar tests have been run at NOL on circular orifices at low supersonic Mach numbers. (Reference 2) The data obtained in this test will provide a check on previous results and extend the Mach number range to 5.0. This extension is required because of the emphasis on sharp-nosed re-entry vehicles with high local surface Mach numbers.

The tests will be performed by mounting a box having a volume of 2.2 ft^3 to the tunnel side wall and placing the various orifice inserts in the side of the box which forms part of the tunnel wall (See Figure 26). Steady state flow rates will be established by evacuating the box to the desired pressure ratio. The flow rate will be measured by a calibrated flow nozzle in the vacuum line. The static pressure upstream of the orifice and within the box will be measured to permit correlation

SECRET

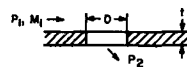
SECRET

of the results in terms of a dimensionless flow coefficient. Pitot surveys of the expanding jet will be conducted within the box at several locations by means of an adjustable probe rake. (See Figure 27) Schlieren photographs will determine the direction of the jet for each run. At the completion of each run, the vacuum pump will be shut down, and photographs taken of the flow pattern existing within the box with no box outflow.

The results will be analyzed to determine theoretical or empirical methods of correlating the flow rates, expanding jet directions, and jet velocity decay and spread as functions of the independent variables.

All hardware has been designed, fabricated, and shipped to AEDC. Testing is scheduled for October 1963. The test agenda is given in Table 6.

TABLE 6. ORIFICE FLOW TEST AGENDA



TEST NO.	INCHES	INCHES	ORIFICE SHAPE	M ₁	P ₂ /P ₁	FLOW RATE	JET PROFILES	PHOTOS
1A	1	0.2	Circular	1.5	0.1 to 0.9	Measure	Measure	Yes
B		0.2		3.0			Measure	
C		0.2		5.0				
D		0.5		3.0				
E		2.0					Measure	
2A	2	0.2						
B	2	1.0						
C	2	2.0						
3A	4	0.5						
B	4	2.0						
4A	-	0.5	Irregular (actual impacts)					
B	-	0.5	Irregular (actual impacts)					
5A	2	0.2	Circular, 30° Obliquity					
B	2	2.0	Circular 30° Obliquity					

IV. MALTA INTERNAL PERFORMANCE TESTS

A new program of ground tests was initiated recently in which a series of seven models will be tested in Pit Four of the G. E. Malta Rocket Exhaust facility. The primary objective of the program is to determine the effect of relatively large machined, actual, and simulated impact perforations on thermostructural behavior of unvented sphere-cone configurations having typical ablative heat shields of phenolic nylon (0.5 inches thickness) bonded to 0.125 inch inconel structures. The external configuration will correspond to that of the Wallops Island flight models. In all cases, a single perforation in the cone region will be tested. Instrumentation will consist of 30 thermocouples and 4 pressure taps, dispersed in a pattern similar to that of the C. A. L. tests (Figure 23).

SECRET

SECRET

The test schedule planned is shown in Table 7. Perforations for tests 1 and 2 will be machined, with a stainless steel sleeve mechanically attached to the inconel structure. These sleeves will provide for calorimetry on the downstream surface of the perforations, and will also insure that from 1 to 3 seconds of data will be obtained prior to debonding causing possible additional structural heating downstream of the perforation. Perforations for tests 3 and 4 will be obtained by NRL in an impact facility, while the perforation for test 5 will be obtained by some explosive technique simulating impact.

TABLE 7. MALTA ROCKET EXHAUST TEST SCHEDULE

TEST NO.	PERFORATION DIA. , IN.	A/V ^{2/3}	TYPE OF PERFORATION
1	2.5	0.12	MACHINED
2	4.0	0.31	MACHINED
3	2.0	0.08	IMPACT
4	4.0	0.31	IMPACT
5	3.0	0.17	SIMULATED IMPACT
6	TO BE SPECIFIED LATER - INTERNAL FOAM PRESENT		
7	TO BE SPECIFIED LATER - INTERNAL FOAM PRESENT.		

Evaluation of the test results will include the following:

- Presentation of internal heat flux distributions and comparison to theoretical and empirical predictions.
- Correlation of results with type and size of perforation.

Heat shield and structure drawings have been completed, and fabrication of the models has begun. The schedule calls for Tests 1 and 2 to be completed in December 1963.

V. PARAMETRIC COMPUTATIONS

A. Internal Heating Computer Program

Modification of the Program

The digital computer program, developed by GE-RSD to calculate the internal heating of a re-entry vehicle having one or more perforations of the heat shield, has been modified to increase its capability and reduce the IBM 7090 computer calculation time, thus providing greater economy of operation. Four significant additions to the program have been instituted:

SECRET

SECRET

- An input option has been added to facilitate use of constant free stream conditions. This will permit direct comparisons of results from wind tunnel and shock tube tests to computer predictions and subsequent adjustments of the orifice flow constants and heat transfer coefficients to correspond to the test data.
- A time step control subroutine has been added to the program which inhibits divergence of the solution by reducing the time step size in regions of steep internal pressure transients. During periods when large time steps produce valid solutions, the subroutine increases the time step size, providing more economical operation.
- An iteration subroutine has been developed which permits the internal pressure change to be calculated from the average mass flow rates during each time period. The procedure greatly improves the stability of the program over that previously obtained with the explicit procedure which calculated the internal pressure change for any time period based upon the mass flow rates at the preceding time step.
- To provide a method of obtaining approximate answers prior to availability of basic experimental data and for subsequent use on irregular internal compartments, a modified energy balance equation was added to the program as an option. In this relation the heat transferred to the wall by the impinging jet is a specified fraction of the total energy entering the compartment.

In addition to the four major changes listed above, a number of minor changes were made to improve the accuracy of the solution and increase the output data.

Figure 27 is a block diagram of the HKM Internal Heating computer program with the latest modifications and additions. Blocks 2 thru 5 and 10 thru 13 have not been changed since they were originally formulated and reported in Reference 2. Blocks 1, 6, 7, 8, and 9 have recently been added to the program and thus warrant some discussion.

Block 1 is an option which allows constant free stream conditions to be utilized as input to the program in place of a trajectory.

The program then employs the Cornell tables (Reference 17) to calculate the air state within the shock layer and the vehicle as it does with the trajectory option. With this subroutine, pre-test predictions can be obtained from the computer for such tests as those conducted in the Cornell Wave Superheater. In addition, the program can be employed for wind tunnel and shock tube data reduction by varying the flow and heat transfer coefficients so that the computer solution matches the test data, thus determining the values of these coefficients.

Block 6 contains an optional method of calculating the internal pressure rise. A set of energy balance equations are used in which a fraction of the total energy entering the compartment is convected to the walls by jet impingement. This fraction can be estimated approximately for irregular compartment shapes and shapes for which the experimental heat transfer distributions are not available. Thus this subroutine provides a method of solution for compartments which could not be analyzed otherwise. The equations used in this section are dependent upon the flow directions at each of the two orifices in the compartment.

SECRET

SECRET

Blocks 7 and 8 constitute the time step control subroutine. In block 7, the following criteria are set up to detect a divergence of the solution:

- a) $P_2 < 0$
- b) $\beta < \frac{P_2 (\theta + 1)}{P_2 \theta} < \alpha$

In these criteria, the values of α and β can be adjusted to fit the particular case under consideration. If either of these criteria are violated, the program reduces the time step size in block 8. In this routine the time step is divided by a factor, K, which is input for each case. The program performs K calculations at the reduced time step size and then returns to the original input time step size. This subroutine is expected to greatly reduce the computer time since it both optimizes the time step size and reduces the incidence of divergent solutions.

Block 9 contains the iteration subroutine for the mass flow rates. The internal pressure at each time step is calculated from the mass flow rates of the previous time step. The mass flow rate at this time step is then calculated and averages with the previous mass flow rate. A new internal pressure is then calculated. This average mass flow rate calculation is iterated until the two successive calculations satisfy the relation

$$\left| \left(\frac{m''_{\text{avg}}}{m'_{\text{avg}}} - 1 \right) \right| < .01$$

This procedure increases the stability of the program as it dampens out oscillations in the calculations.

Parametric Studies

A parametric study was conducted to evaluate the internal heating of the first HKM NASA flight vehicle. Constant orifice areas were assumed throughout the flight. Some of the results from this study are presented in Figures 29 through 32. Two cases were considered. The first case evaluated the effect of 3 values of energy partition factor f_w on the internal pressure and heat transfer. The results are presented in Figures 29 and 30.

It is seen in Figure 29 that an increase in f_w results in an increase in internal pressure during the first portion of the trajectory with a reversal of this trend from 98 seconds onward. The measured pressure data is included for reference. It can be noted that agreement between the predictions and the data is reasonably good up to 88 seconds. The heat fluxes for this case are shown in Figure 30. It is seen that there is good agreement between the average heat flux measured at the center of the back plate and the calculations, again up to 88 seconds with an f_w of 0.6.

In the second case the f_w factor was held constant at 0.6, and the orifice coefficient of the vent ports was varied from 0.9 to 0.5. It is seen in Figure 31 that the internal pressure increased with a decrease in the flow coefficient as is expected. In this case the internal jet Mach number decreased with the decrease in flow coefficient and resulted in a lowering of the heat flux predicted for the back plate. Thus while the internal pressure was increased the heating decreased reversing the trend seen in the previous case.

SECRET

SECRET

The average heat fluxes measured at the center of the backplate are again shown for reference. (Figure 32)

The parametric study of the C1 Advanced Re-entry Vehicle is currently in progress. Partial results have been obtained but are insufficient to warrant presentation at this time.

Status of the Program

The HKM Internal heating program is now in a fully operational state. All equations in the program have been checked with hand calculations with the exception of those in the Radiant Heat Transfer subroutine. In the course of the study of the C1 Vehicle the internal air temperature will become sufficiently high that radiation will be significant and can be checked by hand.

Proposed Modifications

In line with the continuing effort to keep the program abreast of the state of the art, the addition of the current relations of estimating coupled flow heating, should be added to the program. Both the relations developed by D. Nestler and C. du Pont Donaldson should be added to the program with the selection of one of the two methods being an input option. In addition the program will be periodically reviewed in light of the latest test data and modifications made as required to keep the program up to date. Typical revisions will include incorporation of an improved jet velocity decay correlation such as is developed in Appendix E.

B. Thermal Kill Study - C-1 Target Model

To determine the perforation diameters required for thermal kill of the C-1 type of target vehicle, the internal heating was evaluated for uncoupled flow (small perforation) and coupled flow (large perforation) conditions. It was found that for uncoupled flow, assuming no venting of the perforated compartment, insufficient structure temperature rise for the monocoque design. Therefore for perforations everywhere except at the nose, a coupled flow condition was required to produce melting of the structure.

The critical perforation diameters for coupled flow were determined for the C-1 vehicle from the criterion $A/V^{2/3} = .05$. In Figure 33, these perforation diameters are plotted vs a length scale for three locations of perforation. The length scale is intended to imply a family of geometrically similar vehicles having $W/C_D A$ approximately 3000 lb/ft². Such a condition would become unrealistic below some length, probably on the order of one-half the length of the C-1 target vehicle. Figure 33 emphasizes the fact that the perforation diameter required for coupled flow increases in proportion to the size of the target vehicle, for a given external and internal geometry.

Equation (D-6) of Appendix D was applied to the C-1 trajectory to determine the internal heat flux history for a perforation whose area equalled A_{crit} . No allowance was made for the enlargement of the perforation during re-entry, an effect which should increase the internal heat flux substantially. This heat flux history was then used to generate structure temperature - time curves for various locations and altitudes of hit. In all cases, perforation was assumed to occur upon hit, rather than rely on cratering and subsequent burn-through.

SECRET

SECRET

These computations led to the results presented in Figures 34 and 35 in which the altitude of thermostructural kill is plotted vs the altitude of hit for three structural materials in a monocoque structure. It is evident that little is to be gained by intercepting a high $W/C_D A$ target such as the C-1 above an altitude of 100,000 ft, since the heating curve has just begun to rise at this altitude. In these figures, altitude of kill is defined as the altitude at which the structure is completely melted through. The actual structure failure would occur at somewhat higher altitudes, prior to complete melting. These kill altitudes are based on average heat fluxes; hence earlier failure would also be promoted by any high localized heating. In general, kill occurs at from 10,000 to 20,000 feet below the altitude at which intercept occurs. A structural failure would occur for intercepts as low as 20,000 feet; however, higher altitudes of structural kill are desirable to insure defeat of the mission by premature warhead detonation or excessive miss distance of the re-entering warhead of a killed vehicle.

A study was made to determine the maximum structure thickness for a C-1 monocoque structure which could be melted by coupled flow internal heating. The results are presented in Figure 36 as curves of thickness vs altitude of hit, with altitude of kill as parameter. It is seen that by requiring an intercept at altitudes of 70,000 feet or above, structural thicknesses of from 2 to 3 times the normal design values can be melted by 30,000 feet, while thicknesses of from 3 to 8 times the normal design values can be melted by 10,000 feet.

VI. STRUCTURAL STUDIES

A. Introduction

The goal of this phase of the study is to provide sufficient data to allow system studies to incorporate the effects of vehicle structural failure. In order to attain this goal, the following structural study program was conducted.

During the first year of this program, which ended with the September 20, 1962 reporting deadline, the following goals were established:

- The determination of representative vehicles for impact studies, and
- The determination of the effect of penetration size, location and altitude on structural performance of these vehicles.

The structural studies scheduled for the second year effort were, for the first three months, a continuation of the above. This included:

- structural support of aerodynamic studies of aft cone damage, and
- evaluation of the Mark 3 IOC vehicle subjected to particle impact in the forecone.

Upon completion of these studies, additional work was scheduled in the following areas:

- Continuation of parametric studies incorporating specific internal thermal and pressure histories.

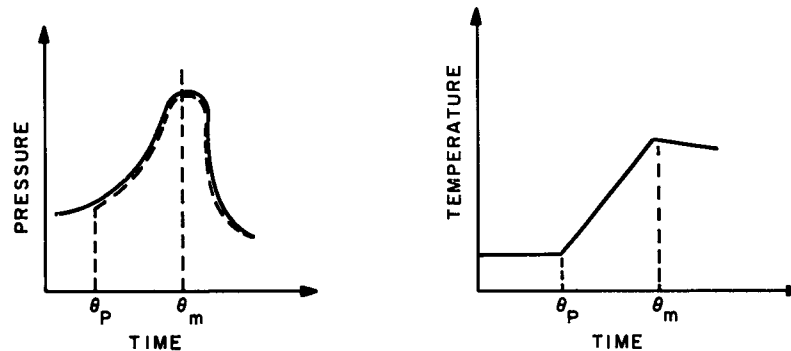
SECRET

SECRET

- Evaluation of local "hot-spot" effects.
- Evaluation of shield-structure interaction.

B. Summary

During the first year of this effort, a parametric study of the C-1 vehicle forecone was presented showing the effect of location and altitude of penetration, and of structural material and configuration on the structural kill of a re-entry vehicle. Because an internal temperature and pressure history was not known at this time, the following assumptions were made.



The internal pressure rise was assumed to be instantaneous at the time of particle penetration (θ_p) and to equalize at the value of the external pressure at the point of impact. Internal temperature was assumed to rise linearly reaching a maximum at the time of maximum pressure (θ_m).

With these assumptions and using T_{max} as a variable, parametric curves were plotted for T_{max} vs. altitude of kill and the following conclusions were obtained:

- A nose or stagnation point penetration would result in the forecone failure of all aluminum alloy vehicles. The most difficult to kill--the monocoque construction--would fail at or above 44,000 feet.
- A nose penetration of an Inconel monocoque structure would result in failure at or above 38,000 feet.
- A nose penetration of a stainless steel monocoque structure would not result in a forecone failure unless the shell temperature attained a value of 670°F or greater.
- A cone penetration of a monocoque shell would result in failure only by melting of the metallic shell.
- A cone penetration of a honeycomb sandwich shell could result in failure if the shell temperatures at peak loading were at least as follows:

SECRET

SECRET

Aluminum	440°F
Stainless Steel	1060°F
Inconel	1320°F

The question remained, however, as to what size hole and altitude of hit was necessary to attain the above temperatures.

During the past year's study, this temperature data was generated for the coupled flow condition ($A/V^{2/3} = .05$) and applied to these parametric studies. A penetration of this size (9.4 in. hole diameter in the C-1 forecone), results in almost "instant" failure for the honeycomb sandwich shells and a slightly delayed failure of the monocoque shells. An example is shown in Table 8 as follows for an aluminum forecone.

TABLE 8. MATERIAL COMPARISON

Alt. of HIT (kilo-feet)	Location of HIT	Altitude of Failure (kilo-feet)		
		honeycomb sandwich bond failure	face melting	monocoque shell melting
100	Forecone	98	95	78
80	Forecone	79	78	67
60	Forecone	59.5	59	53
100	Nose	-	98	88
80	Nose	-	79	74

However, the size of the perforation encountered presents the possibility of an additional type of failure--yielding or instability of the shell due to the removal of the material. A 9.4 inch diameter perforation ($A = .05 V^{2/3}$) mid-way in the C-1 forecone results in a hole subtending on arc of 57°. This size hole located at the extreme fiber of a stiffened cylinder in bending will reduce its load carrying capacity by 40%. In the case of an unstiffened shell with a combination of bending, external pressure and temperature, this reduction is expected to be much greater. However, no analytical procedures could be found which would provide an estimate of the above phenomena.

The Mark 3 forecone was investigated to obtain a performance estimate of an existing vehicle. This also presented data for a low $W/C_D A$ configuration. The forecone is a magnesium monocoque shell which is attached by a breach lock to an integrated warhead section. The combined (shield plus structure) nose section has a thickness of 8.6 inches which makes a stagnation point penetration almost impossible even if statistically probable. Thus, any penetration of the forecone would be on the conical or cylindrical section. As previously stated, failure of a monocoque shell with a cone penetration could be achieved only by melting of the

SECRET

SECRET

inner shell. This was substantiated in this case even with the state of stress caused by the cone-cylinder discontinuity. Table 9 shows the altitude of hit - altitude of kill comparison for a coupled-flow condition (hole diameter = 4.2 in.).

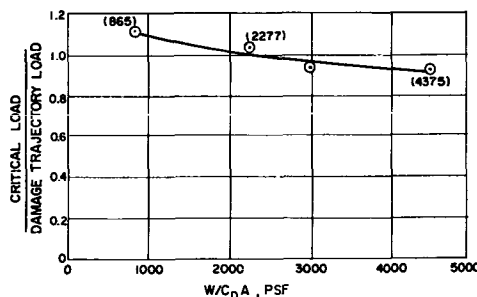
TABLE 9. MARK 3 FORECONE PERFORMANCE

Altitude of Hit (kilo-feet)	Location of Hit	Altitude of Failure (kilo-feet)
120	Conical Section ↓	75
100		70
80		62
60		49
40		14

The Mark 3 configuration was also used to study the effects of shell discontinuity (cone-cylinder transition), shell fixity (breach lock assumed to provide full fixity), and thermal growth of the metallic shell. The effect of shell geometry and fixity was found to increase the shell failure altitude although the "conservative" one inch thick thermal shield provided a safety factor which will delay forecone failure. The influence of thermal growth was found to be a negligible contributor to the forecone failure.

The possibility of the thermal buckling of ring-stiffened shells was also investigated and found not to be critical for the geometry range encountered in vehicle design.

As support to the aerodynamic studies, various structural material-configuration combinations were investigated to determine the feasibility of a "vehicle trim" kill mechanism. Three sphere-cone vehicles with $W/C_D A$ values of 865, 2277 and 4375 psf were initially studied. Later the C-1 vehicle ($W/C_D A = 3000$ psf) with an aluminum monocoque construction was studied. It was found that the failure of a monocoque vehicle with $W/C_D A$ values greater than approx. 2000 psf is possible. However, the applied load was found to be within 10% of the critical load, and it is not felt that the analysis used is accurate enough to indicate a definite kill. A plot of $W/C_D A$ vs. the (critical load/damage trajectory load) ratio is given below:



SECRET

SECRET

It was also found that the impact damage required to cause this type kill is much greater than that which would result in a thermal kill.

C. Future Work Required

In the previous summary, it was shown that the attainment of the melting temperature of the metal can be used as the failure criterion. This applies only if

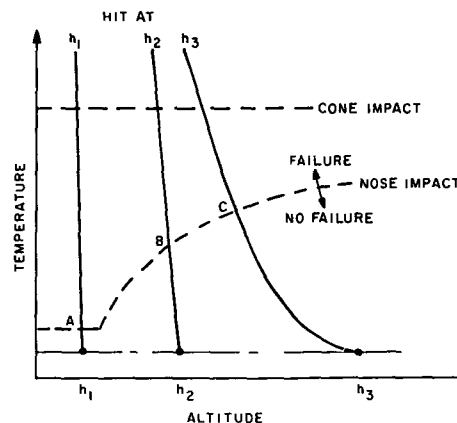
- The internal heating is uniform; and,
- The unsupported thermal shield cannot withstand the loading environment.

In order to cover the cases when the shell temperature is not uniform (which is now considered the most probable case), or the thermal shield is capable of withstanding the loads to a lesser altitude, the mode of failure which must be evaluated is that of the reduction in load-carrying capacity of a shell with an arbitrary hole. This investigation has been initiated and will be conducted during the remaining portion of this present effort.

An additional area of study lies in the addition of more advanced vehicles to this kill mechanism study. Of specific interest are the current hardened vehicles utilizing foam filled interiors. If these types of vehicles are planned for future study or testing, the structural details must be representative of current design thinking.

D. C-1 Vehicle Studies

During the past year the internal heat flux data was generated for the penetration of the C-1 vehicle. This data was for the coupled flow condition and resulted in extremely rapid temperature increases. This negated the use of the curves of Reference 18 at least in their present form. These curves were replotted to obtain those shown in Figure 37, 38, and 39. From this type of presentation, the temperature that the structure must reach for failure can be determined at the given altitude. The curves shown are for the nose impact of a monocoque forecone. Failure due to a cone penetration can only occur by shell melting. The curves of Figures 37 thru 39 were then used in conjunction with the predicted temperature rise curves as shown below.



SECRET

SECRET

The intersections A, B and C represent the points of failure for hits at h_1 , h_2 , and h_3 respectively. This approach was used throughout the parametric studies to obtain the various altitude of kill vs. altitude of hit relationships.

Comparison of Nose vs. Cone Penetration, Monocoque Shell

In Reference 18, it was stated a nose hit could result in a thermal-stress kill. This was brought about by the lowering of the material ultimate strength to the level of the applied loads. It was also shown that the shell stresses were extremely low if a cone hit occurred, and the mode of failure of the shell would be melting. However, sufficient data was not available at that time to show the difference in kill altitude of these two hit locations. This is now given in Figures 40, 41, and 42. A tabulation is also shown in Table 10.

TABLE 10. LOCATION OF HIT COMPARISON

Altitude of Hit (kilo-feet)	Location of Hit	Material	Altitude of Kill (kilo-feet)	Δh (Alt. of Hit) -(Alt. of Kill) (kilo-feet)
145	Nose	Aluminum	105	40
		Inconel	80	65
		Stainless Steel	84	61
	Cone	Aluminum	88	57
		Inconel	67	78
		Stainless Steel	69	76
100	Nose	Aluminum	88	12
		Inconel	74	26
		Stainless Steel	75	25
60	Nose	Aluminum	58	2
		Inconel	53	7
		Stainless Steel	55	5
	Cone	Aluminum	53	7
		Inconel	46	14
		Stainless Steel	48	12

This comparison has the following assumptions:

- Uniform internal heating exists.
- The hole size is sufficient to cause coupled flow ($A/V^{2/3} = .05$). Assuming a circular hole, its diameter is 9.4 inches.
- The thermal shield cannot carry the residual loading and will fail upon failure of the metallic liner.

SECRET

SECRET

Comparison of Hole Size

The C-1 forecone hit, monocoque construction was utilized for this comparison. The internal heat flux was assumed to increase linearly with the area of the hole, and resulting temperature rises found. The technique previously described was then applied to obtain the results of Figures 43, 44, and 45. The hole areas used are shown in Table 11.

TABLE 11. HOLE SIZES, C-1 STUDY

Hole Area (sq. ft.)	Hole Diameter (in.)	$A/V^{2/3}$ Ratio
.483	9.4	.05
.724	11.5	.075
.966	13.3	.10

As expected, this comparison shows that larger impact holes are required with descending hit altitude in order to maintain a constant kill altitude. Typical hole sizes and impact particle masses are tabulated in Table 12. The impact velocity was assumed equal to the re-entry vehicle velocity at the hit altitude in order to eliminate the additional variable of particle velocity. Particle masses were determined from the correlation of hole area developed by Persechino (Reference 19).

TABLE 12. EFFECT OF HOLE SIZE

STRUCTURE: ALUMINUM MONOCOQUE:				
Altitude of Kill (kilo-feet)	Altitude of Hit (kilo-feet)	Hole Size (sq. ft.)	Particle Mass (gms)	Impact Velocity (kilo-feet/sec)
80	105	.483	130	} ~ 25
	92	.724	260	
	87	.966	390	
60	69	.483	150	} ~ 24
	65	.724	270	
	62	.966	430	
40	45	.483	180	} ~ 22
	43	.724	320	
	42	.966	490	

Although the fact remains that larger holes cause more rapid failures, this comparison clearly illustrates the diminishing returns. For a kill altitude of 40,000 feet, a larger hole gains very little in hit altitude difference and loses much in particle mass increase.

SECRET

SECRET

Comparison of Structural Configurations

A comparison of the following three types of structural configurations was made to determine their relative kill altitudes.

- Monocoque Shell.
- Ring Stiffened Shell.
- Honeycomb Sandwich Shell.

This was done by using an equivalent monocoque thickness and determining its altitude at "melting". The results for the honeycomb sandwich are shown in Figures 46 thru 48, and the ring stiffened shell in Figure 49. A comparison of the three constructions, using aluminum, is given in Table 13.

TABLE 13. CONFIGURATION COMPARISON

Alt. of Hit (kilo-feet)	Altitude of Kill (kilo-feet)		
	Monocoque	Ring Stiffened	Honeycomb Sandwich
100	78	92	95
80	67	76	78
60	53	58	59
40	37	39	39

An additional mode of failure of the ring stiffened shell is that of thermal buckling of the skin caused by a temperature difference between the rings and skin. The buckling is caused by the circumferential stresses induced by the restraint of thermal expansion at the ring locations. Anderson (Reference 20) has shown that this mode of failure is not commonly encountered in practical re-entry structures. A temperature difference (avg. skin - avg. ring) of 200°F will fail an aluminum cylindrical shell with a radius/thickness ratio greater than 800. For the skin gages encountered, in the C-1 design approximately 0.10 in., the radius must be 80 inches. This is extremely large for forecone design but applicable in the range of aft cone structures. However, test results on aluminum cylinders (Reference 21) indicate that a shell temperature in excess of 800°F is required to induce a temperature difference of 200°F. The altitude difference between 800°F and melting is approximately 2000 feet in the 60 to 80 kilo feet kill range. The difference is small, and the lower limit of shell melting appears to be adequate as a kill estimate.

Conclusions

The previous investigations indicate that for a coupled flow condition and uniform internal heating, structural failure can be considered that of liner melting. This, of course, assumes no load carrying capacity of the thermal shield. The stresses in the shell from a small pressure differential and inertia loads are small. Their contribution to the formation of yield hinges or structural instability at a much earlier time than shell melting is negligible.

SECRET

SECRET

Thus, failure altitudes for C-1 type vehicles and the influence of particle mass and velocity, material, structure, hole size, hole location and altitude of hit can be obtained from the curves presented herein for the forecone, and from Figures 33 and 35 for the payload section and aft cone.

The assumption of a non-load carrying thermal shield must be further evaluated. This investigation is directly related to that of the load carrying capacity of a shell with an arbitrary hole.

E. Shells With Cut-outs

The understanding of the behavior of this type of structure has become important for the following two reasons.

1. If the assumption of uniform internal heating is used, the failure altitude of the metallic liner can be approximated by melting. However, structural integrity may be maintained by the shield carrying the reduced load. Whether this is possible or not depends on the structural integrity of the plastic shell with an arbitrary impacted hole.
2. When considering a large impacted hole and a highly localized heating condition, the structural integrity of the metal structure itself depends on the hole size and location.

A survey of existing literature on the effects of cutouts on the stability of shells was performed. This search revealed no useful analytical techniques. References 22 through 30 represent the literature found on this subject. This work involved standard aircraft stringer-frame construction of cylindrical shells. The cut-outs were carefully placed and framed by the ring and stringer members. The most extensive work appeared to be that conducted by Hoff during his 1946-48 NACA study. Although this study provided valuable experimental data, the analytical methods which were developed are laborious and limited, and neither the experimental nor the analytical results can be readily extended to unsymmetric cutouts or other geometries. The fact that these results are for pure bending makes them even more inadequate in view of the combined loading which the re-entry vehicle will encounter. However, to provide some idea of the stability reduction caused by cutouts, experimental results of the critical moment ratio vs. cutout angle from the NACA study are shown in Figure 50. For both curves (side and bottom cutouts) the test cylinders were reinforced with 16 equally spaced stringers and 8 equally spaced rings, and the cutouts were taken from the center of the cylinder with a cutout length to cylinder length ratio of 1/3.

It is to be expected that the combined loading due to an unsymmetric pressure distribution will significantly reduce the critical moment ratio. On the basis of present information it is impossible to estimate the magnitude of this reduction. Therefore, if meaningful results are to be obtained from this study, additional information must be made available. It may be of interest to know that some in-house effort has already been directed toward the determination of the effects of unsymmetric cutouts on both cones and cylinders under combined loading. In connection with an independent pilot study of this subject, an extensive experimental investigation has been recommended in lieu of a more complicated and expensive approach by way of analytical solution, a decision which was heavily influenced by the meager returns of NACA's competent attempt at a theoretical solution.

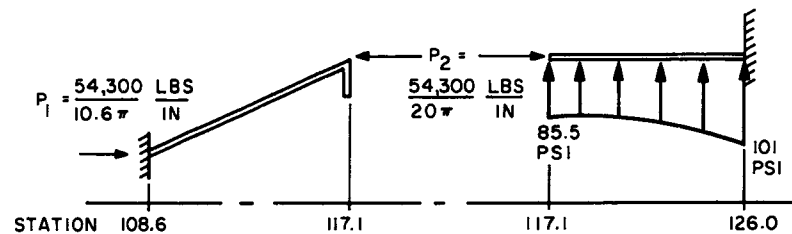
SECRET

SECRET

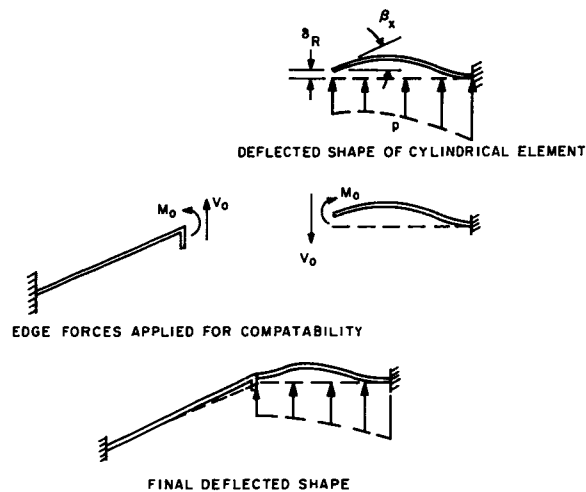
F. Mark 3 Studies

The forecone penetration of the Mark 3 I. O. C. was investigated in order to obtain a performance estimate of an existing low W/C_DA vehicle. The trajectory data used in this study was obtained from the record of Missile Number 221, Flight 54D (Reference 31). The peak dynamic pressure from this trajectory is 71,000 psf. This is 0.87 times that of the limit design pressure. The trajectory data is given in Figure 51.

The vehicle forecone geometry and the externally applied pressure are shown in Figure 52. The combination of cone and cylinder in the forecone structure presents an interesting internal pressure contrast to the C-1 forecone cavity. A cone penetration of the C-1 cavity results in an equalization of internal and external pressure. A cone penetration of the Mark 3 cavity results in an equalization of pressure on the cone but a net internal pressure in the cylindrical section. This is shown below. The numerical values given are those corresponding to peak dynamic pressure.



The analysis was conducted as follows. The stresses and deflections were found for the cylindrical shell subjected to the meridionally varying pressure. End shears and moments were applied to maintain compatibility between the cylinder and edge stiffened cone.



SECRET

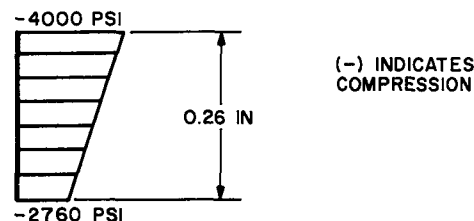
SECRET

Influence coefficients were found for both shells and used in the determination of M_0 and V_0 which were as follows:

$$M_0 = 7.1 \text{ in. lbs/in.}$$

$$V_0 = 62.3 \text{ lbs/in.}$$

The meridional stresses at the juncture due to the airloads and M_0 term are:

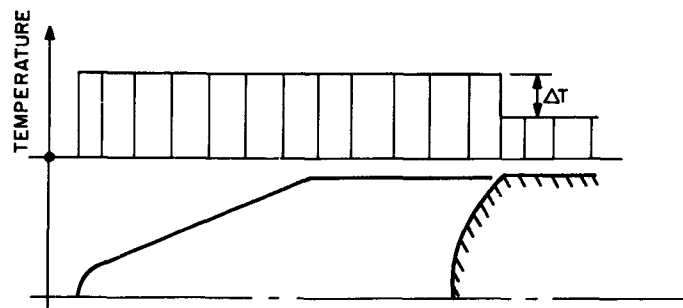


At the fixed end the stresses are -12,260 psi, outer fiber and 5600 psi, inner fiber. Thus, a 4000 psi stress level exists at peak q or 40,000 feet. This stress of course decreases with increasing altitude. Since the juncture stress is only 1/3 that of the fixed-end stress, the latter was used to determine the state-of-stress influence on the thermal kill of the magnesium shell.

Figure 53 illustrates the failure regime for a thermo-stress kill. At the altitude of peak q (40,000 feet), a magnesium temperature of 640°F is required for failure. As the altitude increases (and the applied load decreases) a higher temperature is required for kill. The upper limit is the 1000°F ignition temperature. Figure 54 contains the predicted internal temperature rise as a function of altitude of hit. A combination of these two plots yield the altitude of hit-altitude of kill relationships of Figure 55. The lower limit represents failure at the 1000°F temperature level, and the $\Delta T = 0$ curve represents failure due to the combination of temperature rise and fixed-end stress.

Effect of a Temperature Sink

The Mark 3 vehicle forecone was used as the basis of evaluation of an abrupt temperature difference. This is illustrated below where the forecone shell is assumed to maintain a uniform temperature which is higher than that of the payload section.



SECRET

SECRET

Figure 56 shows the failure regimes as ΔT attains values of 100, 150 and 200°F. These ΔT effects are also shown in the relationships of Figure 55.

Effect of Hole Size

The hole size was also varied to study its effect quantitatively. The areas and circular hole diameters used are shown in Table 14.

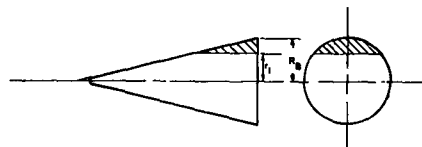
TABLE 14. HOLE SIZES, MARK 3 STUDY

Hole Area (sq. ft.)	Hole Diameter (in.)	$A/V^{2/3}$
.093	4.2	.05
.185	5.9	.10
.278	7.3	.15

The temperature was assumed to increase linearly with hole size. The altitude of hit-altitude of kill relationship vs. hole size is given in Figure 57 for the lower limit "melting" condition and in Figure 58 for the fixed end ($\Delta T = 0^\circ\text{F}$) stress condition.

G. Aerostructural Kill

This study was conducted to evaluate the effect of induced trim angles of attack on the re-entry structure. Three high performance, slender re-entry bodies were studied ($W/C_D A = 865, 2277, 4375 \text{ psf}$). The damage assumed consisted of a horizontal slice parallel to the vehicle centerline. This is shown below.



The procedure used in this Study was as follows:

- The vehicle structure was selected to withstand the design load conditions of the undisturbed trajectory. These are shown in Table 15.

TABLE 15. DESIGN LOAD CONDITIONS

Vehicle No.	$W/C_D A$ (psf)	Dynamic Pressure (psf)	Angle of Attack (deg)	Comments
4	4375	270,000	0	peak axial
		10,000	5	peak lateral
10	2277	150,000	0	peak axial
		7,000	5	peak lateral
21	865	59,500	0	peak axial
		9,000	5	peak lateral

SECRET

SECRET

- For the incurred damage, $r_1/R_B = 0.7$, a resulting trim angle of attack (see Table 16) was determined by Aerodynamic Studies reported in Reference 2.

TABLE 16. INDUCED TRIM

Veh. No.	Trim Angle of Attack (deg)
4	1.223
10	.815
21	.675

- Structural loads were obtained for the trim condition and the vehicle structure evaluated for failure due to instability and yielding.

Figure 59 illustrates the relative performance of various materials. Failure will occur at the percent of peak load indicated. The superiority of the monocoque shell over the honeycomb sandwich structure is clearly illustrated for the 4375 psf W/C_{DA} vehicle. Figure 60 presents a further comparison using the same vehicle. A construction comparison is shown here. Figure 61 presents a comparison of the vehicle performance using W/C_{DA} as the parameter. A monocoque design is utilized.

The aluminum monocoque data of Figure 61 was used in Aerodynamics Studies to further obtain a trim angle of attack versus degree of damage relationships (Reference 2).

VII. ICBM FLIGHT EXPERIMENTS (WAC PROGRAM)

Two HKM experiments will be conducted on board a TVX re-entry vehicle flying an ICBM trajectory at the Atlantic Missile Range. These experiments are deemed highly significant in that they will take place on a sharp-nosed high W/C_{DA} cone typical of probable next-generation target threats. Two internal compartments will be isolated by means of bulkheads, thus permitting two different experiments to be conducted concurrently. (See Figure 62) Each compartment will have a free volume of 0.75 ft³. A 4 inch diameter hole will be opened at 90,000 foot altitude in the shield-structure associated with one compartment. At approximately the same altitude, a 1.2 inch diameter hole will be opened into the other compartment. It is expected that a coupled flow situation will prevail in one compartment, while uncoupled flow should result in the other compartment. Twenty thermocouples will record structure and bulkhead temperatures while four transducers will record internal pressure variations. Continuous data transmission will result due to the use of a graphite nose of 1/4 inch radius to produce a conical flow field of low electron density. It is expected that the large internal heating associated with coupled flow will burn through the confining bulkheads and expose a large area of the primary structure to high heating rates.

SECRET

SECRET

APPENDIX A. DISCHARGE COEFFICIENT INTO SUPERSONIC FREE STREAM

The experimental results of Vick (Reference 12) have indicated that a drastic reduction in discharge coefficient can occur for low orifice pressure ratios when discharging into a supersonic free stream. This effect must be considered whenever a vent outflow exists on the side of a re-entry vehicle or test model.

Discharge coefficients K_g for various shapes and inclinations of orifices for discharge into a free stream of $M = 3.25$ are plotted in Figure A-1, taken from Vick's data. Since there is little difference between the values of K_g for square and circular orifice shapes, the data given by Vick for various Mach numbers and a square orifice inclined 60 degrees have been used in the analysis of the Wallops Island flight models, for circular orifices inclined 60 degrees. These data are cross-plotted versus Mach number in Figure A-2.

APPENDIX B. EXTERNAL VISCOUS EFFECTS ON INTERNAL HEATING

As mentioned under the discussion of the C. A. L. Internal Heating Tests, measured internal heat fluxes for a perforated compartment having venting were an order of magnitude less than the predictions of the venting analysis developed in Reference 4. More detailed computation revealed that the mass flow rate required to satisfy continuity requirements could be obtained from the lower 25 percent of the boundary layer. For the C. A. L. test conditions, the laminar boundary layer thickness was computed to be 0.6 inches. The velocity and enthalpy profiles of Van Driest (Reference 32) at $M_1 = 85$ and $T_w/T_e = 1$ were used to compute the true energy influx compared to the inviscid prediction. An iterative procedure was used to solve for the flow turning angle ϵ and the internal pressure P_2 using first order expansion theory for hypersonic flow:

$$\epsilon \approx \frac{P_1 - P_2}{\gamma P_1 M_1} \approx \frac{y^*}{D^*} \quad (B-1)$$

where y^* is the height within the boundary layer and D^* is properly taken as an effective diameter averaged over the circular orifice cross-section. It was found that the reduction in stagnation enthalpy and Mach number near the wall resulted in an order of magnitude lower energy influx and maximum impingement heat flux than predicted by an inviscid analysis.

The analysis described above was carried out for the vented compartment conditions of Runs 7 and 8, Table 5. The results are tabulated below:

	Run No.	
	7	8
Theoretical pressure ratio P_2/P_1	0.58	0.71
Average measured pressure ratio P_2/P_1	0.67	0.9

This agreement is about as good as could be expected, due to the large scatter in measured pressures.

SECRET

SECRET

In order to ascertain under what conditions viscous effects on internal heating must be considered, a criterion was developed by comparing the mass flow rate from inviscid theory (Equation (11)) for supersonic approach flow with the mass flow rate in the boundary layer for a projected depth equal to the perforation diameter. This ratio is:

$$\frac{m}{m_{BL}} = \frac{C_{m_1}(P_1 - P_2)\delta g A_1}{\rho_1 U_1^2 (\delta - \delta^*) D_1} \approx C_{m_1} \frac{\pi}{4} \left(\frac{P_1 - P_2}{P_1} \right) \frac{D_1}{M_1 (\delta - \delta^*)} \quad (B-2)$$

For cold wall hypersonic flow with local Mach number $M_1 \approx 10$, Kaplan (Reference 33) showed that $\delta^*/\delta \approx 0.6$. Also, the inviscid venting analysis of Reference 4 can be used to show that for hypersonic flow over sharp slender cones:

$$\frac{P_1 - P_2}{P_1} \approx \frac{1}{5} \frac{A_2}{A_1} \quad (B-3)$$

With these substitutions, Equation (B-3) becomes:

$$\frac{m}{m_{BL}} \approx 0.4 C_{m_1} \frac{A_2}{A_1} \frac{D_1}{M_1 \delta} \quad (B-4)$$

Assuming $C_{m_1} \approx 0.7$ and $M_1 \approx 10$, there results:

$$\frac{m}{m_{BL}} \approx .03 \frac{A_2}{A_1} \frac{D_1}{\delta} \quad (B-5)$$

For maximum heating portions of ICBM flights, the boundary layer thickness δ is on the order of 0.25 inches at locations on the order of 4 feet from the cone tip. For this condition, Equation (B-5) was used to compute curves of m/m_{BL} as a function of D_1 and D_2 . From the results plotted in Figure E-1, it is seen that m/m_{BL} can be considerably less than 1.0 for ICBM heating conditions. The values of m/m_{BL} in Figure E-1 are considerably lower than the true values which would result from a viscous analysis, due to the use of the inviscid relation of Equation (11); however, they serve as a rough indication of the importance of viscous effects.

Future studies along these lines will include parametric evaluation of viscous corrections to the internal heating results presented previously (in Reference 4) for vented compartments.

APPENDIX C. COMPRESSIBLE SHEAR LAYER ANALYSIS OF INTERNAL HEAT TRANSFER DOWNSTREAM OF PERFORATION

An engineering analysis has been developed for the prediction of internal heat transfer levels downstream of a perforation for the case of an unvented compartment in which the internal and external pressures have equalized. Referring to Figure C-1, the following assumptions are made:

SECRET

SECRET

- A steady flow situation exists.
- The effects of the approach boundary layer profile are neglected.
- The heating rates on the downstream surface of the perforation (projection BC in Figure C-1) can be predicted by using a "strip theory" stagnation heating method for a flat-nosed two dimensional leading edge.
- The heating rates to the internal structure downstream of the perforation (projection CD in Figure C-1) can be predicted by using flat plate boundary layer theory with origin of the boundary layer at C.
- The dividing streamline of the separated flow is located at AB. It is realized that an idealized steady flow two-dimensional model is being employed to analyze what is probably an unsteady three-dimensional flow; however, such simplification is necessary to obtain tractable relations for analysis purposes. As experimental data become available, the validity of the simplified approach can be checked, and empirical modifications introduced if necessary.

Although turbulent flow is the practical case of interest in studies of ICBM thermal kill, the analysis will also consider the effects of laminar flow for possible application to the C. A. L. Internal Heating Tests. For these tests, an extrapolation of the correlation of separated flow transition data of Larson and Keating (Reference 34) to a local Mach number of 8.5 at a local Re_s of 70,000 and T_w/T_s of 0.1 indicates that a laminar separated layer probably existed even for the largest orifice tested.

As indicated in the assumptions above, the heat transfer rates on the downstream surface of the perforation are predicted by using a "strip theory" stagnation heating method. The use of this technique was shown by Shaw and Nestler (Reference 35) to yield reasonable agreement with experimental values of heat transfer rates to the stagnation line of fins in supersonic shear layer flow. In this approach, the local heating rate on surface PC (Figure C-1) is given by the relation of Lees (Reference 36) for a two-dimensional leading edge, using a velocity gradient of 0.3 that of a hemi-cylindrical leading edge (Nestler and Musser, Reference 37). The resulting relation is:

$$\dot{q} = \frac{0.27}{Pr^{2/3}} (\rho \mu U_o')^{0.5} (h_s - h_w) \quad (C-1)$$

in which U_o' is approximated by the Li-Geiger relation (Reference 38) for supersonic flow:

$$U_o' = \frac{2U}{t} \left[\frac{\rho_1}{\rho_2} \left(2 - \frac{\rho_1}{\rho_2} \right) \right]^{0.5} \quad (C-2)$$

In Equations (C-1) and (C-2), ρ , μ , h_s , h_w , and U are local values at the point in question, and ρ_1/ρ_2 is the inverse density ratio across a normal shock based on the local approach Mach number.

SECRET

SECRET

The heat transfer rates to the internal structure downstream of the perforation (CD in Figure C-1) can be approximated by simple flat plate boundary layer theories for either laminar or turbulent flow. Introducing the approximations $\rho \sim T^{-1}$, $\mu \sim T^{0.63}$, and $h_w < h_s$, it is readily shown that for a sharp cone, the internal heat flux \dot{q}_i on surface CD is related to the external heat flux \dot{q}_e as follows:

$$\text{Laminar boundary layers: } \frac{\dot{q}_i}{\dot{q}_e} = \frac{(U/U_e)^{0.5} (h_s/h_{s_e}) (s_e/s_i)^{0.5}}{\sqrt{3} (T/T_e)^{0.185}} \quad (C-3)$$

$$\text{Turbulent boundary layers: } \frac{\dot{q}_i}{\dot{q}_e} = \frac{(U/U_e)^{0.8} (h_s/h_{s_e}) (s_e/s_i)^{0.2}}{1.18 (T/T_e)^{0.874}} \quad (C-4)$$

In Equations (C-3) and (C-4), values of U , h_s , and T are taken as local values in the shear layer at the location of corner C (Figure C-1). It is obvious that these relations become less accurate for large values of s_i , due to the difference between flat plate boundary layers and wall jet boundary layers.

The local shear layer properties in Equations (C-1) through (C-4) can be evaluated from the analyses of Chapman (Reference 39) for laminar separated flow and Chow and Korst (Reference 40) for turbulent separated flow. Both of these methods allow for compressibility effects; however, neither method allows for the effect of the initial approach flow boundary layer thickness, being essentially analyses of the mixing of a uniform stream with a fluid at rest. Therefore both analyses tend to predict too high a velocity and enthalpy at a given location in the mixing region.

For the local flow conditions which existed for the C. A. L. Internal Heating Tests, the Chapman analysis yields the property profiles shown in Figure C-2 for a 3-inch diameter orifice. The effect of orifice diameter on the velocity ratio U/U_e is tabulated below for the midpoint and bottom corner of the downstream edge of the orifice.

D(inches)	1.5	3.0	4.5	6.0
U/U_e at $y = -0.25$ in.	.17	.26	.31	.35
U/U_e at $y = -0.50$ in.	.01	.07	.12	.17

Thus, it is seen that substantial reductions in velocity below the local free stream value occur, with corresponding reductions in heat transfer. Inserting the local properties obtained from the Chapman analysis for the midpoint location on the downstream edge of the orifice ($y = -0.25$ inches) into Equation (C-1) results in excellent agreement with measured values:

Orifice diameter D_1 inches	1.5	3.0
Theoretical heat flux \dot{q}_i , BTU/ft ² sec	0.5	1.0
Measured heat flux \dot{q}_i , BTU/ft ² sec	0.6	1.3

SECRET

SECRET

Inclusion of the effect of initial boundary layer which exists at the upstream edge of the orifice can be made for the laminar case by using the results of an analysis of Denison and Baum (Reference 41). For a three-inch diameter orifice, their method yields a value for U/U_e of 0.30 for the C. A. L. test conditions on the dividing streamline ($y = 0$), compared to the value of 0.58 shown in Figure C-2 for the Chapman analysis. This difference becomes less as one proceeds down from the dividing streamline, being almost negligible for the downstream lower corner ($y = -0.5$ inches, corner C in Figure C-1).

If the separated flow region is turbulent, additional uncertainty exists in property profiles and impingement heat transfer due to the lack of mixing data at high Mach numbers. The analysis of Chow and Korst (Reference 40) leads to a particularly simple result for the velocity profile when the separated region is on a sharp cone in hypersonic flow:

$$\frac{U}{U_e} = 0.5 \left[1 + \operatorname{erf} \left(\frac{\sigma y}{x} + 1.82 \right) \right] \quad (C-5)$$

(See Figure C-1 for nomenclature). However, for a given location (x, y) within the mixing region, the value of U/U_e can be quite sensitive to the value chosen for σ , the mixing parameter. Values of σ obtained from experimental studies of turbulent mixing of jets expanding into quiescent surroundings were plotted versus Mach number by Maydew and Reed (Reference 42). Additional values of σ from the jet mixing studies of Warren (Reference 43) and Chrisman (Reference 44) have been added to the correlation of Reference 42, and are shown in Figure C-3. For sharp slender cones in hypersonic flow, the local surface Mach number is on the order of 8 to 10. For the C. A. L. Internal Heating Tests, $M_{\text{cone}} \approx 8.5$; values of σ between 34 and 52 can be obtained, depending on the method of extrapolation (See Figure C-3). The velocity and temperature profiles for the C. A. L. test conditions are shown in Figure C-4 for a 3-inch diameter orifice for $\sigma = 35$ and 50, using a cold-wall Crocco distribution for temperature as a function of velocity with $\gamma = 1.4$. Comparison of Figures C-2 and C-4 shows that the turbulent mixing zone is confined to a much narrower region than the laminar zone. (It should be noted that an incompressible analysis yields the opposite results). The magnitude of the heating rates measured by the calorimeter on the downstream edge of the orifice indicate that a laminar mixing region probably existed for orifice diameters of 1.5 and 3.0.

Since no calorimetry existed on the orifice inserts for larger diameters, it is possible that undetected transition of the separated layer may have occurred for $D = 4.5$ and 6.0 inches. The effect of orifice diameter on U/U_e at the downstream corner C (Figure C-1) for turbulent mixing is shown below, for two choices of σ .

Values of U/U_e for Lower Corner of Downstream Edge of Orifice (C. A. L. Tests)

D(inches)	1.5	3.0	4.5	6.0
U/U_e ($\sigma = 35$)	0	0	.002	.060
U/U_e ($\sigma = 50$)	0	0	0	.0005

SECRET

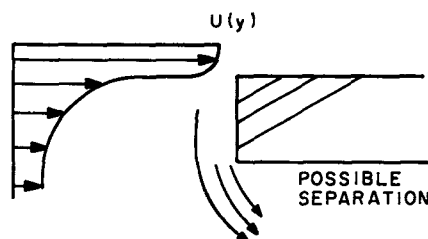
SECRET

Comparison with results presented above for laminar mixing suggests that lower heating of the structure downstream of the orifice will result for turbulent mixing, provided the shear layer is steady and does not fluctuate.

Estimates of the heat flux to the internal structure were made for a location $s_1 = 1.2$ inches downstream of the 6-inch diameter orifice for the C.A.L. tests, corresponding to the location of the thermocouple nearest the orifice. Due to the low value of Re_s of the new boundary layer on the lower surface (CD in Figure C-1), laminar heating was assumed to exist. Hence the heat flux was determined from Equation (C-3) using both laminar and turbulent shear layer analyses for local flow properties. The following results were obtained for \dot{q}_i/\dot{q}_e , the ratio of internal to external cone heat flux:

	\dot{q}_i/\dot{q}_e
Laminar mixing analysis	0.17
Turbulent mixing analysis	
$\sigma = 35$.03
$\sigma = 40$.005
Measured value	<.02

On the basis of this comparison, it would appear that transition to turbulent shear flow occurred for $D = 6$ inches. However, it is possible that the higher pressure along the upper portion of the downstream edge of the orifice produces a jet-like flow which separates as it turns the corner, due to the absence of any high velocity internal free stream parallel to the internal structure (see sketch).



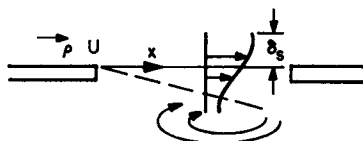
APPENDIX D. COUPLED FLOW HEATING

To provide a first-order estimate of internal heating levels for the immediate needs of vulnerability studies, the results of the rocket exhaust tests of References 8 and 15 were analyzed. Although these tests were primarily of qualitative value, it is possible to deduce from the thermocouple readings and the amount of structure melted that the average internal heat flux for coupled flow in the Malta rocket exhaust environment for a perforation area of 5 square inches on a 20° half angle blunt cone of 15-inch base diameter was on the order of 60 BTU/ft²-sec. Much higher local values of internal heat flux existed, which could lead to local melting of structural segments or overheating of local components; however, for present purposes, an average heat flux and an average structural temperature rise is felt to be a firmer kill mechanism.

SECRET

SECRET

Since this value of heat flux pertains to particular values of compartment geometry, external flow environment, and perforation size, some method of scaling the results to other conditions is necessary. To accomplish this, the concept of a fluctuating shear layer discussed by Charwat (Reference 44) in connection with flow past cavities was assumed to be applicable to the case of a complete perforation. The unsteady nature of the shear layer which develops as flow proceeds past the perforation is assumed to lead to a mass exchange process in which high energy fluid is continually fed into the compartment while lower energy fluid is exhausting through the same perforation (see sketch).



On the basis of this model, Charwat derived the following relation:

$$dw \sim \rho U \sigma_s \quad (D-1)$$

in which:

dw = unsteady mass exchange rate per unit depth of channel

ρ = external local static density

U = external local velocity

δ_s = height of shear layer

Assuming that the shear layer thickness grows proportionally as the distance in the flow direction, the net mass flow rate into a perforation of cross-sectional area A is (see sketch).



$$m \sim \int dw dy \sim \rho U \int_A x dy \sim \rho U A \quad (D-2)$$

and the net energy influx E_{in} is:

$$E_{in} \sim m h_s \sim \rho U h_s A \quad (D-3)$$

SECRET

SECRET

Assuming the relative partition of E_{in} between solids and gas to be independent of compartment geometry, the average internal heat flux \dot{q} is:

$$\dot{q} \sim \frac{\rho U h_s A}{A_s} \sim \rho U h_s \left(\frac{A}{A_{crit}} \right) \left(\frac{A_{crit}}{A_s} \right) \quad (D-4)$$

Since the internal surface area A_s and the critical perforation area for coupled flow A_{crit} are both proportional to the two-thirds power of the compartment volume V , there results:

$$\dot{q} \sim \rho U h_s \left(\frac{A}{A_{crit}} \right) \quad (D-5)$$

Applying the proportionality relationship of Equation (10) to the Malta test results, with the assumption that $A = A_{crit}$ for these tests, yields the following expression:

$$\dot{q} = 0.53 \frac{PU}{zT} \left(\frac{h_s}{10^3} \right) \left(\frac{A}{A_{crit}} \right) \text{ (For } A \geq A_{crit} \text{)} \quad (D-6)$$

in which:

\dot{q} = average internal heat flux, BTU/ft²sec

P = local external pressure, Psia

U = local external velocity, ft/sec

T = local external static temperature, °R

z = local external compressibility factor

h_s = external stagnation enthalpy, BTU/lb.

The values of P , U , T , and h_s are determined by the trajectory and by the location of perforation for a given re-entry vehicle configuration.

Although Equation (D-6) is useful in providing estimates of the temperature rise of the structure (or internal components) within a perforated compartment, its accuracy is unknown when applied to conditions of compartment size, perforation size, and flow environment which are considerably different than those of the Malta tests. The adequacy of this simplified method used to scale the Malta results requires verification over a wide range of conditions before it can be accepted with confidence.

SECRET

SECRET

APPENDIX E. IMPROVED CORRELATION OF AXIAL VELOCITY DECAY OF COMPRESSIBLE JETS

In References 10 and 45, the results of the theory of Warren (Reference 42) for compressible jet diffusion were presented in parametric form and compared to existing experimental data. In general, agreement of the theory with data was sufficient for engineering purposes; however, a lack of high temperature data was evident. Further, no simple yet accurate empirical formulation existed which matched the theory, and which would avoid interpolation and extrapolation.

In a publication by Kleinstein (Reference 46), a compressible turbulent axisymmetric jet diffusion theory was developed which resulted in the following extremely simple relation for axial velocity decay:

$$\frac{U_A}{U_1} = 1 - e^{-\frac{1}{\lambda}} \quad (E-1)$$

in which

$$\lambda = \left[.074 \left(\frac{\rho_a}{\rho_1} \right)^{0.5} \left(\frac{x}{R_1} \right) \right] - 0.70 \quad (E-2)$$

The constants in Equation (E-2) were determined from subsonic heated jet diffusion experiments. Kleinstein showed that his method agreed well with several sets of data, but diverged considerably from Warren's data for a Mach 2.6 jet.

Since the survey of data of Reference 10 was made, two additional sets of very high temperature jet diffusion data have become available (References 47 and 48). These data were compared with the prediction of Equation (E-1), and significant disagreement was noted. In an attempt to retain the convenient form of Equation (E-1), empirical adjustment of the constants and exponents of Equation (E-2) was undertaken. A reasonably accurate fit to several sets of highly compressible jet diffusion data was derived by Charlino (Reference 49), yielding:

$$\frac{U_A}{U_1} = 1 - e^{-\frac{1}{K}} \quad (E-3)$$

in which

$$K = \left[.07 \left(\frac{\rho_a/\rho_1}{1 + 0.1 M_1^2} \right)^{0.365} \left(\frac{x}{R_1} \right)^{0.97} \right] - 0.60 \quad (E-4)$$

The correlation is shown plotted in Figure E-1. The agreement of this method, called the "adjusted Kleinstein" method, with the recent high temperature data mentioned above is shown in Figures E-2 and E-3, along with the predictions of the original Kleinstein and adjusted Warren methods. ("Adjusted Warren method" refers to the extrapolation required to apply Warren's results to the high temperature ratios of the data.) It is seen that the adjusted Kleinstein method gives significantly better agreement with high temperature jet data than either of the other two methods. Further verification of the adequacy of Equation (E-3) must await accumulation of additional data.

SECRET

SECRET

REFERENCES

1. Nestler, D. E., and VandenEykel, E. E., "Results of Rocket Exhaust HKM Internal Heating Tests," GE RSD Document 63SD564, May, 1963. (Secret)
2. Progress Report No. 9, "Hypervelocity Kill Mechanisms Program," NRL Memo Report 5913, Vol. II, Section H, January, 1963. (S-RD)
3. Walker, G. K., "The Turbulent Boundary Layer with Combusting Graphite Surface," GE MSVD PIR AT-8151-200, Nov. 1961.
4. Progress Report No. 5, "Hypervelocity Kill Mechanisms Program," NRL Memo Report 1261, Vol. II, Section H, December, 1961. (S-RD)
5. Musser, I., "Normal Shock Charts for Air in Chemical Equilibrium," GE MSVD Aerophysics Engineering Tech. Memo. No. 131, April, 1959.
6. Johnson, R. H., "Instability in Hypersonic Flow about Blunt Bodies," Physics of Fluids, Vol. 2, No. 5, pp. 526-532.
7. Vrebalovich, T., "Resonance Tubes in a Supersonic Flow Field," JPL Tech. Report No. 32-373, July, 1962.
8. Mathias, R. F., and Vikestad, W. S., "Simulated Re-entry Effects on Ablative Nose Cone Models Predamaged by Fragment Impact," BRL Memo Report 1382, December, 1961. (Secret)
9. Moeckel, W. E., and Weston, K. C., "Composition and Thermodynamic Properties of Air in Chemical Equilibrium," NACA TN 4265, April, 1958.
10. GE MSD, "Hypervelocity Kill Mechanisms Feasibility Study - Internal Heating," GE Document No. 62SD560, May 28, 1962. (Secret)
11. Storer, E. M., "Summary of Flow Field Pressure Distributions on Sphere Cones at Several Mach Numbers and Altitudes," GE MSVD Aero. DM. No. 2:23, Dec. 1961.
12. Vick, A. R., "An Investigation to Determine the Discharge and Thrust Characteristics of Auxiliary - Air Outlets for a Stream Mach Number of 3.25," NASA TN D-1478, Oct. 1962.
13. Progress Report No. 10, "Hypervelocity Kill Mechanisms Program," NRL Memo Report 5931, Section L, Feb. 1963.(S-RD)
14. Botje, J., "Heat Fluxes in the Malta Test Facility," GE RSD TIS 62SD201, Sept. 1962.
15. Donaldson, C., "A Short Review of the Status of the Aerothermal Phase of the HKM Program," presented at the Sixth Hypervelocity Impact Symposium, Cleveland, Ohio, April, 1963.(Secret)
16. Mathias, R. F., and Vikestad, W. S., Personal Communication.

SECRET

SECRET

17. Logan and Treanor, "Tables of Thermodynamic Properties of Air from 3000°K to 10,000°K," C.A.L. Report BE-1007-A3, 1957.
18. Hypervelocity Kill Mechanisms Program, Lethality Phase (Structural Effects), Annual Progress Report, 20 September 1962.
19. Persechino, M., "Hypervelocity Impacts into Ablative Materials," presented at the Sixth Hypervelocity Impact Symposium, Cleveland, Ohio, April, 1963. (Secret)
20. Anderson, M., "Combinations of Temperature and Axial Compression Required for Buckling of a Ring-Stiffened Cylinder," NASA TN D-1224, April 1962.
21. Anderson, M. and Card, M., "Buckling of Ring-Stiffened Cylinders under a Pure Bending Moment and a Non-uniform Temperature Distribution," NASA TN D-1531, November 1962.
22. Cicala, P., "Effects of Cutouts in Semi-monocoque Structures," J. A. Sc., Vol. 15, No. 3, 1948.
23. McComb, H. G., Jr., "Stress Distribution Caused by Three Types of Loading on a Circular Semi-monocoque Cylinder with Flexible Rings," NACA TN 3199, 1954.
24. McComb, H. G., Jr., "Stress Analysis of Circular Semi-monocoque Cylinders with Cut-outs by a Perturbation Load Technique," NACA TN 3200, 1954.
25. Kuhn, "Stresses in Aircraft and Shell Structures," McGraw-Hill Book Co., Inc., 1956.
26. Hoff, N. J. and Boley, Bruno, A., "Stresses in and General Instability of Monocoque Cylinders with Cutouts, I - Experimental Investigation of Cylinders with a Symmetric Cutout Subjected to Pure Bending," NACA TN No. 1013, 1946.
27. Hoff, N. J., Boley, Bruno, A., and Klein, Bertram, "Stresses in and General Instability of Monocoque Cylinders with Cutouts, II - Calculation of the Stresses in Cylinders with Symmetric Cutout," NACA TN No. 1014, 1946.
28. Hoff, N. J., Boley, Bruno, A., and Klein, Bertram, "Stresses in and General Instability of Monocoque Cylinders with Cutouts, III - Calculation of the Buckling Load of Cylinders with Symmetric Cutout Subjected to Pure Bending," NACA TN No. 1263, 1947.
29. Hoff, N. J., Boley, Bruno, A., and Viggiano, Louis R., "Stresses in and General Instability of Monocoque Cylinders with Cutouts, IV - Pure Bending Tests of Cylinders with Side Cutout," NACA TN No. 1264, 1948.
30. Hoff, N. J. and Klein, Bertram, "Stresses in and General Instability of Monocoque Cylinders with Cutouts, V - Calculation of the Stresses in Cylinders with Side Cutout," NACA TN No. 1435, 1948.
31. Van Dusen, H. J., "Aerodynamic and Motion Characteristics of the Mark 3 BC₂ Flight Test Data," Flight Mechanics Memo 3:04, April 1961.

SECRET

SECRET

32. Van Driest, E. R., "Investigation of Laminar Boundary Layer in Compressible Fluids Using the Crocco Method," NACA TN 2597, Jan. 1952.
33. Kaplan, M., "Compressible Hypersonic Laminar Boundary Layer Development with Arbitrary Pressure Gradient," GE MSVD Aerophysics Engineering Tech. Memo. No. 201, June 1961.
34. Larson, H. K., and Keating, S. J., Jr., "Transition Reynolds Numbers of Separated Flows at Supersonic Speeds," NASA TN D-349, Dec. 1960.
35. Shaw, T. E., and Nestler, D. E., "Heat Transfer and Ablation Phenomena in the Interaction Zones of Fin-Body Configurations in Hypersonic Flow," GE Aerophysics Tech. Memo. 198, April 1961. (Secret)
36. Lees, L., "Laminar Heat Transfer Over Blunt-Nosed Bodies at Hypersonic Flight Speeds," Jet Propulsion, April 1956.
37. Nestler, D. E., and Musser, I., "Correlations for Convective Heat Transfer, Pressure Distribution, and Shock Detachment Distance for Blunt Axisymmetric Forebodies," GE MSVD Aerophysics Engineering Tech. Memo. No. 149, Jan. 1960.
38. Li, T. Y., and Geiger, R. E., "Stagnation Point of a Blunt Body in Hypersonic Flow," J. Aero. Sci. 24, No. 1, pp. 25-32 (1957).
39. Chapman, D. R., "A Theoretical Analysis of Heat Transfer in Regions of Separated Flow," NACA TN 3792, Oct. 1956.
40. Chow, W. L., and Korst, H. H., "On the Flow Structure Within a Constant Pressure Compressible Turbulent Mixing Region," NASA TN D-1894, April, 1963.
41. Denison, M. R., and Baum, E., "Compressible Free Shear Layer with Finite Initial Thickness," AIAA J., Vol. 1, No. 2, pp. 342-349, Feb. 1960.
42. Maydew, R. C., and Reed, J. F., "Turbulent Mixing of Compressible Free Jets," AIAA J., Vol. 1, No. 6, pp. 1443-4, June 1963.
43. Warren, W. R., "An Analytical and Experimental Study of Compressible Jets," Princeton Univ., PHD Thesis, 1957.
44. Chrisman, C. C., "Evaluation of the Free Jet Spreading Rate Parameter for Axisymmetric Flow of Air at Mach Number Three," M.S. Thesis, Bradley Univ., Peoria, Illinois, August 1962, AD 283075.
45. Charwat, A. F., Roos, J. N., Dewey, F. C., Jr., and Hitz, J. A., "An Investigation of Separated Flows - Part II. Flow in the Cavity and Heat Transfer," J. Aero Sci., Vol. 28, No. 7, pp. 513-527, July 1961.
46. Progress Report No. 7, "Hypervelocity Kill Mechanisms Program," NRL Memo. Report 5813, Vol. I, Section H, June 1962 (S-RD).
47. Kleinstein, G., "On the Mixing of Laminar and Turbulent Axially Symmetric Compressible Flows," PIBAL Report #756, Feb., 1963.

SECRET

SECRET

48. Mertz, W., G. E. Trip Report, TTR-TPSD-8151-001, January 1963.
49. Bezmenov, V. Y., "Turbulent Air Jet, Heated to 4000⁰K, " ISV Akad NAUK SSSR, FTD-TT-62-142, Feb. 1962.
50. Charlino, R., "Empirical Prediction of Axial Velocity Decay for Jets Exhausting into Quiescent Air, " GE RSD PIR HTT-8151-129, August 1963.
51. Johannesen, N., "Further Results on the Mixing of Free Axially Symmetrical Jets of Mach Number 1.40, " ARC 20,981 FM 2817 N. 88, May,1959.
52. Franklin, R. E., "Pressure Fluctuations Near a Cold, Small Scale Air Jet, " R. M. No. 3162, May 1958.
53. Anderson, A. R., "Characteristics of Free Supersonic Jets Exhausting Into Quiescent Air, " J. ARS, 25, pp. 13-15, January 1955.
54. Frauenberger, J. A. and Forbister, J. E., "The Axial Decay and Radial Spread of a Supersonic Jet Exhausting into Air at Rest, " RAE Report. RPD 34, Dec. 1955.
55. Corrsin, S. and Uberoi, M., "Further Experiments on the Flow and Heat Transfer in a Heated Turbulent Air Jet," NACA TN 1865, 1949.

SECRET

SECRET

NOMENCLATURE

Symbol

A	Perforation cross-section area; also vehicle base area
A _s	Internal surface area
C _D	Drag coefficient
C _m	Orifice flow coefficient
D	Diameter
f _w	Energy partition function, defined in Equation (10)
g	Acceleration of gravity
h	Specific enthalpy
i	Specific internal energy
K _s	Discharge coefficient into free stream (Figure A-1)
m	Mass flow rate through a perforation
m _{BL}	Mass flow rate in boundary layer for depth equal to perforation diameter
M	Mach number
M ₀	End moment
P	Static pressure
Pr	Prandtl number
Q _w	Total rate of heat transfer to walls; $Q_w = \int_{A_s} \dot{q} dA_s$
\dot{q}	Heat flux
r	Wetted length measured from impingement point of jet
r _{0.5}	Half-radius of jet (radius at which $U/U_A = 0.5$)
R ₁	Initial radius of jet prior to diffusion
Re	Reynolds number
s	Wetted length
T	Static temperature
U	Velocity

SECRET

SECRET

U'_0	Velocity gradient at stagnation point
V	Internal volume
V_0	End shear force
W	Weight of vehicle
x	Distance along jet axis, measured from jet origin; also, distance along orifice axis
β	$(M^2 - 1)^{0.5}$
ρ	Density
θ	Time
μ	Viscosity
δ	Boundary layer velocity thickness
δ^*	Boundary layer displacement thickness
γ	Isentropic exponent
ϕ	Orifice flow function, defined in Equation (7)
σ	Jet mixing parameter, Equation (C-5)

Subscripts

a	Ambient surroundings
A	Jet axis
e	Edge of boundary layer
j	Free jet at impingement plane
s	Stagnation value
T	Turbulent
W	Wall value
1	Inlet hole; also external value approaching inlet; also initial jet value
2	Vent hole; also internal value
3	External value at vent exit

SECRET

SECRET

ILLUSTRATIONS

SECRET

H-51

SECRET

SECRET

H-52

SECRET

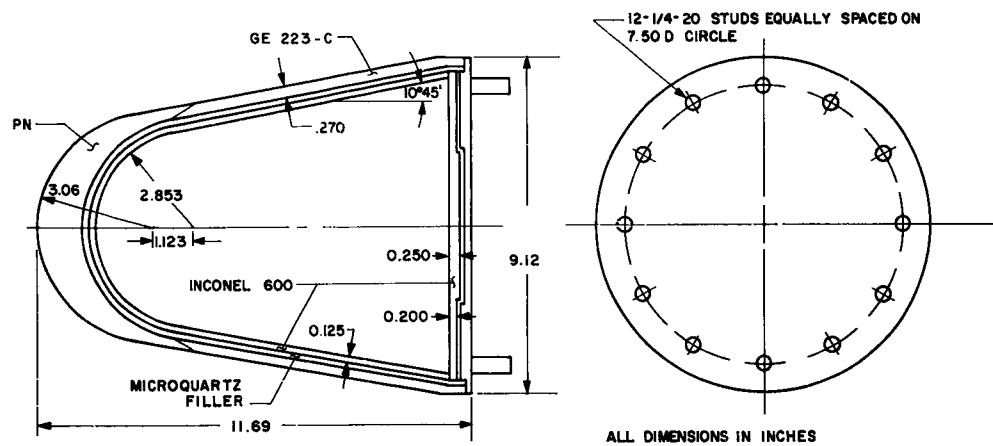


Figure 1. Wallops Island Flight Model

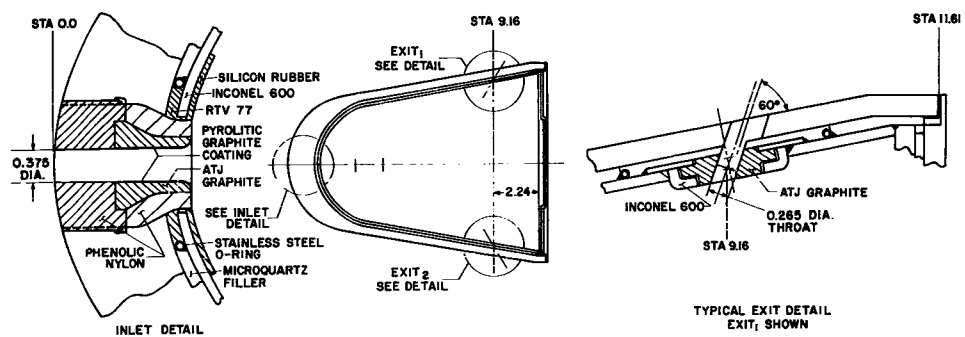


Figure 2. Inlet and Exit Orifice Designs, Configuration One

SECRET

SECRET

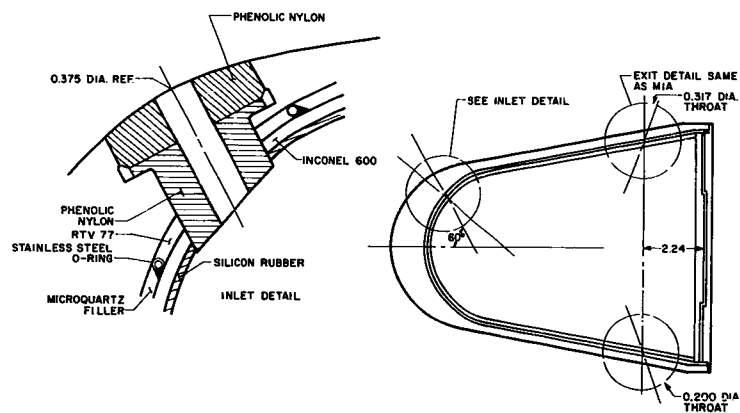


Figure 3. Inlet Orifice Design, Configuration Two

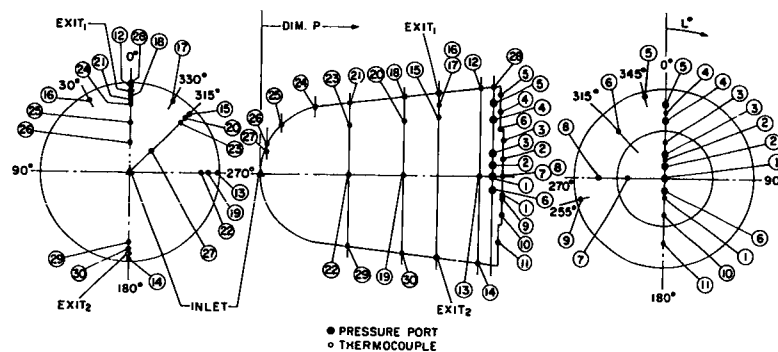


Figure 4. Malta Test M1A Instrumentation Location

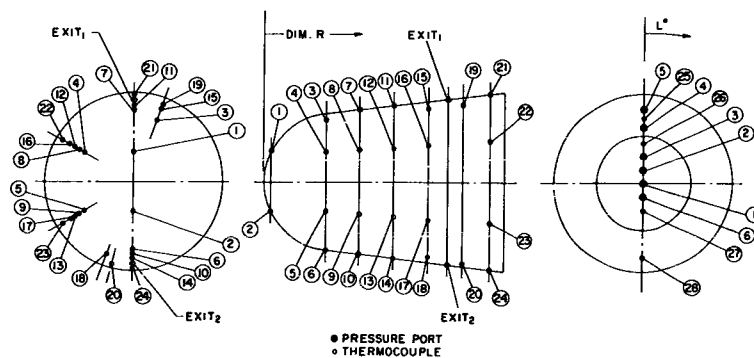


Figure 5. Malta Test M2A Instrumentation Location

SECRET

SECRET



Figure 6. Recovered Experiment Section, Flight One



Figure 7. Recovered Experiment Section, Flight Two

SECRET

SECRET

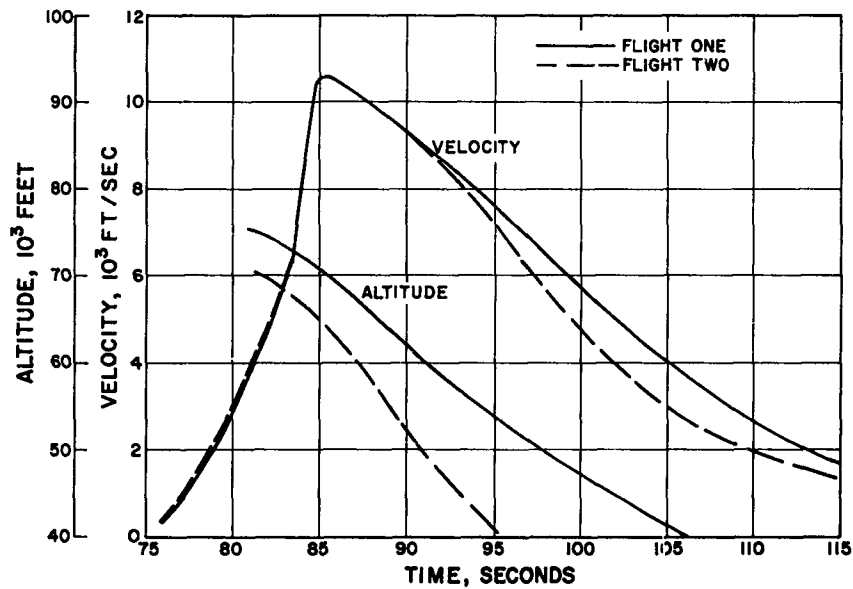


Figure 8. Wallops Island Flight Test Trajectories

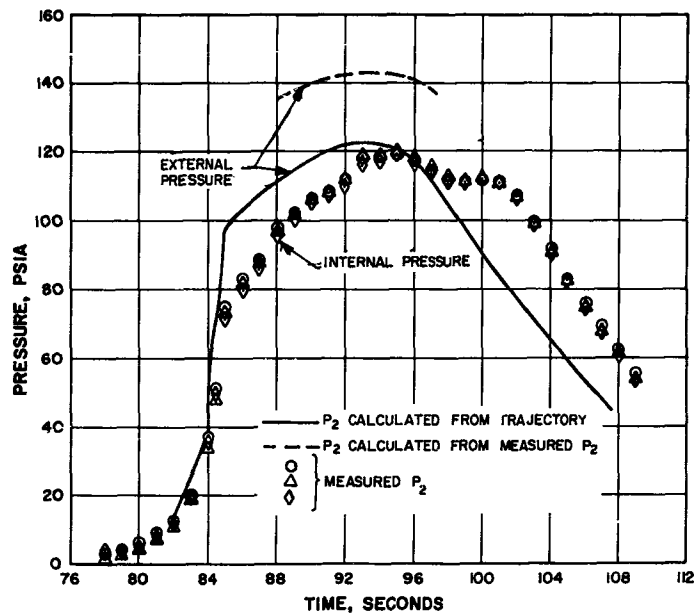


Figure 9. Internal Pressure History, Flight One

SECRET

SECRET

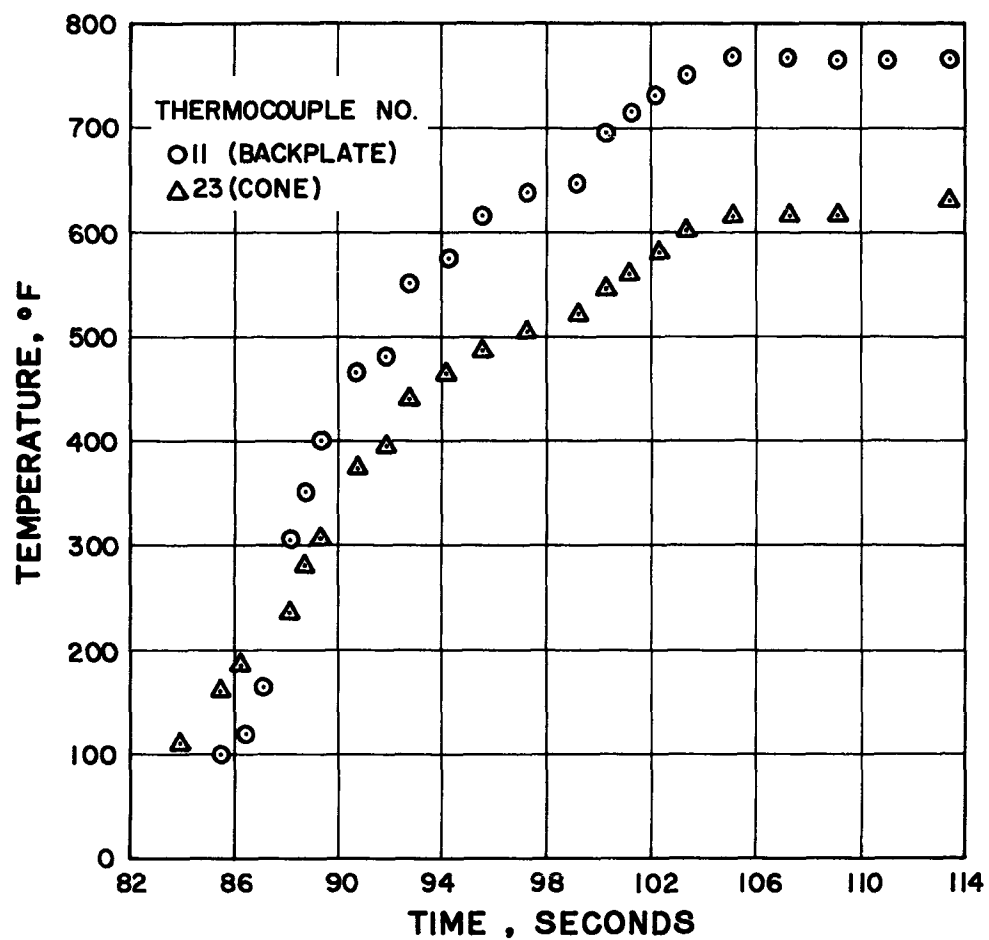


Figure 10. Typical Thermocouple Responses, Flight One

SECRET

SECRET

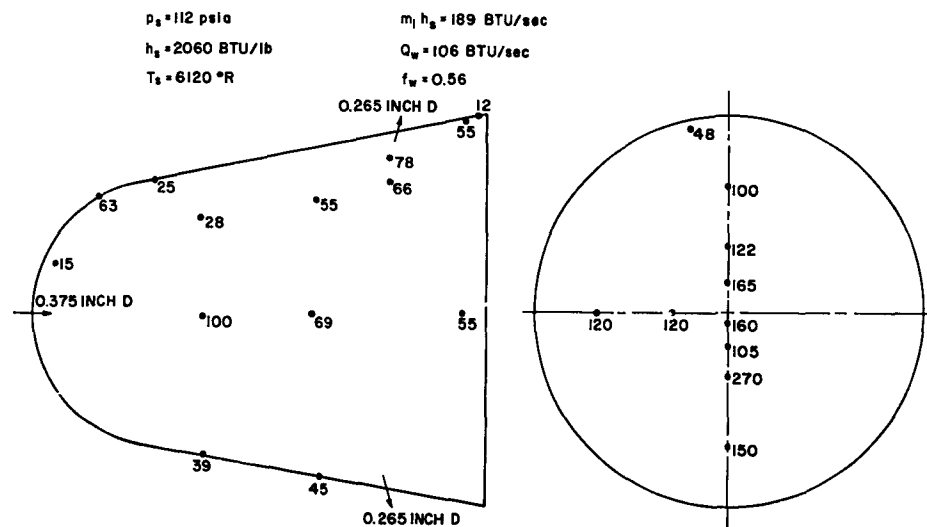


Figure 11. Heat Flux Map for Flight One at 88 Seconds

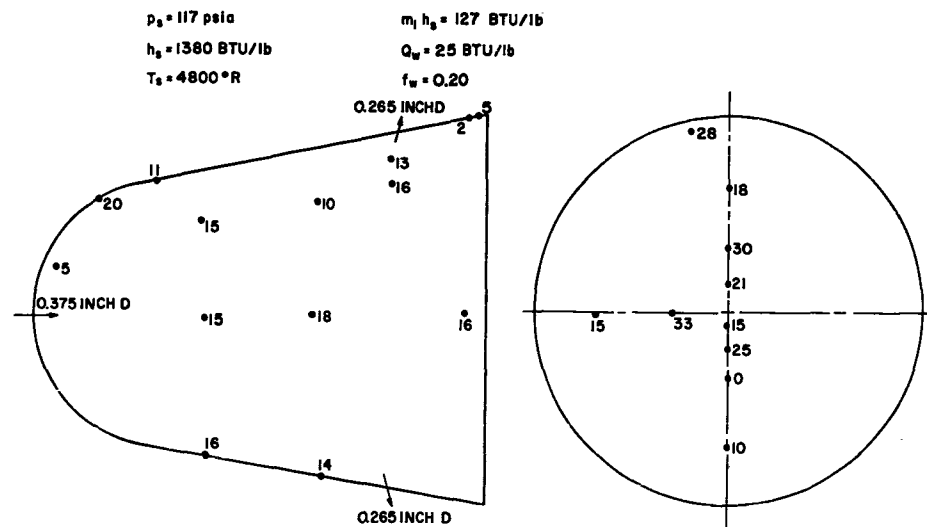


Figure 12. Heat Flux Map for Flight One at 94 Seconds

SECRET

SECRET

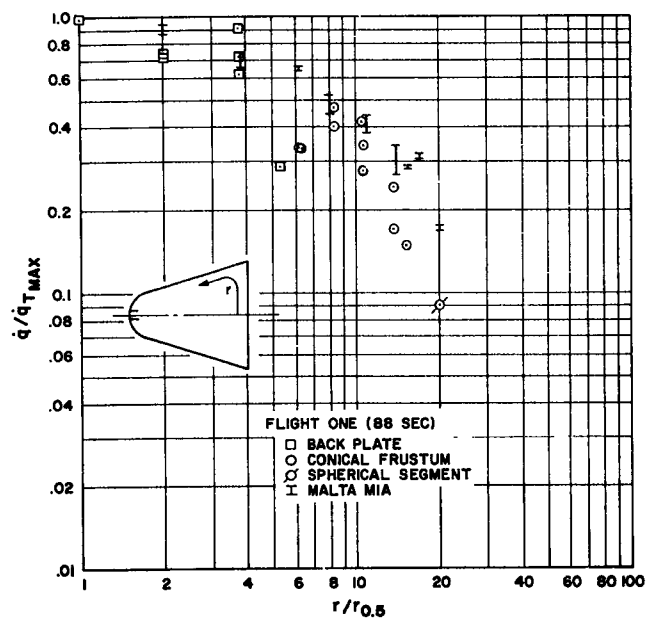


Figure 13. Distribution of Heat Flux away from Impingement Point, Configuration One

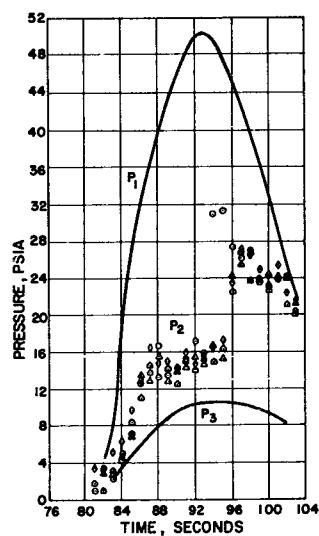


Figure 14. Internal Pressure History, Flight Two

SECRET

SECRET

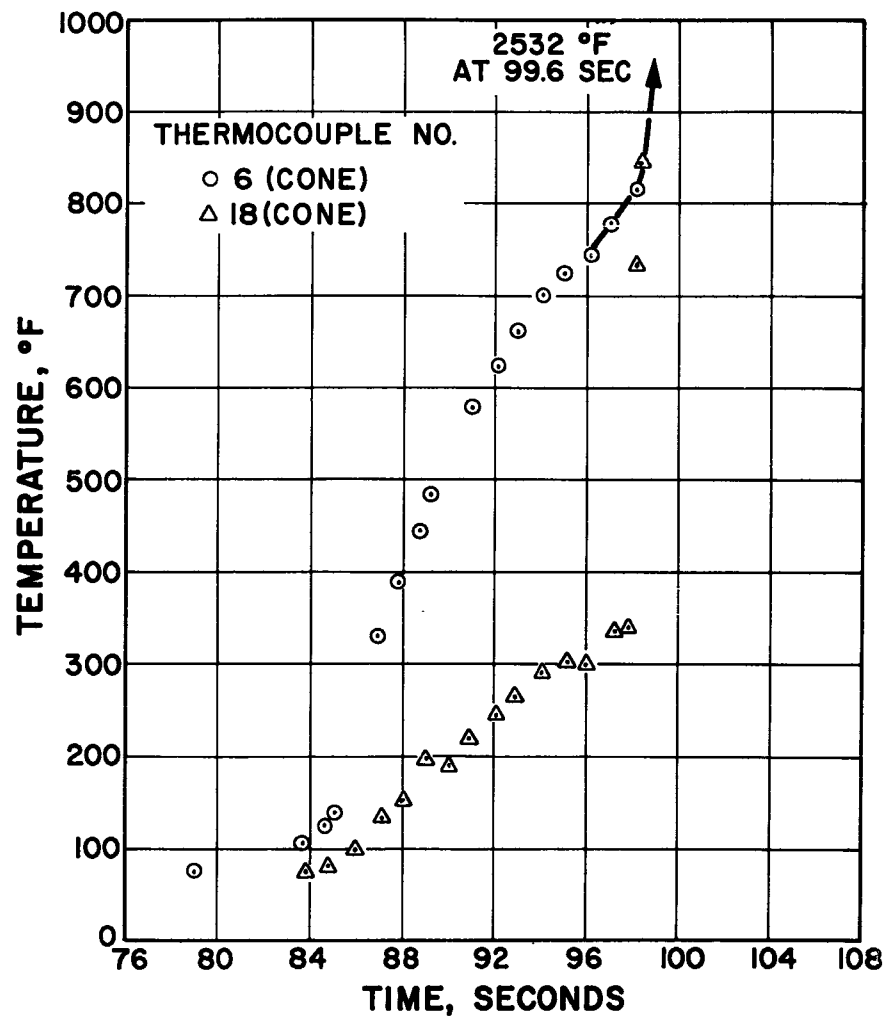


Figure 15. Typical Thermocouple Responses, Flight Two

SECRET

H-60

SECRET

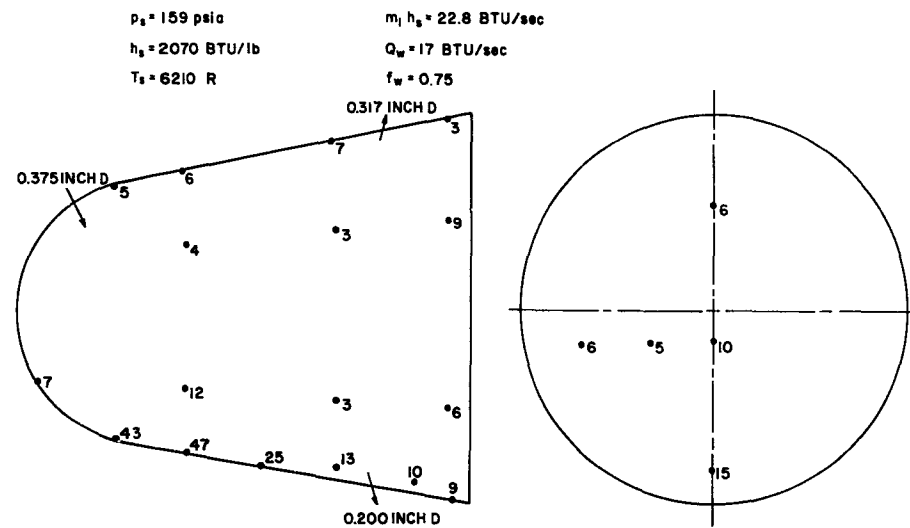


Figure 16. Heat Flux Map for Flight Two at 88 Seconds

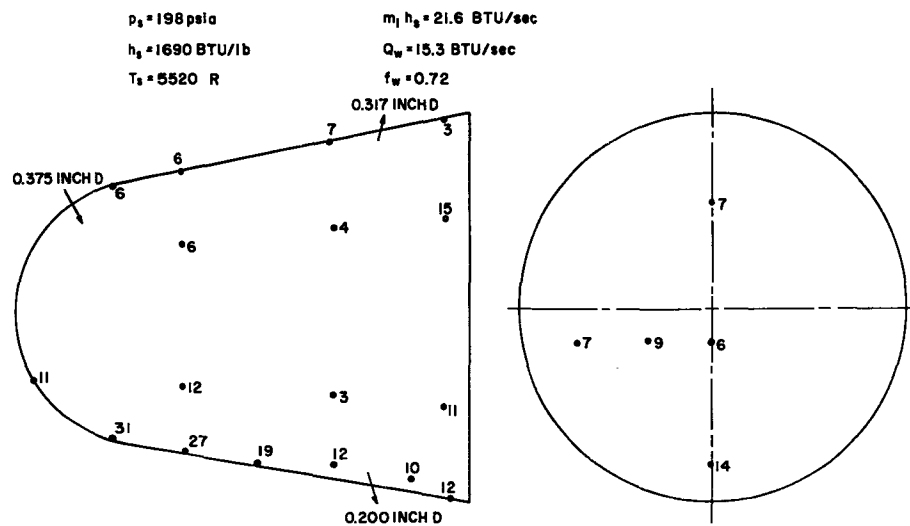


Figure 17. Heat Flux Map for Flight Two at 91 Seconds

SECRET

SECRET

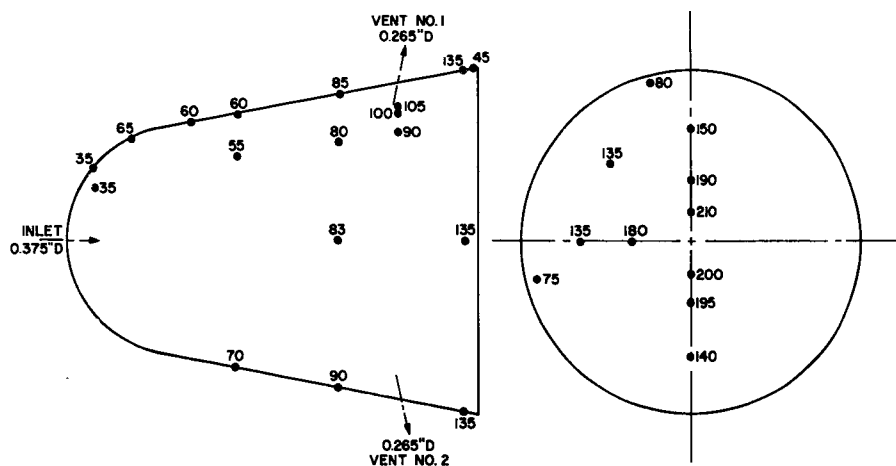


Figure 18. Map of Heat Flux Distribution for Malta Test M1A
 $\theta = 4$ Seconds, $\dot{q} \sim \text{BTU}/\text{ft}^2\text{sec}$

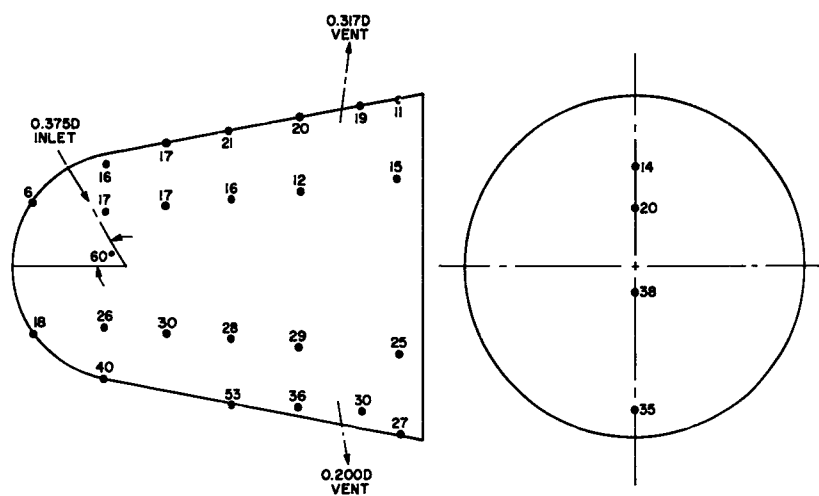


Figure 19. Map of Heat Flux Distribution for Malta Test M2A
 $\theta = 4$ Seconds, $\dot{q} \sim \text{BTU}/\text{ft}^2\text{sec}$

SECRET

SECRET

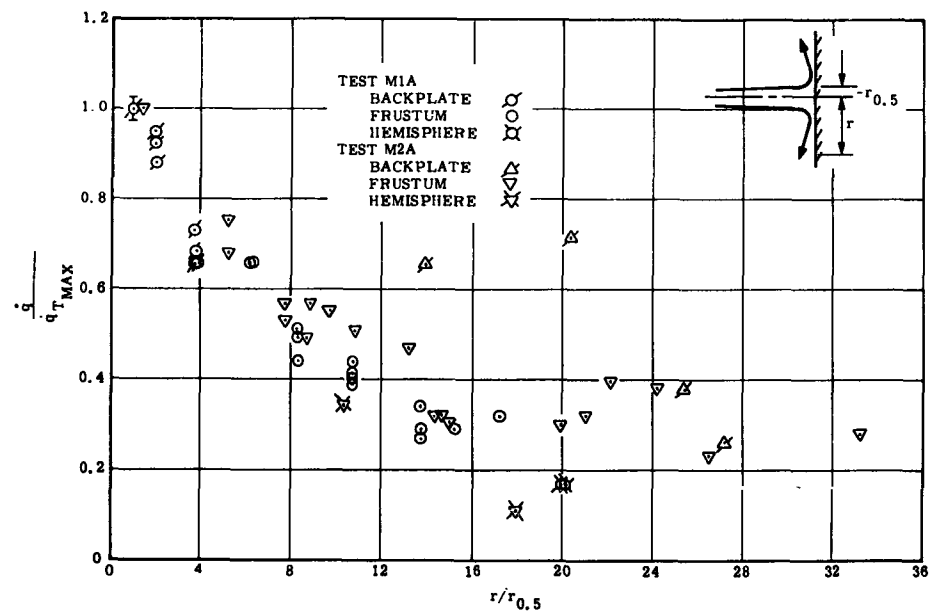


Figure 20. Radial Distribution of Heat Flux away from Impingement Point

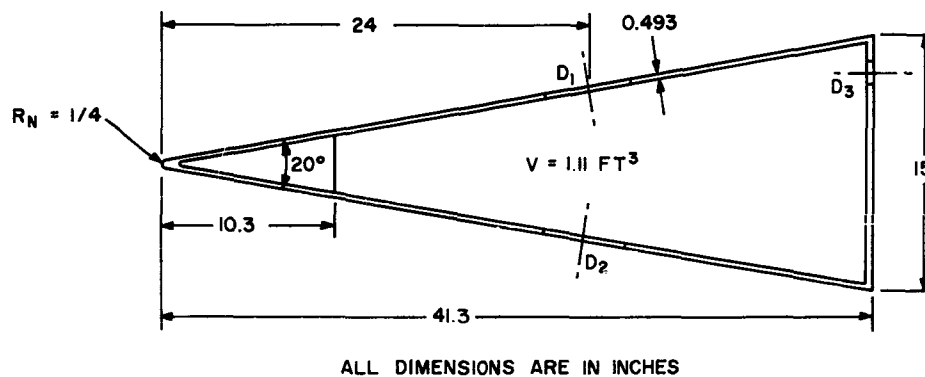


Figure 21. Internal Heating Model, Cornell Aeronautical Laboratory Tests

SECRET

Figure 22. Internal Heating Model, with 6 inch Diameter Insert Installed

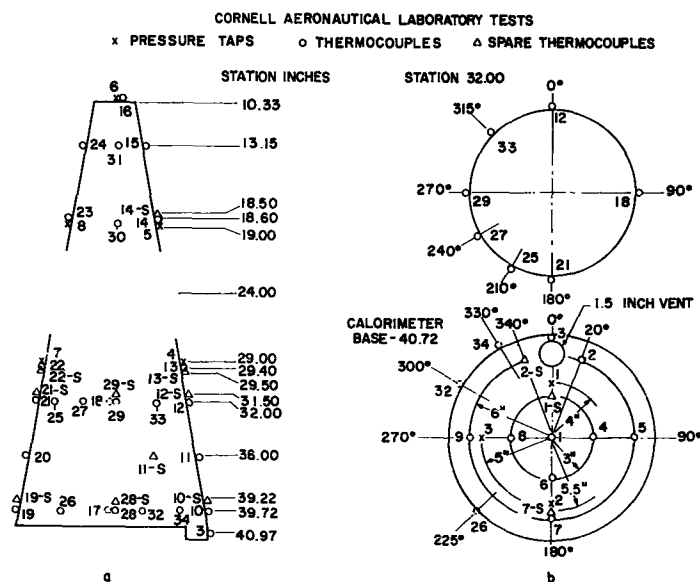


Figure 23. Internal Calorimeter-Thermocouple and Pressure Locations

H-64

SECRET

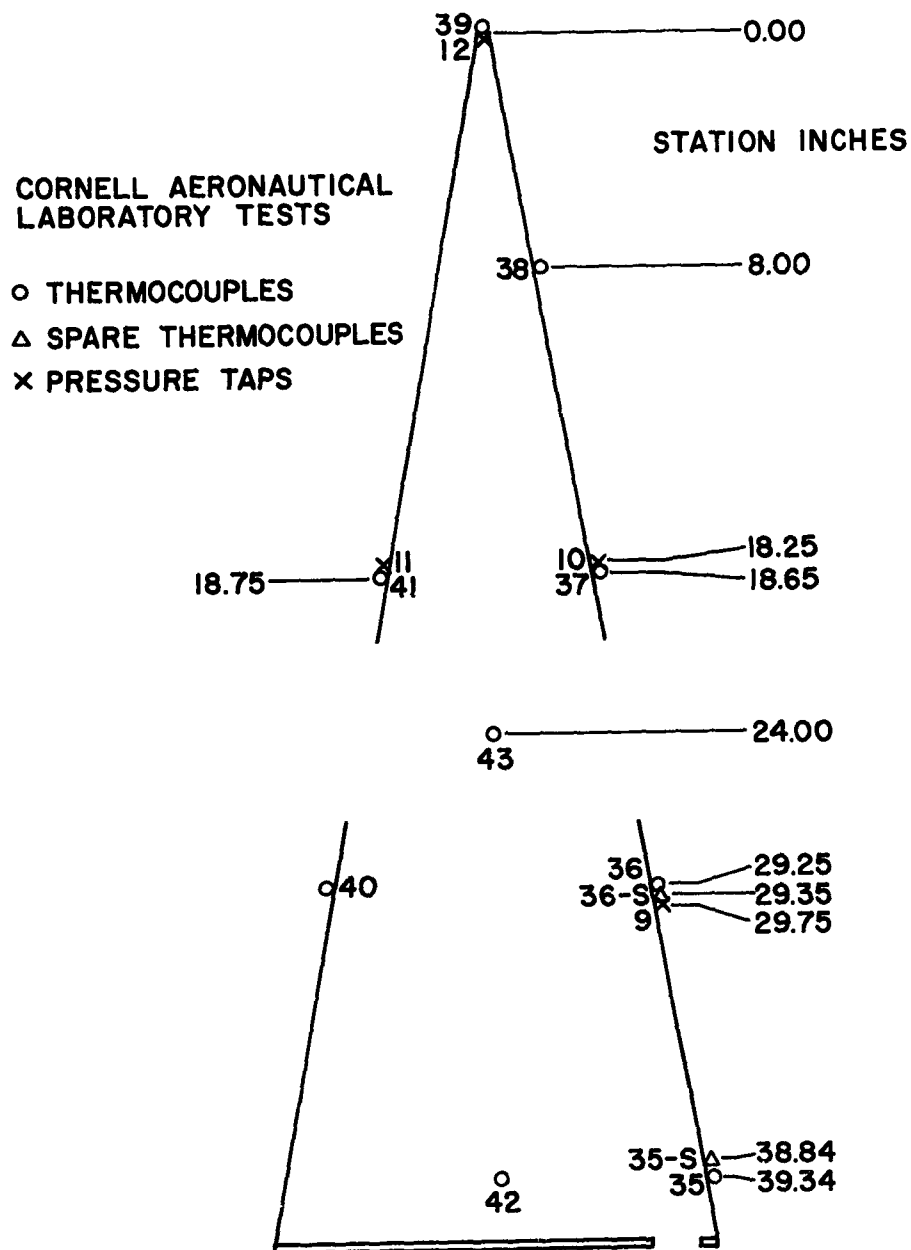
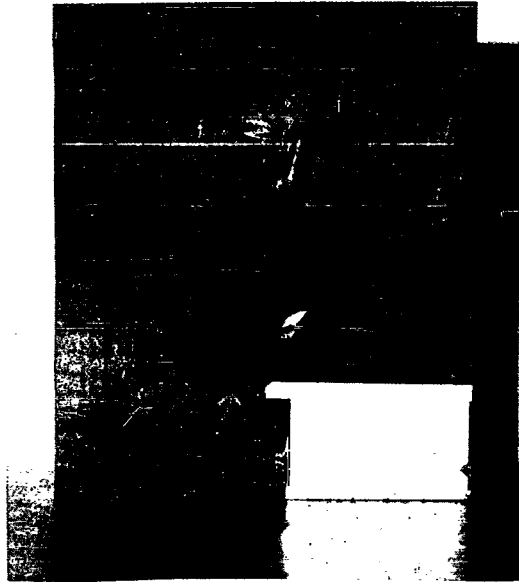


Figure 24. Structural Cone Thermocouple and Pressure Locations

SECRET

H-65

SECRET



**Figure 25(a). Impact Target to be Used in Orifice Flow Tests,
Front Surface**



**Figure 25(b). Impact Target to be Used in Orifice Flow Tests,
Back Surface**

SECRET

H-66

SECRET

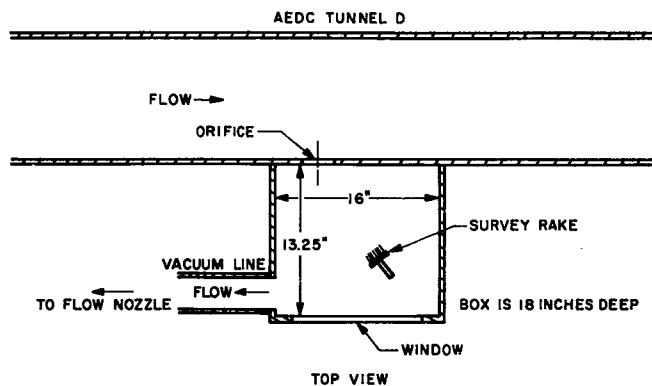


Figure 26. Schematic Diagram of Orifice Flow Tests

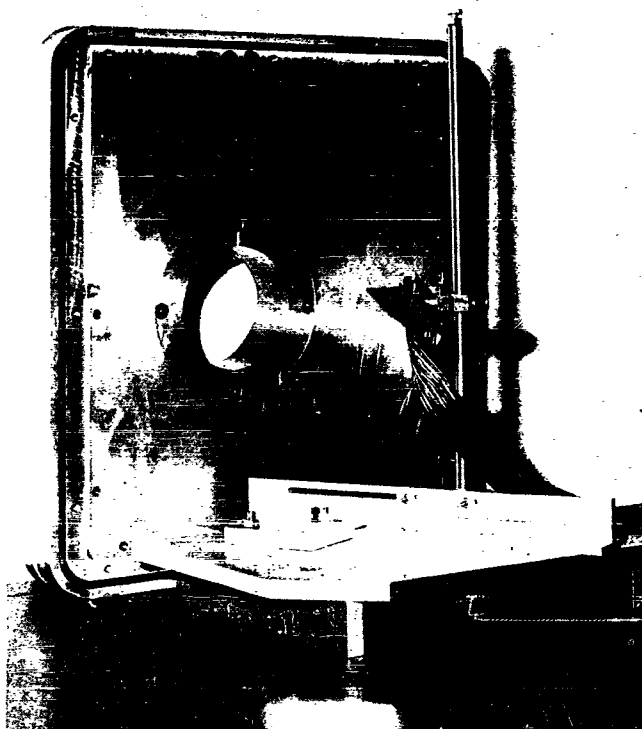


Figure 27. Probe Rake for Orifice Flow Tests

SECRET

H-67

SECRET

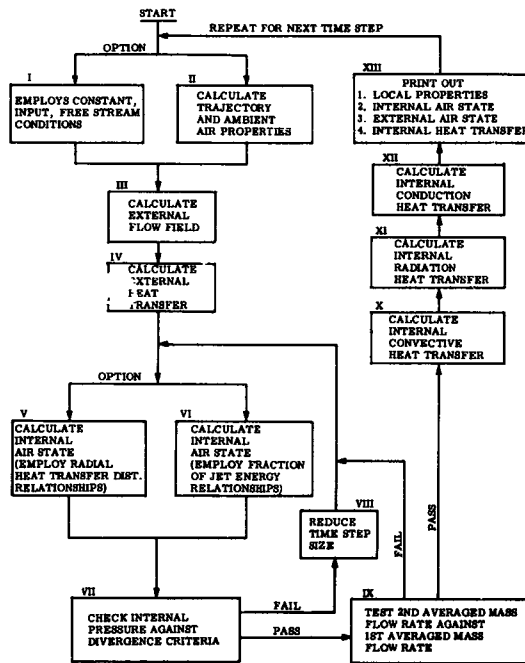


Figure 28. Block Diagram of the HKM Internal Heating Computer Program

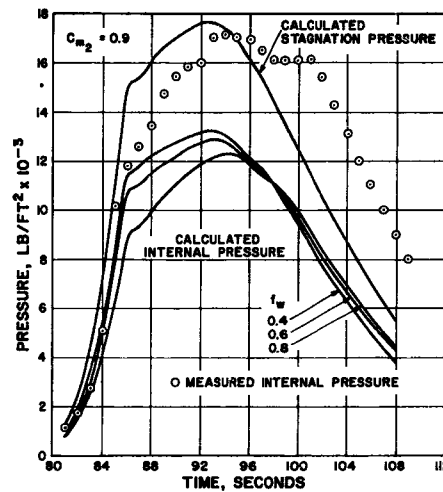


Figure 29. Wallops Island Flight One Stagnation and Internal Pressures for Variation in f_w

SECRET

H-68

SECRET

H-69

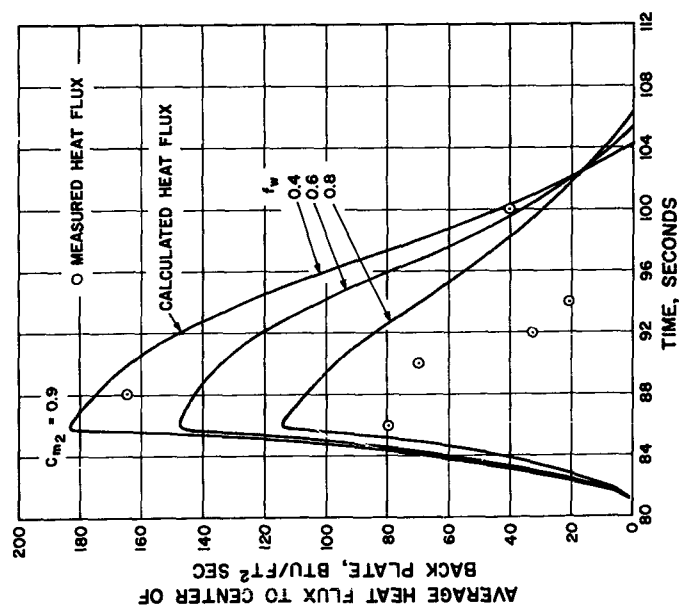


Figure 30. Wallops Island Flight One Heat Flux to Back Plate for Variations in f_w

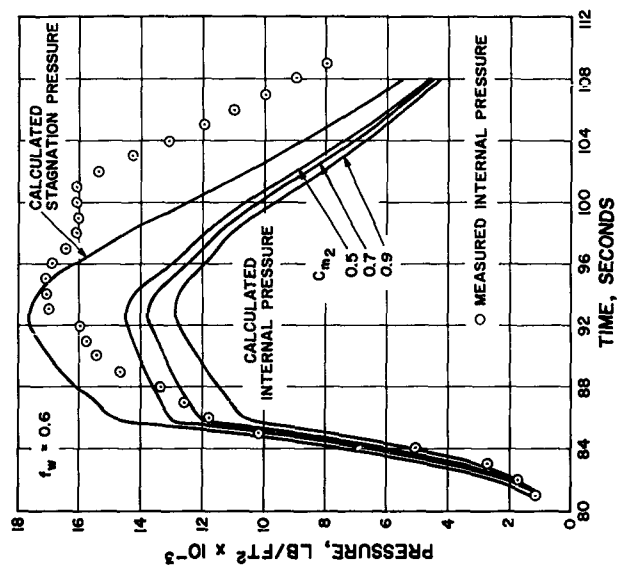


Figure 31. Wallops Island Flight One Stagnation and Internal Pressured for Variations in Vent Flow Coefficients

SECRET

SECRET

H-70

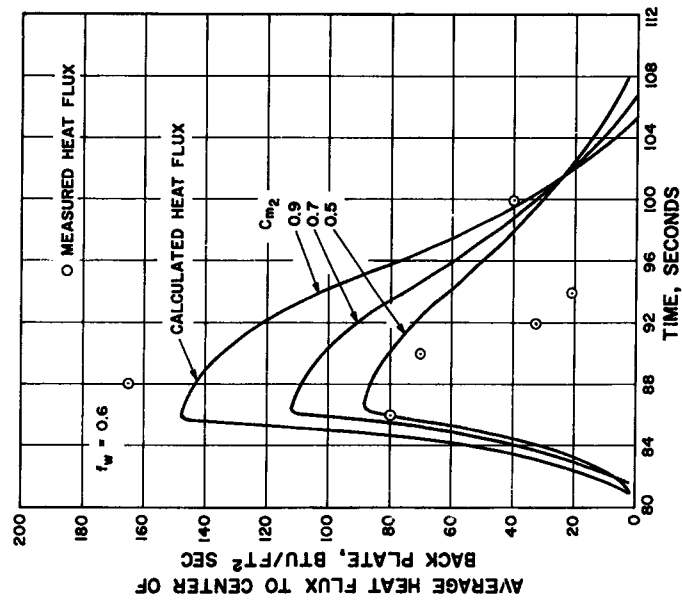


Figure 32. Wallops Island Flight One Heat Flux to Back Plate for Variations in Vent Flow Coefficient

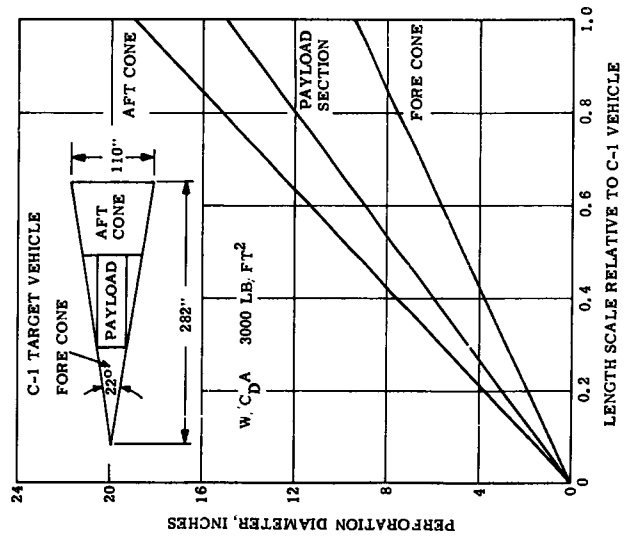


Figure 33. Perforation Diameter Required for Thermo-structural Kill of C-1 Type Targets (Based on $A/V^{2/3} = 0.05$)

SECRET

SECRET

H-71

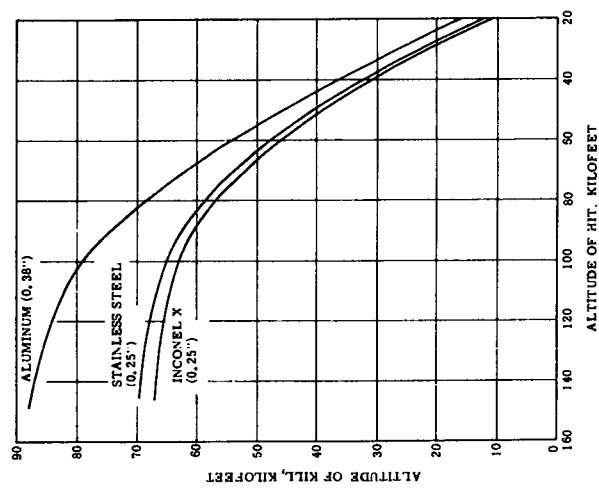


Figure 34. Altitude of Kill vs Altitude of Hit, Forecone Perforation, C-1 Target (Monocoque Structure), Thermostructural Kill

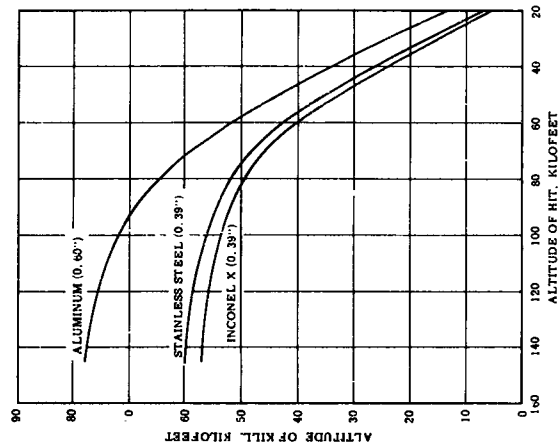


Figure 35. Altitude of Kill vs Altitude of Hit, Payload or Aft Cone Perforation, C-1 Target (Monocoque Structure)

SECRET

SECRET

H-72

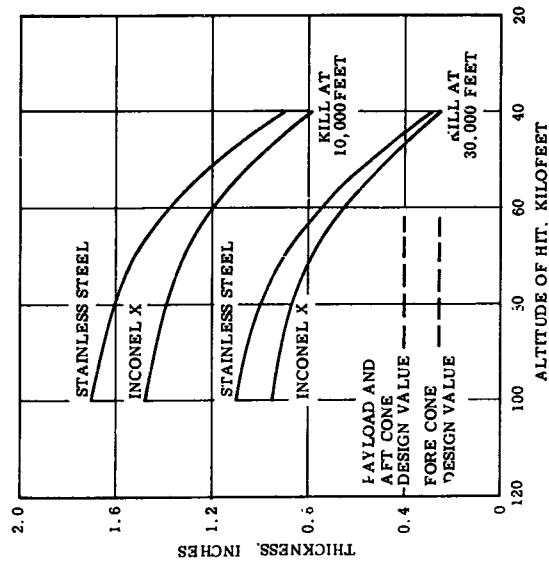


Figure 36. Maximum Structure Thickness Which Can Be Melted by a Specified Altitude, C-1 Target (Monocoque Structure)

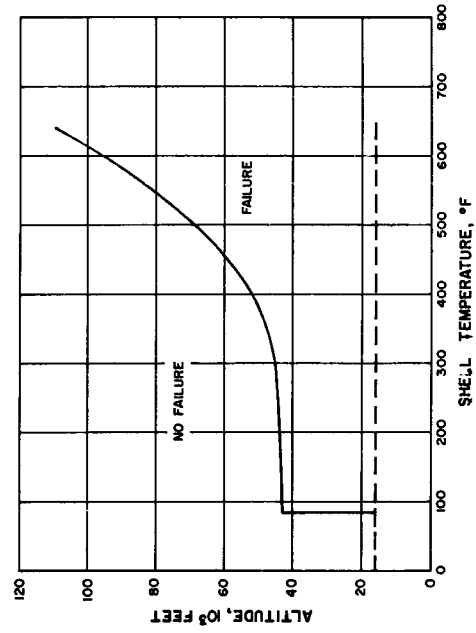


Figure 37. Failure Regime; Nose Impact, Aluminum Monocoque Forecone

SECRET

SECRET

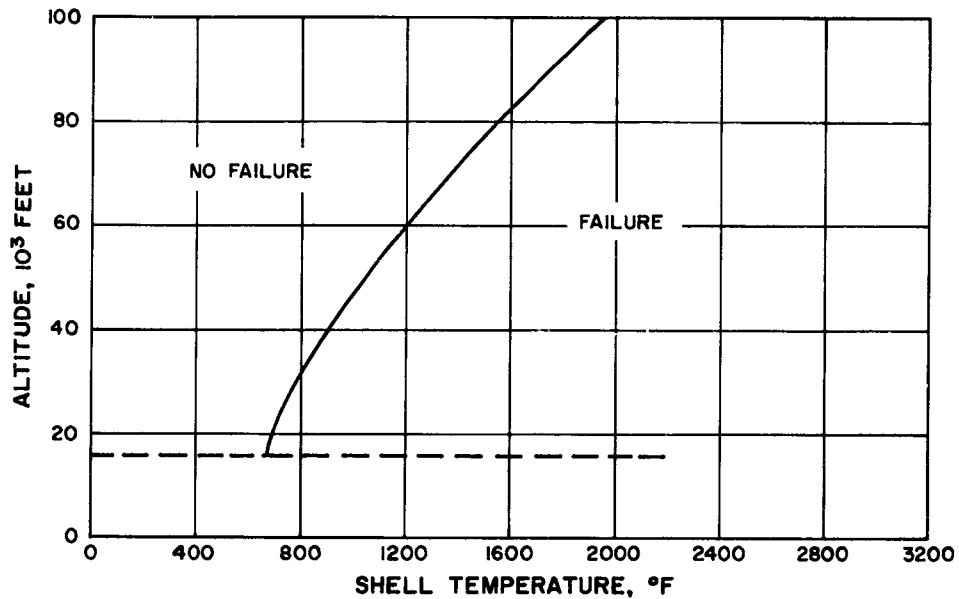


Figure 38. Failure Regime; Nose Impact, Stainless Steel Monocoque Forecone

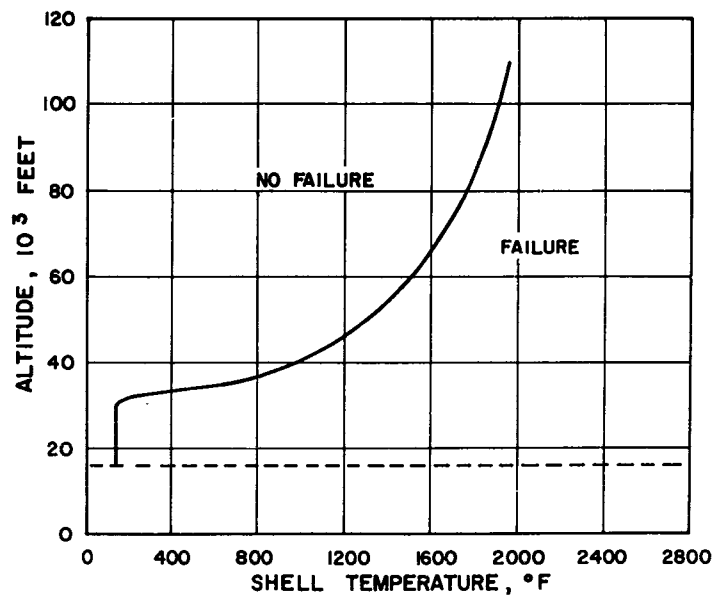


Figure 39. Failure Regime; Nose Impact, Inconel Monocoque Forecone

SECRET

SECRET

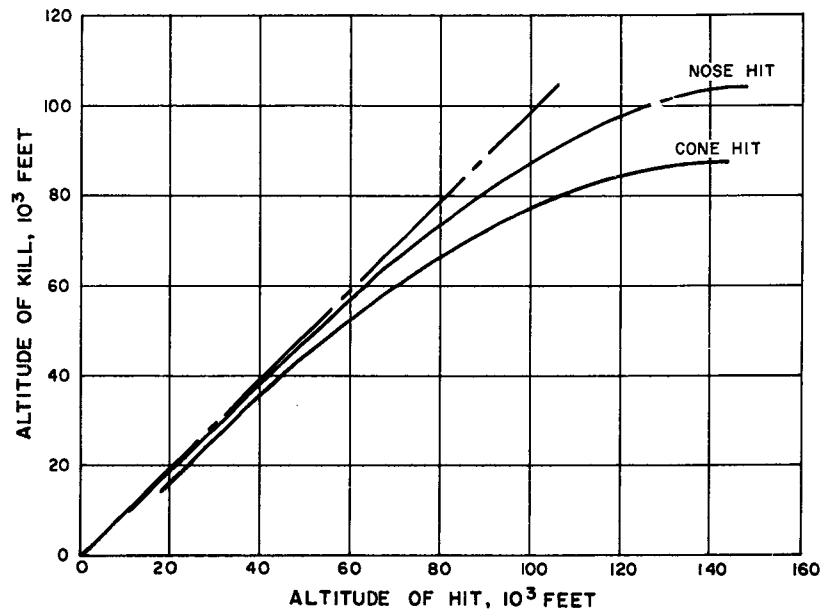


Figure 40. Hit vs Kill Altitude; Aluminum Monocoque Forecone

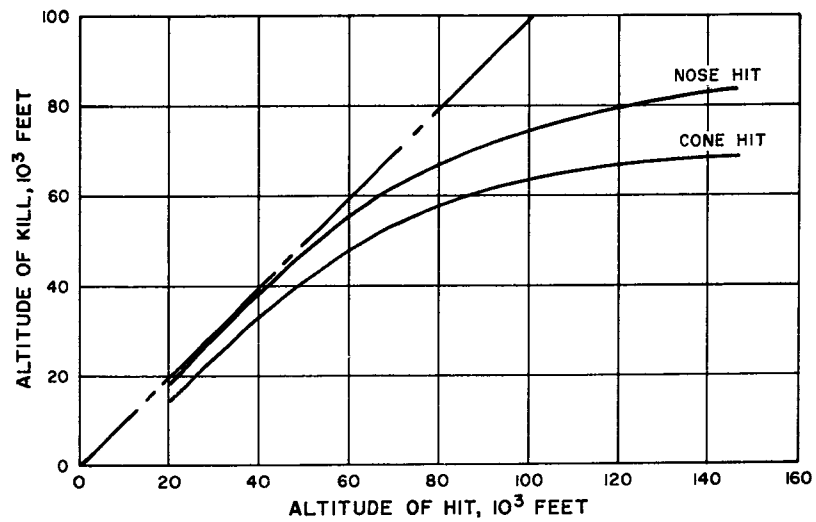


Figure 41. Hit vs Kill Altitude; Stainless Steel Monocoque Forecone

SECRET

SECRET

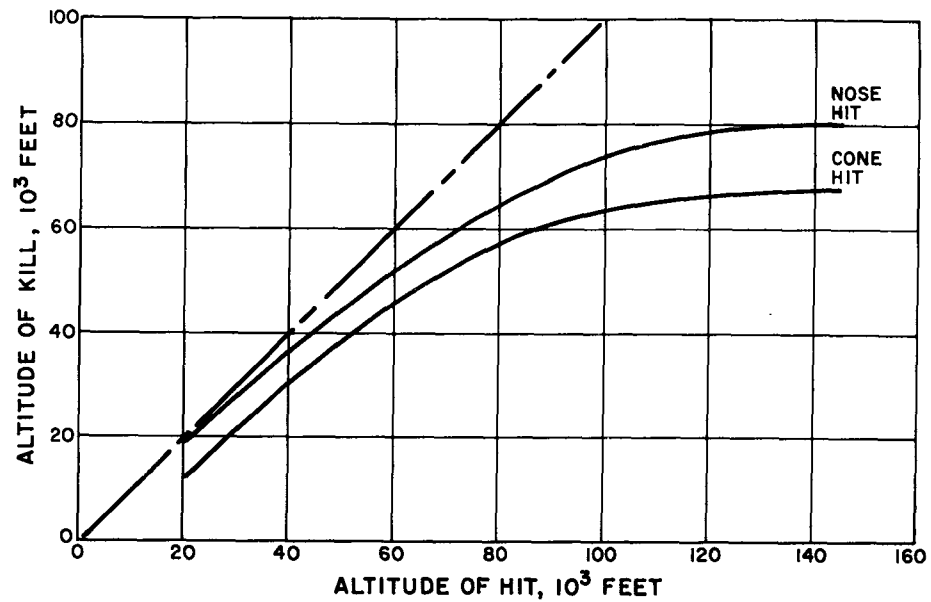


Figure 42. Hit vs Kill Altitude; Inconel Monocoque Forecone

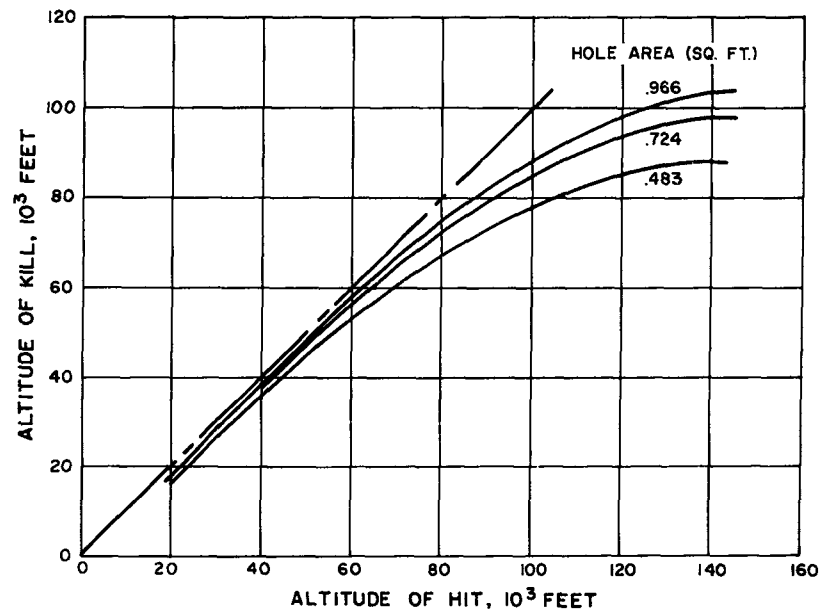


Figure 43. Effect of Hole Size; Cone Impact, Aluminum Monocoque Forecone

SECRET

SECRET

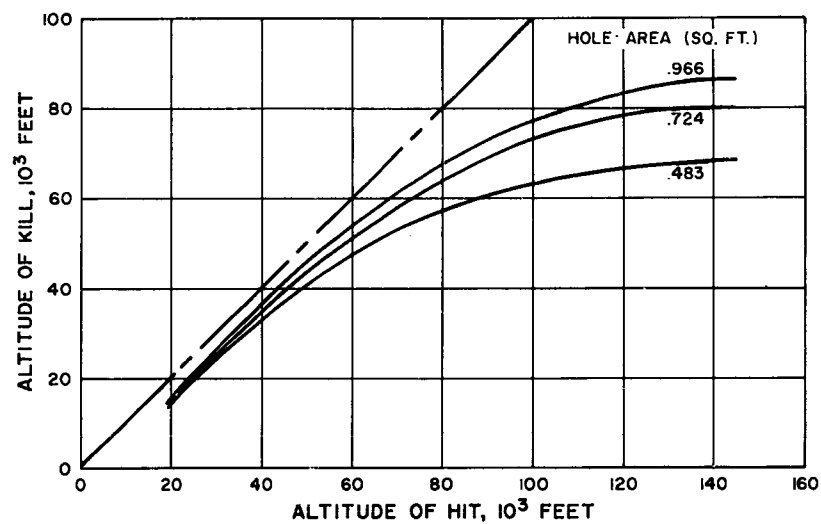


Figure 44. Effect of Hole Size; Cone Impact, Stainless Steel Monocoque Forecone

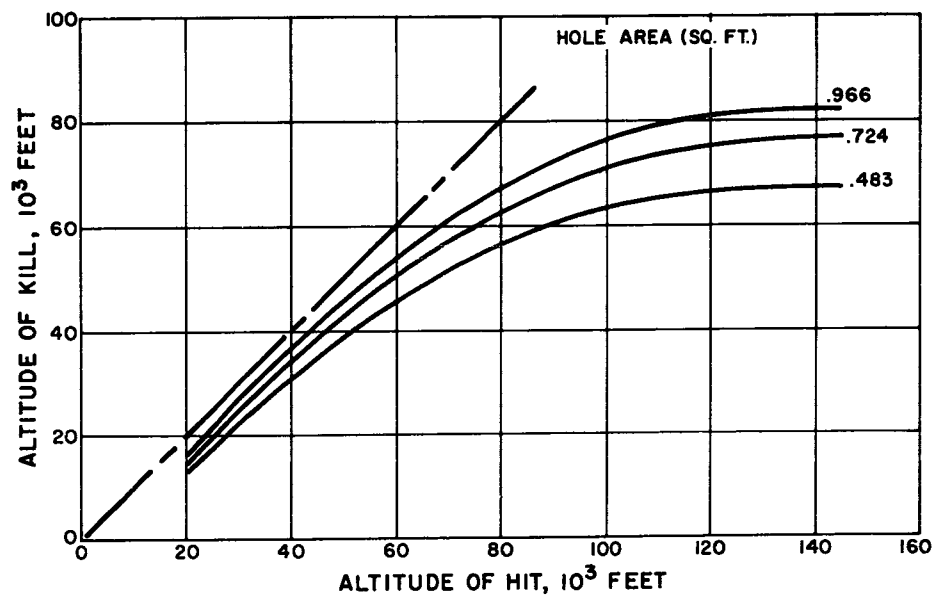


Figure 45. Effect of Hole Size; Cone Impact, Inconel Monocoque Forecone

SECRET

SECRET

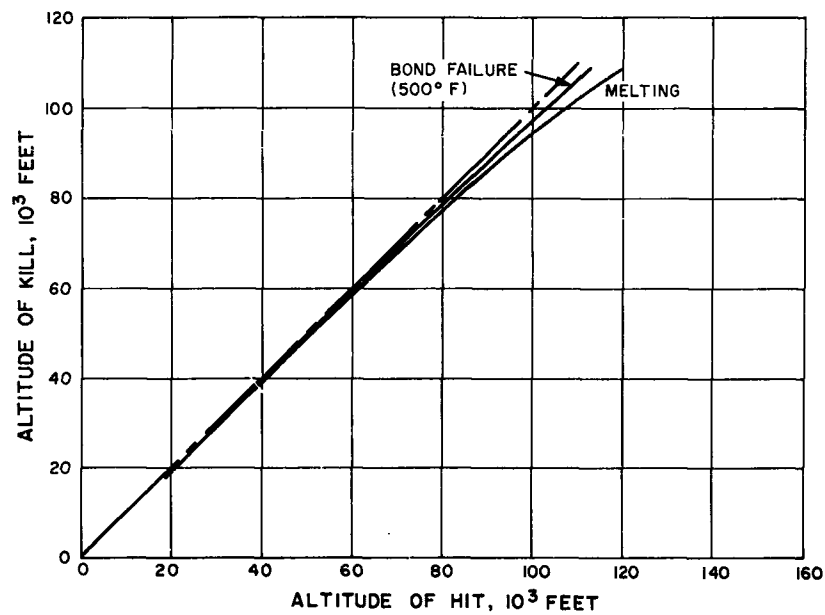


Figure 46. Effect of Construction; Cone Impact, Aluminum Honeycomb Sandwich Forecone

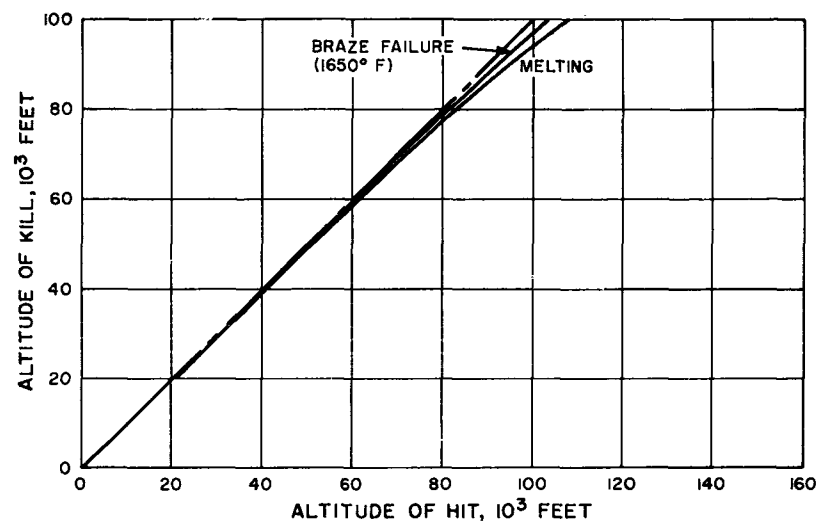


Figure 47. Effect of Construction; Cone Impact, Stainless Steel Honeycomb Sandwich Forecone

SECRET

SECRET

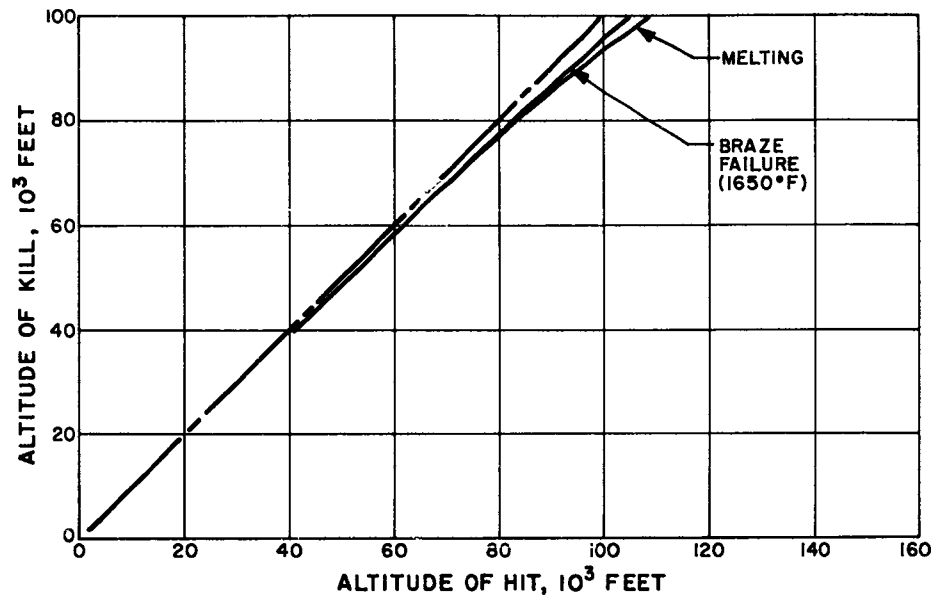


Figure 48. Effect of Construction; Cone Impact, Inconel Honeycomb Sandwich Forecone

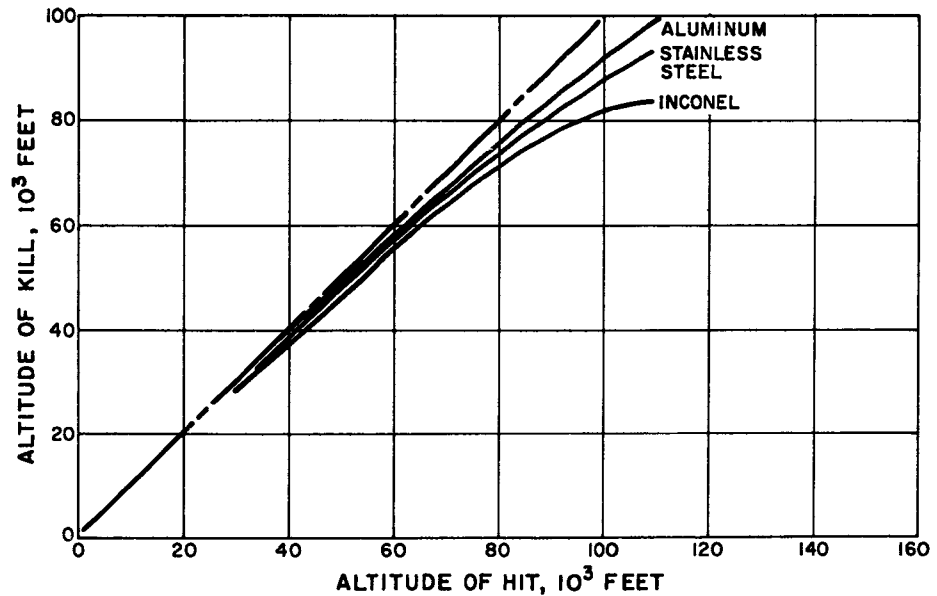


Figure 49. Effect of Construction; Cone Impact, Ring Stiffened Shell Forecone

SECRET

SECRET

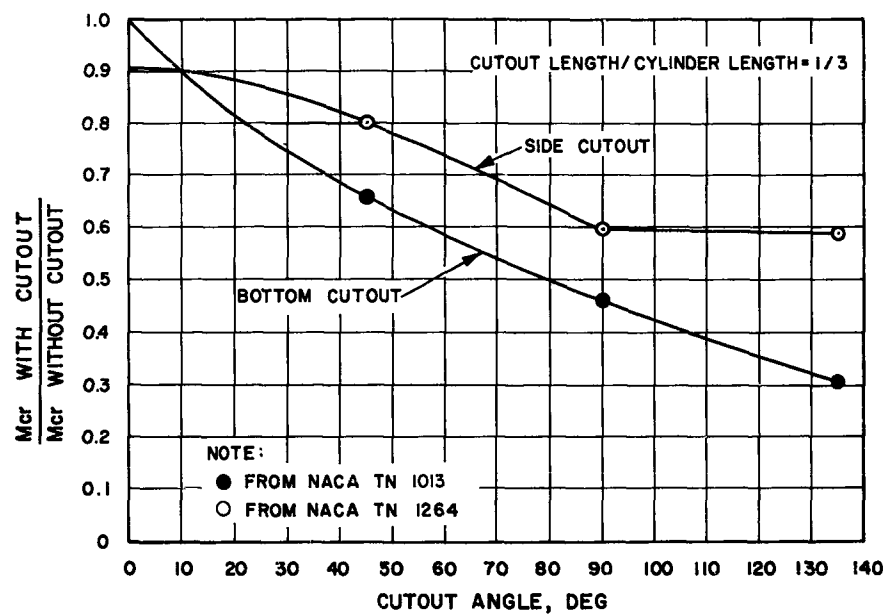


Figure 50. Critical Moment Ratio vs Cutout Angle

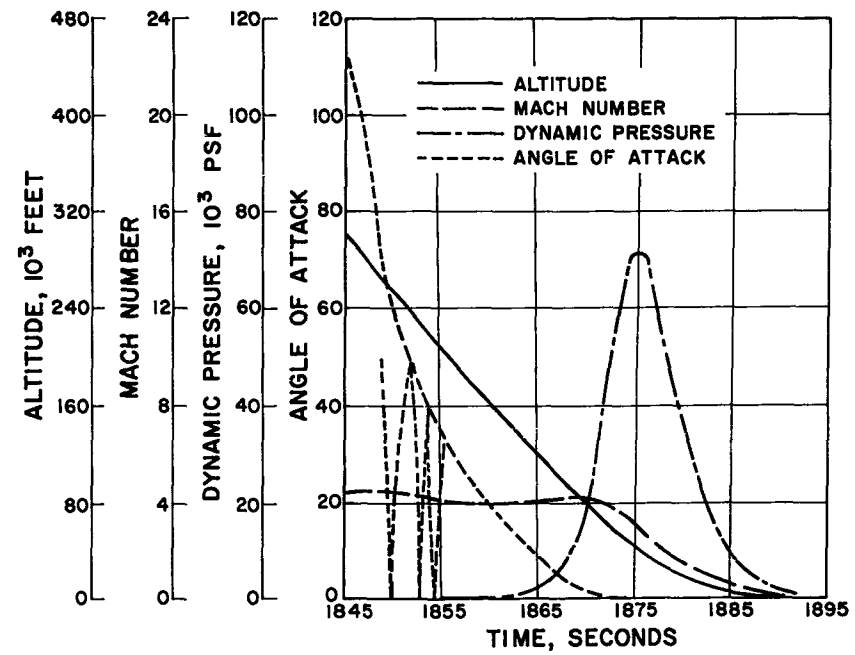


Figure 51. Trajectory Data, Mark 3 IOC

SECRET

SECRET

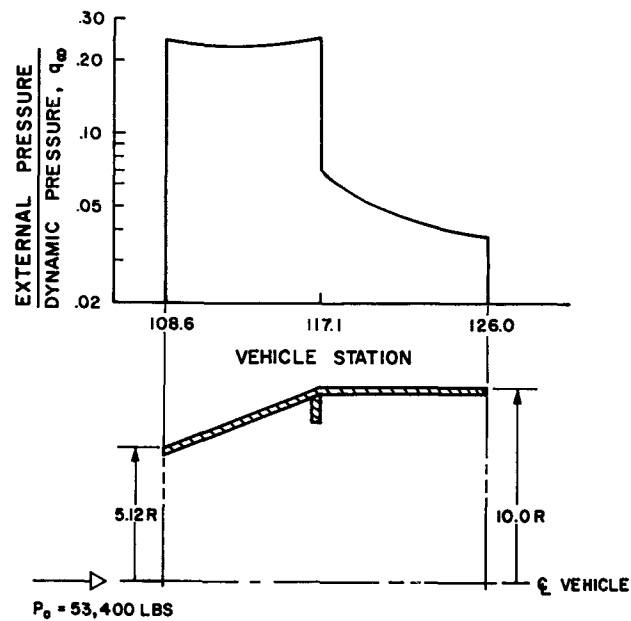


Figure 52. Forecone Geometry and Pressure Distribution

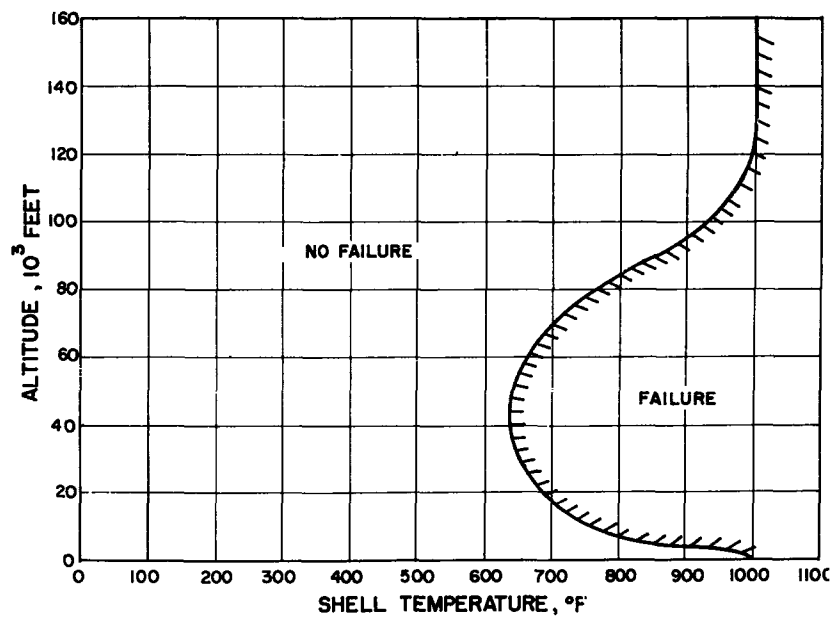


Figure 53. Failure Regime; Cone Impact

SECRET

SECRET

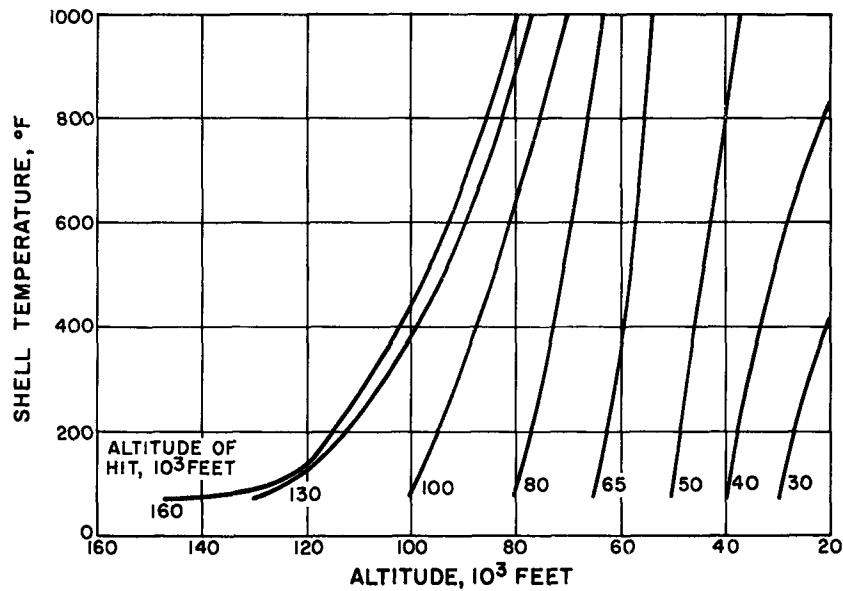


Figure 54. Forecone Temperature Rise, Coupled Flow ($A = .05v^{2/3}$)

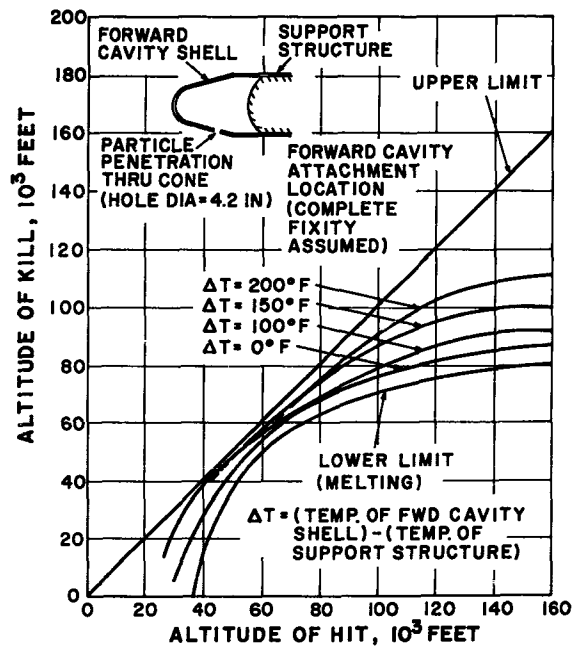


Figure 55. Hit vs Kill Altitude; Forecone

SECRET

SECRET

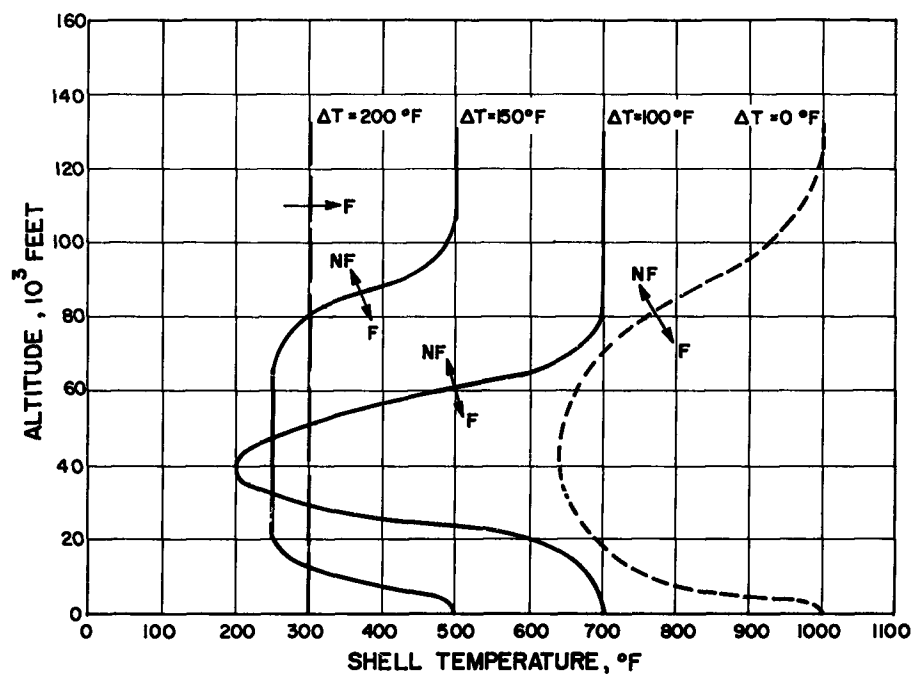


Figure 56. Influence of Temperature Change

SECRET

SECRET

H-83

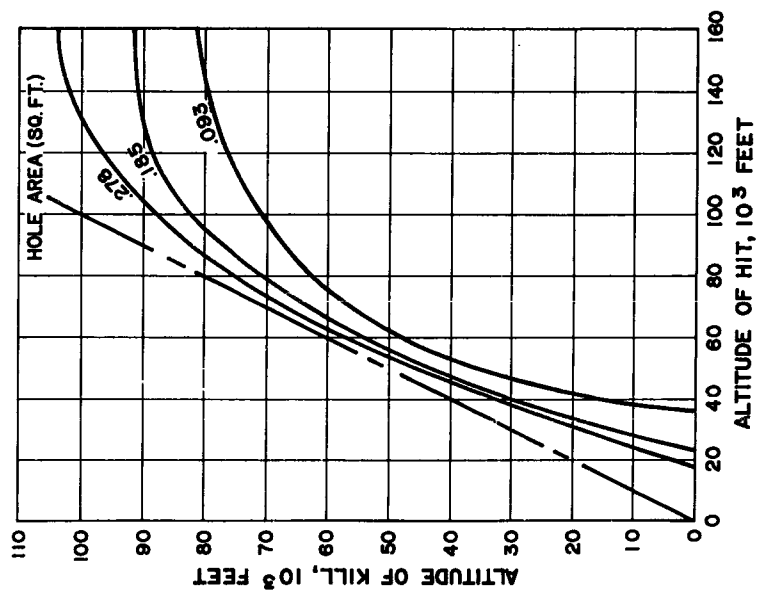


Figure 57. Effect of Hole Size on Melting Altitude

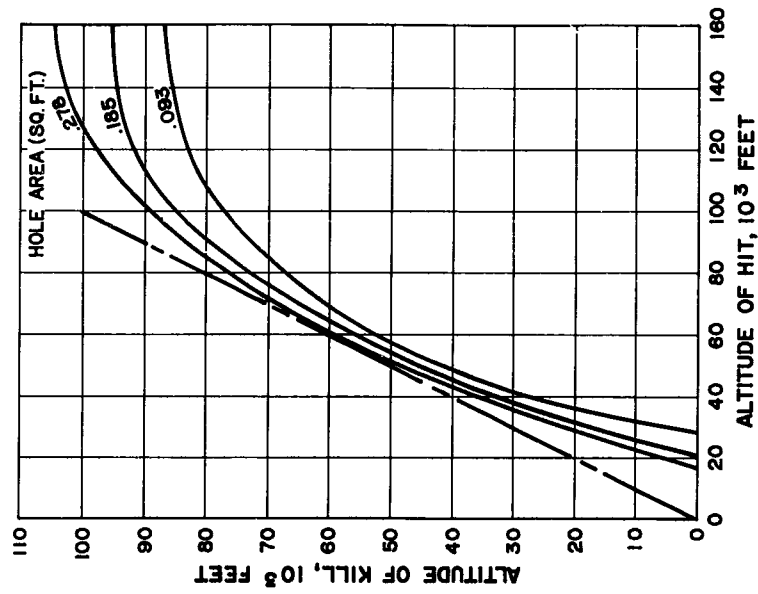


Figure 58. Effect of Hole Size on $T = 0^{\circ}\text{F}$ Failure Condition

SECRET

SECRET

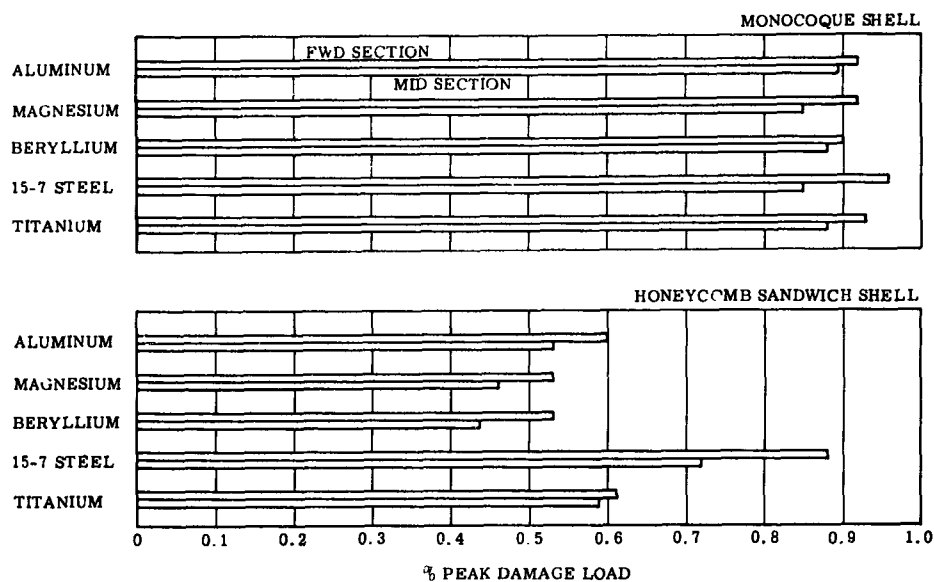


Figure 59. Material Comparison, Vehicle No. 4 ($W/C_D A = 4375$)

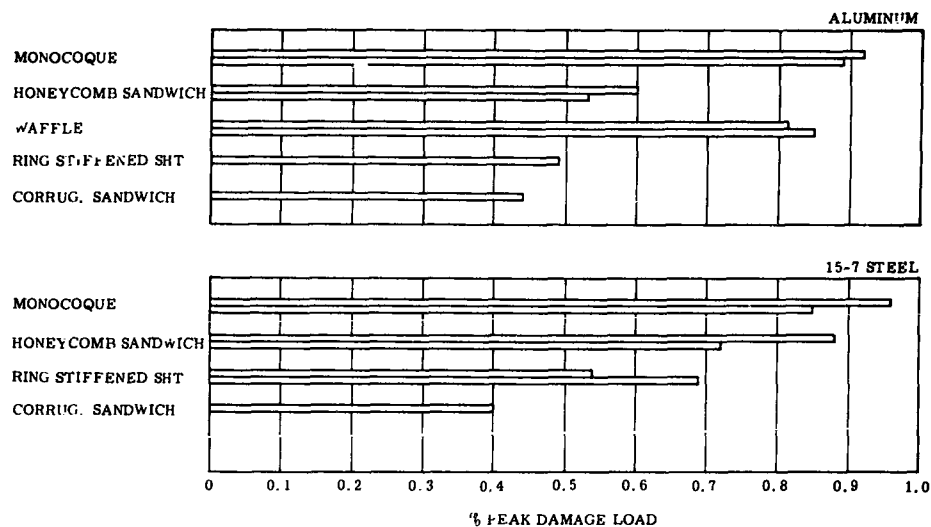


Figure 60. Construction Comparison, Vehicle No. 4 ($W/C_D A = 4375$)

SECRET

SECRET

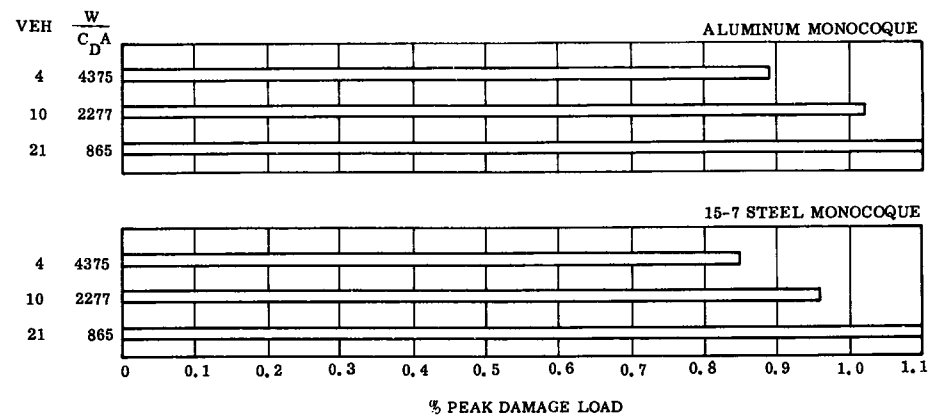


Figure 61. Vehicle ($W/C_D A$) Comparison, Monocoque Structure

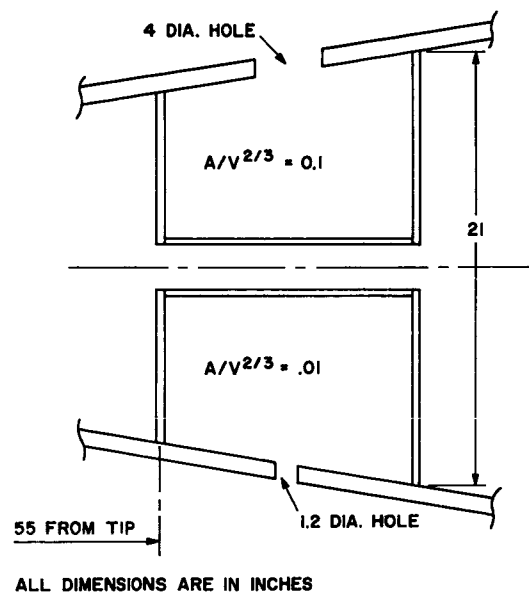


Figure 62. WAC/HKM Experiment Configuration

SECRET

SECRET

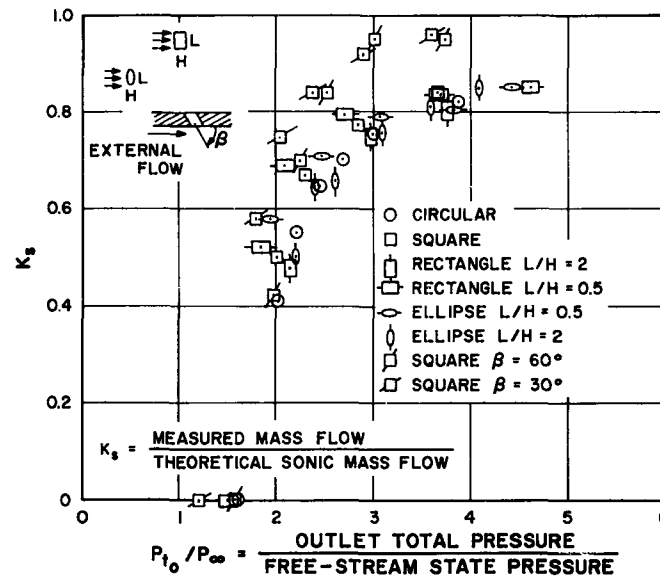


Figure A-1. Discharge Coefficients into Free Stream of $M = 3.25$
(Vick, Reference 12)

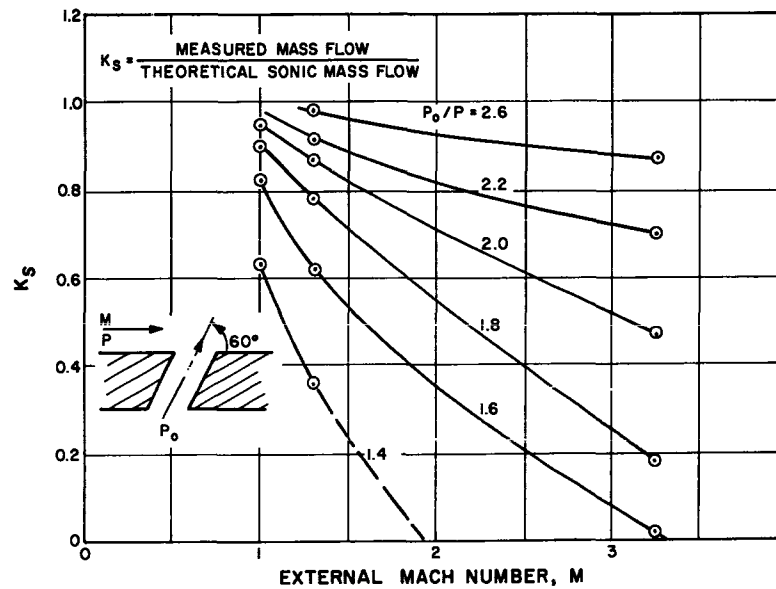


Figure A-2. Effect of External Mach Number on Discharges into Free Stream
(Vick, Reference 12)

SECRET

SECRET

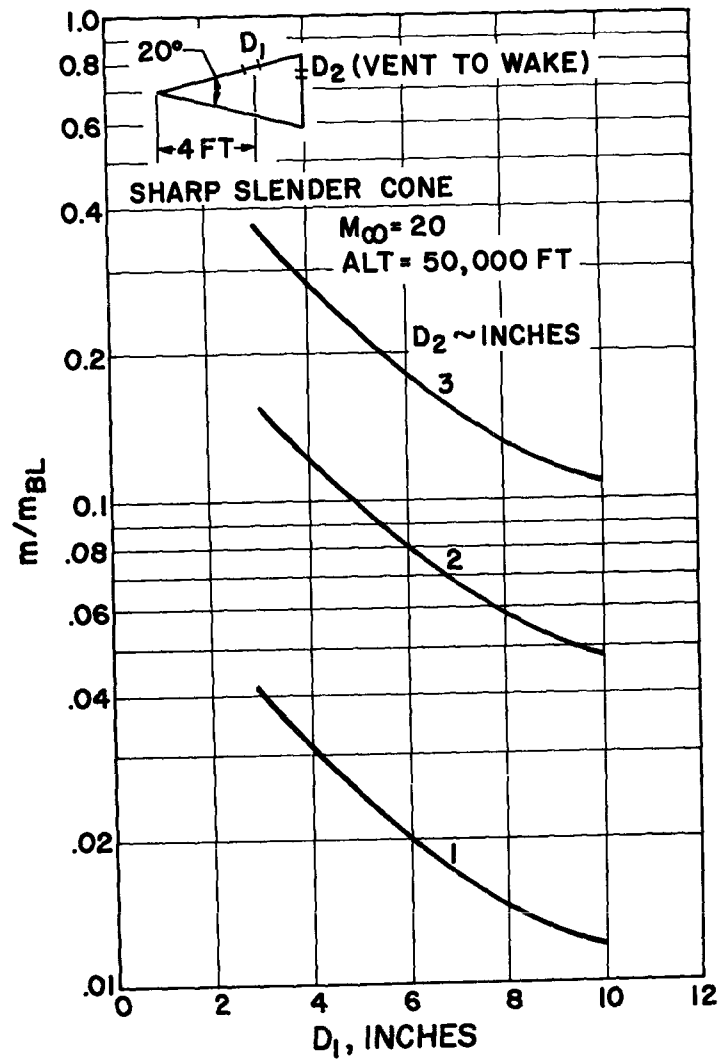


Figure B-1. Variation of Relative Inlet Flow Rate with Inlet and Exit Orifice Diameters

SECRET

H-87

SECRET

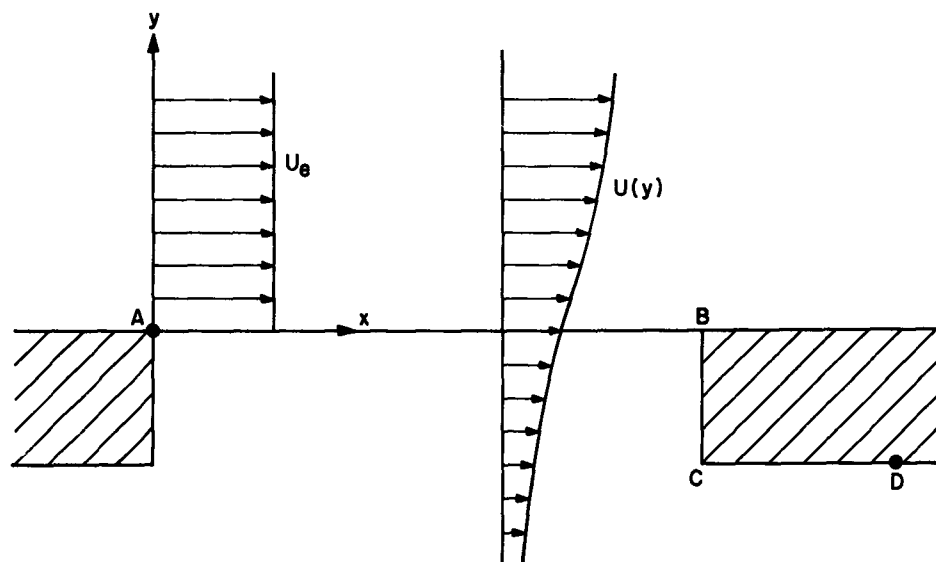


Figure C-1. Shear Layer Flow Past a Perforation

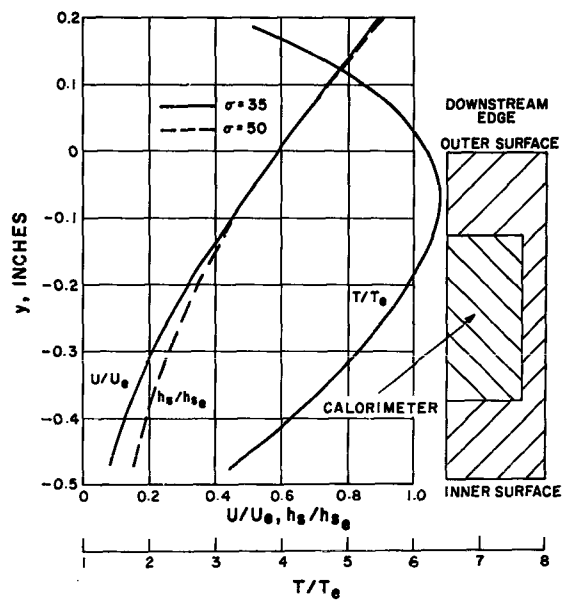


Figure C-2. Laminar Shear Layer Profiles for C. A. L. Internal Heating Tests, $D = 3$ inches

SECRET

SECRET

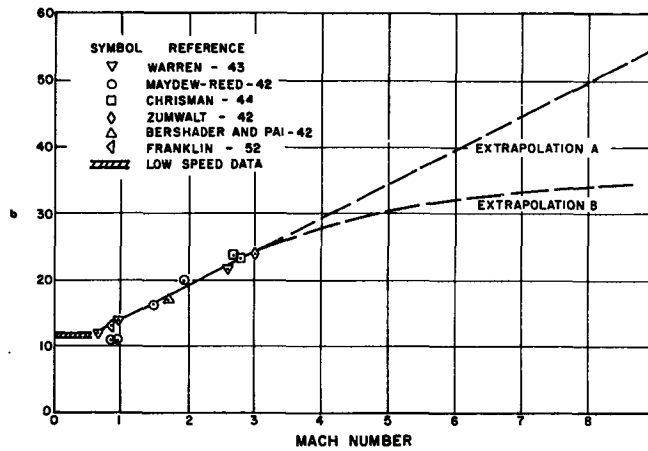


Figure C-3. Effect of Mach Number on Turbulent Mixing Parameter

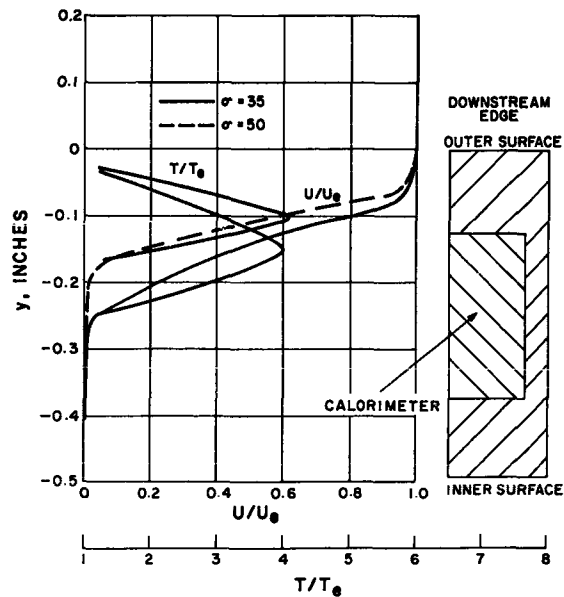


Figure C-4. Turbulent Shear Layer Profiles for C.A.L. Internal Heating Tests, $D = 3$ inches

SECRET

SECRET

H-90

SECRET

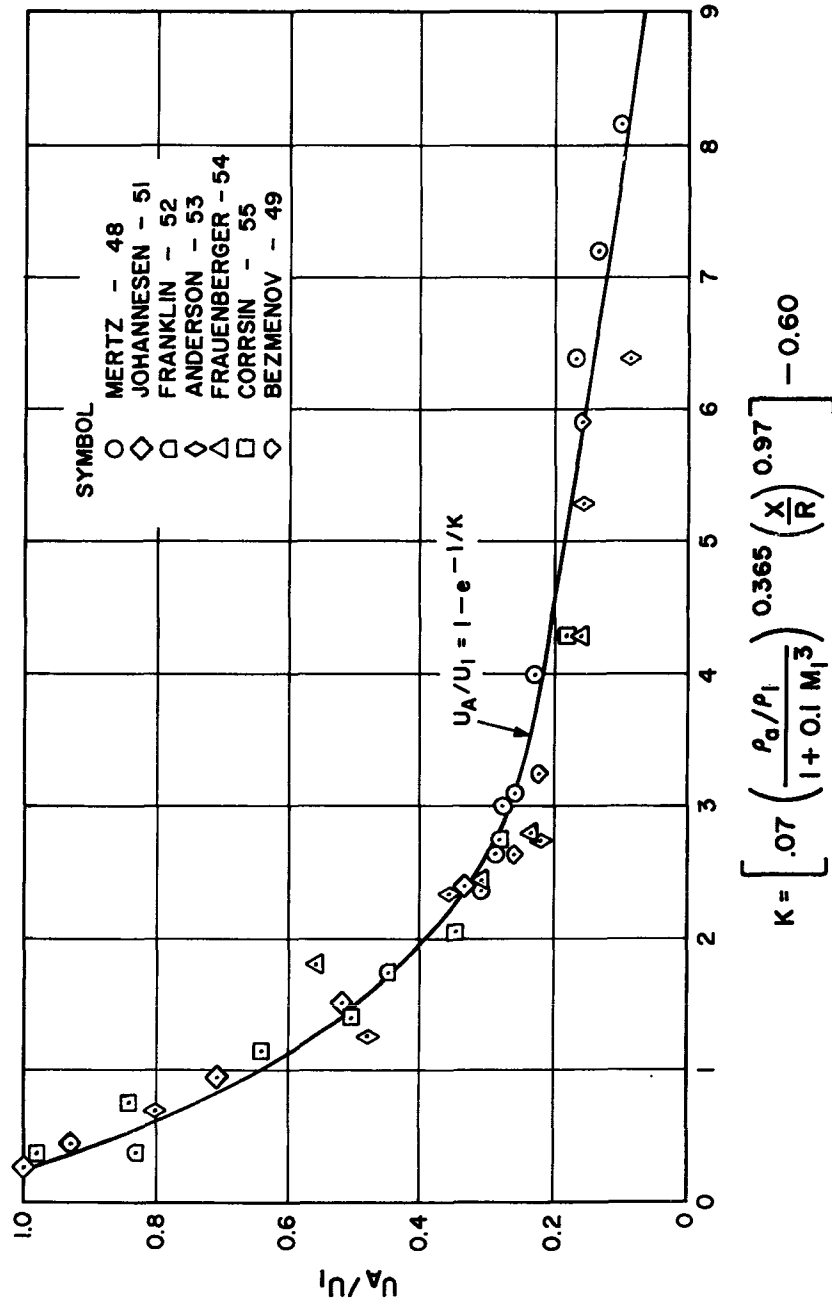


Figure E-1. Comparison of Experimental Axial Velocity Jet Decay to Adjusted Kleinstein Method

SECRET

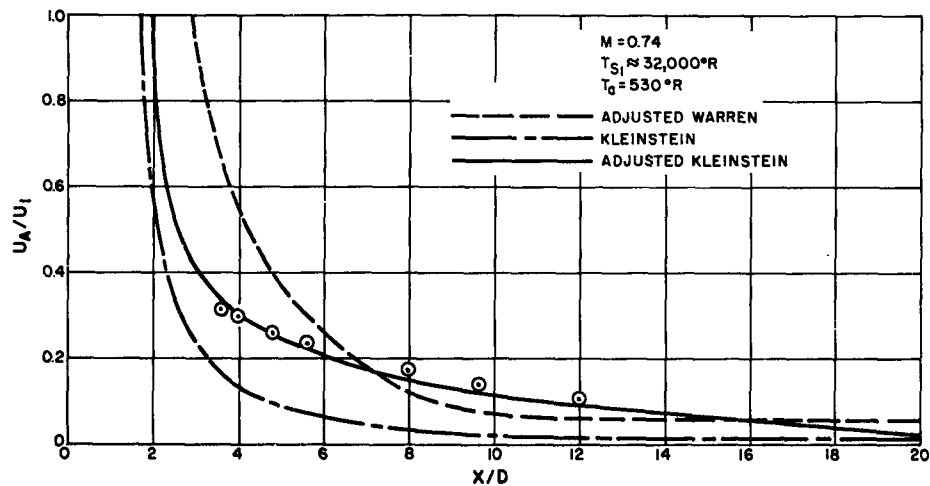


Figure E-2. Comparison of Experimental Axial Velocity Decay with Theoretical and Empirical Predictions, Chicago Midway Arc Jet, $M = .74$

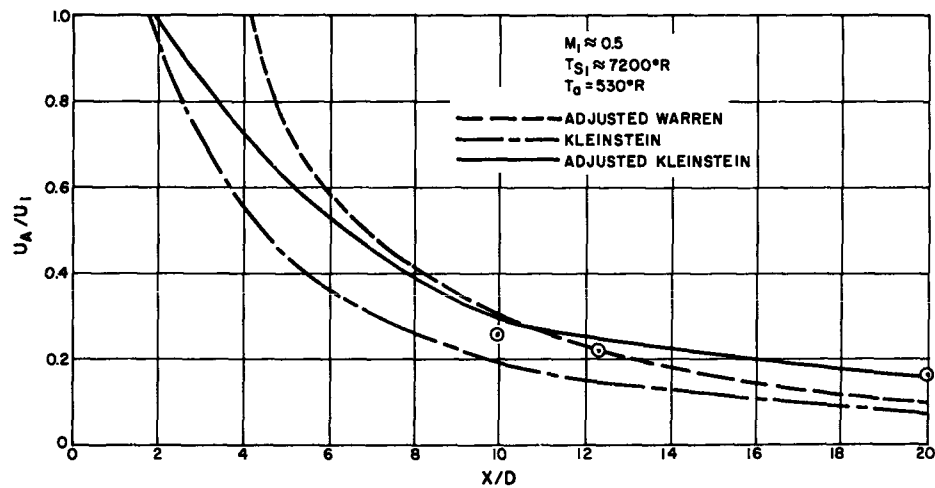


Figure E-3. Comparison of Experimental Axial Velocity Decay with Theoretical and Empirical Predictions; Bezmenov Data (Reference 49)

SECRET

CONFIDENTIAL

ARAP Document Control

No. 7127 Copy 24 of 208

HYPERVELOCITY KILL MECHANISMS PROGRAM (U)

Aerothermal Phase

Annual Technical Progress Report
for Period Ending
20 September 1963

Coleman duP. Donaldson
K. Evan Gray
Roger D. Sullivan
Richard S. Snedeker

Sponsored by
Advanced Research Projects Agency
Ballistic Missile Defense Systems Branch
ARPA Order No. 149-60

This research was supported by the Advanced Research Projects Agency, Ballistic Missile Defense Systems Branch, and was monitored by the U.S. Naval Research Laboratory (Code 6240) under Contract No. Nonr-3903(00)(X).

Aeronautical Research Associates of Princeton, Inc.
50 Washington Road, Princeton, New Jersey

This material contains information affecting the national defense of the United States within the meaning of the espionage laws, Title 18, U.S.C., Sections 793 and 794, the transmission or revelation of which in any manner to an unauthorized person is prohibited by law.

GROUP-3

Downgraded at 12-year intervals;
not automatically declassified.

CONFIDENTIAL

L

UNCLASSIFIED

SUMMARY

Work in support of the Hypervelocity Kill Mechanisms Program carried out by ARAP during the past year in two major areas is summarized and details given of significant results. Studies of special problems encountered under the management and coordination phase of ARAP's program are described as well as the specific theoretical and experimental research on impinging jets and wall jets.

UNCLASSIFIED

L1

UNCLASSIFIED

This page not used

UNCLASSIFIED

L2

INTRODUCTION

Since joining the other contributing research groups under the direction of the Naval Research Laboratory, ARAP has worked in support of the Hypervelocity Kill Mechanisms Program in two distinct areas. This report of progress during the past year therefore, is divided into coverage of the management and coordination aspects of this effort as well as those dealing with basic theoretical and experimental research on jet impingement and wall jet development.

MANAGEMENT AND COORDINATION

Introduction. It has been the responsibility of ARAP, during the past year, to serve the aerothermal phase of the HKM Program in a capacity which may be defined as one of management and coordination. Basically, this task has consisted of assisting NRL in the study and evaluation of the research efforts of the other participating groups, as well as the coordination and planning of their future work in the light of over-all program requirements. Several types of effort have been required, viz., meetings, continuous liaison, special information gathering tasks, and theoretical and experimental investigations of pertinent problems.

In the first instance, three meetings were held among the major participants in order to discuss progress to date and future plans. The recent efforts of each group were summarized and data exchanged where necessary or desirable. In addition, a continuous liaison has been provided between meetings so as to keep the several groups as well as NRL informed of the latest developments.

In response to requests by NRL, ARAP has on several occasions prepared memoranda providing background information on subjects of special interest. Basic theoretical and experimental studies have also been conducted in order to aid in deciding the most likely areas for fruitful investigation on a more comprehensive level by the other major contributors. Several of the problems which have been the subjects of such memoranda or study are discussed in the following paragraphs.

Internal Heating Simulation. One of the first programs to be run at ARAP under the heading of Management and Coordination was a simplified computation to check the prediction of the internal heating of a punctured reentry test vehicle.

CONFIDENTIAL

ARAP's analog-digital hybrid computer provided an ideal facility upon which to run such a computation. A description of this work and a report on the initial results were given in the last annual technical progress report. At that time, the study was concerned with the vented uncoupled flow produced by a hole at the stagnation point plus one or more holes back on the aft portion of the vehicle. (For a discussion of coupled and uncoupled flows, see the section on Coupled Flow Phenomena below.) Recently, as part of the theoretical work pursued at ARAP, an expression for the heat transferred to a cavity for a coupled flow was formulated. The rationale and development of this expression were presented at the Sixth Hypervelocity Impact Symposium as part of a review of the Aerothermal Phase of HKM, and has been included in Progress Report No. 11, Hypervelocity Kill Mechanisms Program, dated June 1963. The analog-digital computer program mentioned above was subsequently modified to obtain heating estimates for coupled flow conditions based upon this newly obtained expression for the heat transfer. Work is currently in progress to predict the internal heating increment of a flight test vehicle subjected to a coupled flow condition by the use of this computational tool.

Kill Probability. One aspect of the Hypervelocity Kill Mechanisms Program which has a direct bearing on its relative feasibility as a potential defense system is the probability of an attacking ICBM running into a destructive pellet. A modest analysis was performed at ARAP during this past year to determine the probability of a warhead hitting two or more pellets as a function of pellet cloud radius, miss distance (the minimum distance from the cloud center to the warhead trajectory), warhead size, and number of pellets. The work is discussed in some detail in ARAP Tech. Memo. 63-2, "Analysis of the Probability of a Vehicle Being Hit while Passing through a Cloud of Particles." Here, only the conclusions will be summarized as follows:

(1) To attain high hit probabilities, the miss distance must be held to very small values for total pellet weight in the 100- to 1,000-pound category. For example, 100 pounds of 10 gram pellets (4,540 pellets) randomly distributed about the surface of an $18r$ -radius cloud must attain a one-sigma miss distance of less than $9r$ to maintain a hit probability of .95 (r is the base radius of the oncoming warhead).

(2) For a specified one-sigma miss distance and number of pellets available, there exists an optimum cloud radius for maximum hit probability. In the above example, this optimum is $18r$. Thus the .95 probability quoted above is the highest attainable for this situation.

(3) For a specified hit probability, the required number

CONFIDENTIAL

of pellets and thus total pellet weight increases approximately as the square of the allowable miss distance.

Localized Heating of Composite Materials. Among the factors contributing to the success or failure of an aerothermal kill is the behavior of the structural material when it is subjected to a high heat flux. While bonded materials of the kind typically used in nose cone construction have been studied intensively for their over-all resistance to thermal loads, little specific information was available on their response to localized heating such as might occur under conditions of a jet impingement-type aerothermal kill mechanism. Under these conditions it appeared possible that a pressure build-up between the outer structural layers due to thermal decomposition outgassing of the bond material could cause structural failure without requiring an amount of heat sufficient to melt the structure. Therefore, a very simple test was carried out in ARAP's laboratory in order to gain some qualitative information for such a localized heating condition. Two material samples were used, each consisting of the same material components, i.e. aluminum, silicone rubber, aluminum filled epoxy resin, and molded phenolic nylon. This material is manufactured by the General Electric Company and is known as GE Target Type 4. One sample had a 1/16" aluminum layer with 1/2" of phenolic nylon and the other had 1/4" of aluminum with 1/16" of phenolic nylon. The bonding materials had a total thickness of about 1/16" in both cases, and the samples measured 7" x 7". Heat was applied at the center of the aluminum side by means of a propane torch flame. Color motion pictures were taken of both sides of the samples during the tests. With a flame temperature of about 2500°F, it was found that both samples tended to fail in the manner suggested, although actual failure occurred only for the sample with 1/16" aluminum. In this case a small crack appeared in the aluminum at the impingement point after the internal pressure build-up had caused an initial bulge. The 1/4" thick aluminum layer of the other sample provided too much heat capacity to allow for a sufficiently rapid localized flux through the material near the impingement point. Although the phenolic nylon did separate at the center initially, the bond release quickly spread to the edges with a subsequent release of internal pressure.

Tests similar to those just described, but with instrumentation for making pressure and temperature measurements and using larger samples are to be conducted in the near future.

Foam Packing Materials. The possibility of protecting reentry vehicle interiors from aerothermal effects by means of a light weight foam packing material was suggested during discussions of possible anti-HKM measures. In order to provide background information on the subject of suitable foams, ARAP prepared

CONFIDENTIAL

CONFIDENTIAL

a memorandum covering the basic characteristics of foams in general and of light weight foams in particular. Of the two families of foams, organic and inorganic, it was found that the organic foams all could be expected to decompose at temperatures much less than 1,000°F, while some of the experimental inorganic foams (graphite, quartz) could be subjected to much higher temperatures. However, the extreme light weights of the organics (urethanes, epoxies, silicones, phenolics) together with the ablative char-layer formation possible in certain cases, seemed to indicate that some existing foams might be applicable for this purpose.

Coupled Flow Phenomena. A coupled flow condition may be described as one in which the presence of a cavity open to the flow has some direct influence on the flow. (Conversely, uncoupled flow is characterized by no such influence on the free stream, the energy addition to the cavity taking place by means of a well defined jet.) However, coupling is more likely when $A/V^{2/3}$ is large, where A is the hole area and V the cavity volume. Computations have shown that very large heat transfer rates are possible across the turbulent shear layer dividing the external and internal flows under such conditions. Some experimental evidence seems to support this conclusion. Because of the many unknown factors peculiar to this phenomenon, however, a small scale wind tunnel investigation has been undertaken by ARAP to try to determine its basic features. A rectangular cavity has been built into the floor of a half-plane Mach 3 supersonic nozzle. The cavity is vented to the free stream through a round hole in the tunnel floor. With provision for changing the cavity volume, a large range of values of $A/V^{2/3}$ is possible depending on the hole size used.

Initial tests with this apparatus which indicated a higher pressure in the cavity than in the free stream, have been superseded by more precise measurements which reveal no such pressure difference. Schlieren pictures of free stream and cavity reveal no observable effects of flow coupling for the range of $A/V^{2/3}$ tested ($.06 \leq A/V^{2/3} \leq .25$). Further study of this problem will involve the measurement of pressure fluctuations in the cavity in the hope that some direct evidence of coupling will be revealed.

IMPINGING AND WALL JET STUDIES

Theoretical. In an effort to achieve a rational theory for the distribution of heat transfer in the region adjacent to an impinging jet three separate, although related, theoretical studies have been undertaken at ARAP. The first, a study of the laminar compressible radial jet, was substantially completed in the previous contract year. The second, a study of the incompressible turbulent wall jet, and the third, a study of transformations relating compressible jet flows to corresponding

CONFIDENTIAL L6

incompressible flows, were undertaken this year.

Early in the year the solution for the laminar compressible radial jet (reported in the last Annual Technical Progress Report, September 20, 1962) was completed by making numerical computations of the term representing the particular solution of the equation for the enthalpy. The term depends on the hypergeometric function with the parameters dependent on the Prandtl number. The calculations were made using ARAP's LGP-30 digital computer for several values of the Prandtl number. The other terms in the solution are elementary functions and so did not need numerical calculation. The rough draft of a paper based in part on that work has been completed. It is intended for submission to the Journal of Fluid Mechanics.

With regard to the second study, the literature on turbulent wall jets has been carefully studied. All previous theoretical investigations have been based on Prandtl's constant exchange coefficient in the outer layer and on Blasius' relation for the wall shearing stress. By virtue of these choices a complete similarity solution of the problem was excluded. However the experiments of all investigators agree on the fact that the nondimensional velocity profiles and shear profiles are independent of the downstream position except possibly for the region nearest to the wall.

Therefore an analysis was made which showed how the experimentally established similarity properties of the flow field could be rationally derived.

In the meantime a new approach to the concept of a transformation which relates a compressible jet flow, either laminar or turbulent, to a corresponding incompressible flow has been developed. This approach uses a general transformation similar to that of Coles. To reduce the transformation to reasonable size, Coles used a limiting value argument which was largely mathematical. The new approach uses the following three assumptions:

- (1) Both the compressible and the corresponding incompressible jet are of the same type of boundary layer flow, specifically, the same type of jets with the same boundary conditions.
- (2) The transformation need be exact only within the boundary layer approximation.
- (3) The order of magnitude of certain of the transformation functions is limited.

The scaling of the coordinate parallel to the jet axis involves the ratio of the shear stresses of the compressible and corresponding incompressible jet. For laminar jets this

UNCLASSIFIED

is no problem. For turbulent jets either a measurement must be performed, or the functional form of the ratio of the compressible shear to the incompressible shear (but not of the shear mechanism itself) has to be specified. Suitable hypotheses for this ratio have been worked out, although they need to be tested by experiment.

This approach shows promise as a very useful tool in analysing and interpreting many compressible jet flows, especially turbulent ones.

Experimental. An experimental program was undertaken for the purpose of clarifying basic gas dynamics effects for compressible free jets impinging on solid surfaces. It is clear that the heat transfer to be expected near the impingement point of a hot jet such as that which might lead to an aerothermal kill, depends on decay processes taking place in the jet before impingement and on the local effects of the impingement itself including the angle of impingement. A major task of this program then, has been to try to establish appropriate parameters for the impingement process so that test data taken under varying conditions might be correlated in a meaningful way. Such correlations might then provide a basis for extrapolation of laboratory results to in-flight conditions.

Stagnation point heat transfer theory shows that the heat transfer rate depends on the radial velocity gradient at the stagnation point. This gradient can, in turn, be computed from the radial pressure distribution with a high degree of accuracy. Such pressure distributions have been measured for a number of impingement conditions.

Four basic shapes were used for impingement surfaces, i.e. flat plate, cylindrical cup, convex hemisphere, and concave hemisphere. Pressure distributions were measured in the vicinity of the stagnation point of each model for three jet pressure ratios at each of four axial impingement distances x . A round sonic nozzle of diameter $d_j = 1/2$ inch blowing down to atmospheric pressure (p_∞) was used. The pressure ratios used were $p_\infty/p^0 = .800, .372, \text{ and } .148$, and the axial locations were $x/d_j = 1.96, 7.32, 23.5, \text{ and } 39.1$. The first pressure ratio (.800) results in a subsonic jet with exit Mach number $M_j = .573$. A pressure ratio of .372 gives an underexpanded jet, sonic at the exit, with oblique shock structure in the core downstream. The third pressure ratio (.148) represents a more highly underexpanded condition in which normal shocks occur in the core structure. Because of the shock structures present in the two underexpanded cases, impingement conditions were found to be highly sensitive to axial position of the model. For this reason, additional pressure distributions were measured at small axial increments in the core region. These additional data were limited to the flat plate model.

UNCLASSIFIED

A typical dependence of radial velocity gradient on axial distance is shown in Figure 1 in which the gradient has been nondimensionalized using jet exit values. It is seen that at axial distances beyond the end of the core, a similar rate of decrease in the parameter takes place. Within the core region, however, there is a strong dependence on local conditions which vary greatly among the three cases tested. When the velocity gradient is nondimensionalized by using the local values of the free jet center line velocity and half-velocity radius for each impingement distance (Figure 2), there is a tendency in the regions downstream of the core to approach a constant value as might be expected for jets with truly "similar" velocity profiles. However, core effects are still seen to be dominant at locations farther upstream. The negative values for $p_{\infty}/p_0 = .148$ in Figure 1, are based on the observation of a region surrounding the stagnation point in which the pressure is higher than it is at the center. This condition could be explained by the presence of an essentially separated region characterized by a vortex ring-like flow in which the flow nearest the surface is toward the center. It appears that such a condition is possible for certain impingement locations within the core when the jet is sufficiently underexpanded to require a normal shock. (This normal shock is, of course, to be distinguished from that associated with the actual impingement of a supersonic flow.) In order to learn more of the details of impingement in such cases, a study of surface flow patterns is under way using a lampblack-grease coating on the model. In addition, a series of schlieren pictures is being taken. Examples of such pictures are shown in Figure 3. These pictures were taken using vertical cut-off and continuous light. Spark pictures will be available in the near future.

A comparison of stagnation point radial velocity gradients for the various model shapes reveals that there is a consistent shape dependence. Values for the convex hemisphere are slightly higher, and values for the concave hemisphere are slightly lower than those for the flat plate. Cylindrical cup values tend to fall close to the concave hemisphere values.

While the results described above are based on conditions of normal impingement ($\alpha = 90^\circ$), additional runs were made for the entire set of jet pressure ratios and impingement distances for the flat plate model at varying impingement angles. Reduction of these data is not complete at this time.

Values of local free jet spreading and decay parameters were taken from results of a separate study of the free jet characteristics of the same nozzle used in the impingement work. This study together with certain of the impingement results will be used as the basis of a paper to be submitted to the Journal of Fluid Mechanics.

UNCLASSIFIED

Experiments on the properties of the wall jet are now under way using the same apparatus described above supplemented with appropriate instrumentation for measuring wall jet velocity profiles. From these measurements, the azimuthal distribution of wall jet momentum will be determined for various flow conditions and impingement angles.

Future experimental work under the HKM Program will examine in more detail the properties of free shear layers such as those which may be encountered in the coupled flow case.

UNCLASSIFIED

L10

UNCLASSIFIED

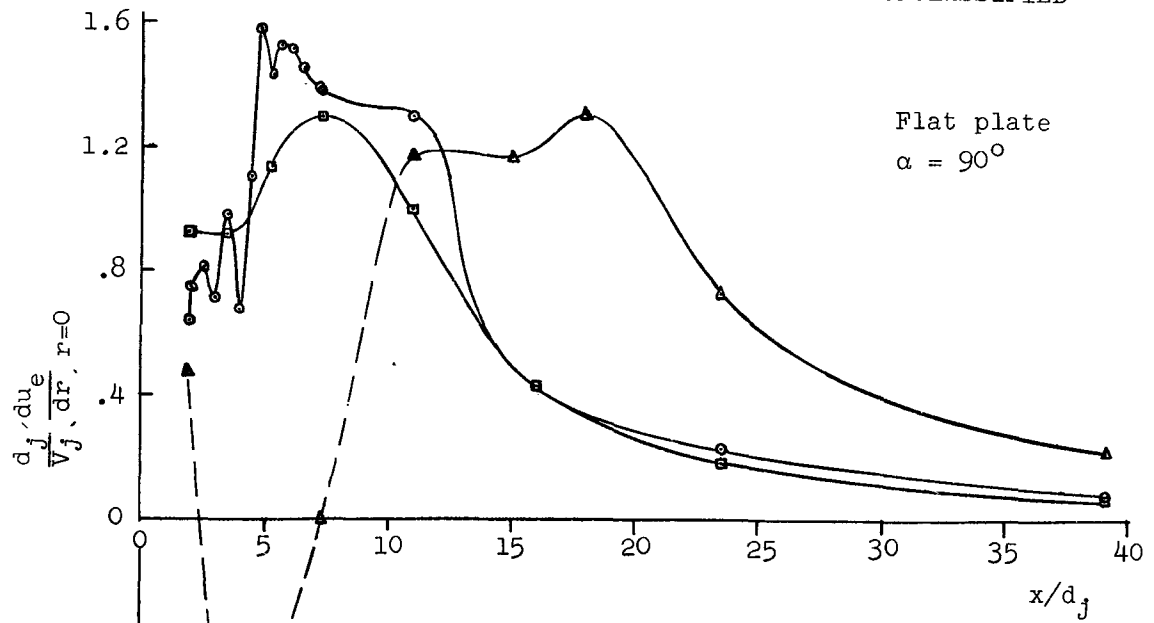


Figure 1

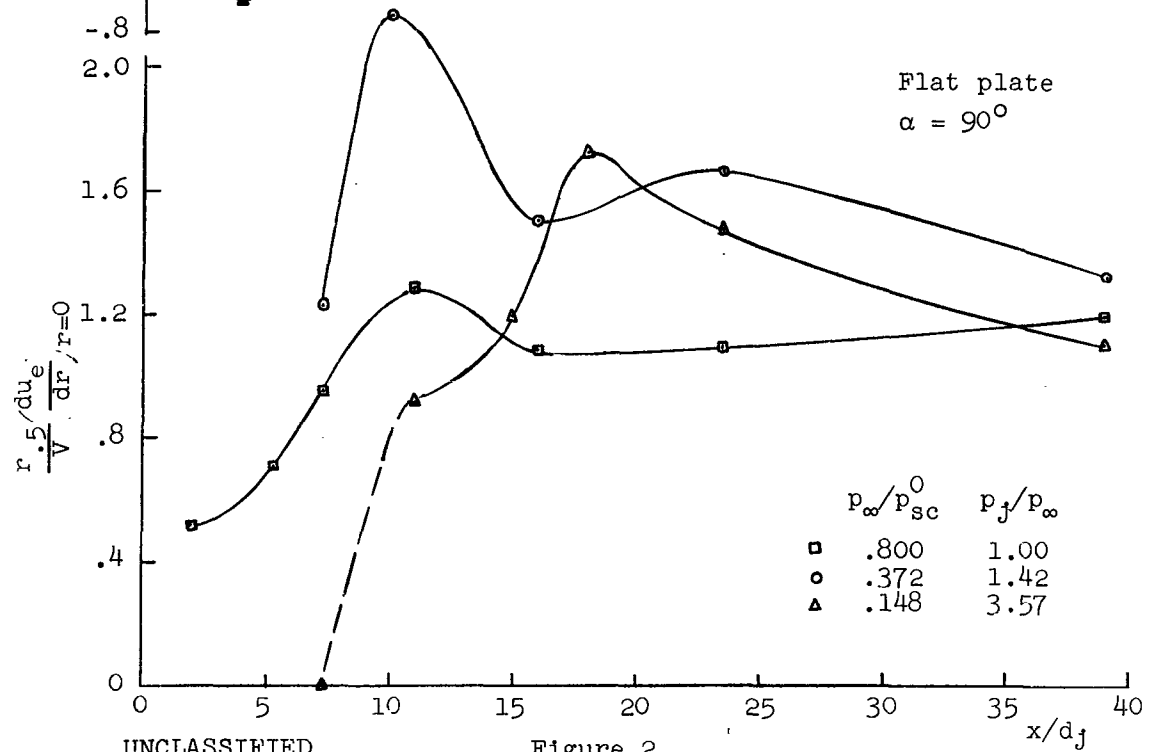
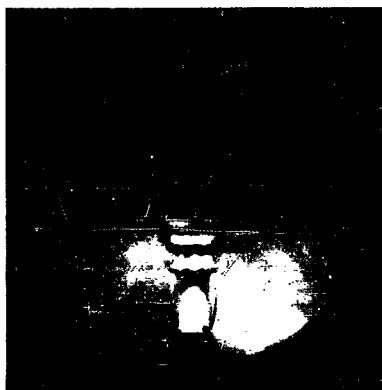


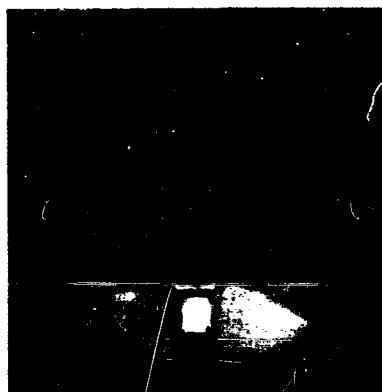
Figure 2



$$x/d_j = 3.91$$



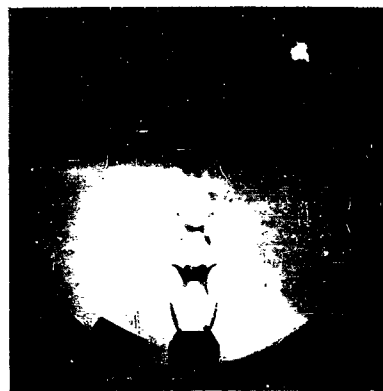
$$x/d_j = 2.60$$



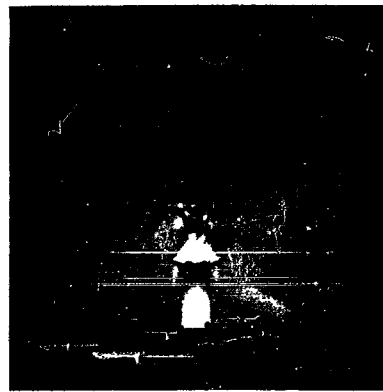
$$x/d_j = 1.96$$



$$x/d_j = 7.32$$



$$x/d_j = 6.24$$



$$x/d_j = 5.32$$

Figure 3. Typical schlieren photographs of axisymmetric jet impinging on flat plate for several impingement distances. $p_\infty/p^0 = .148$, $p_j/p_\infty = 3.57$.

SECRET

HYPERVELOCITY KILL MECHANISMS PROGRAM
ARPA ORDER 149-60

Vulnerability Phase
Final Report

Vulnerability of Nuclear Warheads
to Aerothermal Effects

A. Nordio
TR 3118 (S-RD)

December 1963
Picatinny Arsenal

This report is omitted because prior
distribution has been made by
Picatinny Arsenal

Q

SECRET

SECRET

DISTRIBUTION LIST

	No. of Copies
Director Advanced Research Projects Agency Washington, D. C. 20301	6
Director of Defense Research and Engineering Washington, D. C. 20301	1
Director Weapons Systems Evaluation Group Room 1E 875 Pentagon Washington, D. C. 20301	1
Central Intelligence Agency Washington, D. C. 20505	1
Defense Documentation Center Building #5 Cameron Station Alexandria, Virginia 22314	20
Commander Ballistic Systems Division AFSC, USAF Norton Air Force Base California	2
Commander Space Systems Division AFSC, USAF, AF Unit Post Office Los Angeles 45, California 90045	2
Commander Hq. AFCCDD (ESRB) (Major Hippler) LG Hanscom Field Bedford, Massachusetts 07131	1
Commander Detachment 4, ASD, AFSC U.S. Air Force Eglin Air Force Base, Florida 32542 Attn: Mr. Dale Davis Technical Library (PGTRI)	2
Commander Air Force Special Weapons Center Kirtland Air Force Base, New Mexico 87117 Attn: MAJOR M.R. Nedler, SWRA CAPT Gillespie (S WRA-3175)	2

SECRET

SECRET

No. of Copies

Air University Library	1
U.S. Air Force	
Maxwell Air Force Base 36112	
Alabama	
Commander	3
Aeronautical Systems Division, AFSC, USAF	
Wright-Patterson Air Force Base, Ohio 45433	
Attn: ASRCEA/LT D.L. Wells	
ASRNGW-1/ Leo Krautmann	
AF Technical Information Center	
Headquarters	1
United States Air Force	
Air Force Technical Applications Center/TD, Wash., D.C.	
Director, Ballistic Research Laboratories	2
Aberdeen Proving Ground, Aberdeen, Maryland 21005	
Attn: Dr. R.J. Eichelberger (TBL)	
Dr. C. Glass	
Officer in Charge	1
U.S. Continental Army Command	
Office of Special Weapons Developments	
Fort Bliss, Texas 79916	
Attn: CAPT T.W. Love	
Commanding Officer	
U.S. Army Air Defense Combat Development Agency	1
Fort Bliss, Texas 79916	
Attn: MAJOR J.V. Hemler	
Commanding Officer	1
Army Material Command RD	
Washington, D. C. 20315	
Attn: Mr. G. Stetson	
Commanding Officer	2
Picatinny Arsenal	
Dover, New Jersey 07801	
Attn: Mr. Fred Saxe	
Dr. A. Nordio	
Commander	
U.S. Army Missile Command	5
Redstone Arsenal	
Huntsville, Alabama 35809	
Commander	2
Field Command	
Defense Atomic Support Agency (DASA)	
Sandia Base, P.O. Box 5800	
Albuquerque, New Mexico 87115	
Attn: CDR. P.P. Krell	

SECRET

SECRET

	No. of Copies
Chief of Naval Operations (OP-761) Department of the Navy Washington, D. C. 20350	1
Chief of Naval Operations (OP9221D) Department of the Navy Washington, D. C. Attn: Mr. E. Cecil 20350	1
Chief Bureau of Naval Weapons (RTAD) Attn: D.J. Brockway Washington, D. C. 20360	1
Commanding Officer U.S. Naval Air Development Center Johnsville, Pennsylvania	1
Commanding Officer U.S. Naval Weapons Evaluation Facility Kirtland Air Force Base New Mexico Attn: Code 3432 Mr. C.B. Massengill	1
Director U.S. Naval Research Laboratory Washington, D. C. 20390 Attn: Mr. W. W. Atkins	3
Director, National Aeronautics & Space Administration Langley Research Center, Langley Field, Virginia 23365 Attn: Mr. R. Hopko	1
University of California Lawrence Radiation Laboratory Technical Information Division P.O. Box 808, Livermore, California 94557 Attn: Clovis G. Craig	1
Aeronautical Research Associates of Princeton, Inc. 50 Washington Road Princeton, N. J. 08540 Attn: Dr. C. duP. Donaldson	2
Aerospace Corporation P. O. Box 95085 Los Angeles 45 California Attn: Library Technical Documents Group Dr. D. Singer Dr. J. Brown	3

SECRET

	No. of Copies
AVCO Corporation Research and Advanced Development Division 201 Lowell Street Wilmington, Massachusetts 01887 Attn: Mr. R.S. Timmins	2
Battelle Memorial Institute 505 King Avenue Columbus 1, Ohio 43201 Attn: Battelle - Defender	2
Bell Telephone Laboratories, Inc. Whippany, New Jersey Attn: Mr. D. Pope	1
Douglas Aircraft Company, Inc. Missiles and Space Systems 3000 Ocean Park Boulevard Santa Monica, California Attn: Mr. T.J. Wolinski	1
General Atomic P. O. Box 608 San Diego 12, California Attn: Mr. A. J. Navoy	1
General Electric Company Missile and Space Vehicle Department 3198 Chestnut Street Philadelphia 4, Pennsylvania 19104 Attn: D. Nestler	2
Hughes Aircraft Company Culver City, California Attn: Mr. G. Henry	2
Institute of Defense Analysis 1666 Connecticut Avenue, N. W. Washington, D. C. 20009	1
Rand Corporation 1700 Main Street Santa Monica, California 90406 Attn: Library 79	1
Shock Hydrodynamics 2444 Wilshire Blvd. Santa Monica, California Attn: K.N. Kreyenhagen	1

SECRET

ARPA 149 TECHNICAL REPORTS

1. Raytheon Company, "Soviet ICBM Re-Entry Body Study," BR-1065, 21 November 1960 (S-RD)
2. Progress Report No. 1, "Hypervelocity Kill Mechanisms Program," NRL Memorandum Report 1136, January 1961 (S-RD)
3. AVCO Corporation, "Feasibility Study of a Flight Test Aggravation Program, Hypervelocity Kill Mechanism Program, Aerothermal Phase," TAD-TR-29-61-4, 13 February 1961 (S)
4. Progress Report No. 2, "Hypervelocity Kill Mechanisms Program," NRL Memorandum Report 116, April 1961 (S-RD)
5. Progress Report No. 3, "Hypervelocity Kill Mechanisms Program," NRL Memorandum Report 1209, July 1961 (S-RD)
6. Summary Report, "Fifth Hypervelocity Kill Mechanisms Progress Meeting," of 29-30 June 1961, NRL Memorandum Report 1220, August 1961 (S-RD)
7. Progress Report No. 4, "Hypervelocity Kill Mechanisms Program," NRL Memorandum Report 1240, Quarterly Progress for Period Ending 20 September 1961 (S-RD)
8. "Force Tests on Modified General Electric Mark III Nose Cone Models at Mach Number 18," AEDC-TN-61-151, von Karman Gas Dynamics Facility, ARO, Inc., November 1961 (S)
9. Progress Report No. 5, "Hypervelocity Kill Mechanisms Program," NRL Memorandum Report 1261, Volume I and Volume II, Annual Technical Progress Report December 1961 (S-RD)
10. Progress Report No. 6, "Hypervelocity Kill Mechanisms Program," NRL Memorandum Report 1269, Quarterly Progress for the Period Ending 20 December 1961 (S-RD)
11. NRL Memorandum Report 1314, "Investigation of ICBM Vulnerability to ARPAT Dart," 30 April 1961 (S-RD)
12. General Electric Company, "Hypervelocity Kill Mechanisms Feasibility Study-Internal Heating," Document No. 62SD56, 28 May 1962 (S)
13. Progress Report No. 7 "Hypervelocity Kill Mechanisms Program," NRL Report 5813, Semi-annual Technical Progress Report for period ending 20 March 1962 - June 1962 (S-RD)
14. Progress Report No. 8, "Hypervelocity Kill Mechanisms Program," NRL Report 5840, Quarterly Progress Report for Period ending 20 June 1962 (S-RD)
15. Progress Report No. 9, "Hypervelocity Kill Mechanisms Program," NRL Report 5913, Annual Technical Progress Report for period ending 30 September 1962 (S-RD) Vols. I, and II.
16. Progress Report No. 10, "Hypervelocity Kill Mechanisms Program," NRL Report 5931, Quarterly Progress Report for period ending 20 December 1962 (S-RD)
17. General Electric Company, Results of Rocket Exhaust HKM Internal Heating Tests, Document No. 63SD564 of 20 May 1963 (S).
18. Progress Report No. 11, "Hypervelocity Kill Mechanisms Program," NRL Report 5990, Semiannual Technical Progress Report for Period Ending 20 March 1963.
19. Progress Report No. 12, "Hypervelocity Kill Mechanisms Program," NRL Report 6011, August 1963 (S)
20. NRL Report No. 6032 "Hypervelocity Impact Damage to Space Structures by Massive Projectiles," October 1963 (S).
21. General Electric Company, "Results of Wallops Island HKM Internal Heating Flight Tests," Document No. 63SD885, 4 November 1963 (S)
22. Picatinny Arsenal T.R. No. 3118, "Vulnerability of Nuclear Warheads to Aerothermal Effects", December 1963 (S-RD).

SECRET

JAN 13 2003

Naval Research Laboratory
Technical Library
Research Reports Section

DATE: December 20, 2002
FROM: Mary Templeman, Code 5227
TO: Code 6300 Dr Gubser
CC: Tina Smallwood, Code 1221.1 *ts 1/6/03*
SUBJ: Review of NRL Reports

Dear Sir/Madam:

Please review NRL Report 6214, 6077, 6011, 6265-V1 and 6265-V2 for:

- ☒ Possible Distribution Statement
☒ Possible Change in Classification

Thank you,

Mary Templeman
Mary Templeman
(202)767-3425
maryt@library.nrl.navy.mil

The subject report can be:

- ☒ Changed to Distribution A (Unlimited)
☒ Changed to Classification *unclassified*
☐ Other:

Dr Gubser *1/2/03*
Signature Date